

This electronic thesis or dissertation has been downloaded from the King's Research Portal at <https://kclpure.kcl.ac.uk/portal/>



**A biophysical investigation of a membrane-active cyclodextrin-inliposome formulation for antibiotic delivery**

Vandera, Kalliopi-Kelli Apostolos

*Awarding institution:*  
King's College London

The copyright of this thesis rests with the author and no quotation from it or information derived from it may be published without proper acknowledgement.

**END USER LICENCE AGREEMENT**



**Unless another licence is stated on the immediately following page** this work is licensed

under a Creative Commons Attribution-NonCommercial-NoDerivatives 4.0 International

licence. <https://creativecommons.org/licenses/by-nc-nd/4.0/>

You are free to copy, distribute and transmit the work

Under the following conditions:

- Attribution: You must attribute the work in the manner specified by the author (but not in any way that suggests that they endorse you or your use of the work).
- Non Commercial: You may not use this work for commercial purposes.
- No Derivative Works - You may not alter, transform, or build upon this work.

Any of these conditions can be waived if you receive permission from the author. Your fair dealings and other rights are in no way affected by the above.

**Take down policy**

If you believe that this document breaches copyright please contact [librarypure@kcl.ac.uk](mailto:librarypure@kcl.ac.uk) providing details, and we will remove access to the work immediately and investigate your claim.

# A biophysical investigation of a membrane-active cyclodextrin-in-liposome formulation for antibiotic delivery

A thesis submitted by

Kelly-Kalliopi Vandera

In fulfilment of the requirement for the degree of Doctor of Philosophy in the Institute of Pharmaceutical Science of the School of Biomedical and Life Sciences

2018

Department of Pharmacy

King's College London

October, 2018

## Acknowledgements

First, I would like to express my deepest gratitude to Dr. Richard Harvey and Dr. Cecile Dreiss for imparting their knowledge and offering their invaluable support and guidance throughout my research. They are both exceptional supervisors and friends! I could not have asked for better supervisors. I truly appreciate their help and encouragement!

I would like to thank Dr. Stuart Jones for believing in me during my MSc research project and introducing me to Richard as my PhD supervisor. A further big thank you to Dr. Miraz Rahman for his warm welcome into his lab, as well as Dr. Kazi Nahar and Dr. Pietro Picconi for teaching me drug synthesis. I would also like to thank Dr. Andrew Chan for enlightening me with his expertise; and Dr. Ken Bruce for both letting me work in the microbiology lab and his advice on how to write a thesis. I greatly appreciate the assistance of Dr. Luke Clifton and Dr. Maximilian Skoda during my neutron time at the ISIS facilities. A big thanks goes to Professor Peter Hylands and Nicola Tingley for their assistance when I was “banned” accidentally from KCL (funny, but it is true!).

I acknowledge all the people that helped me throughout my PhD: Dr. Gianluca Bello for giving me advice and tips on Langmuir trough, when I was really struggling to find answers to things that didn't make any sense; Dr. Helene Marbach, Dr. Masirah Zain, Dr. Arcadia Woods, Dr. Giorgia Manzo, Dr. Margarita Valero and Dr. Raquel Barbosa for their invaluable help concerning microbiology and formulation techniques; and Simona Di Blasio, DeDe and Caroline thank you for your advice and your support. I am really grateful to you all for making my PhD life more enjoyable, full of smiles and good vibes.

Last but not least, I would like to thank my family for their endless support. I am exceptionally grateful to my late father, Apostole Vanderas, for providing me with the ethical foundation, strength and patience to achieve my life goals, during the first 17 years of my life, and my mother, Sophia Dimeli, for being both a mother and a father up to now. Mum, thank you from the bottom of my heart for being my mainstay throughout the PhD. Chryssanthi Vandera, thank you for being such a supportive sister and stand beside me at every step of my PhD. I would also like to thank my in-laws, John and Katie Gateley, for supporting me through this journey. A special thanks goes to my beloved husband, Dimitri Gateley, for believing in me, supporting and encouraging me over the last 4 years. I am grateful for having such an affectionate husband, who loves me unconditionally and makes me smile.

Thank you all for being part of this journey!

# List of publications

Hubbard ATM, Barker R, Rehal R, Vandera K-KA, Harvey RD, Coates ARM. Mechanism of Action of a Membrane-Active Quinoline-Based Antimicrobial on Natural and Model Bacterial Membranes. *Biochemistry*. 2017;56(8):1163-1174.

Kumar A, Terakosolphan W, Hassoun M, Vandera K-KA, Novicky A, Harvey RD, Royall PG, Bicer EM, Eriksson J, Edwards K, Valkenborg D, Nelissen I, Hassall D, Mudway IS, Forbes B. A Biocompatible Synthetic Lung Fluid Based on Human Respiratory Tract Lining Fluid Composition. *Pharm Res*. 2017;34(12):2454-2465.

Urbano L, Clifton L, Ku HK, Kendall-Troughton H, Vandera K-KA, Matarese BFE, Abelha T, Li P, Desai T, Dreiss CA, Barker R, Green M, Dailey LA, Harvey RD. Influence of the Surfactant Structure on Photoluminescent  $\pi$ -Conjugated Polymer Nanoparticles: Interfacial Properties and Protein Binding. *Langmuir*. 2018;34(21):6125-6137.



# Abstract

Gram-negative bacteria possess numerous defence mechanisms against antibiotics, due to the intrinsic permeability barrier afforded by their outer membrane and the various efflux mechanisms which pump out drugs, explaining the recalcitrance of some common and life-threatening infections. A novel compound, PPA148, was synthesised in-house and showed promising activity against Gram-negative bacteria. Nevertheless, in some clinical bacterial strains, drug efflux resulted in reduced efficacy was observed, which was reversed in the presence of the efflux pump inhibitor phenylalanine-arginine  $\beta$  naphthylamide (PA $\beta$ N). A formulation of PPA148 consisting of a drug/cyclodextrin (drug/CD) complex encapsulated in liposomes is investigated as a way to increase drug uptake. PPA148 has very low water solubility, which was measured using spectroscopic techniques: photon correlation spectroscopy (PCS) and Ultra-Violet spectroscopy (UV). Its solubility is improved by complexation with  $\beta$ CD derivatives (HP $\beta$ CD and RAMEB) and the complex is characterized by applying nuclear magnetic resonance (NMR) and fluorescence. Fluidosomes, loaded with the drug/CD complex, are manufactured by applying the thin-film hydration method followed by extrusion for reducing the size of liposomes. PCS is used to size the particles and measure their zeta-potential. A Stewart assay and UV were used to quantify the lipid and drug concentration respectively, in the final formulation. A disk diffusion microbiological assay is used to assess the efficacy of the formulation against *E. coli* (DH5a). A variety of in vitro biophysical techniques are used to assess the mechanism of the drug uptake. Phospholipids, Re Lipid A extracted from *S. Minnesota* and Rc J5 LPS extracted from *E. coli* are used to make a synthetic monolayer and bilayer model of the outer and inner bacterial membranes. They are adapted for use with the Langmuir trough (LT) and neutron reflectivity (NR) techniques to monitor changes occurring upon interaction with the drug alone and the formulated drug. The results revealed an possible increase in drug efficacy with a possible fusion mechanism of uptake. NR provides a new method to examine the fusion mechanism of fluidosomes with bacterial membrane.

# Table of Contents

<i>Acknowledgements</i> .....	<i>i</i>
<i>List of publications</i> .....	<i>ii</i>
<i>Abstract</i> .....	<i>iii</i>
<i>Table of Contents</i> .....	<i>iv</i>
<i>Table of Figures</i> .....	<i>viii</i>
<i>Table of Tables</i> .....	<i>xv</i>
<i>Abbreviations</i> .....	<i>xvii</i>
<i>Symbols</i> .....	<i>xix</i>
<i>Physical Constants</i> .....	<i>xxi</i>
<b>Chapter 1    General Introduction</b> .....	<b>1</b>
<b>1.1 Antibiotics and Bacteria: a unique class of medicines and pathogens</b> .....	<b>2</b>
<b>1.2 Antibiotic classification</b> .....	<b>2</b>
<b>1.3 Bacterial classification</b> .....	<b>3</b>
1.3.1 Physicochemical properties of antibiotics.....	3
1.3.2 Gram negative bacterial cell envelope as a barrier to antibiotics .....	4
1.3.3 Drug uptake mechanisms .....	6
<b>1.4 Antimicrobial Resistance (AMR)</b> .....	<b>7</b>
1.4.1 Causes of AMR.....	8
1.4.2 Mechanisms of bacterial resistance .....	9
<b>1.5 Strategies to combat antimicrobial resistance</b> .....	<b>10</b>
1.5.1 Drug development.....	11
1.5.2 Antibiotic combination therapy .....	11

<b>1.6 Formulation approaches for antimicrobials to overcome resistance .....</b>	<b>13</b>
1.6.1 Cyclodextrin-drug complexes .....	13
1.6.2 Liposomal carriers .....	16
<b>1.7 Aims and scope of this project.....</b>	<b>17</b>
1.7.1 Drug-in-Cyclodextrin-in-Liposomes .....	18
1.7.2 Plan of the study and techniques used .....	19
1.7.3 Interfacial techniques used to investigate drug-membrane interactions .....	20
<b>Chapter 2     <i>Synthesis, characterization and solubility of PPA148.....</i></b>	<b>28</b>
<b>2.1 Introduction .....</b>	<b>29</b>
<b>2.2 Materials.....</b>	<b>32</b>
<b>2.3 Methods .....</b>	<b>33</b>
2.3.1 Synthetic pathway of PPA148 .....	33
2.3.2 Thin Layer Chromatography (TLC).....	37
2.3.3 Liquid Chromatography-Mass Spectrometry (LC/MS).....	37
2.3.4 Nuclear Magnetic Resonance (NMR) spectroscopy .....	38
2.3.5 Fourier Transform Infra-Red (FTIR) Spectroscopy.....	38
2.3.6 Adsorption assay .....	38
2.3.7 Ultra Violet Spectroscopy.....	39
2.3.8 Turbidimetric Assay.....	40
2.3.9 Water Solubility Test .....	40
2.3.10 Quantification of drug:cyclodextrin binding constant by fluorescence spectroscopy .....	41
2.3.11 Phase solubility diagram.....	41
2.3.12 Continuous method variation (Job's plot) (156).....	43
<b>2.4 Results .....</b>	<b>44</b>

2.4.1 Synthesis.....	44
2.4.2 Physicochemical characteristics .....	50
<b>2.5 Discussion .....</b>	<b>58</b>
<b>2.6 Conclusion .....</b>	<b>62</b>
<b>Chapter 3    <i>Liposomal encapsulated drug/cyclodextrin inclusion complexes</i> .....</b>	<b>63</b>
<b>3.1 Introduction .....</b>	<b>64</b>
<b>3.2 Materials.....</b>	<b>66</b>
<b>3.3 Methods .....</b>	<b>66</b>
3.3.1 Formation of Large Multi-Lamellar Fluidosomes .....	66
3.3.2 Size reduction methods for the manufacture of Fluidosomes .....	67
3.3.3 Preparation of drug-cyclodextrin inclusion complexes .....	67
3.3.4 Incorporation of drug/cyclodextrin complexes into liposomes .....	67
3.3.5 Size Exclusion Chromatography .....	67
3.3.6 Photon Correlation Spectroscopy (PCS) .....	68
3.3.7 Stewart assay.....	68
3.3.8 Drug quantification.....	69
3.3.9 Kirby Bauer assay .....	70
3.3.10 Dispersion stability of empty fluidosomes .....	71
3.3.11 Statistical analysis.....	71
<b>3.4 Results .....</b>	<b>71</b>
3.4.1 Characterization of empty/control Fluidosomes.....	71
3.4.2 Characterization of drug-CD inclusion complexes in the Fluidosomes .....	75
3.4.3 Encapsulation Efficiency and Drug Loading .....	76
3.4.4 Kirby Bauer assay .....	77

<b>3.5 Discussion .....</b>	<b>80</b>
<b>3.6 Conclusion .....</b>	<b>84</b>
<b>Chapter 4    <i>A biophysical investigation into the uptake mechanism of PPA148 and its delivery system</i>.....</b>	<b>86</b>
<b>4.1 Introduction .....</b>	<b>87</b>
<b>4.2 Materials.....</b>	<b>90</b>
<b>4.3 Methods .....</b>	<b>90</b>
4.3.1 Surface Pressure-Area isotherms at the air-liquid interface .....	90
4.3.2 Drug - monolayer interaction .....	91
4.3.3 Drug - lipid bilayer interaction using fluorescence spectroscopy.....	92
4.3.4 Neutron reflectivity of asymmetric bilayer of DPPC and LPS and interaction with fluidosomes .....	93
<b>4.4 Results .....</b>	<b>97</b>
4.4.1 Surface Pressure-Area isotherms of Langmuir monolayers at the air-liquid interface .....	97
4.4.2 Drug interactions with model inner membranes .....	101
4.4.3 Drug interaction with model outer membranes .....	107
<b>4.5 Discussion .....</b>	<b>115</b>
<b>4.6 Conclusion .....</b>	<b>119</b>
<b>Chapter 5    <i>General Conclusion</i> .....</b>	<b>120</b>
5.1.1 Future Work .....	123
<b>References .....</b>	<b>125</b>
<b>Appendix A.....</b>	<b>141</b>
<b>Quantum-mechanic rule .....</b>	<b>141</b>
<b>Appendix B.....</b>	<b>142</b>
<b>Appendix C.....</b>	<b>145</b>

# Table of Figures

Figure 1.1: Mechanism of action of some major antibiotic agents reproduced from Clatworthy et al. (10). .....	3
Figure 1.2: Cell envelope of Gram-negative bacteria reproduced from Silhavy et al. (18). .....	5
Figure 1.3: Structure of phospholipid headgroups with different substitution in the phosphate group which gives a different curvature and charge. R1 and R2 are the fatty acid chains which can be either saturated (PC with C16:0 is DPPC while PC with C14:0 is DMPC) or unsaturated (PC with C16:1 is POPC). .....	6
Figure 1.4: Different ways by which a substance can be transported across the membranes reproduced from Bolla et al., (34). Hydrophilic components and nutrients can pass through porins (a) and hydrophobic molecules diffuse through the OM and/or IM (b and d respectively). The diffusion through the periplasm which is packed with proteins is represented by (c). Drugs can be recognised as foreign molecules by the efflux pumps (e and f) and can be transported out of the membranes. Several pumps such as AcrA/B and AcrE/F must recruit the OM barrel protein such as TolC (g) in order to expel drugs directly out of the cell (35). .....	7
Figure 1.5: Timeline of antibiotics from their market introduction (red line) to the first observations of drug resistance, which is represented by a blue 'X'. The figure is reproduced and adapted for the needs of this report from Kennedy et al. (37). .....	8
Figure 1.6: Mechanisms through which drug resistance can be spread horizontally from one bacterium to another reproduced from Levy et al. (9). .....	10
Figure 1.7: Mechanism of pro-drug platform, reproduced by Kim Lewis (70). The prodrug enters the cell and is converted into the reactive drug by a bacteria-specific enzyme (E). Inside the cell, the reactive compound covalently binds to unrelated targets, T1, T2 and T3, which causes cell death. This mechanism kills not only dividing cell but also dormant cell. ....	13
Figure 1.8: Native cyclodextrin structures for $\alpha$ -, $\beta$ - and $\gamma$ -cyclodextrin (CD). .....	14
Figure 1.9: Chemical structure of rifampicin, gentamicin and chlorhexidine. ....	20
Figure 1.10: Structure of Ra LPS derived from <i>E. coli</i> EH100, Rc LPS derived from <i>E. coli</i> J5 and Re LPS derived from <i>S. minnesota</i> . .....	22
Figure 1.11: Langmuir trough lipid monolayers and their transition stages upon compression as described by changes in the Surface Pressure-Area isotherm. The illustration depicts the packing or	

the lipid alcy chain upon compression from its 2D gas state until the collapse of the monolayer and the formation of 3D structures..... 23

Figure 1.12: The classic optics of a beam, hitting a planar surface, related to the geometry of this process with the wavevector transfer. The wavevector is the “spatial” frequency of the neutron wave and is described by the  $k = 2\pi/\lambda$ , where  $k$  is the wavevector and  $\lambda$  is the neutron wavelength.  $k_i$ ,  $k_f$  and  $k_r$  are the wavevectors of incident, reflected and refracted neutron beam, respectively.  $Q$  is the wavevector transfer ( $k_i - k_f$ ),  $\theta_{in}$ ,  $\theta_{out}$  and  $\theta_r$  are the incident, outgoing and refracted angle of the neutron beam..... 24

Figure 1.13: (A) The oscillations in the reflectivity profile resulting from the interference which depends on the thickness ( $d$ ) of the layer (in terms of the position) and the difference in scattering contrasts between the respective interfaces (in terms of the amplitude).  $k_t$  is the wavevectors of the incident neutron beam and  $k_{f1}$  and  $k_{f2}$  the outgoing neutron beam from the top and bottom of the interfacial layer, respectively.  $n_1$  and  $n_2$  are the refractive index of light while SLD1 and SLD2 are the refractive indexes of neutrons in two different bulk phases.  $\theta_{in}$ ,  $\theta_o$  and  $\theta_r$  are the incident, outgoing and refracted angle of the neutron beam. (B) The scattering geometry in both Cartesian and spherical polar coordinates with  $\phi$  and  $\theta$  are angles determining the direction of the outgoing neutron beam.  $k_f$  is the wavevectors of reflected neutron beam and  $\lambda$  is the neutron wavelength. .... 25

Figure 1.14: Asymmetric lipid bilayer formed of Ra-EH100 LPS and DPPC and deposited on a silicon surface. The red arrows show the neutron path when the bean hits the surface. .... 27

Figure 2.1: Mechanism of tricyclic PBD core binding to the N2 of guanine in the DNA minor groove reproduced from Bruccoli et al. (143). .... 29

Figure 2.2: Chemical structure of PPA148..... 30

Figure 2.3: Different representations of the structure and conformation of  $\beta$ -cyclodextrin, showing the orientation of the hydrogens and hydroxyl groups. Native  $\beta$ CD contains hydroxyl groups, while its derivatives can be substituted by different functional groups. RAMEB contains either hydrogens or methyl groups, while HP $\beta$ CD has either hydrogens or hydroxypropyl groups..... 31

Figure 2.4: Types of phase solubility diagrams (“A” and “B”) and their deviations (“AP”, “AN”, “BS” and “BI”) (154)..... 42

Figure 2.5:  $^1\text{NMR}$  of sequential reaction monitoring for the synthesis of the final PBD core compound (#9)..... 45

Figure 2.6:  $^1\text{NMR}$  of sequential reaction monitoring for the synthesis of the final tail compound (#11). .... 46

Figure 2.7: <sup>1</sup> NMR signals for the secondary amide and double bond hydrogens of the final de-protected compound (#12), PPA148.....	47
Figure 2.8: <sup>1</sup> H-NMR signals for the hydrocarbon chain, methyl moieties, thiomorpholine and the pyrrole group of the PBD tricyclic core of the final compound, PPA148.....	47
Figure 2.9: FTIR monitoring of the core synthesis.....	48
Figure 2.10: FTIR monitoring the tail synthesis.....	49
Figure 2.11: FTIR monitoring of the final protected and de-protected PPA148.....	49
Figure 2.12: A representative adsorption profile of PPA148 at the air/liquid interface at 23 °C. The drug was injected below a 0.9% NaCl subphase and changes in surface pressure were recorded until a plateau was reached. The representative curve was fitted (red line) based on a 3-parameter Hill equation (Equation 2.4), $R^2=0.99$ ( $P \leq 0.0001$ ). The mean and std of maximum surface pressure ( $12.34 \pm 0.77$ mN/m), Hill slope ( $1.03 \pm 0.22$ ) and $t_{50\%}$ ( $0.33 \pm 0.15$ h) was calculated from a set of 3 runs... 51	51
Figure 2.13: Representative UV/Vis spectra of PPA148 in three solvents: EtOH, H <sub>2</sub> O, EtOH/H <sub>2</sub> O (80:10) at 25 °C.....	52
Figure 2.14: (A) Effect of solvent and drug concentration on the absorbance profile. Inset: concentration range where the Beer-Lambert law is followed ( $y = 0.04x + 0.02$ , $R^2 = 0.98$ for EtOH/H <sub>2</sub> O, $y = 0.04x + 0.06$ , $R^2 = 0.75$ for EtOH, $y = 0.03x + 0.05$ , $R^2 = 0.98$ for H <sub>2</sub> O). First derivative of UV/Vis spectrum of a series of PPA148 concentrations in: (B) H <sub>2</sub> O; (C) EtOH; and (D) EtOH:H <sub>2</sub> O (80:20). The peaks and troughs of the spectrum profile is presented with zero first derivative. The insets show the changes of $\lambda_{max}$ with increasing drug concentration.....	53
Figure 2.15: Increasing concentration of PPA148 in water 7 days under mild stirring at 25 °C. Visual observation of the precipitation point is at 50 µg/mL.....	54
Figure 2.16: Turbidimetric assay: Effect of cyclodextrin concentration in the aggregation of PPA148 using dynamic light scattering (A) and UV/Vis spectroscopy (B).....	54
Figure 2.17: Changes in the fluorescence intensity of PPA148 with increasing cyclodextrin concentration (HPβCD or RAMEB) at 25 °C (A). The lines represent the non-linear regression fit (Equation 2.7) of the experimental data points assuming a 1:1 complex. The phase solubility diagram (B) was built by adding an excess of drug to solutions of cyclodextrin to measure drug solubilisation. In both experiments, the solution used was HEPES buffered saline including CaCl <sub>2</sub> at pH 7.2. ....	55
Figure 2.18: Changes in the fluorescence intensity of rifampicin in increasing cyclodextrin concentration (A) show the drug's affinity to HPβCD and RAMEB at 25 °C. The lines represent the non-linear regression fit of the experimental data points assuming a 1:1 complex. The phase solubility diagram (B) was built to observe the approximate amount of drug that can be solubilized with CDs and gave an	



indication of the complex stoichiometry and affinity. In both experiments, the solution used was Tris buffer pH 9. ....	56
Figure 2.19: Job's plot for rifampicin/DIMEB (A) and PPA148/DIMEB (B) complexes. In the case of rifampicin, the normalized chemical shift ( $\Delta\delta^*X_{CD}$ ) of the H1 protons of DIMEB were plotted against the molar fraction of DIMEB ( $X_{CD}$ ). For, PPA148, protons at position 5 of the cyclodextrin structure.....	58
Figure 2.20: Schematic representation of rifampicin/CD inclusion complex as it was found by molecular simulation by He et al. and Tewes et al. (162,164).....	61
Figure 3.1: Structure DPPC (16:0) and DMPG (14:0).....	65
Figure 3.2: Empty Fluidosomes (SUVs, 1mg/mL) were manufactured with the thin film hydration method and probe sonication for size reduction. (A) Effect of liposome integrity in terms of size and intensity distribution profile of liposomes at a concentration of 1 mg/mL and temperature of 25 °C, measured by dynamic light scattering, over a period of 2 months. The samples were stored at 4 °C and tested between measurement intervals. All samples presented a polydispersity index of approximately $0.2 \pm 0.01$ . (B) Effect of PBS buffer pH 7.4 on the size of a series diluted SUVs (1, 0.5, 0.25, 0.125 and 0.0625 mg/mL) over time. ....	73
Figure 3.3: Fluidosome (1 mg/mL SUVs) encapsulated with a series of HP $\beta$ CD solutions in PBS buffer pH 7.4 (0.1, 1, 2.5 and 5% w/w) manufactured with thin film hydration method and probe sonication for size reduction. (A) Effect of HP $\beta$ CD on the size and polydispersity of Fluidosomes in terms of the intensity distribution profile of liposomes at 25 °C, measured by dynamic light scattering. All samples presented a polydispersity index of approximately $0.3 \pm 0.01$ . (B) Comparison of size changes in the absence and presence of HP $\beta$ CD. ....	74
Figure 3.4: Method development for the separation of unentrapped material from fluidosomes. Empty liposomes (2.5 mg/mL), prepared with thin film hydration method and extrusion through a 100 nm polycarbonate membrane for size reduction, were passed through a Sephadex PD10G25 size exclusion chromatography column, washed 8 times and the eluted volumes (8 fractions) were collected and analyzed. (A) Elution pattern of empty fluidosomes (2.5 mg/mL). The derived count rate profile and lipid content in each aliquot were measured to investigate the elution of liposomes. (B) Representative intensity distribution of empty fluidosomes in HEPES buffered saline at pH 7.2 (aliquot #3). ....	75
Figure 3.5: (A) Elution pattern of PPA148/RAMEB encapsulated fluidosomes (2.5 mg/mL). The derived count rate profile and lipid content in each aliquot were measured to investigate the elution profile of loaded liposomes. (B). Representative intensity distribution of drug/RAMEB encapsulated fluidosomes in HEPES buffered saline at pH 7.2 (aliquot #3). ....	76
Figure 3.6: (A) Drug quantification profile of the eluted fraction from the PD10G25 size exclusion chromatography column with the inset being the calibration curve ( $y=0.7937+5.717x, R^2=0.9966$ ) is	

presented as a function of the area under the curve (AUC). (B) The UV spectra of pure and extracted drug in ethanol/water (80:20). Version 1 and 2 and the two UV spectra of extracted PPA148 from aliquot 3, which present changes in drug peak shape..... 77

Figure 3.7: Kirby-Bauer assay for measuring the growth inhibition of *Escherichia coli* DH5 $\alpha$ . The inhibition zone diameter was measured for PPA148 as a pure substance and as a formulated drug (in a 5% RAMEB complex and incorporated into 0.1 mg fluidosomes as a complex with 5% RAMEB) after 24 hour incubation at 37 °C. Rifampicin and vancomycin were used as positive and negative control samples. The asterisks denote the level of significance going from lower to higher (as follows) and four asterisks indicate the highest level: 0.1244 (ns), 0.0332 (\*), 0.0021 (\*\*), 0.0002 (\*\*\*), <0.0001 (\*\*\*\*). All samples were tested in triplicate apart from the final formulation (PPA148-in-RAMEB-in-fluidosomes) which was tested 5 times. .... 78

Figure 3.8: Tukey's test of experimental data (n=3,5) with confidence interval of 95%. (A) Zero is included in the interval of PPA148-in-CD and PPA148-in-CD-in-liposome which indicates that their mean is not statistically significant. Residuals distribution of experimental observations for each group (B). .... 79

Figure 3.9: Monte-Carlo simulation was carried out based on the standard deviation of the experimental data. 100 observations were generated by the simulation and one-way ANOVA and Tukey's test was carried out with 95% confidence interval (A). All sets of groups have statistical difference. Residual distributions of simulated data (B)..... 79

Figure 3.10: Schematic representation of the possible organization of PPA148/RAMEB complex incorporated into Fluidosomes. The electrophilic center of PPA148 is presented inside the CD cavity while the headgroup of DPPC is associated with the exterior hydrogens of the narrow side of RAMEB molecules. .... 84

Figure 4.1: Langmuir-Blodgett and Langmuir-Schafer deposition on a silicon crystal to manufacture the asymmetric model outer membrane of Gram negative bacteria. .... 95

Figure 4.2: A, C and E present the Surface Pressure-Area (P-A) isotherms generated at 23 °C for a series of pure or mixtures of phospholipids (*E. coli* extract, DPPC, DPPG, POPC, POPG). All phospholipids were suspended in chloroform apart from d62DPPC which was prepared in chloroform:methanol:water (6:4:1) before deposition. The subphase used was 1mM MgCl<sub>2</sub> for all monolayers apart from d<sub>62</sub>DPPC which was 5 mM CaCl<sub>2</sub>. The *E. coli* B monolayer was deposited either on ultra pure water or 0.9% NaCl The subphase for hydrogenous DPPC/DPPG and POPC/POP mixtures monolayers was MgCl<sub>2</sub>. *E. coli* isotherm was measured on ultra pure water and isotonic saline. The red arrows show the L1/L2 and the L2/S transition of the lipids where applicable. B, D and F show the calculated compressibility modulus derived from P-A isotherms at 23 °C. The red arrows show transition phases of the lipids which are more pronounced than in the P-A isotherm. .... 99

Figure 4.3: Collapse surface pressure (A), area per molecule (B) and compressibility modulus (C) at 30 mN/m of all the phospholipid lipid monolayers.....	100
Figure 4.4: (A) Surface Pressure-Area (P-A) isotherms generated at 23 °C for a series of glycolipids: Ra EH100 LPS, Rc J5 LPS and Lipid A. The subphase for Rc-LPS and Lipid A monolayers was MgCl <sub>2</sub> while CaCl <sub>2</sub> was used for Ra-LPS. The red arrows show the L1/L2 and the L2/S transition of the lipids where applicable. (B) Compressibility modulus derived from P-A isotherms at 23 °C. The red arrows show transition phases of the lipids which are more pronounced than in the P-A isotherm. ....	101
Figure 4.5: Collapse surface pressure (A), area per molecule (B) and compressibility modulus (C) at 30 mN/m of three types of glycolipid monolayers. The Ra-LPS did not reach its collapse pressure and it is excluded from the figure. ....	102
Figure 4.6: Representative surface pressure – time isotherms at 23°C of chlorhexidine digluconate (A), rifampicin (B), gentamicin (B), PPA148 (C) and DMSO (0.5, 1 and 1.5 % v/v) (D) against <i>E. coli</i> B monolayer using 0.9% NaCl as a subphase. The black lines are the fitted curves based on the mathematical model, Hill curve, when it was applicable. ....	104
Figure 4.7: CF release from liposomes, manufactured from natural <i>E. coli</i> lipid extract, after administration of PPA148, chlorhexidine digluconate and gentamicin at 25°C. ....	105
Figure 4.8: Representative surface pressure – time isotherms at 23°C of rifampicin (A), PPA148 (B), against DPPC/DPPG monolayer using 1 mM MgCl <sub>2</sub> as a subphase. The black lines are the fitted curves based on the mathematical model when it was applicable. ....	106
Figure 4.9: Representative surface pressure – time isotherms at 23°C of HPβCD (A) and RAMEB (B), against DPPC/DPPG (3:1) and POPC/POPG (3:1) monolayers using MgCl <sub>2</sub> as a subphase.....	108
Figure 4.10: Interaction isotherm of 20 µg/mL PPA148 (A), 20 µg/mL rifampicin (B) and 0.1 mg/mL fluidosomes (C) against different types of OM lipid monolayers (Lipid A and Rc-LPS J5) at constant surface area at 23 °C. The profile was fitted, when applicable, to specific binding Hill slope model to investigate the kinetics and affinity of the interaction. The black lines are the fitted curves based on the mathematical model. ....	109
Figure 4.11: Pressure-time interaction isotherm of HPβCD (A) and RAMEB (B) with 2 monolayers under constant surface area at 23°C. ....	110
Figure 4.12: Neutron reflectivity profile (A) and model data fits with their scattering length density profiles (B) for an assymmetrically deposited DPPC (inner leaflet) and Ra-LPS (outer leaflet) model membrane at room temperature. The sample was measured at three isotopic contrasts (100% D <sub>2</sub> O, 100% H <sub>2</sub> O and SMW). The model membrane was fitted into five-layered mathematical model: Silicon oxide (SiO <sub>2</sub> ), DPPC headgroup (Inner HG), DPPC tails (Inner tails), Ra LPS tails (Outer tails) and Ra LPS headgroups (Core). ....	111

Figure 4.13: Neutron reflectivity profile (A) and model data fits with their scattering length density profiles (B) for an assymmetrically deposited DPPC (inner leaflet) and Ra-LPS (outer leaflet) model membrane at 38 °C. The sample was measured in three isotopic contrasts (100% D <sub>2</sub> O, 100% H <sub>2</sub> O and 38% D <sub>2</sub> O/SMW). The model membrane was fitted into a five-layered mathematical model: Silicon oxide (SiO <sub>2</sub> ), DPPC headgroup (Inner HG), DPPC tails (Inner tails), Ra LPS tails (Outer tails) and Ra LPS headgroups (Core).....	113
Figure 4.14: Neutron reflectivity profile (A) and model data fits with their scattering length density profiles (B) for an assymmetrically deposited DPPC (inner leaflet) and Ra-LPS (outer leaflet) model membrane after being challenged with 0.1 mg/mL fluidosomes (DPPC/DMPG, 18:1) at 38 °C. The sample was measured in three isotopic contrasts (100% D <sub>2</sub> O, 100% H <sub>2</sub> O and 38% D <sub>2</sub> O/SMW). The model membrane was fitted into a seven-layered mathematical model: Silicon oxide (SiO <sub>2</sub> ), DPPC headgroup (Inner HG), DPPC tails (Inner tails), Ra LPS tails (Outer tails) and Ra LPS headgroups (Core), Bridge and Floating bilayer.....	114
Figure 4.15: Representation of the possible structural changes in the model OM system after being challenged by fluidosomes.....	116
Figure 4.16: Schematic representation of the movement of phospholipids within a membrane: transpose diffusion (1), rotation (2), swing (3), flexion (4) and transverse diffusion or “flip-flop” movement (5). 118	
Figure 4.17: Schematic representation of the effect of temperature change on membrane structure and behavior of lipid bilayers adapted from Los and Murata (249). Low temperatures cause “rigidification” of membranes, whereas high temperatures cause “fluidization” of membranes. ....	119
Figure B 1: <sup>13</sup> CNMR of intermediate compounds of the PBD core synthesis. The samples were suspended in deuterated chloroform. ....	145
Figure B 2: <sup>13</sup> CNMR of intermediate compounds of the tail synthesis. The samples were suspended in deuterated DMSO. ....	145
Figure B 3: <sup>13</sup> CNMR of the final compound, PPA148. The sample was suspended in deuterated chloroform. ....	146
Figure B 4: The linear regression (A) met the assumptions that the residuals follow a normal distribution (B) and their variance is constant (B).....	146

# Table of Tables

Table 1.1: Comparison of non-antibiotic drug properties with the generic optimal properties for antibacterial drugs for oral or parental administration as were calculated by O'Shea et al based on data collected from the literature and drug data bases (12). .....	4
Table 1.2: WHO priority list for the development and discovery of new antibiotics for antibiotic resistant bacteria (54).....	11
Table 1.3: Summary of antibiotic-cyclodextrin complexes investigated by research groups to achieve sustained drug release, better bioavailability, increased antimicrobial activity and enhanced drug solubility. ....	16
Table 1.4: Several liposomal carriers investigated against Gram negative bacteria. ....	17
Table 1.5: Physicochemical properties of PPA148, rifampicin, gentamicin and chlorhexidine. ....	20
Table 1.6: Fatty acid composition of <i>E. coli</i> lipid extract as it was found by White et al. (127). ....	21
Table 1.7: Potential isotopic contrasts and main information content of a monolayer on an air/water interface or a deposited lipid bilayer on a silicon surface consisting for tail deuterated phospholipids. NRW and SMW stand for null reflective water (8.2% D <sub>2</sub> O) and silicon match water (38% D <sub>2</sub> O) respectively and are used to cancel out the background of the two mediums and highlight the interface. ....	26
Table 2.1: Comparison of the physicochemical properties of PPA148 estimated by ChemDraw compared (the experimental values are presented in parenthesis) with the generic optimal properties of antibacterial drugs for oral or parental administration as calculated by O'Shea et al. (12) based on data collected from the literature and drug data bases.....	30
Table 2.2: Chemical characteristics of each intermediate and the final compound. ....	50
Table 2.3 Solubility values and aggregation concentration of PPA148 in water, HEPES buffered saline pH 7.2 and HPβCD or RAMEB in HEPES obtained by different techniques. ....	54
Table 2.4: Binding constant of PPA148 and rifampicin as obtained by two different techniques. ....	57
Table 2.5: Gibbs free energy of transfer of rifampicin and PPA148 from pure water to aqueous CD solutions at room temperature calculated using Equation 2.11. ....	57
Table 4.1: Summary of scattering length densities of the lipid components studied, and the solution subphases.....	96

Table 4.2: Kinetic parameters obtained from the fitting of the binding isotherms of rifampicin, gentamicin and PPA148 and the <i>E. coli</i> B monolayers at 23°C on water sub-phase containing isotonic saline. ....	104
Table 4.3: Kinetic parameters obtained from the fitting of the binding isotherms of rifampicin and PPA148 and the DPPC/DPPG monolayers at 23°C on water sub-phase containing 1 mM MgCl <sub>2</sub> . ...	107
Table 4.4: Kinetic parameters obtained from fitting the binding isotherms of rifampicin and PPA148 and the Rc J5 LPS and R595 Lipid A monolayers at 23°C on a water sub-phase containing 1 mM MgCl <sub>2</sub> . .....	109
Table 4.5: Volume fractions of deuterated DPPC tails, hydrogenous LPS tails and water within the bilayers of Ra-LPS/d-DPPC at room temperature (25 °C). ....	111
Table 4.6: Structural parameters, thickness, hydration and roughness, of the Ra-LPS/DPPC membrane at room temperature and 38 °C as obtained from the fitting of the neutron reflectivity data. The numbers in parentheses are the 95% confidence interval error. ....	112
Table 4.7: Volume fraction of deuterated DPPC tails, hydrogenous LPS tails and water within the bilayers of Ra-LPS/d-DPPC 38 °C before and after the challenge by the fluidosomes. ....	113
Table 4.8: Structural parameters, namely, thickness, hydration and roughness, of the challenged Ra-LPS/DPPC membrane at 38 °C as obtained from fits to the neutron reflectivity data shown in Figure 4.14. ....	115
Table B 1: Minimum Inhibitory concentrations (MIC) of PPA148 against Gram-negative bacteria in the absence and presence of the efflux pump inhibitor PaβN. ....	144
Table B 2: Minimum Inhibitory concentrations (MIC) of PPA148 against Gram-positive bacteria in the absence and presence of the efflux pump inhibitor PaβN. ....	144
Table C 1: Number and Volume distribution of empty and loaded fluidosomes. ....	147

# Abbreviations

ABC: ATP binding cassettes

AMR: Antimicrobial Resistance

CE: complexation efficiency

CL: cardiolipins

CymA: cyclodextrin metabolism A

DCR: derived count rate

DIMEB: Heptakis (2,6-di-O-methyl)- $\beta$ -cyclodextrin

DNA: deoxyribonucleic acid

EARS-Net: European Antimicrobial Resistance Surveillance Network

ECDC: European Center of Disease Control

IM: Inner membrane

IUPAC: International Union of Pure and Applied Chemistry

Kdo: 3-deoxy-d-manno-oct-ulosonic acid

LC-MS: Liquid Chromatography-Mass Spectrometry

LPS: Lipopolysaccharide

MATE: multidrug and toxic-compound efflux

MDR: multi-drug resistant

MIC: minimum inhibitory concentration

MW: molecular weight

NRW: null reflected water

OM: Outer membrane

OMP: Outer membrane protein

PC: phosphatidylcholine

PE: phosphatidylethanolamines

PG: phosphatidylglycerols

PSA: polar surface area

RNA: ribonucleic acid

RND: resistance-nodulation-division

SMR: small multidrug resistance

SMW: silicon matched water

US CDC: US Center for Disease Control and Prevention

WHO: World Health Organization



# Symbols

(m:n): stoichiometry of CD/drug complex

$\Delta G_{\text{tro}}$ : Gibbs free energy

A: area per molecule

Cs: Area compression modulus

D: Brownian motion diffusion coefficient

d: thickness

dH: hydrodynamic diameter

Es or Cs-1: Compressibility modulus

f: wave frequency

G: gaseous state

h: Hill slope

I: Fluorescence intensity

K: binding constant

k: wavevector

Ka: distance travelled by the analyte from its origin

Ks: distance travelled by the solvent from its origin

L1: liquid-expanded state

L2: condensed state

p: momentum of neutrons

Q: wavevector transfer

Rf: retardation factor

S: solid state

S0: Solubility in the presence of cyclodextrin

S<sub>int</sub>: intrinsic solubility

T: Temperature in Kelvin

v: neutron velocity

XCD: mole fraction of cyclodextrin

$\Delta\Pi$ : Difference in surface pressure

$\Delta\Pi/\Delta A$ : slope of isotherm

$\eta$ : solvent viscosity

$\theta$ : incident angle

$\lambda$ : wavelength

$\Pi$ : Surface pressure

$\rho$ : Scattering Length Density (SLD)

$\varphi$ : volume fraction

# Physical Constants

h: Planck's constant,  $6.626 \times 10^{-34}$  J

k: Boltzman's constant,  $1.381 \times 10^{-23}$  J K<sup>-1</sup>

mn: neutron mass,  $1.675 \times 10^{-24}$  kg

R: Gas constant 8.314 JK<sup>-1</sup>mol<sup>-1</sup>

# Chapter 1 General Introduction

## 1.1 Antibiotics and Bacteria: a unique class of medicines and pathogens

Antibiotics are a group of drugs used to treat bacterial infections. They are a unique class of medicines because of their complicated mechanisms of action as well as their restricting use and long-term efficacy. Unlike other drugs, antibiotics should selectively target several pathogens that are responsible for conditions ranging from pneumonia to urinary infections, acting in different body sites, whilst at the same time they should not affect the host organism (1). Antibiotics made a significant contribution to public health, having been used not only in medical practice but also in agriculture and other industries. They also help to promote growth in livestock, preserve building materials from contamination and treat blight in orchards (2). Antibiotics have saved countless lives and improved surgery conditions by preventing or curing bacterial infections in patients including those: receiving chemotherapy treatments; suffering from chronic diseases such as cystic fibrosis, diabetes, end-stage renal disease, or rheumatoid arthritis; or having undertaken complex surgical procedures such as organ transplants, joint replacements, or cardiac surgery (3–5). Moreover, they have increased the average life expectancy and decreased the morbidity and mortality caused by food-borne and other poverty-related infections (5,6).

## 1.2 Antibiotic classification

Antibiotics are classified based on their chemical family and mechanism of action. They are separated into 32 groups, based on their chemical functional groups, the larger being aminoglycosides, glycopeptides, imidazole, macrolides, nucleosides, penicillins and cephalosporines ( $\beta$ -lactams), peptides, pyrimidines and pyridines, sulfonamides and tetracyclines. Each of them possesses unique chemical properties and functional groups to target different parts of bacterial cells. For example, penicillins inhibit cell wall synthesis (7), whilst rifampins target RNA synthesis (8). Their action to either kill bacteria (bacteriocidal) or inhibit bacterial growth (bacteriostatic) falls within four categories. Three of those functions are the inhibition of (a) enzymes involved in cell wall and protein synthesis, (b) deoxyribonucleic acid (DNA) replication and/or (c) ribonucleic acid (RNA) transcription as shown in Figure 1.1 (9,10). The fourth category is the disruption of bacterial membrane structure (10). For example, penicillins; cephalosporins; carbapenems; daptomycin and monobactams; glycopeptides cause inhibition of cell wall synthesis. Tetracyclines, aminoglycosides, oxazolidonones, streptogramins, ketolides, macrolides and lincosamides cause inhibition of protein synthesis. Fluoroquinolones act by inhibiting DNA synthesis while rifampins RNA synthesis. Sulfonamides cause inhibition of folate synthesis. Daptomycin depolarizes membrane potential (10).

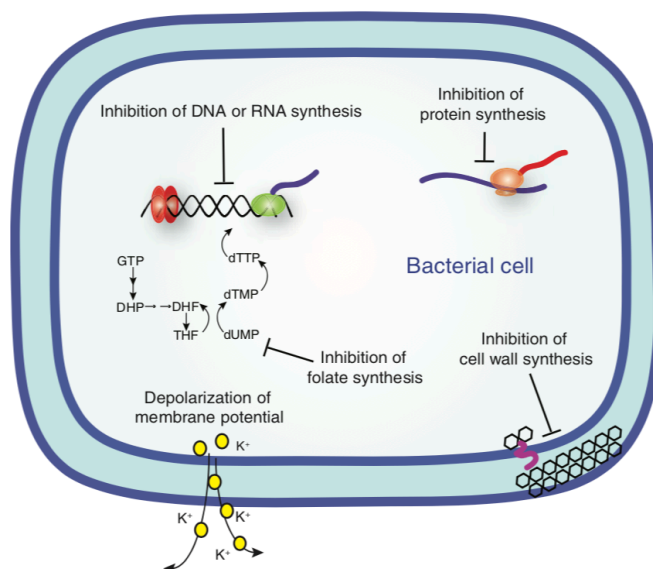


Figure 1.1: Mechanism of action of some major antibiotic agents reproduced from Clatworthy et al. (10).

## 1.3 Bacterial classification

Bacteria are prokaryotic microorganisms which can be classified as either Gram positive or Gram negative, on the basis of their cell envelope structure. The cell envelope of Gram positive bacteria possesses a thick peptidoglycan wall external to their plasma membrane, whereas the peptidoglycan of Gram negative constitutes a thinner layer between their outer and inner membranes.

The activity of antibiotics is designated as broad, intermediate or narrow-spectrum based on the number of different bacterial species they can affect (11). For example, antibiotics that kill both Gram positive and negative bacteria are called broad spectrum antibiotics, while those which kill only Gram positive bacteria are considered narrow spectrum (11). The research conducted in this project is focused exclusively on Gram negative bacteria because their complex outer membrane (OM) hinders drug uptake, resulting in low efficacy.

### 1.3.1 Physicochemical properties of antibiotics

Active pharmaceutical compounds are classified based on their physicochemical properties and fall within the Lipinski's rule of five (i.e., a molecule with a molecular mass under 500 Da, no more than 5 hydrogen bond donors, no more than 10 hydrogen bond acceptors, and an octanol–water partition coefficient, logP, no greater than 5). Antibacterial agents have always been deemed to deviate from Lipinski's rule of five due to their higher molecular weight and polarity (Table 1.1) (12,13). Several research groups have tried to correlate the physicochemical properties of antibiotics with their activity by collecting experimental data from the literature and databases of already marketed drugs to compare them in terms of lipophilicity (clogP), polarity (PSA),

molecular weight (MW), number of H-donors, number of H-acceptors and number of aromatic rings. Leeson and Davis compared drugs, including antibiotics, from five different therapeutic areas (cardiovascular, nervous system, gastrointestinal, respiratory/inflammation and infection) that were launched from 1983 to 2002 (14). Antibiotics, antimalarial, antiviral, antifungal and antiparasitic drugs were all included in the general infection category, known as anti-infectives. Their results showed that anti-infectives have a different physicochemical profile by being larger and less lipophilic than the other classes, which can be explained by their activity against non-human cells and their need to penetrate the bacterial cell envelope. O'Shea and co-workers, particularly, examined the properties of 147 antibacterial agents, classifying the results into activity against Gram negative and Gram positive bacteria, and compared them with results from non-antibiotic drugs (12). Their analysis is presented in Table 1.1.

Table 1.1: Comparison of non-antibiotic drug properties with the generic optimal properties for antibacterial drugs for oral or parental administration as were calculated by O'Shea et al based on data collected from the literature and drug data bases (12).

Physicochemical properties	Non-antibiotic	Antibiotics with optimal properties against Gram negative	Antibiotics with optimal properties against Gram positive
Molecular weight (g/mol)	338	414	813
cLogP	2.7	-0.1	2.1
cLogD <sub>7.4</sub>	1.6	-2.8	-0.2
PSA (Å <sup>2</sup> )	70	165	243

cLogP is the logarithm of the partition coefficient (LogP) between n-octanol and water and is a measure of the compound's hydrophilicity and an indication of absorption and permeation. clogD<sub>7.4</sub> is the logarithm of the distribution coefficient at pH 7.4 which is another measure of lipophilicity of unionized and ionized forms. PSA is the polar surface area, which provides a prediction of drug passive intestinal permeability (<140 Å<sup>2</sup>) and blood-brain barrier penetration (<60 Å<sup>2</sup>) (15–17).

Table 1.1 shows that in general, antibiotics have significantly higher molecular weights and polarities compared to non-antibiotic drugs. Interestingly, there are variations between drugs acting against Gram negative and positive bacteria which can be explained by the differences in the constitution of the cell envelopes between these two groups. The lipophilicity of non-antibacterial drugs and the Gram positive activity group present similarities, but a substantially higher polarity is noted for the Gram negative specific group. This difference in lipophilicity is more obvious when comparing the cLogD<sub>7.4</sub> (4 log units lower, which means more hydrophilic) and PSA values.

### 1.3.2 Gram negative bacterial cell envelope as a barrier to antibiotics

Gram negative bacteria possess a complex envelope structure with two main permeability barriers: the outer membrane (OM) and the inner (cytoplasmic) membrane (IM). The OM is a unique feature of the Gram negative bacterial cell envelope providing cell protection. It is a lipid

bilayer whose outer leaflet consists of lipopolysaccharide (LPS) while the inner leaflet is composed of phospholipids (18).

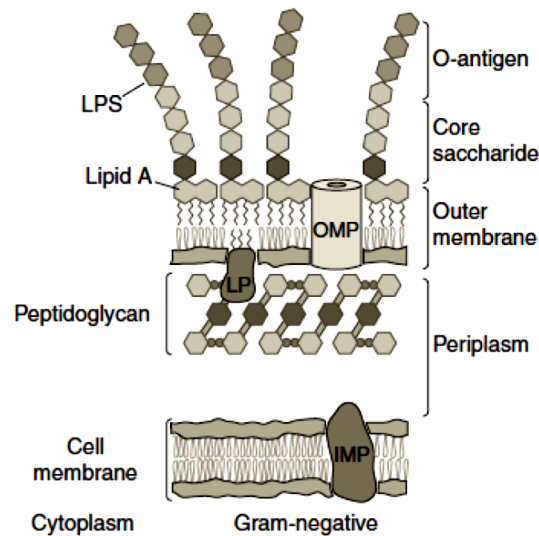


Figure 1.2: Cell envelope of Gram-negative bacteria reproduced from Silhavy et al. (18).

LPS belongs to the category of glycolipids and consists of Lipid A, a hydrophilic oligosaccharide core and a hydrophilic O-antigenic polysaccharide side chain (O-chain) (Figure 1.2). Lipid A provides the membrane anchor for the LPS molecule, and is made up of a  $\beta(1 \rightarrow 6)$ -linked glucosamine disaccharide backbone which is acylated at positions 2 and 3 of each monosaccharide portion involving six to seven fatty acid chains (Figure 1.10). This acylated disaccharide is also mostly phosphorylated at positions 1 and 4' or even further substituted (19–21). The core oligosaccharide is subdivided into an inner and outer core. The inner core is composed of 3-deoxy-d-manno-oct-ulosonic acid (Kdo) and L-glycerol-D-manno-heptose which are typically phosphorylated or modified with phosphate containing groups, increasing their overall negative charge helping stabilize the structure through divalent cation cross-linking (22). Kdo links the core oligosaccharide with Lipid A anchor while the outer core attaches to the O-antigen. The outer core is more diverse than the inner and is composed of three to six additional saccharides such as D-glucose and N-acetyl-D-glucosamine and D-galactose (23,24). There are also proteins present in the outer membrane (OMP); lipoproteins and  $\beta$ -barrels. OMP such as porins are of major importance because they are transmembrane and their function is to allow the uptake of nutrients and hydrophilic compounds. LPS provides protection against hydrophobic compounds (18), and makes the OM a semipermeable barrier which protects the cell from harmful organic compounds such as antimicrobials and allows the uptake of sufficient nutrients.

A thin peptidoglycan layer sits between the OM and IM to provide extra support and flexibility to the IM, which is the last part of the cell envelope and is composed of phospholipids and proteins. IM proteins are responsible for the energy production, lipid biosynthesis, protein secretion and transport of materials in and out of the cell. The principal lipids which are present in the IM of the majority of bacteria, such as *P. aeruginosa* and *Escherichia coli* (*E. coli*), are



phosphatidylcholines (PCs), phosphatidylethanolamines (PEs), phosphatidylglycerols (PGs) and cardiolipins (CL) (25) (Figure 1.3). Bacterial efflux pumps present in the cell envelope prevent the accumulation of toxic compounds, such as antimicrobial drugs, in the cell. Efflux pumps are comprised of a transporter (protein) in the IM, an accessory protein (membrane-fusion protein) in the periplasm and an outer membrane protein channel in the OM (Figure 1.4 e, f, g) (26).

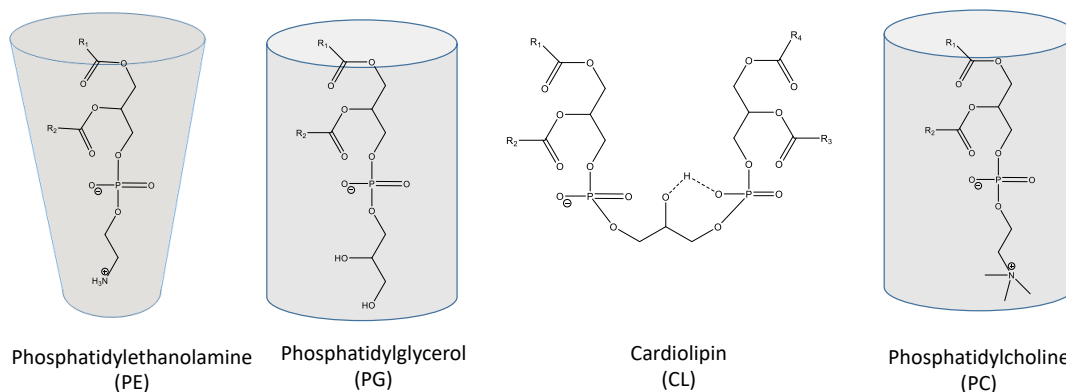


Figure 1.3: Structure of phospholipid headgroups with different substitution in the phosphate group which gives a different curvature and charge. R1 and R2 are the fatty acid chains which can be either saturated (PC with C16:0 is DPPC while PC with C14:0 is DMPC) or unsaturated (PC with C16:1 is POPC).

### 1.3.3 Drug uptake mechanisms

Based on the cell envelope structure (Figure 1.2) it can be seen that there are several mechanisms of drug and ion uptake (Figure 1.4). They are divided into two major categories: passive and active transport (27). Hydrophobic compounds diffuse passively through the membrane because of their lipid solubility (passive diffusion) while hydrophilic agents are transported through the water channels (facilitated diffusion). General diffusion porins form water channels facilitating the passage of small hydrophilic molecules (~ 400 Da, >600 pass very slowly) and ions (non-specific diffusion) while the specific porins allow the passage of specific molecules or classes of molecules that binds to the substrates that preferentially flow through these channels (self-promoted diffusion) (18,28–30). For instance, it has been found that uptake of native  $\alpha$ - and  $\beta$ -cyclodextrin depends on specific membrane protein channels (cyclodextrin metabolism A or CymA) in the outer membrane of the Gram negative bacterium, *Klebsiella oxytoca* (31). Drugs might have a different mechanism of uptake across OM and IM as is the case with the aminoglycosides. Gentamicin is known to pass passively (self-promoted) through the OM and actively through the IM (32,33).

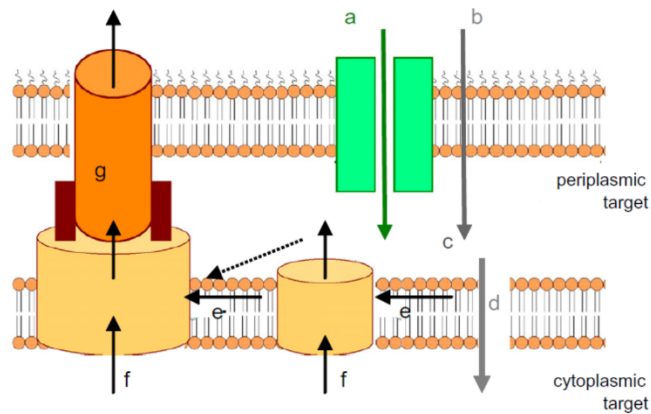


Figure 1.4: Different ways by which a substance can be transported across the membranes reproduced from Bolla et al., (34). Hydrophilic components and nutrients can pass through porins (a) and hydrophobic molecules diffuse through the OM and/or IM (b and d respectively). The diffusion through the periplasm which is packed with proteins is represented by (c). Drugs can be recognised as foreign molecules by the efflux pumps (e and f) and can be transported out of the membranes. Several pumps such as AcrA/B and AcrE/F must recruit the OM barrel protein such as TolC (g) in order to expel drugs directly out of the cell (35).

## 1.4 Antimicrobial Resistance (AMR)

Although antibiotics have been highly effective against pathogens, they impose substantial selective pressures on bacteria, which are living organisms and thus tend to adapt to changes and evolve. Antibiotic-resistance is a natural process because bacteria develop their own resistance mechanisms and constantly acquire those that had evolved over billions of years in environmental bacteria (36). Therefore, resistance is not a new phenomenon, as it is shown in Figure 1.5. It first emerged in hospitals in the late 1930s with the sulfonamide-resistant *Streptococcus pyogenes* bacteria, shortly after sulfonamides were made available on the market, and penicillin-resistant *Staphylococcus aureus* appeared 6 months after being used in clinical practice in the UK (36–38). After 1985, the antibiotic pipeline began to dry up and fewer new drugs were introduced; leading to a situation now, where we are in danger of entering a “post-antibiotic” era (2,10,36,37,39–41).

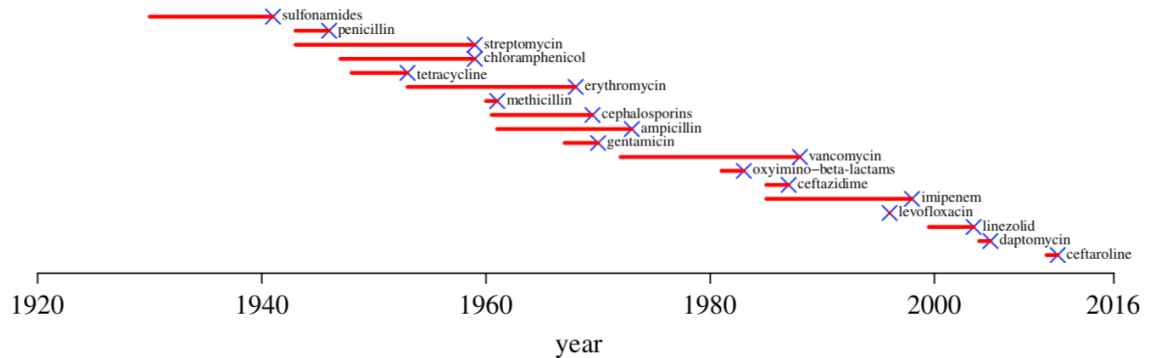


Figure 1.5: Timeline of antibiotics from their market introduction (red line) to the first observations of drug resistance, which is represented by a blue 'X'. The figure is reproduced and adapted for the needs of this report from Kennedy et al. (37).

### 1.4.1 Causes of AMR

Antimicrobial resistance is driven by natural factors. The results of human activity, clinical use, extensive use of antibiotics in agriculture and public behavior and perception have all contributed to its widespread proliferation. Bacteria are small prokaryotic organisms with simple intracellular features and circular DNA (chromosomal DNA) which coexists with independent DNA pieces (plasmids). Plasmids encode traits and genes required for ever-varying environmental challenges. Due to the small size of bacterial cells, individual pathogens contain a limited number of those genes, thus hindering its ability to face environmental changes. The key to bacterial natural adaptive strength is their ability to reproduce rapidly, creating bacterial populations with wide variability in terms of advantageous characteristics. Even though changes in the genes of plasmids are rare, the rapid generation time ensures that these advantageous changes will become rapidly predominant in the bacterial population and help them evolve in response to the environmental changes.

Although antimicrobial resistance is a natural process, the main reason for the widespread proliferation was both the misuse and overuse of antibiotics in humans and animals. Once antibiotics were introduced, they were effective and efficient. Thus, there was a general public belief that antibiotics should be applied in the first instance for every type of illness. This perception, along with the over-prescription and extended regimens in clinical practice, created strong selective pressures on bacteria which, in turn, generated resistant strains responding to prolonged antibiotic exposure. The more bacteria are exposed to antibiotics, the more likely the emergence of resistant strains. Empirical treatment and prescription of antibiotics by general practitioners based on local epidemiology before the results of the diagnostic tests often leads to their misuse. If the initial antibiotic regimen is not the appropriate one, the patient's microbiota is subjected to an intense and repeated selective pressure that encourages and conserves the development of AMR among currently non-pathogenic organisms. In addition, poor hygiene and infection prevention leads to an increased number of infections and thus increased use of

antibiotics. Moreover, the use of antibiotics in agriculture too, may have increased productivity but it has been increasing the abundance and diversity of AMR genes across rural and urban environments.

Bacteria have become resistant to a number of drugs because they have resistance mechanisms to first and second line of infection treatment. The deficiency of existing antibiotics and the widespread proliferation of antimicrobial resistance has been examined in depth by the US Center for Disease Control and Prevention (CDC) (42), European CDC (ECDC) (43), WHO (44) and European Antimicrobial Resistance Surveillance Network (EARS-Net) (43). These organizations reported that Gram negative bacteria are becoming pan-drug or extensively-drug resistant which leads to increased morbidity and mortality.

#### 1.4.2 Mechanisms of bacterial resistance

Resistance to antibiotics falls into two broad categories: intrinsic and acquired. The conventional example of intrinsic resistance is the multi-drug resistant (MDR) phenotype existing in Gram negative bacteria which includes inherent active drug efflux and low permeability of the OM. As mentioned previously, the Gram negative bacterial outer membrane outer leaflet consists of LPS which is anchored by Lipid A and stabilized by divalent cation crosslinking between the phosphate groups which decorate the inner core oligosaccharides (Figure 1.10). This cross-linking facilitates tight packing of the Lipid A hydrocarbon chains, decreasing OM fluidity and increasing the permeability threshold for drugs whose main mechanism of uptake is passive diffusion (45). For those drugs requiring other means of being transported into the bacterial cell envelope, the limiting step is the structure and properties of the porins and proteins present in the OM (45). Porins selectively retard the influx of drugs and nutrients according to their size, hydrophobicity and charge. The OM can also control the efflux of materials via efflux pumps which primarily actively transport toxins out of the cell. Efflux pumps can either be substrate specific, and only export one molecule, or they can be broad-spectrum, and export structurally distinct classes of molecules (26). There are five types of efflux pumps: ATP binding cassettes (ABC), major facilitators (MF), multidrug and toxic-compound efflux (MATE) pumps, small multidrug resistance (SMR) pumps, and the resistance-nodulation-division family (RND). However, only the latter is the main facilitators of intrinsic resistance (26,46,47). RNDs are also known as outer membrane proteins and are transmembrane. For example, MexAB-OprM contributes to  $\beta$ -lactam and fluoroquinolone intrinsic resistance in *P. aeruginosa* (48) and the AcrAB-TolC in *E. coli* facilitates resistance to a broad range of antibiotics such as the tetracyclines, fluoroquinolones,  $\beta$ -lactams and the macrolides (26). The high level of intrinsic resistance in Gram negative bacteria is a result of the synergistic effect between the low permeability of the outer membrane and the efflux pumps. Mutations in genes encoding efflux pump expression may lead to their upregulation which is clinically associated with the multi-drug resistance phenotype of bacteria (9,26,29,34).

Acquired antimicrobial resistance mechanisms includes genetic modifications in the efflux pumps and porins or incorporation of new genetic material through plasmids, bacteriophages, transposons and naked DNA (Figure 1.6). The genes for single drug resistance traits developed from a mutation in an intrinsic chromosomal gene can spread from one generation to another (vertical gene transfer). These genetic mutations can not only cause upregulation of efflux pumps but also alter antibiotic targets or cause target overexpression (9,45). Moreover, acquired resistance can occur by transferring genetic material between related or unrelated species (horizontal gene transfer), which accounts for the rapid proliferation of acquired resistances. Multiple genes can accumulate in the same organism, leading to multi-, pan- or extensive- drug resistance (9,45).

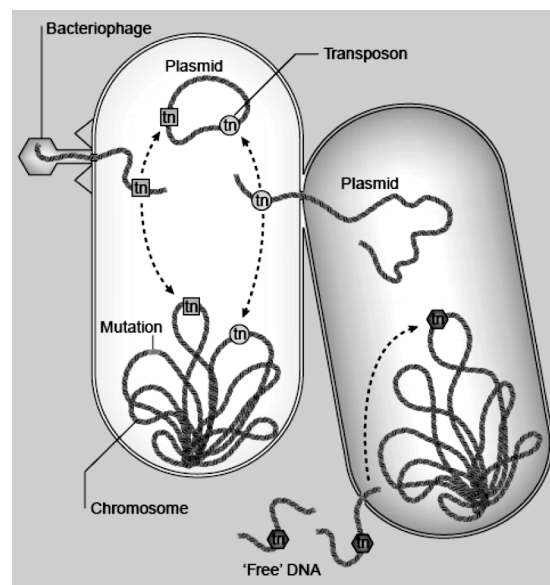


Figure 1.6: Mechanisms through which drug resistance can be spread horizontally from one bacterium to another reproduced from Levy et al. (9).

## 1.5 Strategies to combat antimicrobial resistance

Several reviews have stated that the last resorts for treatment of infections caused by resistant bacteria were the broad spectrum carbapenem agents. Over recent years, the emergence of carbapenem-resistant *Enterobacteriaceae* as well as carbapenem-resistant Gram negative bacilli (*Acinetobacter baumannii*, *Pseudomonas aeruginosa*) have left a few treatment options, while the spread of carbapenem-resistant *Enterobacteriaceae* has created a serious threat to public health worldwide (49). In this context, older drugs with adverse effects, such as polymyxins (colistin and polymyxin B), have been used by clinicians. The re-introduction of polymyxins for antimicrobial therapy has been followed by an increase in reports of acquired polymyxin resistance in clinical isolates such as *P. aeruginosa*, *A. baumannii* and *Klebsiella pneumoniae* (50). Therefore, there is an urgent need to overcome antimicrobial resistance by either discovering new antibiotics, applying combined antibiotic therapy or developing new drug carriers and rapid diagnostics.

### 1.5.1 Drug development

The development of new drugs was initiated by modifying already marketed antibiotics to extend their spectrum activity (51). Examples of this initiative are penicillins, fluoroquinolones and cephalosporins. However, bacteria also became resistant to those drugs because the modifications in their structure failed to change their site and mechanism of action. Attempts have been made by research groups to introduce new drugs but the majority of these attempts have failed because their physicochemical properties reduce their bioavailability and reduce outer membrane penetration. Teixobactin was discovered in 2015 as a new class of antibiotics against Gram positive bacteria but its activity is limited. Therefore, new drugs need to be discovered as was proposed by O'Neill (52) in his wide-ranging report into antimicrobial resistance strategies for the UK government. Table 1.2 presents a list of resistant bacteria deemed by the WHO as urgently requiring the discovery and development of new antibiotics in order to tackle them (53).

### 1.5.2 Antibiotic combination therapy

The rise of multi-drug resistant (MDR) Gram negative bacteria and the lack of new antibiotic classes make monotherapy inadequate for treating infections and increases the likelihood that combination therapy would be more effective (54). Antibiotic combination therapy is widely used to treat severe infections caused by Gram negative bacteria and may be divided into two categories: antibiotic synergism and antibiotic/adjuvant combination (55,56).

Table 1.2: WHO priority list for the development and discovery of new antibiotics for antibiotic resistant bacteria (57).

<b>Priority 1: Critical</b>
<i>Acinetobacter baumannii</i> , carbapenem-resistant <i>Pseudomonas aeruginosa</i> , carbapenem-resistant <i>Enterobacteriaceae</i> , carbapenem-resistant, 3rd generation cephalosporin-resistant
<b>Priority 2: High</b>
<i>Enterococcus faecium</i> , vancomycin-resistant <i>Staphylococcus aureus</i> , methicillin-resistant, vancomycin intermediate and resistant <i>Helicobacter pylori</i> , clarithromycin-resistant <i>Campylobacter</i> , fluoroquinolone-resistant <i>Salmonella spp.</i> , fluoroquinolone-resistant <i>Neisseria gonorrhoeae</i> , 3rd generation cephalosporin-resistant, fluoroquinolone-resistant
<b>Priority 3: Medium</b>
<i>Streptococcus pneumoniae</i> , penicillin-non-susceptible <i>Haemophilus influenzae</i> , ampicillin-resistant <i>Shigella spp.</i> , fluoroquinolone-resistant

### 1.5.2.1 Combination of two or more antibiotics

The combination of antimicrobial agents to produce potent synergistic effects has been applied to combat MDR in Gram negative bacteria. Combination therapy of two to four different antibiotics against multidrug-resistant *Pseudomonas* spp. typically includes a broad-spectrum beta-lactam and an aminoglycoside or a fluoroquinolone, colistin, a macrolide, or rifampin (55,58). The mechanisms of synergistic bacteriostatic activity are not fully understood for all drug combination but plausible explanations exist for some antibiotics. For example, colistin increased membrane permeability by acting as a disruptive agent, enabling rifampin to exert its action against colistin-resistant *Klebsiella pneumoniae* carbapenemase (KPC)-producing bacteria (59). Co-administration of colistin and sulfamethoxazole causes an increased in vitro activity against colistin resistant and susceptible Gram negative bacterial strains when compared to monotherapy (50). The combination of colistin with meropenem or doripenem has also resulted in synergistic effects in vitro against multidrug-resistant *Pseudomonas* spp., *Acinetobacter* spp., and carbapenemase-producing *Enterobacteriaceae* and has been reported as a successful treatment in case reports (55).

### 1.5.2.2 Antibiotic-adjuvant

Antibiotic-adjuvant combination is an alternative approach for reviving antibacterial drug discovery by targeting the resistance processes (60). Adjuvants are compounds that enhance antibacterial drug activity but do not act as antibacterial agents themselves. Products consisting of beta-lactam antibiotics and an inhibitor of the beta-lactamase enzyme are already on the market and represent a successful approach in targeting resistance to a defined class of antibiotics (61,62). A well-known example is the combination of amoxicillin with clavulanic acid, which is a beta-lactamase inhibitor but is not effective as an antibiotic by itself (63). There are newly synthesized beta-lactamase inhibitors for co-administration with cephalosporins and carbapenemes, i.e. avibactam (64) and vaborbactam (65), respectively. The combination of avibactam and ceftazidime has recently been approved for therapeutic use in the US and Europe (66).

Within a similar conceptual framework, efflux pump inhibitors have also been investigated as adjuvants. A common synthetic efflux pump inhibitor, widely used in vitro, is phenylalanine-arginine  $\beta$ -naphthylamide (PA $\beta$ N), capable of inhibiting clinically relevant pumps for resistance in *P. aeruginosa*, as well as similar pumps in other MDR Gram-negative bacteria (63,67). The combination of PA $\beta$ N and levofloxacin decreased resistance to the drug by eight-fold in wild-type strains of *P. aeruginosa*, while in efflux pump overexpressing strains it increased efficacy by up to 64-fold (68). In addition, PA $\beta$ N has been shown to have membrane permeabilizing activity in a concentration dependent manner. It promotes its own entry into the cells where it can access its efflux pump targets (69). Therefore, PA $\beta$ N has an excellent potential as an antibiotic adjuvant by increasing outer membrane permeability and/or impairing drug efflux pumps.

### 1.5.2.3 Pro-drug formation

A promising platform to overcome antimicrobial resistance is to design and develop prodrug antibiotics which are ineffective until they are activated by specific bacterial enzymes, allowing them to covalently bind to unrelated targets (Figure 1.7) (70). The irreversible binding to the target overcomes the efflux from the MDR pumps, resulting in increased drug penetration and accumulation into the cells. Prodrug antibiotics were discovered in 1950 in an attempt to eliminate antibiotics without specific targets, but screening tests eliminated them from being used (70). For instance, metronidazole, which was overlooked as an antibiotic, is an ideal prodrug with broad spectrum activity because it becomes non-specific after activation by binding to different targets (proteins and DNA) (71). Fleck and co-workers investigated three new nitrofurans prodrugs (ADC111, ADC112, ADC113) which all showed sterilizing capability and broad-spectrum activity (72).

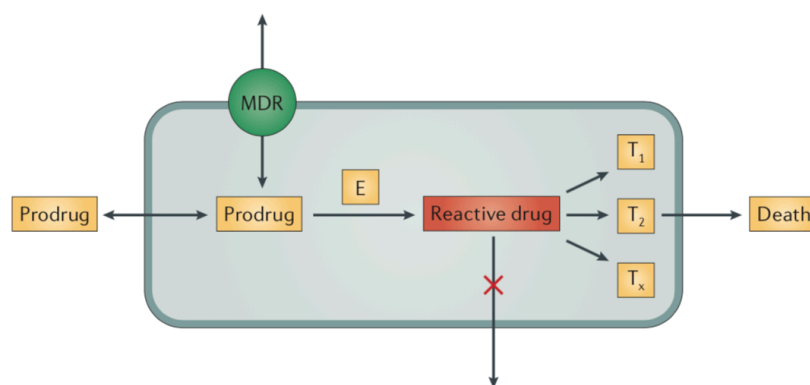


Figure 1.7: Mechanism of pro-drug platform, reproduced by Kim Lewis (70). The prodrug enters the cell and is converted into the reactive drug by a bacteria-specific enzyme (E). Inside the cell, the reactive compound covalently binds to unrelated targets, T<sub>1</sub>, T<sub>2</sub> and T<sub>3</sub>, which causes cell death. This mechanism kills not only dividing cell but also dormant cell.

## 1.6 Formulation approaches for antimicrobials to overcome resistance

### 1.6.1 Cyclodextrin-drug complexes

Cyclodextrins, also known as cyclomaltodextrins and cycloamyloses, were first identified as a bacterial digestion product of starch (73,74). Three native cyclodextrins have been isolated:  $\alpha$ -cyclodextrin ( $\alpha$ CD),  $\beta$ -cyclodextrin ( $\beta$ CD) and  $\gamma$ -cyclodextrin ( $\gamma$ CD). They are cyclic oligosaccharides containing 6 ( $\alpha$ CD), 7 ( $\beta$ CD) or 8 ( $\gamma$ CD) ( $\alpha$ -1,4)-D-glucopyranose units respectively. Due to the chair configuration of the glucopyranose unit, cyclodextrins are toroidal molecules with a truncated cone structure having a lipophilic inner cavity and hydrophilic outer surface (Figure 1.8) (75).



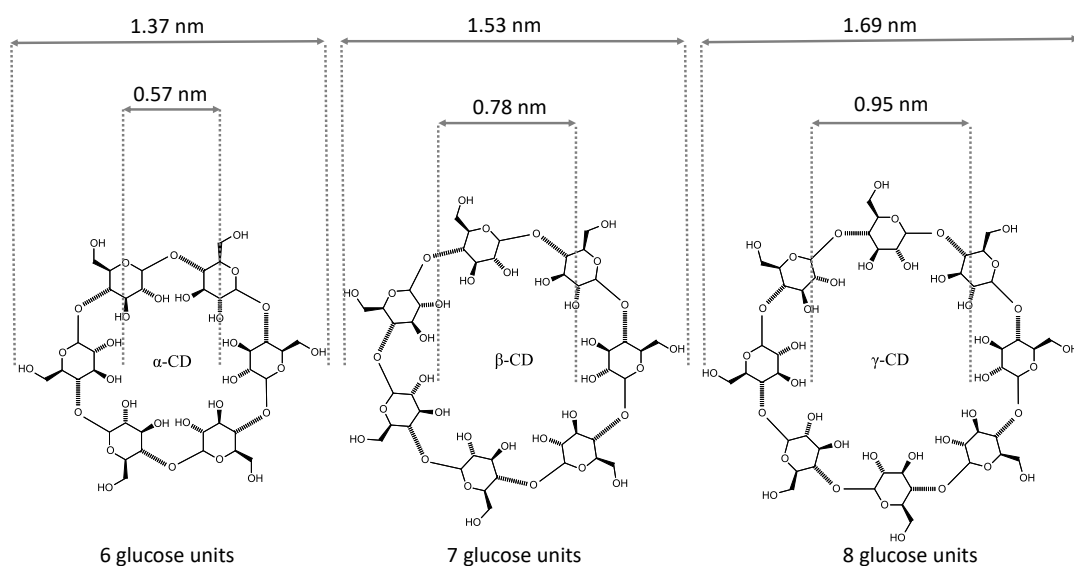


Figure 1.8: Native cyclodextrin structures for  $\alpha$ -,  $\beta$ - and  $\gamma$ -cyclodextrin (CD).

Despite the presence of numerous hydroxyl groups on the exterior of the CD molecule, natural CDs have limited water solubility. Both  $\alpha$ CD and  $\gamma$ CD have higher solubility (145 and 232 mg/mL respectively) than  $\beta$ CD (18 mg/mL at 25 °C) (76). The low water solubility is a result of CD self-association in an aqueous environments, which is concentration-dependent (73,77,78). CDs form channel-type aggregates, which are connected through hydrogen bonding between the cyclodextrin molecules (79). The geometry and axial symmetry of the intermolecular hydrogen bonded aggregates possibly affects their interaction with the surrounding water structure. The 7-fold symmetry of  $\beta$ CD creates perturbations in the water structure resulting in their abnormally low water solubility (80).

Advances in biotechnology have led to the synthesis and modification of CDs, enhancing their water solubility. Substitution of any hydroxyl group (primary and/or secondary) yields a dramatic increase of their water solubility (81). Methylated or hydroxypropyl derivatives of  $\beta$ CD and  $\gamma$ CD are of pharmaceutical interest (73). The solubility in water of hydroxypropyl- $\beta$ CD (HP $\beta$ CD) and randomly methylated  $\beta$ CD (RAMEB) is more than 600 and 500 mg/mL compared to 18 mg/mL of the native  $\beta$ CD (82,83). The same behavior applies for HP $\gamma$ CD (>500 mg/mL) (82,83). Optimum aqueous solubility is achieved when the number of methyl groups reaches 13-14; and above that threshold the solubility decreases (83).

All the native cyclodextrins are classified as “Generally Regarded As Safe” (GRAS) by the FDA (84). Hydroxypropyl  $\beta$ - and  $\gamma$ -Cyclodextrin (HP $\beta$ CD and HP $\gamma$ CD) and sulfobutylether  $\beta$ -cyclodextrin (SBE- $\beta$ -CD) are listed in the FDA’s compiled list of inactive formulation ingredients (85). Alfadex ( $\alpha$ -CD), Betadex ( $\beta$ -CD),  $\gamma$ -cyclodextrin, SBE- $\beta$ -CD, HP $\beta$ CD, randomly methylated  $\beta$ - cyclodextrin (RAMEB) are listed in the updated guidelines on the ‘Excipients in the labelling and package leaflet of medicinal products for human use’ (SANTE-2017-11668) (86). The most pharmaceutically appropriate  $\beta$ -CD derivatives are RAMEB with a 1.8 average number of

substituents per repeated glucose unit and HP $\beta$ CD with 0.65 (73,87). All the aforementioned cyclodextrins have been approved and marketed by the European Pharmacopoeia, Japanese Pharmaceutical Codex and the US Pharmacopoeia/National Formulary. Particularly,  $\alpha$ CD can be found in intravenous alprostadil solution (Carveject<sup>®</sup> Dual from Pfizer). Native  $\beta$ -cyclodextrin ( $\beta$ CD) can be found in numerous marketed oral, topical, buccal and rectal drug formulations: notable examples are Nicorette<sup>®</sup> (sublingual tablets, Pfizer) and Nimedex<sup>®</sup> (tablets, Novartis). Hydrocortisone solution (Dexocort, Actavis), indomethacin eye drop solution (Indocid, Chauvin) and itraconazole oral and i.v. solutions (Sporanox<sup>®</sup>, Janssen) contain HP $\beta$ CD and insulin nasal sprays which contain RAMEB. Voltaren<sup>®</sup> Ophthalmic (Novartis) is an eye drop solution containing diclofenac sodium salt and HP $\gamma$ CD (73).

Cyclodextrins have long been known for their ability to increase the water solubility of hydrophobic drugs by entrapping them into their non-polar cavity (88). Long before that, the purpose of using CDs in the pharmaceutical industry has been to protect drugs from oxidation and heat, prolong their shelf-life and masking unpleasant flavours and odours (89).

Cyclodextrins have been investigated for the treatment of infectious diseases by formulating them with anti-infective drugs. Their unique structure enables cyclodextrins to fully or partially incorporate hydrophobic drugs in the cavity providing the drug with improved solubility properties and enhanced biological activity. Table 1.3 shows a summary of antibiotic-cyclodextrin complexes that have been studied and how the complex improved drug efficacy. In 2003, a US patent was filed for improved growth inhibition of several Gram negative bacteria by HP $\beta$ CD and RAMEB complexes with chlorhexidine, gentamycin, tobramycin and tetracycline via improved permeation through the bacterial cell envelope (90). The inventors claimed that this patent was of great interest for a wider range of antibiotics: penicillin derivatives, cephalosporins, aminoglycosides, macrolides, rifamycin, chloramphenicol, imipenem, vancomycin, tetracyclines, fusidic acid, novobiocin, neomycin, bacitracin, polymyxin, colistimethate, colistin and gramicidin. Over the last few years, the interest in using drug-CD complexes to enhance antibiotic efficacy is not based only on their enhanced permeation but also on improving drug water solubility, stability and dissolution. For instance, native  $\beta$ CD and  $\gamma$ CD protected penicillins from  $\beta$ -lactamase hydrolysis in *E. coli* and improved the cell permeation in vitro (91). Cyclodextrin complexes have been investigated as drug release modifiers for sustained and prolonged drug delivery, such as in the case of rifampicin, tobramycin and meropenem (92–95).

Table 1.3: Summary of antibiotic-cyclodextrin complexes investigated by research groups to achieve sustained drug release, better bioavailability, increased antimicrobial activity and enhanced drug solubility.

Cyclodextrin	Drug	Outcome	Bacteria used	Ref
$\beta$ -CD or $\gamma$ -CD	Penicillins	Protection against $\beta$ -lactamase hydrolysis in vitro/ internalization into cells	<i>E. coli</i>	(91)
b-CD modified with crosslinkers	rifampicin, novobiocin, vancomycin	Sustained drug release/ Increase bioavailability	<i>S. aureus</i>	(92)
modified CDs	rifampicin, tobramycin	Sustained drug release for hip-prosthesis		(93)
HP $\beta$ CD	fluoroquinolones	Increased drug solubility by two to five times and increased stability		(96)
$\beta$ CD	meropenem	Enhance stability in aqueous solutions and in the solid phase Sustained transfer/Constant drug concentration/greater inhibition (bactericidal action)	<i>P. aeruginosa</i> , <i>Rhodococcus equi</i> , <i>Listeria ivanovii</i>	(94)
HP $\beta$ CD RAMEB	chlorhexidine, tetracycline, tobramycin, gentamicin	Improved biological activity (inhibit microbial growth/ eliminated toxic effects/ improved the dosing treatment)	<i>P. gingivalis</i> <i>B. forsythus</i> <i>B. cereus</i>	(90)
Triacetyl $\alpha$ -, $\beta$ -, or $\gamma$ CD	vancomycin	Prolonged drug release and maintained the antimicrobial activity of delivery systems for parenteral site-specific administration	<i>Staphylococcus aureus</i> or <i>Enterococcus hirae</i>	(95)

### 1.6.2 Liposomal carriers

The use of liposomal carriers has been regarded as a promising tool to enhance antibiotic activity, reduce drug toxicity and overcome bacterial resistance mechanisms (97,98). Liposomes are universal carriers for both hydrophilic and hydrophobic compounds and offer a biocompatible, biodegradable and non-immunogenic delivery system. Their unique physicochemical properties, such as small and controllable size, large surface area and potential to target a specific site of action via surface functionalization, enables them to improve drug pharmacokinetics and biodistribution.

A wide variety of promising liposomal carriers for antimicrobial agents have been reported, which are classified according to their lipid composition, membrane rigidity, surface properties and ability to trigger drug release. These classes are: conventional, fusogenic and surface-modified liposomes. Conventional liposomes are comparatively rigid carriers composed of phospholipids

with or without cholesterol, while fusogenic liposomes, also known as fluidosomes, are characterized by more fluid lipid bilayers and their ability to fuse with other lipid membranes. Table 1.4 presents several examples of how liposomes have been investigated and the outcome of the research in Gram negative antibacterial activity.

Liposomes can enhance the activity against both intracellular (*Brucella melitensis*, *Salmonella enterica* serovar *Typhimurium* and *Francisella tularensis*) and extracellular (*Pseudomonas aeruginosa*, *Escherichia coli*, *Klebsiella pneumoniae* and *Burkholderia cepacia*) pathogens (99). Liposomal carriers designed for the eradication of intracellular pathogens are taken-up by cells of the mononuclear phagocyte system. For instance, conventional liposomes encapsulating gentamicin lead to drug accumulation in the liver and spleen as a result of MPS cell phagocytosis, resulting in decreased bacterial number in these tissues (99). Liposomes designed for targeting extracellular pathogens can function in two main ways to aid drug delivery. Firstly, they can entrap, dissolve or encapsulate the active ingredient or, secondly, they can attach, conjugate or absorb the active substance. These properties can be applied to facilitate the administration of antimicrobial drugs, thereby overcoming some of the limitations of antimicrobial drug uptake.

Table 1.4: Several liposomal carriers investigated against Gram negative bacteria.

Liposome composition	Drug	Bacteria	Outcome	Ref
DPPC/Chol/SA, DPPC/DPPG, DPPC/PI, DPPC/Chol/DDAB	Chlorhexidine	<i>P. vulgaris</i>	Enhanced bactericidal activity Diffusion mechanism	(97)
DPPC/Chol (2:1)	Amicacin	<i>P. aeruginosa</i>	Superior activity of inhaled liposomes than to free drug	(100)
DPPC/DMPG in several molar ratios (15:1, 18:1, 10:1)	Tobramycin	<i>P. aeruginosa</i> <i>B. cepacian</i> <i>E. coli</i> <i>S. maltophilia</i>	Superior activity of fluidosomes than free drug Fusion mechanism	(101–103)
DPPC/DMPG (1:1)	Gentamicin-gallium	<i>P. aeruginosa</i>	Eradication of biofilm	(104)
PC(60 mg/mL)/Chol	Rifampicin		High encapsulation and nebulization efficiency Good stability	(105)

## 1.7 Aims and scope of this project

Most of the antimicrobial drugs in the current clinical pipeline are modified versions of existing classes of antibiotics which are likely to offer only short-term solutions to the current AMR crisis (106). A novel antimicrobial agent, PPA148 (belonging to the byrrolobenzodiazepine (PBD) group of anticancer and antimicrobial drugs), has shown very promising activity against Gram negative bacteria, and was synthesized at King's College London (107). Among other antimicrobial agents, PPA148 was included in a patent filed by Rahman et al. regarding its activity

against both Gram positive and negative bacteria (107). Its inhibitory concentration (MIC) in the presence and absence of the efflux pump inhibitor PA $\beta$ N (107,108) revealed promising activity against Gram negatives amongst the ESKAPE pathogens. A possible drug efflux from the bacterial membrane was also observed because the MIC decreased in all bacterial strains tested in the presence of the pump inhibitor (107). The focus of this project is on Gram negative bacteria because of their increasing contribution to the incidence of ventilator-associated pneumonia (VAP) (109), low OM permeability and high activity of multiple efflux pumps (29), which facilitate resistance. Therefore, the aim of this project has been to develop a suitable carrier to overcome the drug efflux and increase drug efficacy against Gram negative bacteria. Taking into account the physicochemical properties of PPA148, the challenges of drug uptake across bacterial membrane and multi-drug resistance in Gram negative bacteria, a formulation based on a drug-cyclodextrin complex incorporated into fluidosomes was selected.

### 1.7.1 Drug-in-Cyclodextrin-in-Liposomes

The system described as drug-in-cyclodextrin-in-liposomes allows delivery of hydrophobic, insoluble and membrane-destabilizing drugs by combining the unique properties of liposomes, with those of cyclodextrins (110). As mentioned above, each delivery system individually enhances drug bioavailability and stability (chemical and physical) and reduces toxicity; but their combination offers a superior formulation (111).

This formulation was first introduced by McCormack and Gregoriadis to enhance the delivery of dehydroepiandrosterone, retinol and retinoic acid (111). This approach has also been used in the food industry to increase the stability and water solubility of natural molecules, decrease their volatilization, allowing controlled release, while maintaining the biological effects (antioxidant activity) of free ones (112). Nerolidol, which is a natural sesquiterpene with antibacterial activity, exhibited prolonged release and increased photostability when encapsulated as a complex with HP $\beta$ CD-in-liposomes, making it a strong candidate for a natural preservative use in the food industry (113). Recent reviews reveal that a number of drugs have been encapsulated in liposomes as inclusion complexes with cyclodextrins (CDs) (110,114). Particularly, this type of formulation was tried with anti-inflammatory drugs (115,116) and anesthetics (117) to improve their encapsulation efficiency and membrane permeation; with anti-cancer drugs to improve their solubility and prolonged retention (118,119); with Ca<sup>2+</sup> channel blocker drugs to increase entrapment and liposome stability (120); and with immunosuppressants to improve solubility, drug uptake and penetration (121).

While there are reports of antibiotics solubilized by either inclusion complexes with CDs (Table 1.3), or encapsulated in liposomes (Table 1.4), we are not aware of any publication on antibiotics formulated in CD complexes encapsulated into liposomes.

### 1.7.2 Plan of the study and techniques used

This work is an attempt to increase the water solubility and enhance the antimicrobial activity of the novel antimicrobial agent, PPA148, against Gram negative bacteria by formulating it with cyclodextrins and liposomes. The first experimental chapter (Chapter 2) introduces the novel antimicrobial compound, its synthetic pathway and presents the efforts used to enhance its water solubility by using two types of modified  $\beta$ CD, HP $\beta$ CD and RAMEB. The binding constant of a 1:1 complex is measured through the band shift method using fluorescence spectroscopy. Fluorescence was studied as a function of host (CD) concentration at fixed guest (drug) concentration. The increase in fluorescence intensity and blue shift in the spectra indicates the formation of the host-guest inclusion complexes of drug with cyclodextrin. The overall stoichiometry of the complex was better investigated measuring changes in the proton resonances using NMR.

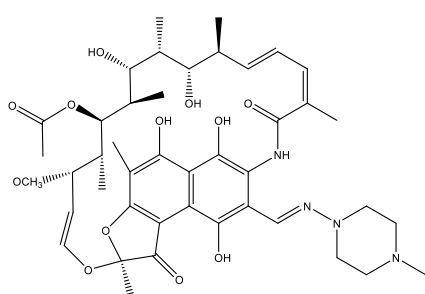
The objective of Chapter 3 is to develop a robust method for the fabrication of the drug-in-cyclodextrin-in-liposome formulation and compares its microbial activity with that of the free drug. The encapsulation efficiency and loading capacity of the carrier is determined by spectroscopic techniques. The formulated drug was used to challenge live bacteria to assess its antimicrobial efficacy and compare it with the efficacy of the unformulated drug.

Chapter 4 investigates the diffusion through lipid membranes of pure PPA148, PPA148/CD complex and empty liposomes separately using interfacial techniques. Model lipid monolayers are used to mimic the lipidic content of IM and OM of the Gram negative bacterial envelope, to assess their interaction with drug and carrier components using the Langmuir trough technique. An asymmetric model Gram negative bacterial outer membrane is used to investigate the interaction of the liposomal carrier with the lipidic content of the OM. Details on the interfacial techniques used throughout this work is given in the next section (1.7.3).

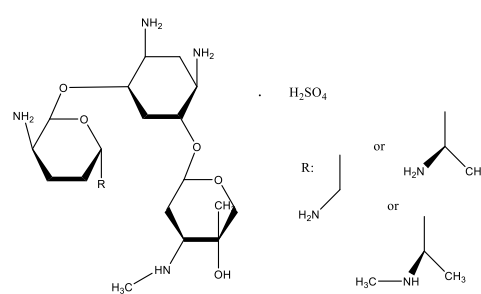
Throughout this study, rifampicin and gentamicin sulfate were used as positive and negative controls for the novel PP-A148 in the membrane interaction studies using monolayers at the air/liquid interface, whilst in bilayer studies chlorhexidine digluconate (CHD) was used as a control drug (Table 1.5, Figure 1.9). Rifampicin and gentamicin are both broad spectrum antibiotic agents against a series of Gram negative bacteria. The former passively diffuses through the cell envelope, while gentamicin follows a self-promoted diffusion across the OM and active transport across the IM (32,33,122). Chlorhexidine is known for its ability to damage membranes (123).

Table 1.5: Physicochemical properties of PPA148, rifampicin, gentamicin and chlorhexidine.

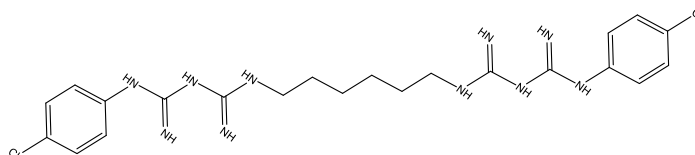
Physicochemical properties	PPA148	Rifampicin	Gentamicin Sulfate	CHD
Molecular weight (g/mol)	698.25	822.41	477.6	897.76
LogP	0.76	2.7	-3.1	6.2
logS	-7.461	-	-	-
S (mg/mL)	-	2.5	100	50%w/v
tPSA (Å <sup>2</sup> )	142.11	217	200	455



Rifampicin



Gentamicin sulfate



Chlorhexidine

Figure 1.9: Chemical structure of rifampicin, gentamicin and chlorhexidine.

### 1.7.3 Interfacial techniques used to investigate drug-membrane interactions

In the current work, the interaction of pure PPA148 and its formulated form with OM and IM Gram negative bacterial membranes was investigated using two interfacial techniques: subphase injection techniques using Langmuir monolayers and neutron reflectivity (NR) on substrate-supported asymmetric bilayers. In both techniques, phospholipids and glycolipids (specifically lipopolysaccharides), were used to mimic the lipidic component of the IM and the OM, respectively.

PE and PC possess zwitterionic headgroups and PG and CL are acidic lipids (Figure 1.3). The relative proportions of these lipids and their generalized molecular shapes affect the way in which they pack together in a membrane. PE has a conical shape (Figure 1.3) which imparts a large negative curvature to the membrane, CL also favors negative curvature, whilst PG and PC have

cylindrical shapes and are considered as low curvature lipids (124–126). *E. coli* lipid extract, DPPC/DPPG and POPC/POPG mixtures were used to simulate the lipidic component of the Gram negative IM. The composition of the lipid extract was 67% PE, 23.2% PG and 8.9% CL. White and co-workers (127) analyzed the same *E. coli* extract as the one used in this research and determined the composition of fatty acids as well (Table 1.6).

Table 1.6: Fatty acid composition of *E. coli* lipid extract as it was found by White et al. (127).

<b>R1 or R2: Fatty Acid</b>	<b>Molecular Formula</b>	<b>w/w% (127)</b>
C14:0	CH <sub>3</sub> (CH <sub>2</sub> ) <sub>12</sub> CO-	1.5
C16:1	CH <sub>3</sub> (CH <sub>2</sub> ) <sub>5</sub> CH=CH(CH <sub>2</sub> ) <sub>7</sub> CO-	4.2
C16:0	CH <sub>3</sub> (CH <sub>2</sub> ) <sub>14</sub> CO-	37.3
C17:0cyclo	CH <sub>3</sub> (CH <sub>2</sub> ) <sub>5</sub> CHCH <sub>2</sub> CH(CH <sub>2</sub> ) <sub>7</sub> CO-	18.2
C18:1	CH <sub>3</sub> (CH <sub>2</sub> ) <sub>5</sub> CH=CH(CH <sub>2</sub> ) <sub>9</sub> CO-	31.1
C18:0	CH <sub>3</sub> (CH <sub>2</sub> ) <sub>16</sub> CO-	0.9
C19:0cyclo	CH <sub>3</sub> (CH <sub>2</sub> ) <sub>5</sub> CHCH <sub>2</sub> CH(CH <sub>2</sub> ) <sub>7</sub> CO-	6.7

Glycolipids and lipopolysaccharides (LPS) in particular, are a different category of lipids and were used in this work to mimic the outer leaflet of the OM. In this study, we have used three different types of LPS as shown in Figure 1.10 with different lengths of oligosaccharide chain. Rc J5 and Ra EH100 LPS are extracted from the J5 and EH100 *E. coli* bacteria, respectively, while Re Lipid A is extracted from R595 *S. minnesota*. Rc J5 LPS and Re Lipid A were used in the interaction studies on monolayers at the air/liquid interface of a Langmuir trough. The Ra EH100 LPS was used to form the outer leaflet of a model asymmetric bilayer, which was used to examine the interaction of fluidosomes with the model membrane by neutron reflectivity.

### 1.7.3.1 Langmuir trough isotherms

The Langmuir trough technique is used to form planar monolayers at the air-liquid interface and measure the partitioning properties and kinetics of molecules binding to biomimetic model membranes. The most important indicator of the monolayer properties of an amphiphilic material is given by measuring the surface pressure as a function of the area of water surface available to each molecule. This is carried out at constant temperature and is known as a surface pressure - area isotherm or simply Langmuir isotherm. Usually an isotherm is recorded by compressing the film (reducing the area with the barriers) at a constant rate while continuously monitoring the surface pressure (Figure 1.11). When the available area for the monolayer is large, the distance between adjacent molecules is large and their interactions are weak. The monolayer can then be regarded as a two-dimensional gas (2D). Under these conditions, the monolayer has little effect on the surface tension of water. If the available surface area of the monolayer is reduced by a barrier system, the molecules start to exert a repulsive force on each other. This two-



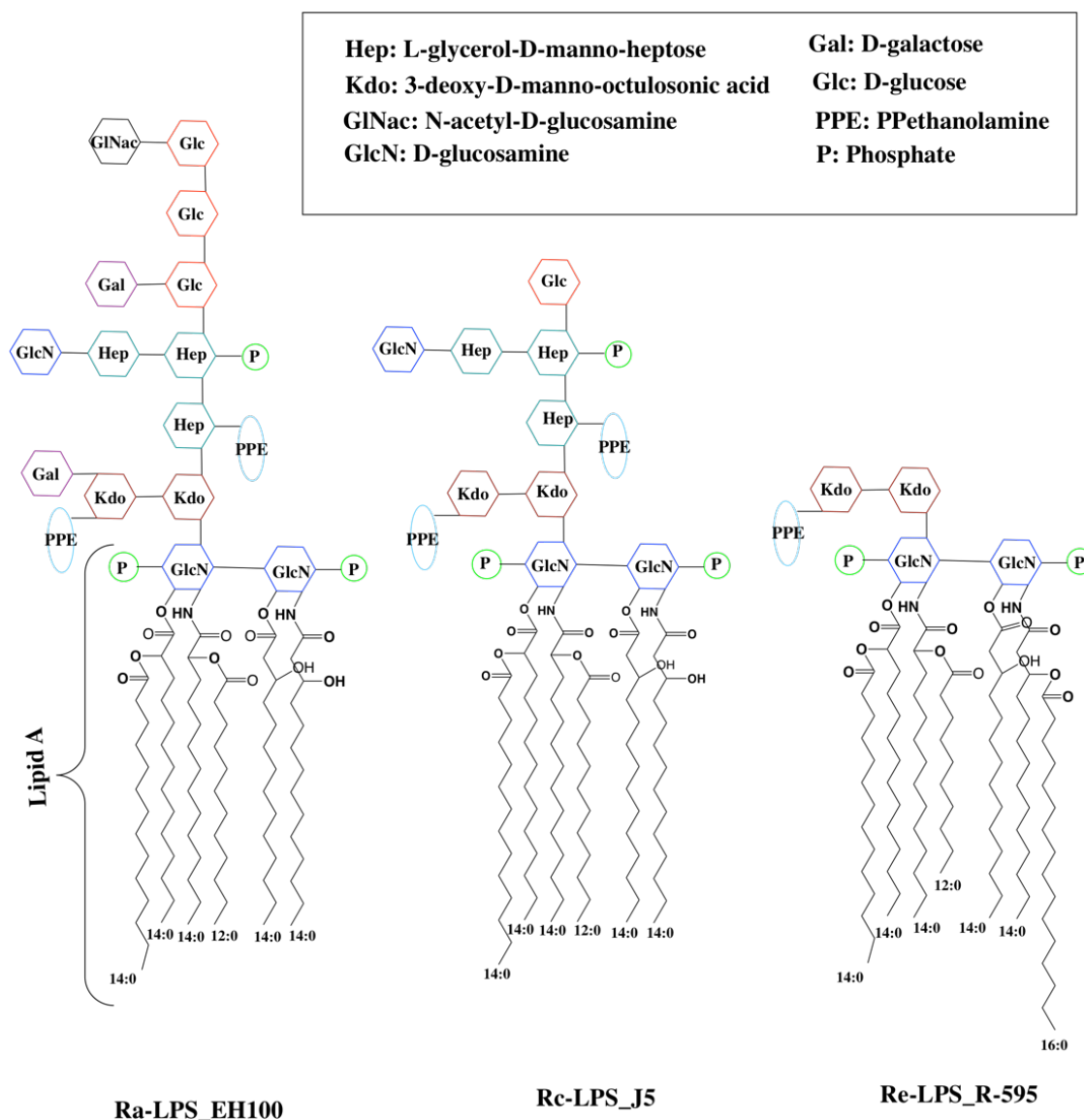


Figure 1.10: Structure of Ra LPS derived from *E. coli* EH100, Rc LPS derived from *E. coli* J5 and Re LPS derived from *S. minnesota*.

dimensional analogue of a pressure is called surface pressure. At low surface pressures the monolayers exist in the gaseous state (G) and upon compression might undergo a phase transition to the liquid-expanded state (L1) (128). Upon further compression, the L1 phase undergoes a transition to the liquid-condensed state (L2), and at even higher pressure the monolayer finally reaches the solid state (S) (Figure 1.11). If the monolayer is further compressed after reaching the S state, it will collapse into three-dimensional structures. The collapse is generally seen as a rapid decrease in the surface pressure or as a horizontal break in the isotherm if the monolayer is in a liquid state.

The advantage of using such films is that they are of defined lipid composition and controlled in terms of their surface area (129). P-Area isotherms show the relationship between the molecular area of a film occupied on the liquid surface and the surface pressure observed. Langmuir films

were used as a convenient platform for studying the interaction of the novel compound with the lipid monolayers at the air/liquid interface at 30 mN/m, which is widely accepted as a monolayer surface pressure yielding lipid packing with molecular areas most accurately corresponding to those in biological membranes (130).

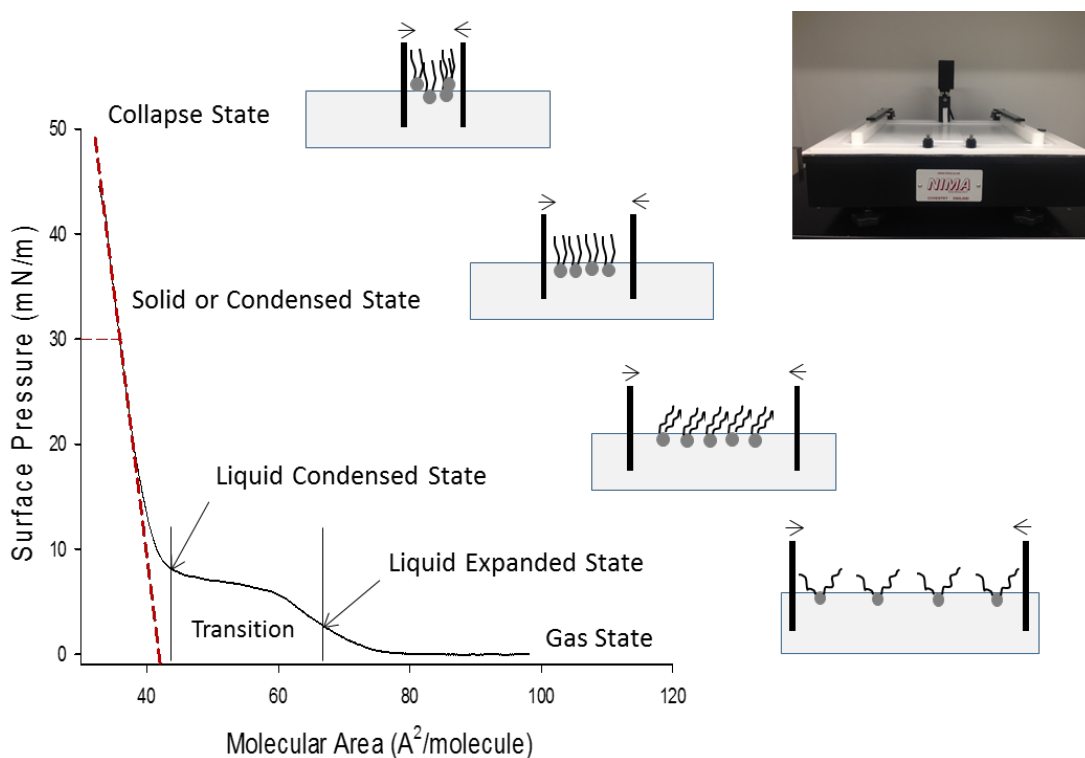


Figure 1.11: Langmuir trough lipid monolayers and their transition stages upon compression as described by changes in the Surface Pressure-Area isotherm. The illustration depicts the packing or the lipid alcy chain upon compression from its 2D gas state until the collapse of the monolayer and the formation of 3D structures.

### 1.7.3.2 Neutron reflectivity

Neutron reflectivity is a more sophisticated way of investigating the composition and the relative location of molecules within and at the interface of supported asymmetric bilayers. Neutrons are neutral particles which are characterized by their non-destructive nature, sensitivity to light elements (hydrogen/deuterium, carbon, nitrogen and oxygen) and long penetration depths into matter (131,132). Neutrons interact directly with the nuclei of molecules in a sample and are scattered due to the presence of the strong nuclei observed in classical optics.

Neutrons behave as particle waves and thus follow in principle the quantum-mechanic rule described by Planck and de Broglie (Appendix A). The kinetic energy of a neutron beam is related to the wavelength of the periodic neutron wave by its momentum (particle mass and velocity, Equation A1. 4). Modifications of neutron momentum  $p$  and their energy ( $E$ ) indicate changes in the neutron track (Figure 1.12).

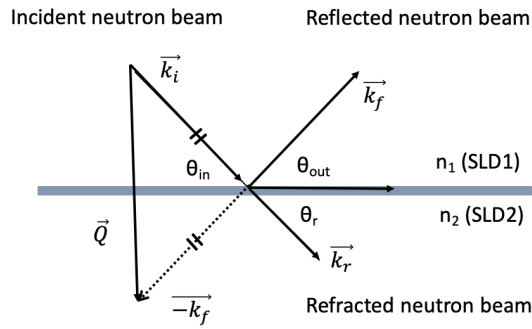


Figure 1.12: The classic optics of a beam, hitting a planar surface, related to the geometry of this process with the wavevector transfer. The wavevector is the “spatial” frequency of the neutron wave and is described by the  $|k| = \frac{2\pi}{\lambda}$ , where  $k$  is the wavevector and  $\lambda$  is the neutron wavelength.  $\vec{k}_i$ ,  $\vec{k}_f$  and  $\vec{k}_r$  are the wavevectors of incident, reflected and refracted neutron beam, respectively.  $\vec{Q}$  is the wavevector transfer ( $\vec{k}_i - \vec{k}_f$ ),  $\theta_{in}$ ,  $\theta_{out}$  and  $\theta_r$  are the incident, outgoing and refracted angle of the neutron beam.

In an ideal simple scattering experiment, the scattering is elastic and, therefore, there is no energy transfer to be considered. The scattering event is restricted to the wavevector transfer ( $Q = |k_i| - |k_f|$ ) (Figure 1.12). The condition of “no energy exchange” ( $E_i = E_f$ ) between the neutron and the sample implies that there is no modification of the wavelength of the neutron ( $|k_i| = |k_f|$ ). Based on elementary trigonometry (Figure 1.12) leads to the following wavevector transfer formula:

$$Q = \frac{4\pi \sin \theta_{in}}{\lambda} \tag{Equation 1.1}$$

, where  $Q$  describes the wavevector transfer position in reciprocal space in the  $z$  direction (Figure 1.13B),  $\theta_{in}$  is the incident angle and  $\lambda$  the wavelength of the neutron beam. Reflected neutrons from a thin film may undergo strong interference depending on the wavelength of the neutron, their state of polarization, the thickness of the layer and the neutron refractive indices of the media involved (Figure 1.13). The scattering length densities (SLD) reflects the magnitude of scattering by each molecules in the sample, and is similar to a refractive index in light scattering. The relative values of SLDs of the constituting molecules is of major importance for the analysis of complex structures.

A standard multilayer method is used to calculate the reflectivity profile. Neutrons travel through the matter at different speeds and, thus, penetrate the layers to different depths (Figure 1.13A). The difference between the wavevector transfer of the two ejected neutrons ( $k$ ), which appears as interference fringes in the reflectivity profile (Figure 1.13A), is directly related to the thickness of the interfacial layer by:

$$k = Q_2 - Q_1 = \frac{2\pi}{d} \tag{Equation 1.2}$$

, where  $Q_2 - Q_1$  describes the separation of between the interference fringe and  $d$  is the thickness of the interfacial layer. Although the wavevector transfer ( $Q$ ) links the magnitude of momentum

transfer with the scattering angle, it does not capture all the spatial aspects. The scattering of a neutron occurs in a three-dimensional system; therefore the position of the scattered wavevector  $k_f$  is defined by a second angle  $\phi$  (Figure 1.13B), which is required for the measurement of rotation about  $k_i$ . The angles  $\theta$  and  $\phi$  determine the direction of the outgoing neutron, the same way as longitude and latitude give the position of a point on the surface of the Earth.

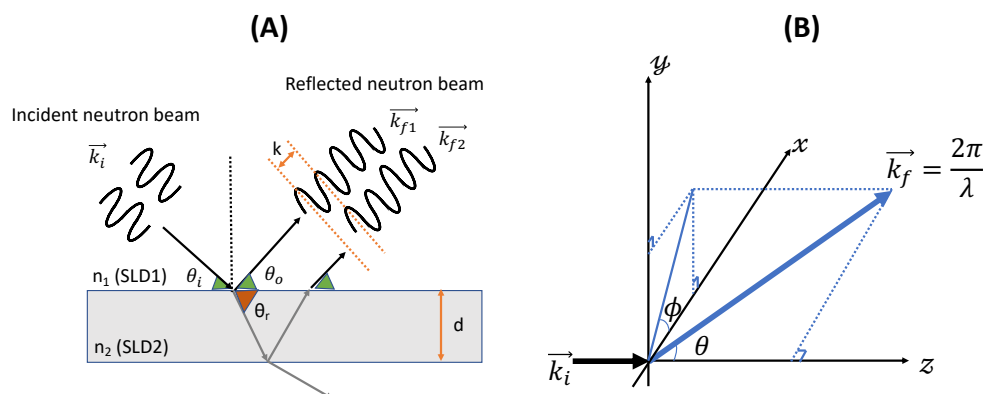


Figure 1.13: (A) The oscillations in the reflectivity profile resulting from the interference which depends on the thickness ( $d$ ) of the layer (in terms of the position) and the difference in scattering contrasts between the respective interfaces (in terms of the amplitude).  $\vec{k}_i$  is the wavevectors of the incident neutron beam and  $\vec{k}_{f1}$  and  $\vec{k}_{f2}$  the outgoing neutron beam from the top and bottom of the interfacial layer, respectively.  $n_1$  and  $n_2$  are the refractive index of light while SLD1 and SLD2 are the refractive indexes of neutrons in two different bulk phases.  $\theta_{in}$ ,  $\theta_o$  and  $\theta_r$  are the incident, outgoing and refracted angle of the neutron beam. (B) The scattering geometry in both Cartesian and spherical polar coordinates with  $\phi$  and  $\theta$  are angles determining the direction of the outgoing neutron beam.  $\vec{k}_f$  is the wavevectors of reflected neutron beam and  $\lambda$  is the neutron wavelength.

The SLD profile is directly related to the distance along the  $z$  axis and gives information about the thickness, roughness and solvation of a particular layer. The use of contrast variation is essential in NR experiments in order to obtain as much information as possible about each layer. A way to achieve this is the use of isotopic substitutions in the whole molecule or part of a molecule, to manipulate contrast (neutron refractive index). The SLD is related to the refractive index by the following formula (133):

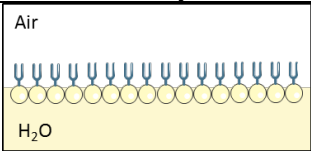
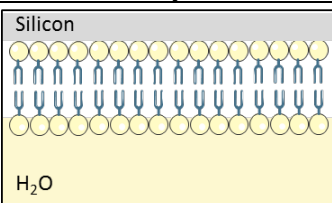
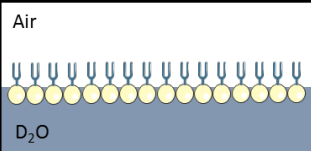
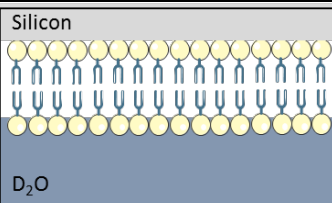
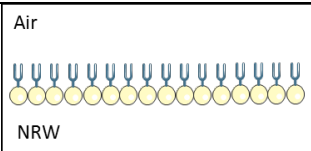
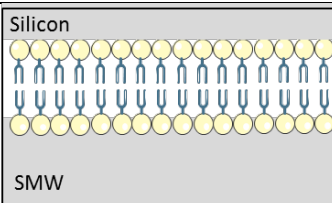
$$n \approx 1 - \frac{\rho\lambda^2}{2\pi} \quad \text{Equation 1.3}$$

, where  $n$  is the refractive index,  $\rho$  is the SLD and  $\lambda$  is the neutron/light wavelength. The possibility to selectively labelling a molecule with isotopes of different SLD allows the neutron beam to highlight or mask specific regions of the molecule. One of the most extensively used contrast variations is between hydrogen and deuterium (134,135), since the scattering length densities of these two isotopes are markedly different.

Examples of contrast variation are described in Table 1.7. If tail-deuterated lipids are spread on the air/D<sub>2</sub>O interphase in pure D<sub>2</sub>O, the total scattering intensity is given by the lipid headgroup

(135). It is possible to match the SLD of an H<sub>2</sub>O and D<sub>2</sub>O mixture to the scattering length density of specific biological molecules and materials. For instance, a mixture of approximately 38% D<sub>2</sub>O in H<sub>2</sub>O (v/v) matches the SLD of silicon, whereas a mixture of 13% D<sub>2</sub>O in H<sub>2</sub>O (v/v) would match the SLD of hydrogenated lipids. The matched molecules would not contribute to the neutron scattering and the scattering profile contains no information regarding these molecules. In air/water Langmuir interface experiments, it is convenient to use 8% D<sub>2</sub>O in H<sub>2</sub>O (v/v) solution which has no scattering (SLD=0) (136). The SLD is identical to that of air and, therefore, the solution is called null reflected water (NRW). In contrast, in supported lipid bilayers on a silicon surface, a mixture of 32% D<sub>2</sub>O and 62% water matches the SLD of silicon and is called silicon matched water (SMW).

Table 1.7: Potential isotopic contrasts and main information content of a monolayer on an air/water interface or a deposited lipid bilayer on a silicon surface consisting for tail deuterated phospholipids. NRW and SMW stand for null reflective water (8.2% D<sub>2</sub>O) and silicon match water (38% D<sub>2</sub>O) respectively and are used to cancel out the background of the two mediums and highlight the interface.

Contrast cartoon/ Mololayer	Main information	Contrast cartoon/ Bilayer	Main information
	Lipid hydrocarbon tail		Hydrocarbon lipid tails
	Lipid headgroup		Lipid Headgroups
	Lipid components		Interface Lipid bilayer
$SLD_{D_2O} = 6.35 \times 10^{-6} \text{ \AA}^{-2}$ $SLD_{NRW} = 0 \text{ \AA}^{-2}$		$SLD_{H_2O} = -0.56 \times 10^{-6} \text{ \AA}^{-2}$ $SLD_{SMW} = 2.00 \times 10^{-6} \text{ \AA}^{-2}$	

All these advantages have made neutrons an ideal tool for studying the composition and structure of supported model lipid membranes by measuring the diffracted neutron beam. In this study, specular neutron reflectivity is used to characterize the in- plane model asymmetric membranes and study changes in their structure caused by exposure to a liposomal drug carrier. Ra-EH100 LPS and DPPC, which account for the lipidic component of the outer and inner leaflet respectively of the OM, were deposited on a flat silicon surface forming a model asymmetric membrane as presented in Figure 1.14.

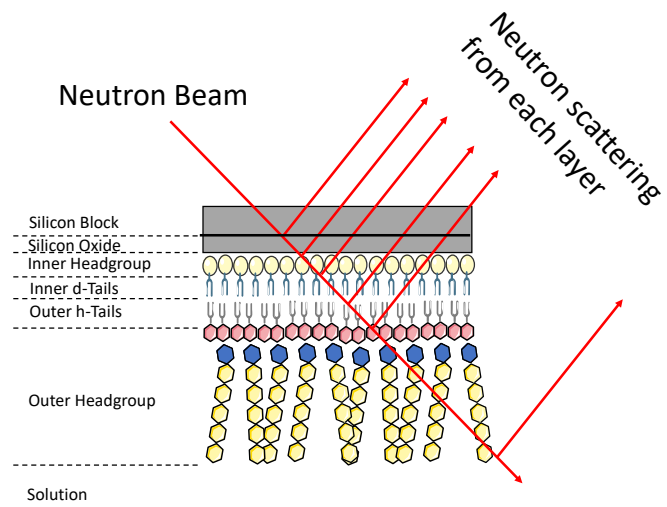


Figure 1.14: Asymmetric lipid bilayer formed of Ra-EH100 LPS and DPPC and deposited on a silicon surface. The red arrows show the neutron path when the beam hits the surface.

A highly collimated beam of neutrons hits the flat surface and the neutrons travel through the individual layers of the membrane. The intensity of the reflected radiation is measured as a function of angle or neutron wavelength and plotted against neutron momentum. This reflectivity data sets (all three contrasts) are then transformed into SLD vs distance and these data are fitted to a mathematical layered model, providing a real space distribution of the data sets.

# Chapter 2 Synthesis, characterization and solubility of PPA148

## 2.1 Introduction

Pyrrolobenzodiazepine (PBD) drugs are a family of natural anticancer-antibiotics isolated from various Actinomycetes bacteria. They are a class of sequence-selective DNA minor-groove agents. The first PBD monomer, anthramycin, was originally discovered as a metabolite of *Streptomyces refuineus* (137). Since then, several natural PBDs have been isolated from *Streptomyces*, *Micrococcus* (138) and *Klebsiella* (139) bacteria and various PBDs have been chemically synthesized (140). A tricyclic scaffold is the basic skeletal structure of the PBD molecules (Figure 2.1) (107,108,141,142). The system consists of a substituted aromatic A-ring, a diazepine B-ring and a pyrrolidine C-ring (Figure 2.1). Their biological activity is facilitated via covalent binding of the imine moiety at position N10-C11 to the C2-amino group of guanine. The imine moiety at N10-C11 is the electrophilic center responsible for DNA binding (142). It has been reported that PBDs have antimicrobial activity against Gram positive and Gram negative bacteria. However, their high degree of toxicity has hindered their use as antibiotics (108). Derivatization and the use of different synthetic routes from several research groups have attempted to decrease their toxicity while maintaining their antibacterial activity (108).

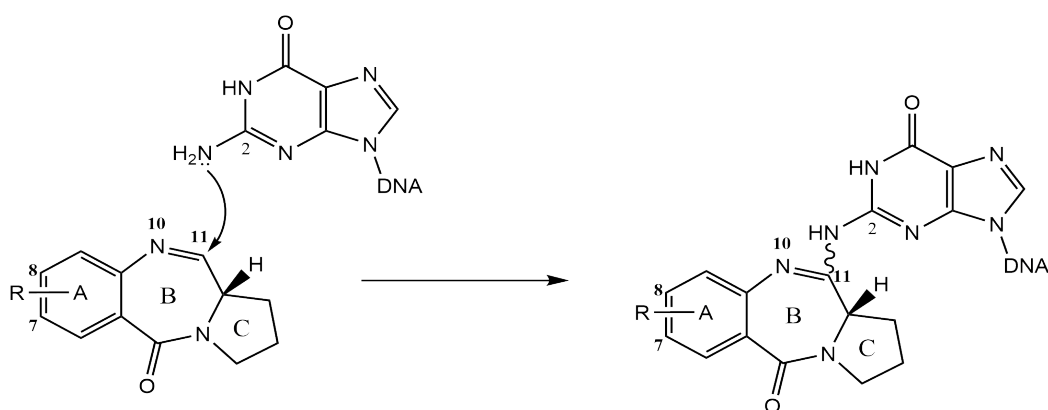


Figure 2.1: Mechanism of tricycle PBD core binding to the N2 of guanine in the DNA minor groove reproduced from Brucoli et al. (143).

A novel series of modified PBD biaryl hybrids with lower cytotoxicity against eukaryotic cells compared to the monomer was chemically synthesized at King's College London (108). The chemical structure of this class is described as a tricycle PBD scaffold linked to a lateral polyamidic tail in position 8 via a 4-carbon aliphatic chain. PPA148 is the lead antimicrobial compound of this novel class of molecules. Its tail comprises three units linked with an amide bond, an N-methyl-pyrrole-4-amino methyl ester, a benzofuran unit and a thiomorpholine unit (Figure 2.2). Three building blocks have been proven to give optimum antibacterial activity (108). A screening of the physicochemical properties was performed using ChemDraw software to obtain a first indication of the lipophilicity and polarity of PPA148. Based on the structure, drug family and physicochemical properties estimated by ChemDraw (Mw = 698.25 g/mol, clogP = 2.09 and logP = 0.76) (Table 2.1), PPA148 is a large and non-ionic lipophilic molecule, whose bactericidal activity is attributed to its binding onto bacterial DNA. According to O'Shea et al. (12)



and Brown et al. (144), antimicrobial agents have distinct properties, which often violate Lipinski's rule of five (Table 1.1) (12,13) and depend on their activity against Gram positive and/or Gram negative bacteria due to differences in the constitution of the bacterial cell envelope as presented in Table 2.1. Based on these findings, PPA148 seems to have a similar lipophilicity (clogP) to antimicrobials acting against Gram positive, and similar polarity (tPSA) to those acting against Gram negative bacteria (Table 2.1). Nevertheless, measurements of the minimum inhibitory concentrations (MIC) showed that PPA148 is active against both types of bacteria (Appendix B, Table B 1; Table B 2) but present reduced permeability in Gram negative. In fact, MIC experiments were conducted in the presence of the efflux pump inhibitor, PA $\beta$ N, which showed significantly reduced MIC values, thus indicating that PPA148 is affected by the efflux pump. The low water solubility and the results from the microbiological assay suggest that enhancing the solubility of the drug may improve its uptake and thus help increase its antimicrobial activity against Gram negative bacteria.

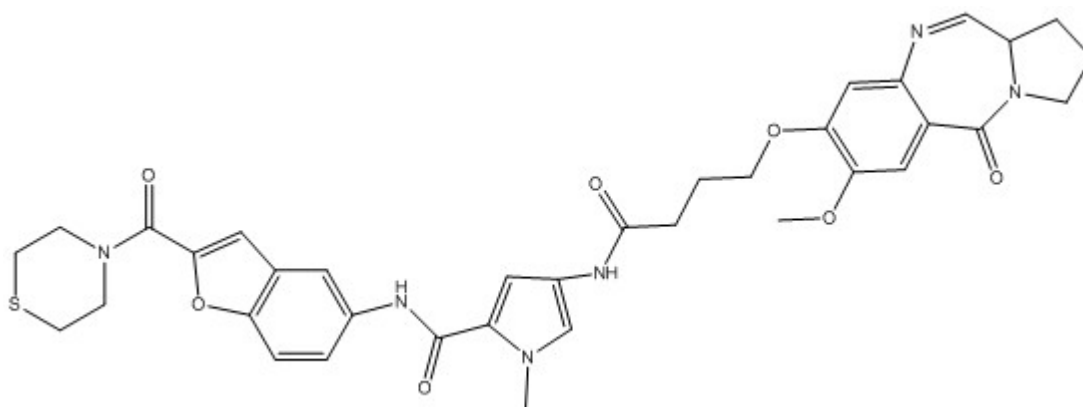


Figure 2.2: Chemical structure of PPA148.

Table 2.1: Comparison of the physicochemical properties of PPA148 estimated by ChemDraw compared (the experimental values are presented in parenthesis) with the generic optimal properties of antibacterial drugs for oral or parental administration as calculated by O'Shea et al. (12) based on data collected from the literature and drug data bases.

Physicochemical properties	PPA148	Optimal properties against Gram negative	Optimal properties against Gram positive
Mw (g/mol)	698.25	414 (cutoff of 600)	813
LogP	0.76	-	-
cLogP	2.09	-0.1	2.1
LogS	-7.461 (-4.37)	-	-
tPSA (Å <sup>2</sup> )	142.11	165	243

Mw: Molecular weight

The approach to enhance water solubility is to use cyclodextrins, which are well-known pharmaceutical excipients, capable of forming inclusion complexes with a wide range of poorly soluble molecules (72,144) (Figure 2.3). Cyclodextrins are cyclic oligosaccharides containing 6 ( $\alpha$ CD), 7 ( $\beta$ CD) or 8 ( $\gamma$ CD) ( $\alpha$ -1,4)- $\alpha$ -D-glucopyranose units, respectively. All hydroxyl groups are oriented to the cone exterior with the primary hydroxyl groups at the narrow side of the toroid

cone and the secondary on the opposite (wider) side (145) (Figure 2.3). The hydrogens of the skeletal carbons at position 1, 2 and 4 are mainly located on the exterior side of the toroid molecule and the hydroxyl groups at position 2, 3 and 6 are oriented toward the exterior of the cone. The central cavity includes the hydrogens at position 3 and 5 and the ring of glycosidic ether oxygen is present with H-6 located near the cavity (145) (Figure 2.3). This central cavity has a polarity similar to ethanol (146). Due to this unusual structure, cyclodextrins are able to encapsulate (partially or wholly) a wide variety of guest molecules of suitable size, shape, structure and physicochemical properties, resulting in a stable association without the formation of covalent bonds (77,87). In an aqueous environment, the hydroxyl groups form hydrogen bond with water molecules, creating a hydration shell around the CD molecule.

This capability of CDs to form water-soluble complexes with (lipophilic) poorly soluble drugs has been used extensively to increase their solubility (73,147). Two types of complexes can be formed: inclusion and non-inclusion. With inclusion complexes, the central cavity provides a lipophilic microenvironment to the molecule; the guest (drug) and host (CDs) are in dynamic equilibrium with the complex (Equation 2.1). Non-inclusion complexes are formed by hydrogen bonds between the outer surface of the CDs (hydroxyl or another substituted group) and the drug (73). It is possible that both types of complexes can co-exist (148,149).

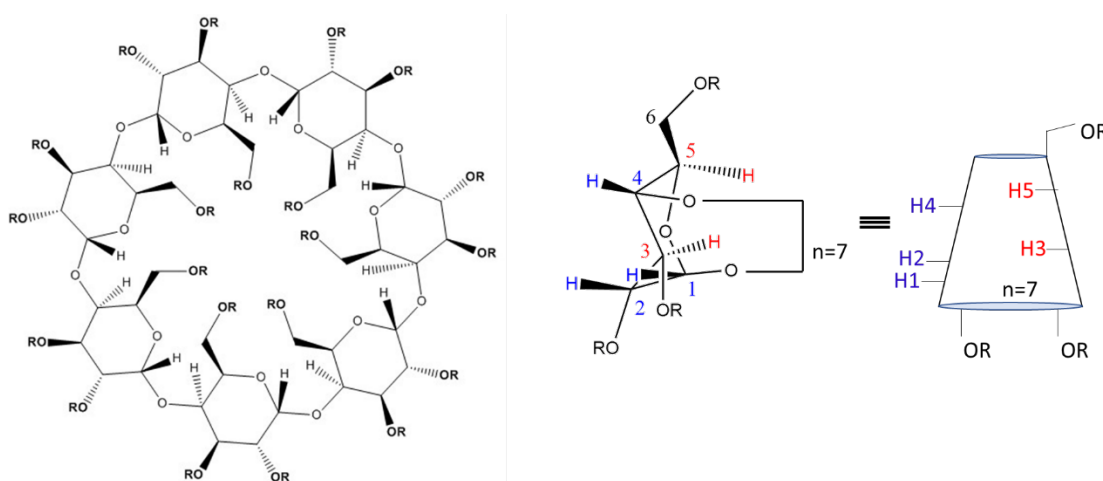


Figure 2.3: Different representations of the structure and conformation of  $\beta$ -cyclodextrin, showing the orientation of the hydrogens and hydroxyl groups. Native  $\beta$ CD contains hydroxyl groups, while its derivatives can be substituted by different functional groups. RAMEB contains either hydrogens or methyl groups, while HP $\beta$ CD has either hydrogens or hydroxypropyl groups.

The complexation process is characterized by the equilibrium or binding constant ( $K$ ) (Equation 2.2). The binding constant provides a measure of the affinity between the guest and the host. The following equations describe the interaction and the stoichiometry of the complexes formed.



$$K = \frac{CD_mD_n}{CD^m \times D^n} \quad \text{Equation 2.2}$$

, where  $m$  and  $n$  describe the stoichiometry of the CD/drug complex. For instance, a 2:1 CD/drug complex would have  $m$  of 2 and  $n$  of 1. Binding constants for cyclodextrin lie between 50 and 2000  $M^{-1}$  (73) and inconsistencies among the methods used to determine the binding constant have been reported (75).

In this chapter we report the synthesis of a novel antibiotic, PPA148, its characterization and the formation of inclusion complexes with either HP $\beta$ CD or RAMEB to increase its solubility. A convergent synthetic route was applied based on the separate synthesis of the tricyclic PBD scaffold and the lateral polyamidic tail (107,108). The two final pure core and tail molecules were linked via an amidic bond to form the final PPA148. Following the synthesis, the physicochemical characteristics, such as solubility, of this novel antimicrobial agent were measured. Finally, the drug was formulated with HP $\beta$ CD and RAMEB and drug/CD binding constants measured using fluorescence spectroscopy. Given the low solubility of the drug, this was the first step towards potentially enhancing its efficacy by forming inclusion complex with a  $\beta$ CD derivative. Enhancement of water solubility will help to optimize the drug for local use to the lungs by avoiding precipitation and side effects (150). The second step for achieving increased antibacterial activity was to prepare a liposomal carrier to help PPA148 breach the bacterial cell envelope and bind to the chromosomal DNA (Chapter 3).

## 2.2 Materials

**Reagents and chemicals used for the synthesis:** (Diacetoxyiodo)benzene (BAIB), 3,4-dihydro-2H-pyran (DHP), 4-(dimethylamino)pyridine (DMAP), p-toluenesulfonic acid monohydrate (PTSA) ( $\leq 100\%$ , sulphuric acid 1 - 5%), 2,2,6,6-tetramethylpiperidinoxy (TEMPO), tetrakis(triphenylphosphine)palladium(0), triphenylphosphine and N-(3-dimethylaminopropyl)-N'-ethylcarbodiimide hydrochloride (EDCI) were purchased from Sigma-Aldrich, UK. Dichloromethane (DCM), dioxane, N,N-dimethylformamide (DMF), methanol, acetone, ethyl acetate (EA), acetonitrile (ACN) and thiomorpholine were purchased from Sigma-Aldrich, UK. LC/MS grade water was supplied by Merck, UK. Ethyl-5-amino-1-benzofuran-2-carboxylate and 4-tert-butoxycarbonylamino-1-methyl-1H-pyrrole-2-carboxylic acid were purchased by Fluorochem Ltd (Hadfield, UK). Citric acid, sodium chloride (NaCl), brine and sodium bicarbonate (NaHCO<sub>3</sub>) were purchased from Sigma-Aldrich, UK. Formic acid for use in LC/MS was purchased by Fisher Scientific UK. Silica was purchased from Sigma-Aldrich, UK, and TLC silica gel 60 F254 aluminium sheets (20 cm) were supplied by VWR International, UK. Deuterated water, chloroform and DMSO were purchased by Sigma-Aldrich, UK.

**Cyclodextrins:** Hydroxypropyl- $\beta$ -cyclodextrin (HP $\beta$ CD), randomly methylated  $\beta$ -cyclodextrin (RAMEB) and heptakis (2,6-di-O-methyl)- $\beta$ -cyclodextrin (DIMEB) were purchased from Sigma-Aldrich, UK

**Active Pharmaceutical Compounds:** Rifampicin, gentamicin sulfate and chlorhexidine digluconate were purchased by Sigma-Aldrich, UK.

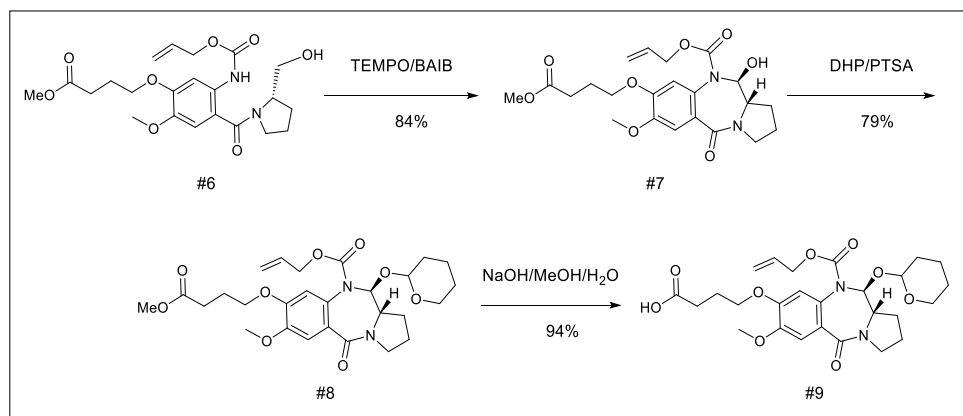
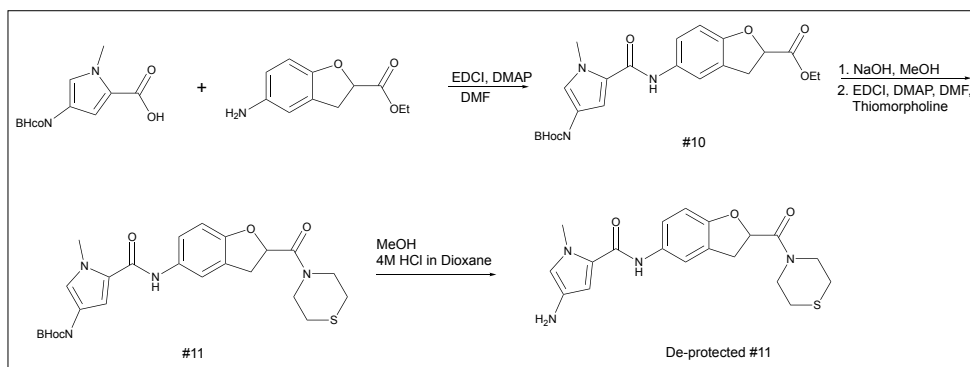
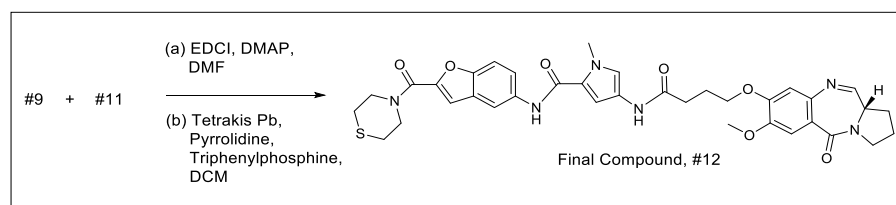
**Buffer preparation:** Trizma(R) hydrochloride (BioUltra, for molecular biology,  $\geq 99.0\%$ ) and HEPES ( $\geq 99.5\%$ ) purchased from Sigma-Aldrich, UK. Sodium chloride (NaCl), calcium chloride ( $\text{CaCl}_2$ ) and magnesium chloride ( $\text{MgCl}_2$ ), supplied from Sigma-Aldrich, UK. The ultrapure water at 18.2 M $\Omega$  was produced by a Purelab Ultra machine from ELGA process water (Marlow, UK).

## 2.3 Methods

This section describes the methods applied for the synthesis and characterization of all intermediate and final compounds. All the compounds were tested with TLC (2.3.2), LC/MS (2.3.3), proton and carbon NMR (2.3.4) and FTIR (2.3.5). The conditions of these tests are stated in separate sections from that of the synthetic pathway (2.3.1). Methods used for further characterization of the final compound (aqueous solubility) and complex formation for enhancing water solubility will be described at the end of this section (2.3.6: Adsorption assay using the Langmuir trough, 2.3.7: Ultra Violet Spectroscopy, 2.3.8: Turbidimetric Assay, 2.3.9: Water Solubility Test, 2.3.10: Quantification of drug binding affinities to Cyclodextrin (Fluorescence Binding constant assay), 2.3.11: Phase solubility diagram, 2.3.12: Continuous method variation (Job's plot))

### 2.3.1 Synthetic pathway of PPA148

The complete reaction sequence is shown in Scheme B 1, Appendix B (107). In the present work, the synthetic route was performed according to Scheme 2.1. It is separated into 3 sections. The first (Scheme 2.1A) describes the core synthesis, the second (Scheme 2.1B) the tail and the last (Scheme 2.1C) shows the coupling of the two parts to form the final compound #12 (PPA148).

**(A)****(B)****(C)**

Scheme 2.1: Synthesis of C8-linked pyrrolobenzodiazepine-carboxylate conjugate (A: PBD corecarboxylate, B: Tail conjugate and C: final core and tail coupling and deprotection steps)

Synthesis of core compound #7 (IUPAC name: allyl 11-hydroxy-7-methoxy-8-(4-methoxy-4-oxobutoxy)-5-oxo-2,3,11,11a-hexahydro-1H-pyrrolo[2,1-c][1,4]benzodiazepine-10(5H)-carboxylate) was achieved by the following method. Compound #6 (1.73g, equiv. 1) underwent a mild aerobic oxidation by adding TEMPO (65.85 mg, equiv. 0.11) and diacetoxyiodobenzene (BAIB, 1.48 g, equiv. 1.2) in dichloromethane (88 mL). The reaction was left under stirring for 12 hours with regular TLC monitoring (EA as mobile phase). The reaction mixture was washed with saturated sodium metabisulphite (44 mL) followed by saturated aqueous NaHCO<sub>3</sub> (2 × 44 mL), water (44 mL) and finally brine (44 mL). The resulting solution containing crude #7 was dried over MgSO<sub>4</sub> and the solvent was removed by rotary evaporation under reduced pressure. The crude product was purified using flash chromatography (EA/DCM).

The synthesis of core compound #8 (IUPAC name: allyl 7-methoxy-8-(4-methoxy-4-oxobutoxy)-5-oxo-11-(tetrahydro-2H-pyran-2-yl)oxy)-2,3,11,11a-hexahydro-1H-pyrrolo[2,1c][1,4]benzodiazepine-10(5H)-carboxylate) was carried out by the following method. The N10-alloc protected carbinolamine #7 (1.3 g, equiv. 1) was added to a solution of DHP (2.6 mL, 10 equivalents) and a catalytic amount of PTSA (11 mg, equiv. 0.06) in ethyl acetate (24 mL). After two hours of stirring, TLC analysis (DCM/EA (90:10) as mobile phase) showed completion of reaction and the reaction mixture was diluted with ethyl acetate (23 mL). The resulting solution was washed with saturated aqueous NaHCO<sub>3</sub> (20 mL), followed by brine (20 mL). The ethyl acetate layer was then dried (MgSO<sub>4</sub>) and evaporated using a rotary evaporator (RC 600 with a SC920 G vacuum pump system and a C 900 chiller, KNF Lab (Oxford, UK), under reduced pressure. Product #8 was purified by flash chromatography (DCM:EA 90:10).

Core compound #9 (IUPAC name: 4-(10-(allyloxycarbonyl)-7-methoxy-5-oxo-11-(tetrahydro-2H-pyran-2-yl)oxy)-2,3,5,10,11,11a-hexahydro-1H-pyrrolo[2,1c][1,4]benzodiazepine-8-yl)butanoic acid) was synthesized using the following steps. Excess NaOH 0.5M was added to a solution of #8 in dioxane at room temperature. The reaction mixture was left under stirring for 4 hours at which point TLC showed completion of the reaction. Dioxane was evaporated under vacuum and the residue was diluted with water. The resulting solution was acidified with 1 M citric acid followed by extraction with ethyl acetate (2 × 100 mL). The combined organic layers were washed with brine (100 mL), dried over MgSO<sub>4</sub> and finally concentrated using a rotary evaporator under reduced pressure. Product #9 was purified by flash chromatography (DCM:EA 90:10).

The synthesis of the tail compound is a series of three amide coupling reactions. The tail compound #10 (IUPAC name: 4-((tert-butoxycarbonyl)amino)-1-methyl-1H-pyrrole-2-carboxamido)benzofuran-2-carboxylic acid) was synthesized according to the following procedure. 4-((tert-butoxycarbonyl)amino)-1-methyl-1H-pyrrole-2-carboxylic acid (900 mg, equiv. 1.2) was dissolved in DMF (4-5 mL). EDCI (598 mg, equiv. 2.5) and DMAP (558 mg, equiv. 3) were added to the solution and was left under magnetic stirring in a pure N<sub>2</sub> atmosphere for 20 minutes. At this point, ethyl 5-amino-1-benzofuran-2-carboxylate (300 mg, equiv. 1) was added to the reaction and left under magnetic stirring pure N<sub>2</sub> atmosphere overnight. EA was added (30 mL) and then the organic phase (DMF and EA) was extracted with citric acid 0.1 M aqueous solution (15 mL), saturated NaHCO<sub>3</sub> (15 mL) and brine (15 mL). The collected organic phase was dried with MgSO<sub>4</sub> and subsequently evaporated under reduced pressure using a rotary evaporator giving the crude compound #10. The crude was purified by column chromatography using silica as a stationary phase and DCM/EA as a mobile phase to give the final pure compound #10.

The next intermediate tail compound, #11, (IUPAC name: 1-methyl-5-((2-(thiomorpholine-4-carbonyl)benzofuran-5-yl)carbamoyl)-1H-pyrrol-3-yl)carbamate) was made following the steps described below. Compound #10 (369 mg, equiv. 1) was dissolved in MeOH/dioxane. Excess NaOH 1M (equiv. at least 5) was added to the mixture and left under magnetic stirring at room

temperature overnight. Disappearance of the starting material, shown by TLC, led to completion of hydrolysis. MeOH/dioxane was evaporated under reduced pressure using a rotary evaporator. Citric acid 1M was added until pH became acidic (~2) causing formation of precipitate (acid). The precipitate was extracted with EA, the organic phase was collected and the solvent was evaporated using rotary evaporator. The acid produced (equiv. 1.2) was dissolved in DMF (4-5 mL). EDCI (equiv. 2.5) and DMAP (equiv. 3) were added to the solution which was left under magnetic stirring (in N<sub>2</sub> atmosphere) for 20 minutes. At that point, thiomorpholine (equiv. 1) was added to the reaction and left under magnetic stirring overnight. EA was added (30 mL) and then the organic phase (DMF and EA) was extracted with citric acid 0.1 M aqueous solution (15 mL), saturated NaHCO<sub>3</sub> (15 mL) and brine (15 ml). The collected organic phase was dried with MgSO<sub>4</sub> and subsequently evaporated using a rotary evaporator giving the crude compound #11. The crude compound was purified by column chromatography using DCM:EA (90:10) as a mobile phase to give the final pure compound #11.

The synthesis of the final compound #12, also called PPA148, included the first amide coupling of compound #9 and #11 followed by the deprotection of the diazepine B-ring of the PBD scaffold with the formation of the imine bond. Pure compound #11 (100 mg) was de-protected by being dissolved in MeOH (6 mL) and HCl 4M in dioxane (6 mL) at a ratio of 50:50 and left under stirring for 2 h. The reaction was monitored with TLC. The reaction mixture was evaporated using a rotary evaporator and the intermediate de-protected #11 was formed. The protected PBD derivative (compound #9, equiv. 1.2) was dissolved in DMF and EDCI (equiv. 2.5) and DMAP (equiv. 3) were added to the solution. The mixture was left under magnetic stirring (in N<sub>2</sub> atmosphere) for 20 minutes. At that point, the de-protected compound #11 (equiv. 1) was added to the reaction and left under magnetic stirring overnight (in N<sub>2</sub> atmosphere). EA was added (30 mL) and then the organic phase (DMF and EA) was extracted with citric acid 0.1 M aqueous solution (15 mL), saturated NaHCO<sub>3</sub> (15 mL) and brine (15 ml). The collected organic phase was dried with MgSO<sub>4</sub> and subsequently evaporated using a rotary evaporator giving the intermediate crude compound #12. The crude was purified by column chromatography using DCM:Acetone (90:10 to 60:40) as a mobile phase.

The final compound was formed by de-protecting the pure intermediate compound #12. This intermediate (equiv. 1) was dissolved in DCM. Tetrakis Pb (equiv. 0.05), triphenylphosphine (equiv. 0.25) and pyrrolidine (equiv. 1.2) were added and the reaction kept under stirring for 20 min. The completion of the reaction was monitored with TLC. At that point the solvent was evaporated using a rotary evaporator and high vacuum giving the crude of the final compound #12. The crude was purified by column chromatography using DCM:Acetone (90:10 to 60:40) as mobile phase.

### 2.3.2 Thin Layer Chromatography (TLC)

TLC is a planar chromatographic technique extensively used in synthetic organic chemistry as a rapid and straightforward tool to determine each compound's purity and a means of following the progress of a reaction. It was performed for all intermediates and the final compound. As a mobile phase a mixture of organic solvents was used depending on the nature and affinity of each compound (DCM:EA at different ratios for the intermediate and DCM:Acetone for the final compound). Silica gel-coated aluminium sheets were used as a stationary phase. The mobile phase travels through the stationary phase and carries the components of the mixture with it. The movement of the analyte can be seen under the UV light and expressed by the retardation factor ( $R_f$ ).  $R_f$  depends on the distribution coefficient ( $K$ ) and is the relation between the distance travelled by the analyte from its origin ( $K_a$ ) to the distance travelled by the solvent from its origin ( $K_s$ ) using the following formula:

$$R_f = \frac{K_a}{K_s} \quad \text{Equation 2.3}$$

If the analyte spot is not UV visible, a number of solutions can be applied on the dried TLC plate and produce colored products. Potassium permanganate ( $\text{KMnO}_4$ ) was used for all compounds that can be oxidized such as phospholipids and cyclodextrins. UV radiation at 254 nm was used for all samples.

### 2.3.3 Liquid Chromatography-Mass Spectrometry (LC/MS)

LC-MS was conducted with the triple quadrupole Agilent Infinity Automated LC/MS Purification System to identify the purity and mass of the compounds at every step of the synthetic route. The physical separation was performed on a Onyx<sup>TM</sup> monolithic C18 column with dimensions of 50mmx4.60mm and pore size of 130 Å. The mobile phase was a mixture of HPLC grade water with 0.1% formic acid (Solvent A) and HPLC grade ACN with 0.1% formic acid (Solvent B). The gradient was ramped from 95% A at  $t = 0$  min to 50% A at 2 min, then to 10% at 2.5 min, and kept it until 4.5 min and finally ramped to 95% at 4.6 min and keep there for 5 min. The injection volume was 10  $\mu\text{L}$ , the flow rate was 1 mL/min and minimum/maximum flow ramp up/down was 100 mL/min<sup>2</sup>. The LC detector was an Agilent 1260 Infinity II Diode Array Detector (DAD) G7115A and the detection wavelength range was 220-400 nm. The UV absorbance was recorded at 260 nm with a slit width of 4 nm at 0.8 °C. The LC was coupled with the mass spectrometer via an electrospray ionization (ESI) interface operating in both positive (ESI+) and negative (ESI-) modes. The nebulization pressure was 50 psig, the gas used  $\text{N}_2$  and the quadrupole temperature set at 0 °C. The voltage capillary was 4000 V and 3500 V for ESI+ and ESI- respectively and the drying gas temperature and flow were 350 °C and 13 L/h. The sample cone (skimmer) voltage and ion energy was set at 8 and 5 V respectively for both ionization modes. Lens1, Lens2, IRIS lens and HED were set at 2.4, 23, -400 and 10000 V for the ESI+ and -4, 23, 400 and 10000 V for the ESI-.



For all the compounds, the relative purity was assessed based on the LC chromatogram because there were no analytical standards to assess their absolute purity. Therefore, it was calculated based on the relative area of each intermediate and final compound as a percentage of all other peak areas in the chromatogram. For the purpose of this research, the term relative purity will be referred to as purity or RP.

#### 2.3.4 Nuclear Magnetic Resonance (NMR) spectroscopy

Liquid state NMR spectroscopy was carried out on an Ascend™ 400 MHz spectrometer equipped with a SampleXpress autosampler system (Bruker, UK) for all intermediates and the final compound of the synthetic procedure to identify their molecular content and purity. 1-dimensional (<sup>1</sup>D) proton (<sup>1</sup>H) and carbon (<sup>13</sup>C) NMR were performed to assign the resonances. The spectra were recorded using TOPSpin software for data acquisition and MestReNova software for data analysis. <sup>1</sup>H NMR parameters included sweep width of 8012.82 Hz, acquisition time of 4.09 sec and 16 scans and were collected with a zg30 pulse program. <sup>13</sup>C NMR used a sweep width of 24038.46 Hz, acquisition time of 1.36 sec and 1024 scans. The solvent used was either deuterated chloroform (CDCl<sub>3</sub>) or deuterated DMSO, depending on the solubility of the compound.

#### 2.3.5 Fourier Transform Infra-Red (FTIR) Spectroscopy

FTIR was carried out to confirm the presence of the basic functional groups of newly synthesized compounds. It is an additional technique to NMR to confirm the structure of each intermediate and the final compound. A Perkin Elmer, UK, Frontier FTIR (serial number 95462) with a LiTaO<sub>3</sub> detector, IR-laser wavenumber of 15798 cm<sup>-1</sup> and a zinc selenide (ZnSe) crystal was used to analyze the samples in their solid state. For a better contact of the sample with the crystal, the DATR 1 bounce diamond accessory with a pressure arm force indicator (part number L1250240, Perkin-Elmer Ltd, UK) was attached to the main piece of equipment. All spectra were produced using 16 scans and collected at a scan speed of 0.2 cm<sup>-1</sup>/min and spectral resolution of 2 cm<sup>-1</sup>. The data were analyzed using Spectrum One software (version 10.03.06, Perkin-Elmer Ltd, UK). Each spectrum was scale-base normalized by dividing the absorbance of each point with that of the C-H stretch at around 2950 cm<sup>-1</sup> (internal standard) to minimize the errors caused by the amount of sample used.

#### 2.3.6 Adsorption assay

The adsorption of the drugs chlorhexidine digluconate, rifampicin, gentamicin and PPA148 at the air/water interface was recorded by measuring changes in surface pressure after subphase injection. A Langmuir trough (NIMA Technologies Ltd., Coventry, UK) equipped with a calibrated NIMA PS4 pressure sensor and a Wilhelmy plate (Whatman, grade 1, chromatographic paper), connected to a controlling computer with the NIMA IU4 interface unit. For all the experiments a 50 mm diameter perfluoroalkoxy (PFA) petri dish (Saint-Gobain Performance Plastics) with a 20

mL volume capacity, was placed over a magnetic stirring plate and referred to as the “small trough”. A dust and contaminant free subphase (approximately 20 mL filtered ultrapure water containing 0.9% w/v NaCl) was poured into the petri dish and a clean Wilhelmy plate was suspended from the NIMA PS4 pressure sensor and partially submerged into the subphase. The subphase surface was cleaned by sweeping and suction using a pressure pump (Aspirator A-3S, EYELA, Tokyo Rikakikai Co, Ltd) in order to remove any remaining dust and contaminants from the surface ( $\Pi = 0 \pm 2$  mN/m).

Drug solution was injected (0.1  $\mu$ L) below the surface directly into the subphase using a 1 mL disposable plastic syringe (fitted with a 25 G x 25 mm needle) of 1 mL volume (BD biosciences UK, Oxford, UK) whilst continuously stirring. Chlorhexidine digluconate (CHD) and gentamicin sulfate were dissolved in water whilst rifampicin and PPA148 were dissolved in DMSO. In each case, the final drug concentration in the trough was 2  $\mu$ g/mL. The adsorption of the drug on the surface causes changes in surface pressure which are recorded over time whilst maintaining a constant surface area (21.3 A<sup>2</sup>/m) at 23 °C. Each sample was run in triplicate (n=3) and the changes in surface pressure were plotted against time ( $\Pi$  and A-Time isotherm). Nonlinear regression was applied to estimate the kinetics of the Pressure-Time isotherm curves. The isotherm was fitted with a sigmoidal model (Hill plot with 3 parameters) using GraphPad Prism 7.03 software (USA). The Hill plot model explained approximately 99% of the pressure variability in time for all individual data and is described by the following formula:

$$f(x) = \frac{(a \cdot x^b)}{(c^b + x^b)} \quad \text{Equation 2.4}$$

, where  $a$  is the maximum difference in surface pressure reached at the plateau ( $\Delta\Pi_{max}$ ),  $b$  is the hill coefficient of sigmoidicity (hill slope at its midpoint) and  $c$  is the time for which 50% of maximum pressure is obtained ( $t_{50\%}$ ).

### 2.3.7 Ultra Violet Spectroscopy

The UV spectrum of PPA148 was recorded on a Lamda 2 spectrophotometer (Perkin Elmer, UK), at 25 °C using a quartz cuvette (Hellma 114-QS) with a pathlength of 1 cm and volume capacity of 1400  $\mu$ L. The absorbance was recorded within a wavelength range of 200-550 nm with spectral slit width of 2 nm and scan speed of 60 nm/min. The drug concentration was 20  $\mu$ g/mL and it was measured in DI water, ethanol and ethanol/water (80:20).

The linearity of this method was determined by analysing the solutions of PA148 in the range of 2-200  $\mu$ g/mL. For quantification purposes, the Limit of Detection ( $LOD$ ) and Quantification ( $LOQ$ ) were established by regression analysis of the linear part (calibration curve). Both values were calculated using the standard error mean ( $se$ ) and slope ( $S$ ) taken from the regression line. The linear regression assumes that the errors between observed and predicted values, i.e. the residuals of the regression, should not fall outside the straight line (normal distribution) and its

variance should be equally distributed (homoskedasticity) (Appendix B, Figure B 4). Otherwise, the residuals are not constant and normally distributed, leading to false estimations. All the formulas are as follows:

$$LOD = \frac{3.3 \times se}{s} \quad \text{Equation 2.5}$$

$$LOQ = \frac{10 \times se}{s} \quad \text{Equation 2.6}$$

### 2.3.8 Turbidimetric Assay

Turbidimetric assay is a preliminary screening test to rapidly evaluate the enhancement of water solubility of compounds at their early stage of development. Initially, a stock solution of PPA148 (5 mM) in DCM was used to produce a range of concentrations (0, 5, 10, 15, 20, 25, 30, 40, 50, 60, 70, 100, 130 and 160 µg/ml) in water or aqueous buffer. DCM was evaporated before the addition of the water to a final volume of 4 mL. The samples were left under mild stirring (290 rpm) for 7 days and changes in the light scattering of the samples were tracked using two techniques. Photon correlation spectroscopy (PCS), also known as dynamic light scattering (DLS), was the first technique used at 25 °C. A Malvern Zetasizer, Nano-ZS (Malvern Instruments, UK) was used with a laser of wavelength 623.8 nm and backscatter detection angle of 173°. The value of the viscosity of water (as the dispersant) and refractive index were used, respectively 0.889 cP and 1.33211. The samples were placed in disposable semi-micro dynamic light scattering cuvettes with volume capacity of 1.5 mL (VWR International, UK). The linear derived count rate (DCR) was recorded and plotted against drug concentration.

UV/Vis spectroscopy was also used as an additional technique to measure the scattered light at a wavelength of 620 nm at 25 °C. Solutions were placed a quartz cuvettes (Hellma 114-QS) with a pathlength of 1 cm and measured on a spectrophotometer (Perkin Elmer, UK) with slit width set at 2 nm. The absorbance value at 620 nm was recorded and plotted as a function of drug concentration.

In the absence of aggregates, scattering from the samples is nearly zero; the onset of aggregation is denoted by a break in the slope, with scattering (or turbidity) increasing linearly with concentration. The intersection of the two linear profiles is used as an estimation of the aggregation concentration.

### 2.3.9 Water Solubility Test

An excess amount of PPA148 (1 mg) was added to deionized water and 20 mM HEPES, 2 mM CaCl<sub>2</sub>, 145 mM NaCl (pH =7.2) buffer (1 mL). The samples were left under mild stirring (290 rpm) for 7 days. After incubation, samples were centrifuged (5 min at 10,000 rpm) and the supernatant was freeze-dried overnight and resuspended in ethanol: water (4:1). The saturated concentration

was assayed by UV/Vis spectroscopy using a calibration curve as described in the corresponding methods section (2.3.7).

### 2.3.10 Quantification of drug:cyclodextrin binding constant by fluorescence spectroscopy

The increase in aqueous solubility of the antimicrobial agents (PPA148 and rifampicin) obtained by their incorporation into cyclodextrins was measured by fluorescence spectroscopy. Two types of modified  $\beta$ -cyclodextrins were used: HP $\beta$ CD and RAMEB and the binding constant was measured as reported by Valero et al. (151). Specific volumes of either PPA148 in DCM, or rifampicin in ethanol were transferred into separate vials and the solvent evaporated. CD solutions (0, 1, 2, 3, 4, 5, 6, 10, 15, 20, 25 and 30%) in HEPES (20 mM) buffered saline, pH 7.2, or 50 mM Tris buffer pH 9 were then added to achieve a final drug concentration of 10  $\mu$ g/mL. The samples were left under mild stirring overnight. The fluorescence intensity of the drug was measured as a function of concentration. The fluorescence intensity of the drug increases upon complexation with CDs until the drug is fully complexed with the CD and a plateau is reached.

The fluorescence intensity from PPA148 was measured with a Luminescence spectrometer LS 50 B (Perkin Elmer, UK), and was conducted with an excitation wavelength of 300 nm, and an emission wavelength scan range of 340-530 nm, with emission/excitation slit widths of 5 nm. Shifts in the fluorescence drug peak at 422 nm for PPA148 and the ratio of 338/419 nm for rifampicin are due to inclusion complex formation. Assuming that the drug forms a 1:1 complex with CD, the binding constant ( $K$ ) was determined by fitting the data with the following equation (152):

$$I = \frac{I_0 + I_t K[CD]}{1 + K[CD]} \quad \text{Equation 2.7}$$

, where  $I_0$ ,  $I$  and  $I_t$  are the fluorescence intensity from the drug in the absence of cyclodextrin, at intermediate and infinite cyclodextrin (excess) concentration,  $K$  is the binding constant and  $[CD]$  is the molar concentration of free cyclodextrin. A non-linear least squares method was used to fit the experimental results to Equation 2.7. The differences between the calculated solubility and the experimentally derived data were minimized by varying the values of the binding constant (the iterative approach of Nelder–Mead) using the Microsoft Excel Solver function (153).

### 2.3.11 Phase solubility diagram

Complex formation between cyclodextrin (solubilizer) and drug was also investigated by studying phase solubility (147). Twelve vials containing an excess of drug, i.e. 1 mg (1.4 mM) for PPA148 and 10 mg (12 mM) for rifampicin, were prepared. The aqueous solution used for PPA148 was HEPES buffered saline including  $\text{CaCl}_2$  at pH 7.2; for rifampicin, Tris buffer at pH 9 was used. Each vial contained varying amounts of cyclodextrin (0, 0.2, 0.4, 0.6, 0.8, 1, 1.5, 2, 4, 6, 10 and

15% w/v). The mixtures were left under stirring for 7 days at room temperature (23 °C). For rifampicin, a photosensitive drug, the vials were covered with aluminum foil to avoid drug degradation. The undissolved drug was separated from the mixture by centrifugation (Heraeus™ Pico™ 21 Microcentrifuge, UK) at 5000 rpm for 5 min. The supernatant was freeze-dried (ALPHA 1-2 LD plus freeze drier with chemistry hybrid pump RC6). PPA148 was resuspended in EtOH:H<sub>2</sub>O (80:20), rifampicin in Tris buffer pH=9 and assayed by fluorescence spectroscopy (Luminescence spectrometer, LS 50 B, Perkin Elmer, UK). Each sample was scanned over the range 340-550nm, the excitation wavelength was set at 300 nm, and the scan speed at 120 nm/min. The measurements were performed at 25 °C and the final spectrum was an average of 10 scans. Excitation and emission slit widths were set to 5 mm. A calibration curve for each drug was prepared in the same solvent and measured under the same instrument settings for each drug on the same day. The molar drug concentration, which was determined from the calibration curve, was plotted against the CD molar concentration.

The phase solubility diagram is classified into “A” and “B” type depending on the type of complex formed. Type “A” curves indicate the formation of soluble complex, while “B” types represent the formation of insoluble complexes (147,154). Type “A” curve is obtained when the solubility of a drug increases with increasing ligand concentration. Negative or positive deviation of linearity produce the “AL” and “AP” or “AN” curve, “BS” describes complex of limited solubility and “BI” illustrates the formation of insoluble complex (Figure 2.4) (154).

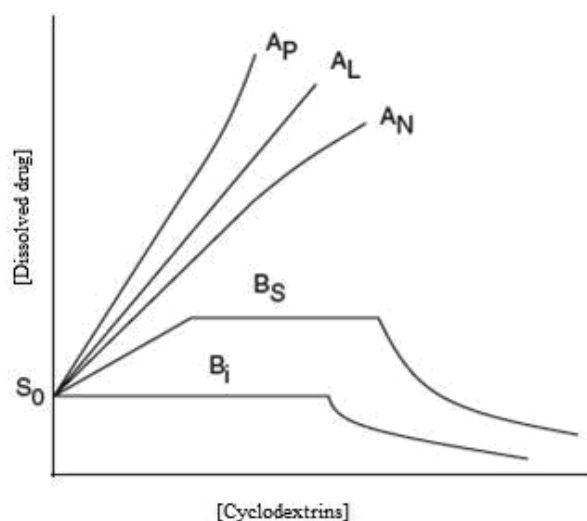


Figure 2.4: Types of phase solubility diagrams (“A” and “B”) and their deviations (“AP”, “AN”, “BS” and “BI”) (154).

In the “A” type curve, the binding constant ( $K_f$ ), assuming a 1:1 complex and the overall complex stoichiometry is estimated by using the linear region of the diagram, which is fitted with a linear model. The slope of the linear regression, the y-intercept representing the drug solubility in the absence of cyclodextrin ( $S_{int}$ , the intrinsic solubility) and the solubility in the presence of cyclodextrin ( $S_0$ ) is used in the following equations:

$$K_f = \frac{\text{slope}}{S_{int}(1-\text{slope})} \quad \text{Equation 2.8}$$

$$\text{guest: CD} = 1: \frac{1+S_0}{(1-S_0)} \quad \text{Equation 2.9}$$

Due to poor water solubility of hydrophobic drugs, the y-intercept is not always equal to the intrinsic solubility because of the presence of dimers, trimers or other water-soluble oligomers, which render the formation of the complexes (147). Therefore, complexation efficiency (CE) is a more accurate method to determine the solubilizing effect of cyclodextrins. CE is the concentration ratio between cyclodextrin in the complex and its free form in the system (155). CE is calculated based on the slope of the linear part of the phase solubility diagram.

$$CE = S_0 \times K_f = \frac{\text{slope}}{1-\text{slope}} \quad \text{Equation 2.10}$$

The Gibbs free energy of transfer  $\Delta G_{tr}^o$  is the energy needed for the drug to be transferred from the aqueous environment to the cyclodextrin cavity and is calculated using the function:

$$\Delta G_{tr}^o = -RT \log\left(\frac{S_{int}}{S_0}\right) \quad \text{Equation 2.11}$$

, where  $R$  is the gas constant ( $8.314 \text{ JK}^{-1}\text{mol}^{-1}$ ),  $T$  is temperature in Kelvin,  $S_{int}$  and  $S_0$  are the molar solubility of the drug in the absence (y-intercept of the linear part of the phase solubility diagram or intrinsic solubility) and presence of CD, respectively.

### 2.3.12 Continuous method variation (Job's plot) (156)

The molecular association of the drug and CD was also studied by NMR spectroscopy. Equimolar solutions (1mM) of drug and CD in D2O were prepared and mixed in varying volume fractions while keeping the total concentration constant (1 mM). DIMEB was used instead of RAMEB as it provides a high resolution spectrum from which all protons can be assigned, unlike RAMEB and HP $\beta$ CD, which are randomly substituted and therefore lead to spectra with broad peaks (157). Rifampicin and DIMEB solutions were mixed in volume fractions ranging from 0 to 1 mL with an increment of 0.1. The inclusion of rifampicin into the DIMEB cavity is evidenced by changes in the chemical shift observed with selected protons of the cyclodextrin. The spectral peaks of cyclodextrin hydrogens were assigned according to the literature (158). The settings were the same as those described in the NMR method section (2.3.4). The resonances of the DIMEB interior hydrogens (in positions 3 and 5) and exterior (position 1) were selected as changes in those hydrogens indicate inclusion of drug into the cyclodextrin cavity (159). The chemical shifts of H1 was presented as a doublet at 5.19 and 5.18 ppm, that of H3 was observed as a triplet at 3.90, 3.92 and 3.94 ppm and of H5 as a doublet at 3.84 and 3.86 ppm. The stoichiometry of the complex was obtained by normalizing the variations of the chemical shifts of the host by its mole fraction ( $X_{CD}$ ) and plotting them against cyclodextrin mole fraction ( $X_{CD}$ ) (160). The shift of CD's

hydrogen resonance depends on the mole fraction of pure drug, pure CD and drug/CD complexes. A 1:1 complex presents a maximum signal at 0.5 CD mole fraction.

## 2.4 Results

### 2.4.1 Synthesis

PPA148 is a novel modified biaryl PBD hybrid analogue and its synthesis is based on a convergent strategy. The PBD tricyclic scaffold and the lateral polyamidic tail were synthesized separately and the two pure compounds (#9 and #11) were coupled to give the final PPA148 (#12). The synthesis of PPA148 was performed according to Scheme 2.1, starting from the intermediate core compound #6 which was previously synthesized by another group member. The complete synthetic route can be found in Appendix B, which is the one described in the patent (107). Each reaction was monitored with TLC and upon completion the compounds were characterized with LCMS, both  $^1\text{H}$  and  $^{13}\text{C}$  NMR, TLC and FTIR to verify their structure and the mass.

The PBD core followed a retrosynthetic pathway. The pro-imine bond was formed on N10C11 via intramolecular oxidative cyclization of the protected amino-alcohol compound #6. Compound #7 was obtained with a 74.6% yield and 76.2% relative purity (RP). In order to control the final bonding site of the core and tail coupling, the -OH group of compound #7 was protected (93% yield and 71.2% RP) prior to the saponification reaction (83% yield, 85.9% RP) of the terminal methyl ester group. Proton NMR revealed all the differences in magnetic environment during the series of reactions (Figure 2.5, Figure 2.6).

Compound #6 was the starting material for this project. Its  $^1\text{H}$ NMR generated a signal at 8.73 ppm which was assigned to the amide hydrogen (Figure 2.5). This signal disappeared in compound #7 which indicated that the pro-imine bond had formed. All proton NMR spectra contained several overlapping signals due to the similar magnetic environment of the hydrocarbon chains. The tetrahydropyran protective group added more hydrocarbon chains to compound #8 which increased dramatically the signal of the protons at 1.63 ppm. The two sharp peaks in compounds #6, 7 and 8 were assigned to the two methyl groups (Figure 2.5). Although compound #6 generated the signals at 3.68 and 3.89 ppm, there was a slight shift in signal towards higher frequencies in #7 and 8. Compound #9 generated only one signal for the methyl hydrogens which validates the hydrolysis of the methyl ester to create the equivalent acid (83% yield and 85.9% RP) (Figure 2.5). In all spectra traces of solvent signals might be present or hidden.  $^{13}\text{C}$  NMR was performed for all molecules and it showed all the different carbon environments (Appendix B, Figure B 2).

The tail consisted of three constitutive units at the C8 position which were sequentially connected via an amide bond (Scheme 2.1). The Boc-protected pyrrole-2-carboxylic acid (first unit) was bonded with the benzofuran carboxylate (second unit) to give the intermediate compound #10

which was derivatized with the cyclic secondary amine, i.e. thiomorpholine (third unit), after being hydrolysed.

The series of amide couplings for the tail formation were successful (Figure 2.6). Compound #10 was formed with a 65.4% yield and 99.4% purity. The final tail was obtained with 56.3% yield and 89.4% purity. The signals at 4.39-4.34 ppm (quadruplet) and 1.36-1.32 (triplet) assigned to the ethyl group in compound #10 disappeared while the thiomorpholine hydrocarbon chains appeared at both higher and lower frequencies depending on the neighboring atom (3.93, 3.88 and 2.72 ppm (Figure 2.6). This was an indication that there was no starting material left because if both compounds were present all peaks would be observed in the final spectrum. The four methyl groups generated from the Boc-protection and the tertiary amine were assigned in the final spectrum, too, at 1.46 and 3.82 ppm respectively. This was another indication that the coupling of compound #10 and thiomorpholine succeeded.

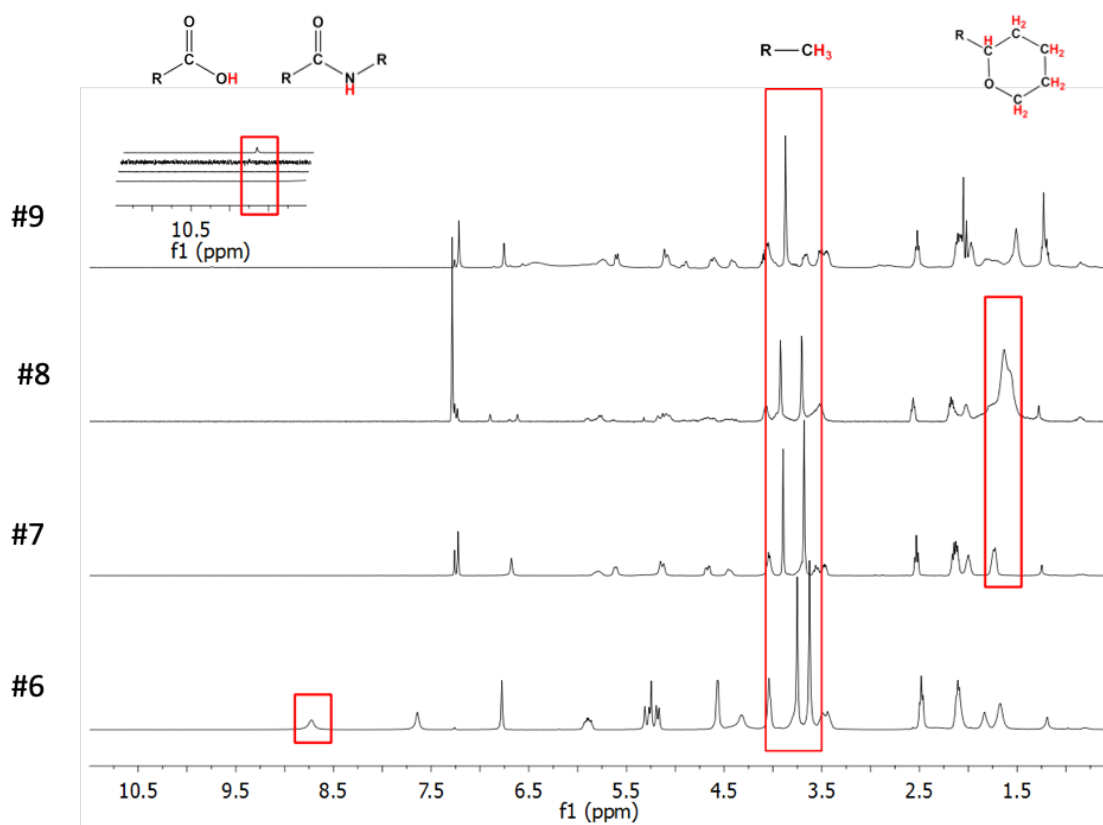


Figure 2.5: <sup>1</sup>H NMR of sequential reaction monitoring for the synthesis of the final PBD core compound (#9).



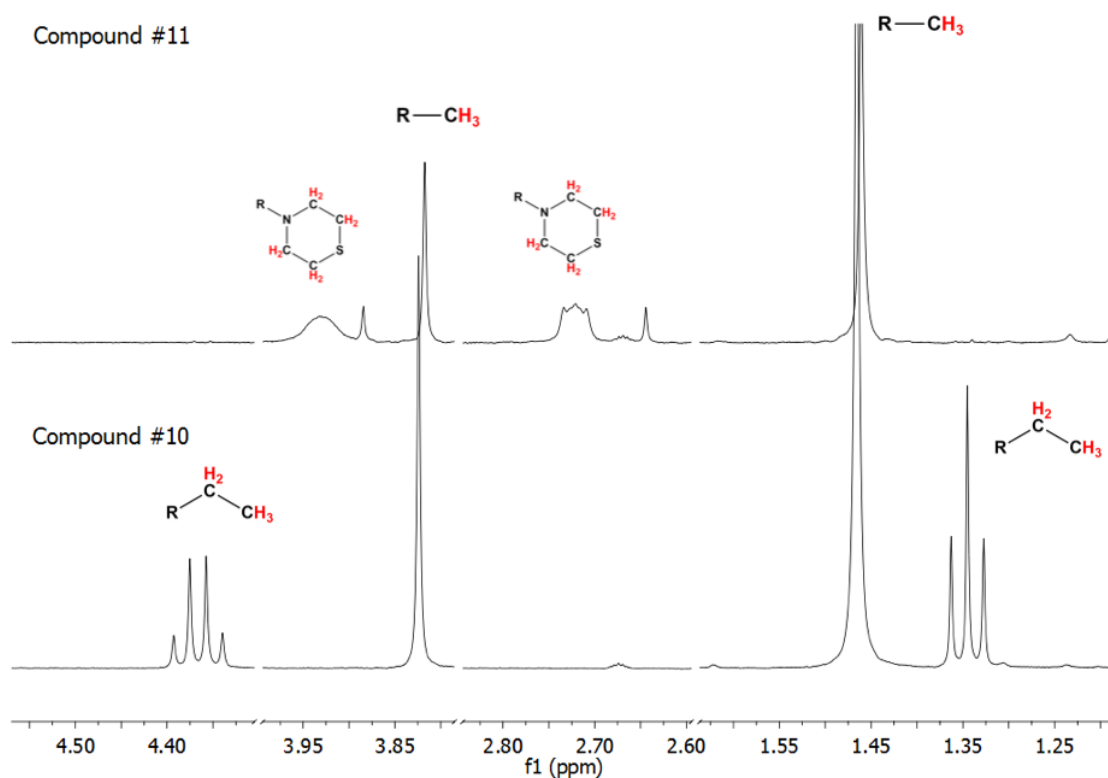
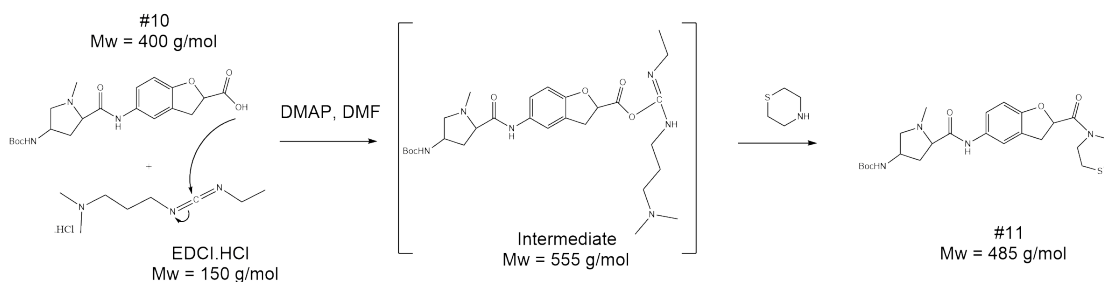


Figure 2.6:  $^1\text{H}$ NMR of sequential reaction monitoring for the synthesis of the final tail compound (#11).

The conversion of compound #10 to the intermediate acid is a crucial step. Citric acid was used for precipitation of the acid which was formed during hydrolysis with methanol and dioxane. However, if traces of citric acid remain in the precipitant, it prevents the final amide coupling. The intermediate product with molecular weight of 555 g/mol was formed but it did not interact with thiomorpholine to give the expected tail product (Scheme 2.2). An attempt to overcome this issue was to increase the concentration of reagents. Unfortunately, that was not the case, even after doubling the amount of EDCI and DMAP.



Scheme 2.2: A detailed scheme presenting the second amide coupling of the tail synthesis. When citric acid is present, the reactions did not go to completion and instead only the intermediate product was formed.

The final amide coupling of the PBD core (#9) and tail (#11), de-protection and purification were successful with 82% yield and 78.1% RP. The proton NMR of PPA148 contained overlapping signals for the secondary amides, giving a “W” shaped peak instead of two singlets (Figure 2.7).

For the hydrogens being involved in double bonds, 9 different signals were generated for each different environment (Figure 2.7).

In Figure 2.8, there is evidence of the rest of the structure. The hydrogens in the alkyl hydrocarbon chain were generated at 3.92, 2.72 and 2.04 ppm which agrees with the equivalent hydrogens in compound #9. The signal of the methyl moieties overlapped as it may be seen in Figure 2.8. Thiomorpholine group was present at 2.66 and 3.33 ppm because there are 2 different magnetic environments. The signal of pyrrole of the PBD tricyclic moiety was generated at 2.33 ppm as a multiplet. There are several similar magnetic environments but the signals were not strong.  $^{13}\text{C}$  NMR was performed for all molecules and it showed all the different carbon environments (Appendix B, Figure B 3 and Figure B 4).

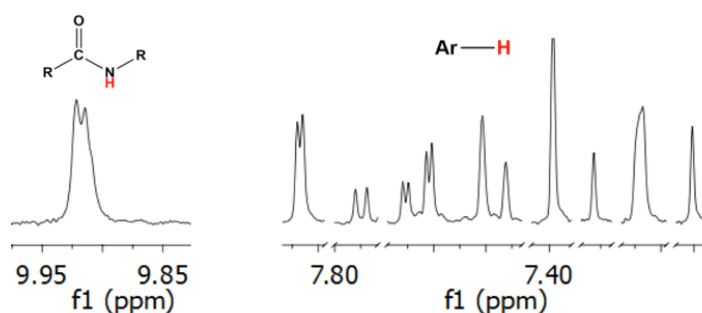


Figure 2.7:  $^1\text{H}$ -NMR signals for the secondary amide and double bond hydrogens of the final de-protected compound (#12), PPA148.

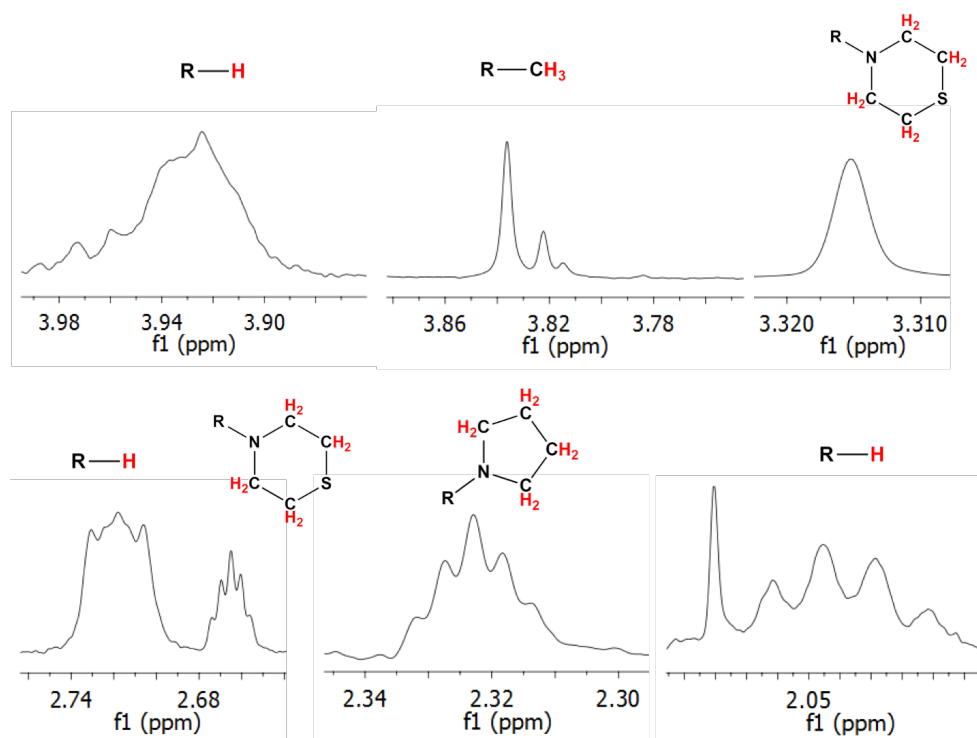


Figure 2.8:  $^1\text{H}$ -NMR signals for the hydrocarbon chain, methyl moieties, thiomorpholine and the pyrrole group of the PBD tricyclic core of the final compound, PPA148.

Additional information on the structure and functional groups of each compound were collected by FTIR. The product of each reaction was analyzed as a tool for monitoring each step of the synthetic route. Figure 2.9, Figure 2.10 and Figure 2.11 outline the changes in functional groups of the PBD core (#9), tail (de-protected #11) and the final compound (#12, PPA148) as they progress through every synthetic step. This technique reveals the hydroxyl groups which are difficult to observe in the NMR spectra.

FTIR confirmed the functional groups within the structures of each compound (Figure 2.9, Figure 2.10, Figure 2.11). Particularly, in compound #6 the band at  $3328\text{ cm}^{-1}$  is associated with the -OH and NH stretching vibration bands, which overlap in the spectrum (Figure 2.9). The bands between  $2900\text{--}1860\text{ cm}^{-1}$  result from the asymmetric and symmetric stretching vibration bands of -CH, -CH<sub>2</sub>, -CH<sub>3</sub> and the band at  $1726\text{ cm}^{-1}$  is generated by the carbonyl group of the ester. Amide I absorption originates from the C=O stretching of the amide group (coupled to in-phase bending of the N-H bond and stretching of the C-N bond), which gives rise to bands in the region between  $1660\text{--}1560\text{ cm}^{-1}$ . Amide II comes from the N-H bending and C-N stretching vibrations which generate a band at  $1520\text{ cm}^{-1}$ . Amides III is a very complex band resulting from mixtures of several coordinate displacements (-H-N-C bend, -CC stretch and -NH bend). The band at  $1263\text{ cm}^{-1}$  possibly arises from the amide III. The aromatic -C-C- stretches and the C-H deformation bands of the phenyl ring are generated at  $1452\text{--}1406\text{ cm}^{-1}$ ,  $872\text{--}768\text{ cm}^{-1}$  respectively.

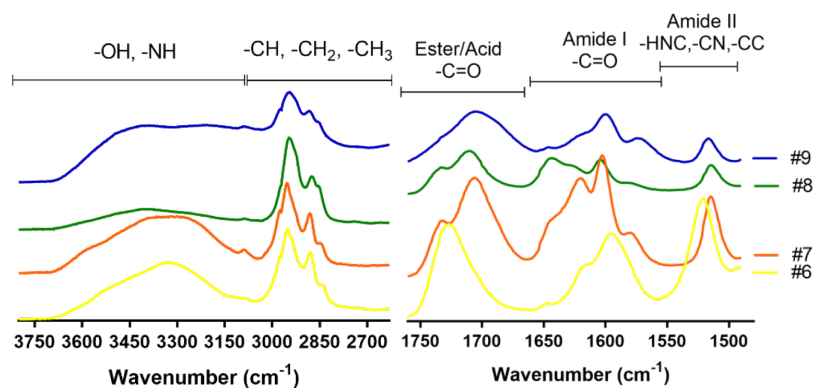


Figure 2.9: FTIR monitoring of the core synthesis.

Upon oxidative cyclization, the amide converted into amino-alcohol. Unfortunately, this change was not depicted in the FTIR spectrum because the two peaks were overlapping in #6. However, the ester, amide I and II bands changed position, which indicated change in the hydrogen bonding of the molecule (Figure 2.9). This reaction was followed by the protection of the -OH group of #7 by tetrahydropyran which led to marked changes in the  $\nu(\text{OH})$ , amide III  $\nu(\text{C-N})$  and saturated ether  $\nu(\text{C-O-C})$  region of the spectra. The last step is the hydrolysis of the ester. The PBD carboxylate (#8) was transformed to the equivalent acid, as indicated by the presence of the -OH band of the acid.

Figure 2.9 shows the spectra of the two-step tail synthesis. The sharp peaks indicate the formation of crystalline compounds. In compound 11, the absorption band at  $1710\text{ cm}^{-1}$  is associated with the stretching vibrations of the ester carbonyl group, which disappeared in the spectrum of compound 12 due to the amide coupling with thiomorpholine at that site. The bands between  $1500\text{--}1700\text{ cm}^{-1}$  relates to the  $\text{-C=O}$  and  $\text{-H-C-N}$  stretching (amide I), N-H bending, C-N and C-C stretching (amide II). The bands between  $3500\text{--}3200\text{ cm}^{-1}$  result from the NH stretching vibrations; and that between  $3000\text{--}2800\text{ cm}^{-1}$  arise from the CH,  $\text{CH}_2$  and  $\text{CH}_3$  stretching.

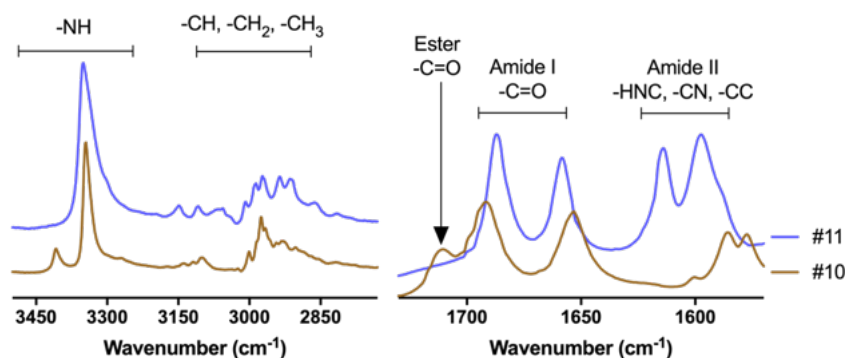


Figure 2.10: FTIR monitoring the tail synthesis.

The final amide coupling resulted in an amorphous material because the peaks are broad and not well defined. However, the functional groups were established within the spectrum (Figure 2.11). The final compound is the deprotected #12 which means less  $\text{-CH}$ ,  $\text{-CH}_2$  and  $\text{CH}_3$  bonds. This is presented in Figure 2.11 with a change in the band shape at the corresponding region.

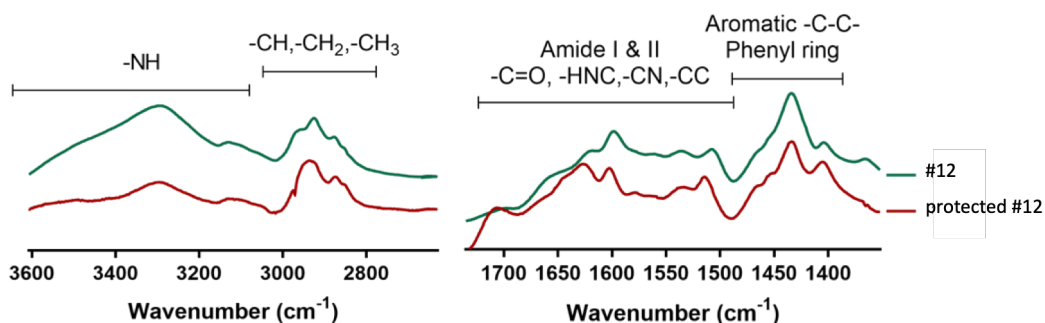


Figure 2.11: FTIR monitoring of the final protected and de-protected PPA148.

Table 2.2 presents the mass to charge ratio ( $m/z$ ) of each compound, estimated by ChemDraw<sup>®</sup> and calculated by LC/MS. The experimental  $m/z$  was calculated from samples that were assessed by positive mode ESI. It can be seen that the mass of the parent ion  $[\text{M}+\text{H}]^+$  was as predicted for all the products. TLC was used to monitor the reactions and become a fast and straightforward means of identification. The retardation factor ( $R_f$ ) was calculated from the distance travelled by the solvent and the individual spots created by the compounds (Table 2.2).

All compounds travelled up the plate at different rates depending on their affinity with the solvent. Compound #9 stayed on the baseline because the mobile phase, used (100% ethyl acetate) was not polar enough to carry the compound with it. That was a way of observing whether the hydrolysis had been completed since compound #8 was able to travel. It was observed that PPA148 decomposed in methanol and at temperatures above 65 °C (data not shown), by changing color from light yellow to orange which was confirmed by LC/MS.

Table 2.2: Chemical characteristics of each intermediate and the final compound.

Compound #	Estimated M/Z	Measured M/Z by LCMS	Rf (cm)
6 (C <sub>22</sub> H <sub>30</sub> N <sub>2</sub> O <sub>8</sub> )	450.4	451.2	0.34
7 (C <sub>22</sub> H <sub>28</sub> N <sub>2</sub> O <sub>8</sub> )	448.4	449.2	0.38
8 (C <sub>27</sub> H <sub>36</sub> N <sub>2</sub> O <sub>9</sub> )	532.2	532.6	0.45
9 (C <sub>26</sub> H <sub>34</sub> N <sub>2</sub> O <sub>9</sub> )	518.5	519.2	N/A
10 (C <sub>22</sub> H <sub>27</sub> N <sub>3</sub> O <sub>6</sub> )	429.2	429.1	0.44
11 (C <sub>24</sub> H <sub>30</sub> N <sub>4</sub> O <sub>5</sub> S)	486.2	485.2	0.75
12 (C <sub>36</sub> H <sub>38</sub> N <sub>6</sub> O <sub>7</sub> S)	698.2	699.3	0.23

## 2.4.2 Physicochemical characteristics

### 2.4.2.1 Adsorption at the air/water interface

PPA148's water solubility ( $\log S = -7.461$ ) and  $\log P$  (0.76) estimated by ChemDraw suggest a very hydrophobic drug with low water solubility (Table 1.5). The adsorption of PPA148, rifampicin, gentamicin sulfate and chlorhexidine digluconate (CHD) at the clean air/water interface were measured in order to present the hydrophilic and/or hydrophobic character of each antimicrobial agent and to use it as a control in the interaction studies (Section 4.3.3; Section 4.3.4; Figure 4.6; Figure 4.7; Table 4.2) with model lipid membranes presented in Chapter 4. The concentration of the drug in the small trough was 2  $\mu\text{g/mL}$ . Changes in surface pressure due to the adsorption of the molecules at the air/water interface were recorded. Figure 2.11 shows the changes in surface pressure over time after injection of PPA148.

PPA148 reached a maximum surface pressure of  $12.34 \pm 0.77$  mN/m with a Hill slope of  $1.03 \pm 0.22$  (Figure 2.12). The time needed to reach half of the adsorption equilibrium surface pressure

was  $0.33 \pm 0.15$  h, which reflects a rather slow kinetic profile. This was probably a result of the co-solvent (0.5% of DMSO) in the small trough since PPA148 is barely soluble in water and thus DMSO was used to prepare the stock solution and avoid drug precipitation in water. The data for gentamicin sulphate, rifampicin and chlorhexidine digluconate are not shown here because no increase in surface pressure was observed. All three drugs are soluble in water at the concentration used and they did not adsorb at the air/liquid interface.

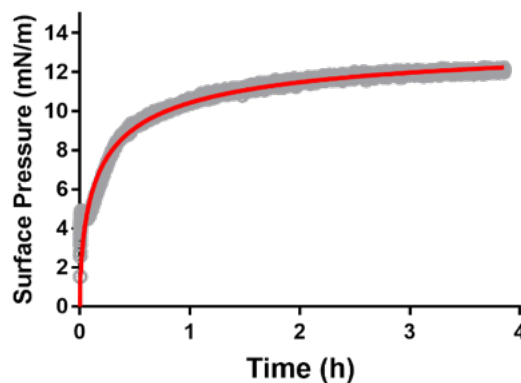


Figure 2.12: A representative adsorption profile of PPA148 at the air/liquid interface at 23 °C. The drug was injected below a 0.9% NaCl subphase and changes in surface pressure were recorded until a plateau was reached. The representative curve was fitted (red line) based on a 3-parameter Hill equation (Equation 2.4),  $R^2=0.99$  ( $P \leq 0.0001$ ). The mean and std of maximum surface pressure ( $12.34 \pm 0.77$  mN/m), Hill slope ( $1.03 \pm 0.22$ ) and  $t_{50\%}$  ( $0.33 \pm 0.15$  h) was calculated from a set of 3 runs.

#### 2.4.2.2 Solubility and UV profile of PPA148

The UV absorbance spectrum of PPA148 was measured in ethanol/water mixtures (0, 80 and 100% ethanol) over a range of drug concentrations. The experimental data were fitted by linear regression and met the assumptions regarding the normal distribution and homoscedasticity of data as described in section 2.3.7 (Appendix B, Figure B 4). The absorbance intensity of the drug in water was lower than in ethanol, which, in turn, was slightly lower than in ethanol/water (80:20) (Figure 2.13). The shape of the peak was broader in water and better separated in the other two solvents (Figure 2.13). Figure 2.14A presents the effect of increasing concentration on the linearity of the UV/Vis method and thus in the Beer-Lambert's law. For concentrations between 1-15  $\mu\text{g/mL}$ , the drug absorbance in water is proportional to concentration. However, it deviates at higher concentrations, which is an indication of the presence of molecular aggregates. Visual observation of the samples showed cloudiness and turbidity for 40-70  $\mu\text{g/mL}$  and drug precipitation was pronounced for 100-200  $\mu\text{g/mL}$  (Figure 2.15). In ethanol and ethanol/water, the linearity was extended up to 30  $\mu\text{g/mL}$ , at which point the absorbance reached the highest value regarding the sensitivity of the instrument Figure 2.14A.

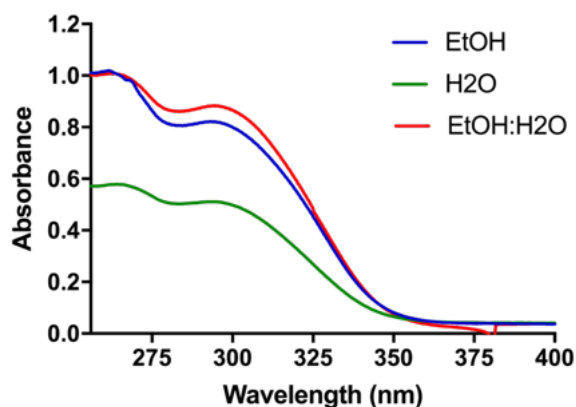


Figure 2.13: Representative UV/Vis spectra of PPA148 in three solvents: EtOH, H<sub>2</sub>O, EtOH/H<sub>2</sub>O (80:10) at 25 °C.

The first derivative of the spectroscopic spectra was used to enhance the separation of overlapping absorbance peaks at around 290 and 255 nm (Figure 2.14B, C, D). It was observed that the peak at around 290 nm shifts towards higher wavelength with increasing drug concentration, whereas the one at 255 nm remains stable. This bathochromic shift occurs at stages when PPA148 is in water and presents a hyperbolic shape when in ethanol and ethanol:water (80:20).

UV/Vis spectroscopy was used for the quantification of PPA148. The limits of detection and quantification in two different systems (100% ethanol and 80:20 ethanol:water) were initially calculated by a regression analysis of the calibration curve. The assumptions of linear regression were met and, thus, the results are reliable (Figure 2.14A-inset, Figure B 4). It was found that the LOD/LOQ (Equation 2.5 and 2.6) for 100% and 80% ethanol were 2.23/6.76  $\mu\text{g/mL}$  and 2.97/8.99  $\mu\text{g/mL}$ , respectively. Once these limits were established, the thermodynamic solubility ( $S_0$ ) was investigated in water and HEPES buffer (pH=7.2). The experimental  $S_0$  was  $30.3 \pm 1.8 \mu\text{g/mL}$  and  $60.7 \pm 15.6 \mu\text{g/mL}$  in water and HEPES buffered saline, respectively, after equilibration for one week.

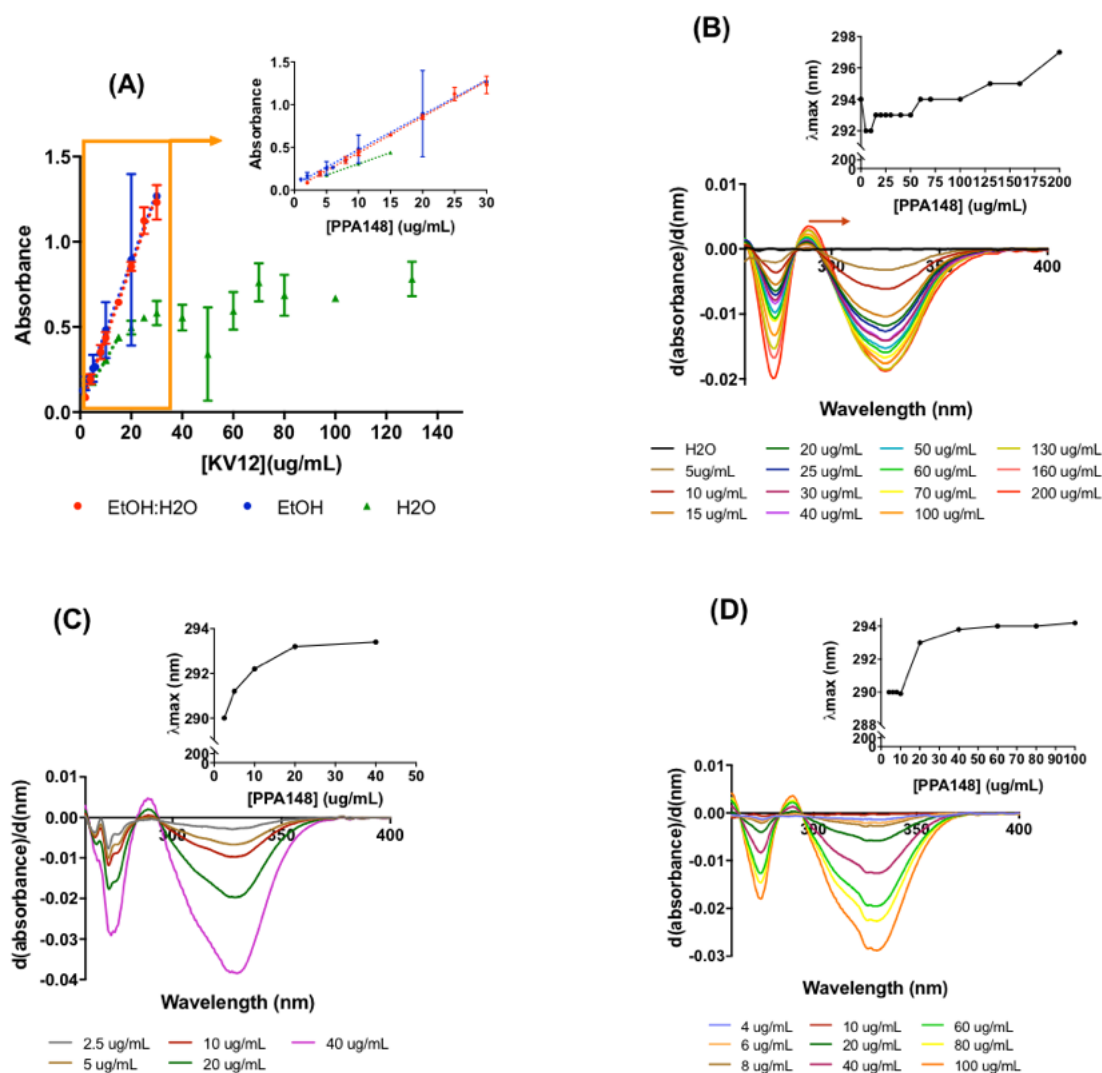


Figure 2.14: (A) Effect of solvent and drug concentration on the absorbance profile. Inset: concentration range where the Beer-Lambert law is followed ( $y = 0.04x + 0.02, R^2 = 0.98$  for EtOH/H<sub>2</sub>O,  $y = 0.04x + 0.06, R^2 = 0.75$  for EtOH,  $y = 0.03x + 0.05, R^2 = 0.98$  for H<sub>2</sub>O). First derivative of UV/Vis spectrum of a series of PPA148 concentrations in: (B) H<sub>2</sub>O; (C) EtOH; and (D) EtOH:H<sub>2</sub>O (80:20). The peaks and troughs of the spectrum profile is presented with zero first derivative. The insets show the changes of  $\lambda_{max}$  with increasing drug concentration.

#### 2.4.2.3 Aggregation and solubility studies

The solubility of PPA148 in aqueous media was further investigated with dynamic light scattering. DLS is a sensitive technique to detect the presence of small aggregates based on temporal fluctuations in the intensity of scattered light, as a result of Brownian motion. The derived count rate (DCR) is a measure of the count rate (average scattering intensity) and is useful to compare the signal strength in different samples. Figure 2.16 presents the changes in DCR against increasing drug concentration in water at room temperature (25 °C). The results show that PPA148 generates aggregates at drug concentrations above ~20  $\mu\text{g/mL}$  with an average size of 1  $\mu\text{m}$  and high polydispersity index (0.7). Precipitation of the drug was visually observed at concentration higher than ~30  $\mu\text{g/mL}$  (Figure 2.15).



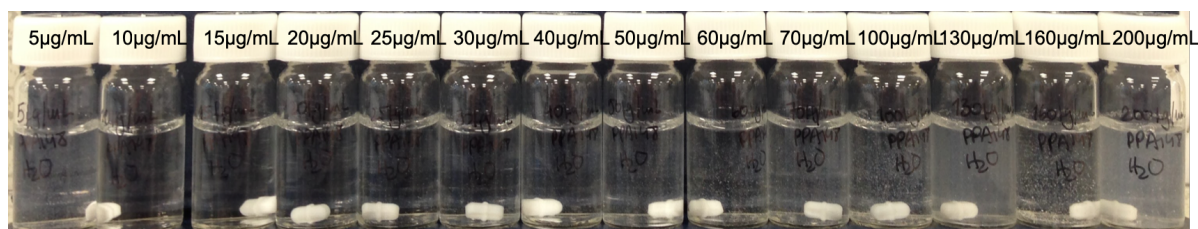


Figure 2.15: Increasing concentration of PPA148 in water 7 days under mild stirring at 25 °C. Visual observation of the precipitation point is at 50 µg/mL.

Cyclodextrins were used as a means of increasing the water solubility of the drugs and avoiding its self-association. As explained above, the increased scattered light or turbidity reflects the onset of aggregation (Figure 2.16). In the presence of cyclodextrin (HP $\beta$ CD), the onset of aggregation takes place at higher drug concentrations, as seen from a shift in the intersection point between a flat region and a linear region. The values obtained are  $51.1 \pm 2.6$  µg/mL (PCS) and  $53.9 \pm 12.1$  µg/mL (UV scattering) (Figure 2.16, Table 2.3).

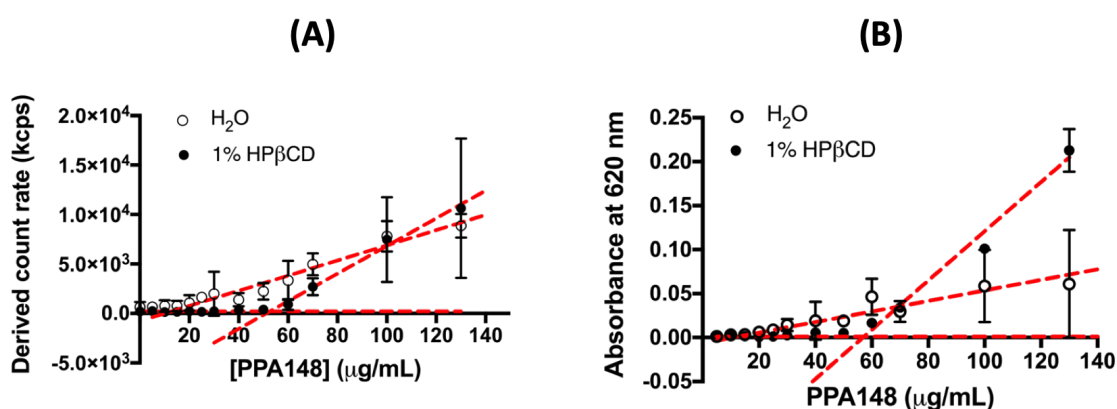


Figure 2.16: Turbidimetric assay: Effect of cyclodextrin concentration in the aggregation of PPA148 using dynamic light scattering (A) and UV/Vis spectroscopy (B).

Solubility of PPA148 in pure water and HEPES buffered saline pH 7.2 was determined using different techniques. The results are summarized in Table 2.3.

Table 2.3 Solubility values and aggregation concentration of PPA148 in water, HEPES buffered saline pH 7.2 and HP $\beta$ CD or RAMEB in HEPES obtained by different techniques.

Solvent	Solubility (µg/mL) using:		Aggregation concentration (µg/mL)	
	Thermodynamic solubility	Phase solubility diagram	Turbidimetric assay (PCS)	Turbidimetric assay (UV)
H <sub>2</sub> O	$30.3 \pm 1.8$	-	$18.1 \pm 4.7$	$16.3 \pm 11.1$
HEPES	$60.7 \pm 15.6$	$153.8 \pm 52.9$	-	-
HP $\beta$ CD/HEPES	-	938.8	$51.1 \pm 2.6$	$53.9 \pm 12.1$
RAMEB/HEPES	-	966.8	-	-

## 2.4.2.4 Drug/Cyclodextrin inclusion complex formation: binding constant

The formation of an inclusion complex between CD and drug was examined by two methods: binding constant determination by fluorescence spectroscopy (161) (section 2.3.10) and phase solubility diagram (section 2.3.11) (147). Rifampicin was used as a positive control to evaluate and establish the method because it is known to form an inclusion complex with CDs (158,162–164). With the spectroscopic method, the binding of the drug to the CD is reflected by a hyperbolic function in UV absorbance as the concentration of CD is increased while the total drug concentration is held constant. The addition of increasing cyclodextrin (either RAMEB or HP $\beta$ CD) from 0 to 30 % w/v to a fixed concentration of 10  $\mu$ g/mL PPA148 and 50  $\mu$ g/mL rifampicin produces a hyperchromic effect (Figure 2.17, Figure 2.18) reflecting an interaction between the drug and HP $\beta$ CD or RAMEB. For both types of cyclodextrin, a good fit (Equation 2.7) of the experimental data was obtained by assuming a 1:1 stoichiometry. Higher affinity of PPA148 to RAMEB ( $102 \pm 26 \text{ M}^{-1}$ ) over HP $\beta$ CD ( $63 \pm 20 \text{ M}^{-1}$ ) could be attributed to the different hydrophobicity of the methylated and hydroxypropyl substitutions. The data were fitted using a 1:2 PPA148:CD complex (data not shown) but the root mean squared error between the experimental and the fitted data was better when a 1:1 complex was assumed, which illustrated a better fitting. The binding constants of rifampicin to RAMEB and HP $\beta$ CD at 50 mM Tris buffer pH 9 were found to be  $38 \pm 9 \text{ M}^{-1}$  and  $22 \pm 2 \text{ M}^{-1}$  (Figure 2.18) respectively, which are lower than values from the literature, namely,  $73.4 \pm 8.2 \text{ M}^{-1}$  and  $68.5 \pm 5.2 \text{ M}^{-1}$  for RAMEB and HP $\beta$ CD, respectively in sodium tetraborate buffer, pH 9 (162). A much higher binding constant ( $209.0 \text{ M}^{-1}$ ) was found for HP $\beta$ CD at pH 6 (164) and with DIMEB at PBS buffer pH 5.7 ( $300 \text{ M}^{-1}$ ) (158). Chadha et al. obtained the binding constant using solution calorimetry and the reported values are  $1564 \pm 8 \text{ M}^{-1}$  for RAMEB and  $1038 \pm 11 \text{ M}^{-1}$  for HP $\beta$ CD in PBS (163). The difference in the binding constants may be the different methods used and buffer used during the experiment.

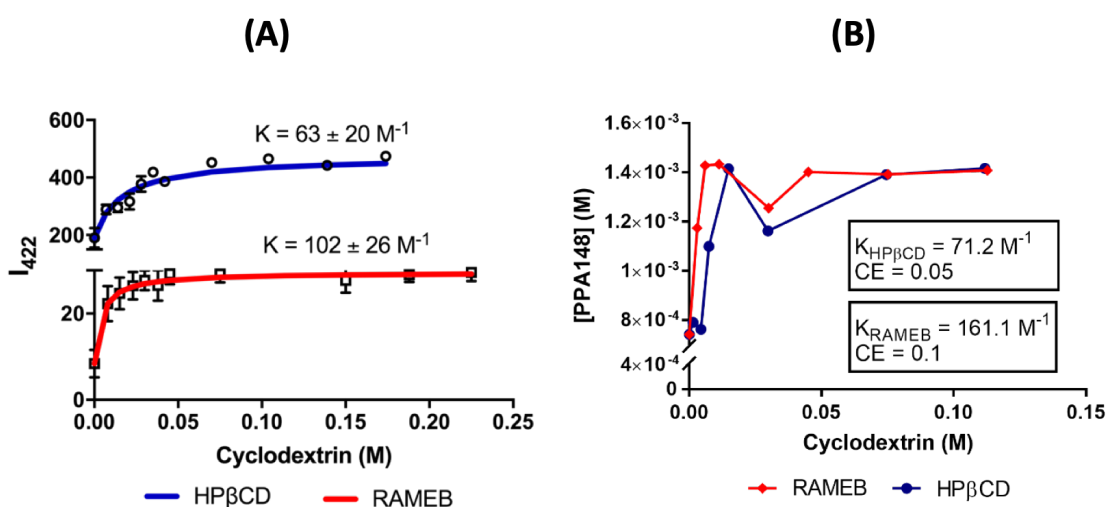


Figure 2.17: Changes in the fluorescence intensity of PPA148 with increasing cyclodextrin concentration (HP $\beta$ CD or RAMEB) at 25 °C (A). The lines represent the non-linear regression fit (Equation 2.7) of the experimental data points assuming a 1:1 complex. The phase solubility diagram (B) was built by adding an excess of drug to solutions of cyclodextrin to measure drug

solubilisation. In both experiments, the solution used was HEPES buffered saline including  $\text{CaCl}_2$  at pH 7.2.

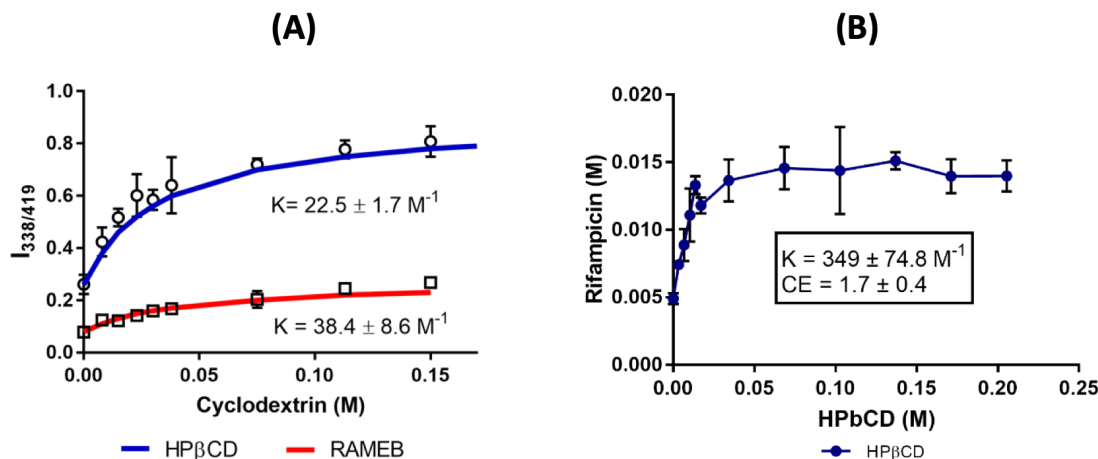


Figure 2.18: Changes in the fluorescence intensity of rifampicin in increasing cyclodextrin concentration (A) show the drug's affinity to HP $\beta$ CD and RAMEB at 25 °C. The lines represent the non-linear regression fit of the experimental data points assuming a 1:1 complex. The phase solubility diagram (B) was built to observe the approximate amount of drug that can be solubilized with CDs and gave an indication of the complex stoichiometry and affinity. In both experiments, the solution used was Tris buffer pH 9.

The phase solubility diagram was constructed by measuring the apparent drug solubility (of rifampicin and PPA148) as a function of increasing CD concentration. It was used as a tool to identify the drug behavior and its solubility profile based on the shape of the diagram (147). The phase solubility diagram obtained for rifampicin agrees with published data in terms of shape, binding constant and complex stoichiometry (164). Rifampicin presents an increase in solubilization as the amount of CD is increased, up to ca. 34 mM (5% w/v) HP $\beta$ CD (Figure 2.18B). In the plateau region, the concentration of the drug is  $13.6 \pm 1.0 \text{ mM}$  ( $11.2 \pm 1.2 \text{ mg/mL}$ ). Additional quantities of CD do not alter the diagram, suggesting that saturation has been reached. The intercept of the phase curve with the y-axis ( $S_{int}$ ) should reflect the intrinsic drug solubility. Here a value of  $4.9 \pm 0.4 \text{ mM}$  ( $4.0 \pm 0.3 \text{ mg/mL}$ ) was obtained, which is higher than the water solubility given by the manufacturer ( $2.5 \text{ mg/mL}$  or  $3 \text{ mM}$ ). The linear region of the diagram suggests the formation of a 1:1 complex with a binding constant of  $349 \pm 75 \text{ M}^{-1}$ , which is higher than the value found using the fluorescence spectroscopy method (Figure 2.18A). The ratio of cyclodextrin concentration in complex over free form (CE) found from the phase solubility diagram is  $\text{CE} = 1.7 \pm 0.4$  which is higher than that found by Tewes et al. ( $\text{CE} = 0.3$ ) (162). Similar solubility behaviour was observed for PPA148 with both RAMEB and HP $\beta$ CD (Figure 2.17B). However, the phase solubility test was performed only once because of the large quantities of drug needed to perform the experiment, thus, only qualitative results are presented. PPA148 (1 mg) was completely solubilized ( $0.99 \text{ mg/mL}$  or  $1.4 \text{ mM}$ ) with 6 mM (0.8%) RAMEB and 15 mM (2.0%) HP $\beta$ CD. In the solubility diagram with RAMEB, the intercept of the linear part gives  $S_{int} =$

153.8  $\mu\text{g/mL}$  (0.2 mM), whereas in that with HP $\beta$ CD to 191.3  $\mu\text{g/mL}$  (0.3 mM) (Table 2.3). As in the case of rifampicin, the solubility obtained from the phase solubility diagram is around double the thermodynamic concentration.

Table 2.4: Binding constant of PPA148 and rifampicin as obtained by two different techniques.

CD	Binding Constant ( $\text{M}^{-1}$ )						
	PPA148		Rifampicin		Rifampicin (reported values)		
	Binding assay	Phase solubility diagram	Binding assay	Phase solubility diagram	Phase solubility diagram		
HP $\beta$ CD	63 $\pm$ 20	71.2	22 $\pm$ 2	349 $\pm$ 74	18*	120/125**	68.5 $\pm$ 5.2***
RAMEB	102 $\pm$ 26	161.1	38 $\pm$ 9	-	-	-	73.4 $\pm$ 8.2***

\*The buffer used in the experiment was 10 mM Tris pH 6.9 and ionic strength of 10 mM.

\*\* The buffer used in the experiment was 30 mM citrate/10 mM Tris pH 6.9 with ionic strength of 0.8 mM.

\*\*\* The buffer used in the experiment was 50 mM sodium tetraborate pH 9.

Gibbs free energy change ( $\Delta G_{TR}^0$ ) values for the process of transferring a drug from pure water to aqueous cyclodextrin solution were calculated based on Equation 2.11 and presented in Table 2.3.  $\Delta G_{TR}^0$  values were found to be negative at all concentrations of CD in all cases, indicating the spontaneous nature of complex formation. The values were negative upon increasing CD concentration, indicative of more favorable solubilization reaction as the concentration of CD increased.

Table 2.5: Gibbs free energy of transfer of rifampicin and PPA148 from pure water to aqueous CD solutions at room temperature calculated using Equation 2.11.

HP $\beta$ CD or RAMEB (%)	$\Delta G_{TR}^0$ RIF: HP $\beta$ CD	$\Delta G_{TR}^0$ PPA148: HP $\beta$ CD	$\Delta G_{TR}^0$ PPA148: RAMEB
0.2	N/A	-67	N/A
0.4	N/A	N/A	-491
0.5	-443	N/A	N/A
0.6	N/A	-29	-700
1	-627	-420	N/A
1.5	-860	N/A	-704
2	-1066	-690	N/A
4	N/A	-480	-562
5	-1091	N/A	N/A
10	-1160	-672	-672
15	-1131	-691	-685

### 2.4.2.5 Stoichiometry of drug/CD complexes

The stoichiometry of the complex was examined using the Job's plot method from NMR data (section 2.3.12, Figure 2.19). The normalized NMR signal is plotted against the mole fraction of one reactant (molar fraction of cyclodextrin in this case), while the total reactant concentration is kept constant (1 mM). Figure 2.19 presents changes in protons at position 1 (external) and 5 (internal) in a series of cyclodextrin molar fraction for rifampicin and PPA148, respectively. The Job's plot of H1 for rifampicin and DIMEB reflects the formation of a 1:1 inclusion complex, with a maximum at  $X_{CD}=0.5$ . This stoichiometry is in agreement with published data (158).

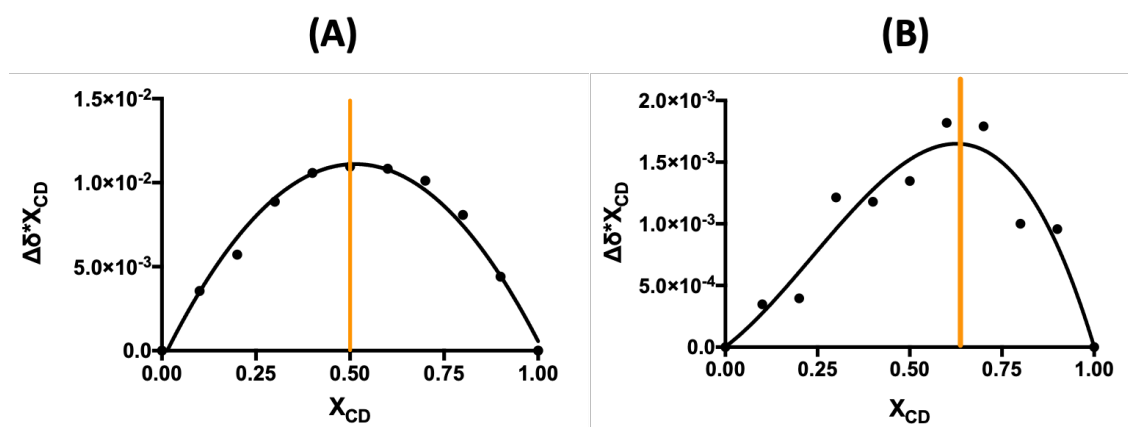


Figure 2.19: Job's plot for rifampicin/DIMEB (A) and PPA148/DIMEB (B) complexes. In the case of rifampicin, the normalized chemical shift ( $\Delta\delta^*X_{CD}$ ) of the H1 protons of DIMEB were plotted against the molar fraction of DIMEB ( $X_{CD}$ ). For, PPA148, protons at position 5 of the cyclodextrin structure.

In order to build a Job's plot, PPA148 was used at very low concentration (20  $\mu\text{g/mL}$ , or 0.03 mM) because of its poor solubility in water (Table 2.3). The spectra were noisier, due to the low concentration, but the chemical shift of H5 shows a skewed Job's plot with a maximum around  $X_{CD}=0.6$ , thus revealing a dominating 1:2 PPA148/DIMEB complex, namely, the drug is encapsulated by two cyclodextrins in two different positions.

## 2.5 Discussion

A novel biaryl pyrrolobenzodiazepine (PBD) hybrid analogue, PPA148, was successfully synthesized based on the reported synthetic route (107). Specifically, a convergent synthetic strategy was used, based on the separate synthesis of the PBD tricyclic scaffold (core) and the lateral polyamidic tail. The two constituents of the final core and tail molecules were coupled to give the final PPA148 with 82% yield and 78.1% relative purity. Based on the ICH guidelines, the purity of new compounds should be calculated based on an analytical standard (165). Here, the purity was calculated based on PPA148's peak areas as a percentage of all other peak areas in the LC/MS chromatograms because there was no analytical standard. The drawback of this approach is that any non-UV active impurities present in the sample are not detected.

Affinity for the air/water interface, a measure of amphiphilicity, was investigated at the molecular level using the Langmuir trough technique (Figure 2.12). PPA148 adsorbed at the air-water interface and reached a surface pressure of  $12.3 \pm 0.7$  mN/m. It was expected that the adsorption would be instantaneous because of the properties estimated by ChemDraw ( $\log P = 0.76$  and  $\log S = -7.461$ ). However, PPA148 reached half of the maximum pressure within 20 min and from that point it took another 2 h to reach the final maximum. This slow kinetic profile can be explained by two possible transport-limiting steps. The drug was injected below the air/water interface under mild stirring in order to mix the drug with the subphase. The initial adsorption was delayed due to the diffusion of the co-solvent (0.5% DMSO) in the aqueous subphase of the trough. DMSO is miscible with water and forms strong hydrogen bonding interactions with 3 water molecules (166). It was introduced into the aqueous system as a solvent for the drug via injection which possibly affected the kinetic profile of the drug absorption process (167). The second stage was due to the saturated surface after 40 min (Figure 2.11). In the early stages of adsorption, i.e. after drug injection, the surface is relatively empty and molecules adhere as fast as they reach the surface. However, as the surface gets saturated by drug molecules, the diffusion at the interface might be slowed down before the pseudo-steady equilibrium is reached (168).

PPA148 is a hydrophobic antibiotic with low water solubility. It presented a water solubility of  $30.3 \pm 1.8$   $\mu\text{g/mL}$  and aggregation occurred at concentrations above 18  $\mu\text{g/mL}$  (Table 2.3). Sedimentation arose by attraction forces between drug molecules and repulsion forces between drug and water, which are responsible for low-concentration agglomeration, possibly leading to drug sedimentation at around 50  $\mu\text{g/mL}$  (Figure 2.15). (169). In addition, the fact that the absorption intensity of PPA148 decreased with increasing water content in the EtOH/H<sub>2</sub>O mixture (Figure 2.13) and in 100% water deviated from linearity with increasing amount of drug (Figure 2.14A and Figure 2.16) indicated the formation of agglomerates/aggregates. The thermodynamic water solubility ( $30.3 \pm 1.8$   $\mu\text{g/mL}$ ) was higher than the aggregation concentration (Table 2.3), which implies the presence of both monomers and small aggregates (169). The aggregates were not optically visible at 30  $\mu\text{g/mL}$  which implies that the aggregates might have been dimers, trimers or other water-soluble oligomers whose size is below the visible light wavelength range (400-700 nm) (110,155).

Drug aggregation can have a negative impact on antimicrobials, because their bioavailability is reduced and less substance is available to interact with microorganisms (170). Cyclodextrins were successfully used to improve the solubility of the drug through inclusion complex formation. RAMEB and HP $\beta$ CD were shown to solubilize PPA148 up to approximately 50  $\mu\text{g/mL}$  in HEPES buffered saline pH 7.2 (Table 2.3) in HEPES buffered saline (pH 7.2) by delaying the formation of aggregates. Rifampicin and PPA148 possess hydrophobic moieties (Figure 1.9, Figure 2.2) capable of entering the apolar CD cavity through inclusion complex formation (171). One of the aims of this project was to avoid the formation of aggregates and improve drug water solubility by forming cyclodextrin inclusion complexes, as a way to improve bioavailability and as a first

step in the formulation, which would then involve encapsulation in liposomes (Chapter 3). Rifampicin, an antimicrobial agent that would benefit from an optimized formulation, was used as a control drug because it is hydrophobic and is known to form complexes with cyclodextrins (162). The data obtained from fluorescence spectroscopy was fitted by a 1:1 binding constant both for rifampicin and PPA148 with RAMEB and HP $\beta$ CD. Based on the calculated binding constant for a 1:1 complex from the fluorescence intensity, PPA148 present a higher affinity for RAMEB ( $102 \pm 26 \text{ M}^{-1}$ ) than HP $\beta$ CD ( $63.3 \pm 20.3 \text{ M}^{-1}$ ) (Figure 2.17A, Table 2.4). The method based on phase solubility showed a lower value for the PPA148/RAMEB complex ( $161.1 \text{ M}^{-1}$ ) but a similar value for PPA148/HP $\beta$ CD ( $71.2 \text{ M}^{-1}$ ) (Figure 2.17B, Table 2.4). In the spectroscopic method, the total drug concentration is kept constant at a low value but the free (soluble) drug decreases due to inclusion into the CD cavity, up to a plateau value. Instead, in the phase solubility diagram, an excess of drug is added, which is solubilized by increasing amounts of cyclodextrin (73). In contrast to the binding constant and phase solubility methods, NMR (Job's plot) showed that a 2:1 PPA148/DIMEB complex was formed. Both the phase solubility diagram and fluorescence spectroscopy illustrated higher affinity for both drugs towards the randomly methylated cyclodextrin (RAMEB). This is also observed for rifampicin (162,163) and hemisuccinate ester, prodrug of  $\Delta^9$ -Tetrahydrocannabinol, (172). The methylation of  $\beta$ CD creates a more hydrophobic environment and enhances molecular flexibility, which allows an increased adaptability of the cyclodextrin towards the guest molecule (163).

Although the findings on the complex stoichiometry for rifampicin agree with the literature, the binding constant values differ slightly from previous reports (158,162,164). Rifampicin has three ionization states (Figure 1.9) with a maximum water solubility at pH between 6-9 because the predominant state is anionic. In this study, the binding constant between rifampicin and cyclodextrin was determined at pH = 9 using two methods, a phase solubility diagram and the shift in fluorescence intensity, with slightly different results (Table 2.4). The binding constants for rifampicin with RAMEB or HP $\beta$ CD reported in the literature vary between 500 and 5000  $\text{M}^{-1}$  depending on the pH, temperature, buffer solution and calculation method. The binding constant  $K$  for a 1:1 rifampicin/HP $\beta$ CD complex calculated from the phase solubility study was  $349.4 \pm 74.8 \text{ M}^{-1}$  and it approaches the value reported by He et al. (164) ( $227.3 \text{ M}^{-1}$ ). However, the binding constant determination by fluorescence spectroscopy (assuming a 1:1 complex) resulted in lower  $K$  values ( $22.5 \pm 1.7 \text{ M}^{-1}$  for HP $\beta$ CD and  $38.4 \pm 8.6 \text{ M}^{-1}$  for RAMEB in Tris buffer pH 9), compared to those found by the phase solubility diagram under the same experimental conditions, and to those published by Tewes et al. ( $68.5 \pm 5.2 \text{ M}^{-1}$  for HP $\beta$ CD and  $73.4 \pm 8.2 \text{ M}^{-1}$  for RAMEB in sodium tetraborate pH 9) (162). Overall, the interaction with RAMEB was stronger compared to HP $\beta$ CD, which is in agreement with Chadha et al., who found binding constants of 1038 and  $1564 \text{ M}^{-1}$  using solution calorimetry (163). Job's plot actually showed that a 1:1 rifampicin/DIMEB complex was formed, which confirms the binding constant and phase solubility assumption of the calculations. It has been reported that it is the piperazine moiety of rifampicin that inserts into the

CD cavity with both types of CD used in this study (Figure 2.20). This postulated structure of rifampicin/CD complex is established by using  $^1\text{H}$  and  $^{13}\text{C}$ -NMR and  $^{15}\text{N}$ -NMR (173).

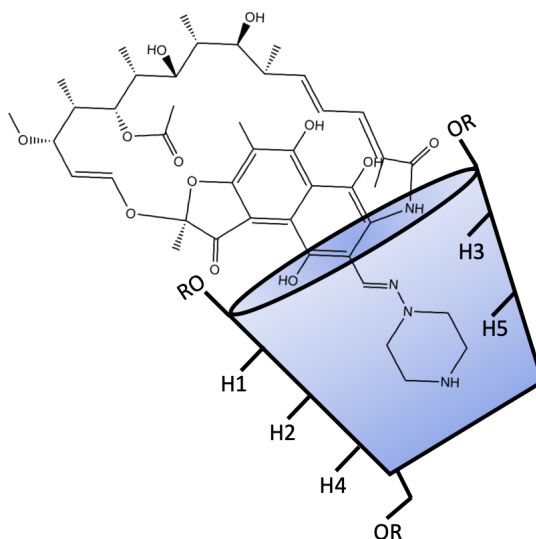


Figure 2.20: Schematic representation of rifampicin/CD inclusion complex as it was found by molecular simulation by He et al. and Tewes et al. (162,164).

Another measure of solubilizing efficiency is to determine the molar concentration ratio of cyclodextrin in a complexed form to the free cyclodextrin; this is referred to as complexation efficiency (CE). According to Loftsson and Brewster (155), CE is a better measure of efficiency because it is less sensitive to errors related to the estimation of the intrinsic solubility. The aggregation of highly hydrophobic drugs in aqueous solutions may affect the slope obtained in the phase solubility diagram and may cause deviations in the value of the y-intercept ( $S_{int}$ ) from  $S_0$ , leading to possible inaccuracies and over-estimation of the binding constant (73). The CE calculated for rifampicin was 1.8 at pH 9 (Figure 2.18B) which is higher than values cited in the literature using the same method at pH 9 (0.347) (174). This means that one in two cyclodextrin molecules are forming a water-soluble complex with rifampicin, compared to the cited one in four. The values of CE for PPA148/HP $\beta$ CD and PPA148/RAMEB were found to be 0.05 and 0.1, respectively (Figure 2.17B). CE is correlated with drug hydrophobicity and  $S_0$  (155). Hydrophobic drugs with  $S_0$  higher than 0.01 mg/mL possess a high CE (175). For example, it has been found that clotrimazole ( $S_0 = 0.037$  mg/mL) has a CE of 0.05 with HP $\beta$ CD in water, hydrocortisone ( $S_0 = 0.4$  mg/mL) has a CE of 1.3 with HP $\beta$ CD at pH 7 and fluoxetine HCl ( $S_0 = 12.6$  mg/mL) has a CE of 4.7 at pH 3.6 (175).

The driving force for complex formation is a combination of electrostatic interactions, van der Waals forces, hydrogen bonding and charge-transfer interactions (146,175,176). The binding process can be separated into 3 steps (146). The first step is the exclusion of cavity-bound high energy water molecules into the gas phase, accompanied by changes in CD conformation energy. The second is the solvent (water) rearrangement and transformation of the excluded



gaseous water molecules into a liquid phase which is accompanied with a negative enthalpy and entropy change. The third step is the fit of the hydrophobic guest molecule into the nonpolar CD cavity accompanied by host-guest intermolecular interactions and a change in the conformation energy of the host (176). Therefore, van der Waals forces and hydrophobic interactions constitute the basic driving force for complex formation and hydrogen bonding, and electrostatic interaction can affect the conformation of complexes (146).

The estimated Gibbs free energy of transfer for both rifampicin and PPA148 were negative, indicating that the complexation is spontaneous, as expected. The interaction of both drugs with RAMEB were found to be sterically favored compared to other CDs, because the methyl substitution creates a more hydrophobic microenvironment compared to the hydroxypropyl substitution (163).

## 2.6 Conclusion

The novel antimicrobial agent was successfully synthesized and characterized. It was found that PPA148 is barely soluble in water ( $30.3 \pm 1.8 \mu\text{g/mL}$ ) and self-associates when dispersed in an aqueous environment above its water solubility level. To enhance water solubility and avoid aggregation, cyclodextrins (RAMEB and HP $\beta$ CD) were used to form an inclusion complex with PPA148. Water solubility increased 6-fold through the incorporation of PPA148 into cyclodextrin's cavity and a higher affinity was obtained with RAMEB compared to HP $\beta$ CD. Enhancing water solubility was the first step towards developing a formulation for PPA148 to enhance its antibacterial efficacy against Gram negative bacteria. The next two chapters focus on incorporating the PPA148/RAMEB complex into fluid liposomes (fluidosomes) to improve its antibacterial activity and drug uptake, which are assessed using biophysical approaches.

# Chapter 3 Liposomal encapsulated drug/cyclodextrin inclusion complexes

### 3.1 Introduction

The development of new antimicrobial agents and the understanding of their mechanism of action is a pressing need because of the widespread proliferation of drug resistance, especially in Gram-negative bacteria, the most common cause of nosocomial infections in Europe and USA (177,178). Antimicrobials are losing their effectiveness at an increasing rate, resulting in growing difficulty in treating bacterial infections. The World Health Organization (WHO) has developed the global priority pathogen list, which includes critical, high and medium risk pathogens for public health (Table 1.2) (44). Among the critical and high-risk pathogens are *Enterococcus faecium*, *Staphylococcus aureus*, *Klebsiella pneumoniae*, *Acinetobacter baumannii*, *Pseudomonas aeruginosa* and *Enterobacter spp*, also known as the ESKAPE pathogens, which cause hospital acquired infections (57). In the same report in 2017 (57), the WHO stated the need to support R&D, and furthermore, discover and develop new antibiotics against multi- and extensively drug-resistant Gram negative bacteria.

The objective of this work was to develop a suitable carrier to increase drug uptake and drug efficacy against Gram negative bacteria. This chapter describes our attempt at developing and characterizing a formulation for the newly discovered antimicrobial PPA148, combining cyclodextrins and liposomes, based on their respective characteristics which were considered advantageous to achieve criteria of improved efficacy and higher solubility. The rationale behind this formulation is that the liposomal carrier (fluidosomes) will enhance the permeation of PPA148 through the Gram negative OM, while cyclodextrins enhance its water solubility and permeation through the IM.

Fluidosomes are fluid liposomes composed of DPPC/DMPG (18/1), which are characterized by their ability to fuse into lipid membranes (179). Beaulac and co-workers were the first to evaluate the efficacy of tobramycin encapsulated into several types of liposomes against *Pseudomonas aeruginosa* (102,103). Their results showed antibacterial efficacy of the encapsulated tobramycin, and that the most efficient carriers were the fluid (fluidosomes) rather than the more rigid liposomes. Sachatelli et al. then published encouraging results on fluidosomes, using immunoelectron microscopy and Gram staining techniques to show that fluidosomes may fuse with the bacterial cell envelope and release tobramycin in the cytoplasm (179). Until now, only a few antibiotics encapsulated in fluidosomes have been examined for their increased efficacy (Table 1.4).

Molecules with poor water solubility, such as PPA148, are mainly loaded in the hydrophobic tail region of the bilayer, leading to limited drug loading and immediate drug release (180). Therefore, the first step of this work was to increase the water solubility of PPA148 by using pharmaceutically acceptable  $\beta$ CD derivatives, as we showed in Chapter 2. Water solubility increased 5-fold by incorporating PPA148 into the cavity of cyclodextrins (Figure 2.16, Table 2.3).

In addition to the higher solubility achieved, RAMEB was also chosen because of its expected permeation through the phospholipid bilayer of the IM (181). RAMEB has been reported to induce phospholipid exchange (181), which could be of great assistance for the transport of drug through the IM. Phospholipids with longer alanyl chains are difficult to extrude from liposomes because in complexing with CD, their chain may protrude into the aqueous environment, which is not energetically favorable (181). There is also a limit on the chain length that can be fully complexed with  $\beta$ -cyclodextrins: phospholipids with 14 carbons can be fully incorporated into the CD cavity but not those with 16 carbons (182,183). DPPC (Figure 3.1) was found to interact with CDs less than other phospholipids, due to its chain length and its high phase transition temperature ( $T_m$  at 41°C), thus forming a tightly packed gel phase lipid film at room temperature (181,181).

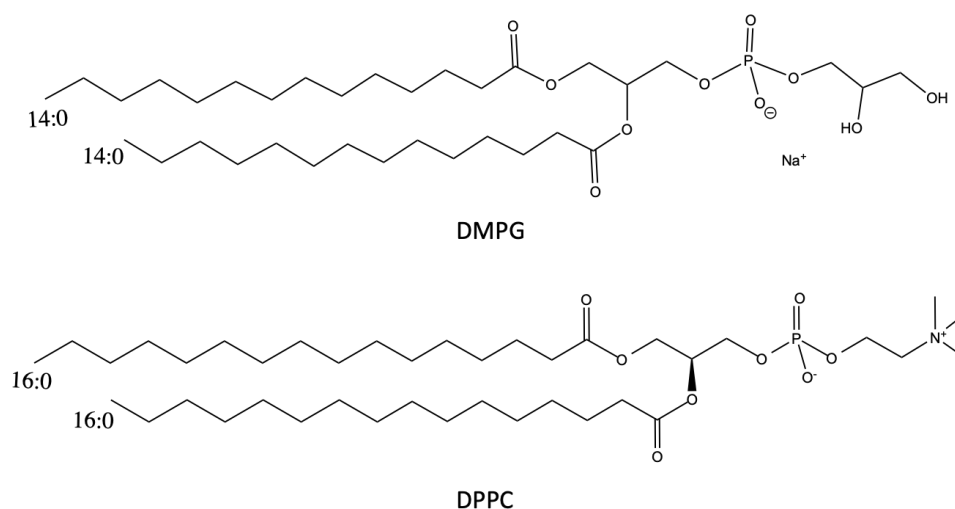


Figure 3.1: Structure DPPC (16:0) and DMPG (14:0).

In this chapter, PPA148/RAMEB complexes (presented in Chapter 2) were incorporated into fluidosomes to enhance the antimicrobial efficacy of the novel compound. Empty fluidosomes were initially used to develop a robust manufacturing method. The thin film hydration method was used to form the fluidosomes, followed by extrusion for size reduction to ~100 nm. Fluidosomes encapsulated within the drug/CD complex were separated from unloaded vesicles using size exclusion chromatography. The elution profile of the lipids and drug through the size exclusion column was quantified by UV spectroscopy. The aliquot containing most of the loaded fluidosomes was used to determine, spectroscopically, the encapsulation efficiency and loading capacity of the formulation. A microbiological assay (Kirby Bauer or disk diffusion assay) (184,185) was carried out to examine the efficacy of PPA148 alone, PPA148/RAMEB complex and PPA148/RAMEB in fluidosomes. The inhibition zones created by PPA148 (both alone and formulated) were compared with that of rifampicin (positive control) and gentamicin (negative control). For this assay, a disk preparation method was developed to generate valid results comparable to commercially available disks.

## 3.2 Materials

**Lipids:** 1,2-dipalmitoyl-sn-glycero-3-phosphocholine (DPPC, 16:0 PC) and 1,2-dimyristoyl-sn-glycero-3-phosphoglycerol, sodium salt (DMPG, 14:0 PG) were obtained from Avanti polar lipids (Alabama, USA) and supplied by Stratech Scientific (Newmarket, UK).

**Microbiological Assay:** Blank, rifampicin (30 µg) and vancomycin (30 µg) susceptibility disks, agar powder and Muller Hinton broth for microbiology were purchased from Oxoid (UK). LC/MS grade water was supplied by Merck, UK. E. coli bacteria DH5α were obtained from Invitrogen Life Science Technology (Thermo Fisher Scientific, UK).

**Salts used for buffer and reagent preparation:** Sodium chloride (NaCl), magnesium chloride (MgCl<sub>2</sub>), monosodium phosphate (NaH<sub>2</sub>PO<sub>4</sub>), sodium hydroxide (NaOH) Ammonium thiocyanate, ferric chloride and HEPES (>=99.5%) were supplied by Sigma-Aldrich, UK.

**Cyclodextrins:** Hydroxypropyl-β-cyclodextrin (HPβCD), randomly methylated β-cyclodextrin (RAMEB) supplied from Sigma-Aldrich, UK.

**Solvents:** Dichloromethane (DCM), chloroform and deuterated water were purchased by Sigma-Aldrich, UK. The ultrapure water at 18.2 MΩ was produced by a Purelab Ultra machine from ELGA process water (Marlow, UK).

## 3.3 Methods

### 3.3.1 Formation of Large Multi-Lamellar Fluidosomes

Fluidosomes consisted of DPPC/DMPG in a molar ratio of 18:1 and were manufactured by the thin film hydration method (186). The mixture of lipids (10 mg) was dissolved in 1 mL of chloroform in a round-bottom flask and sonicated in a sonicating bath (Fisherbrand®, FB11203, Fisher Scientific, UK) at 25°C for approximately 1 min until achieving a clear solution. The solvent was evaporated using a rotary evaporator (Rotavapor® R11, Büchi, Switzerland) attached to a vacuum pump (KNF Lab, UK). The temperature of the water bath was set to 40°C and the rotation speed to approximately 190 rpm. The resulting thin lipid film was kept under reduced pressure in a pyrex vacuum desiccator for 12 h to further remove traces of organic solvent. The lipid film was then solvated by adding 4 mL of phosphate buffer pH 7.4 (50mM PBS, 40mM NaH<sub>2</sub>PO<sub>4</sub> and 26 mM NaCl) or 20 mM HEPES buffered saline pH 7.2 (145 mM NaCl and 10 mM CaCl<sub>2</sub>) under vigorous stirring and bath sonication (Fisherbrand®, FB11203, Fisher Scientific, UK) at 40°C to facilitate vesicle formation. The lipid suspension was dipped into an ice bath (4°C) for 1 min and then placed in the water bath (40°C) for another minute. This temperature changing sequence was repeated 5 times followed by a 1 h resting period at 4°C before using them for size reduction.

Empty liposomes of the desired size were used to validate the separation method of free molecules from the drug-in-CD encapsulated liposomes using a PD10 G25 Sephadex column (GE Healthcare, UK). The method is described in section 3.3.5.

### 3.3.2 Size reduction methods for the manufacture of Fluidosomes

Size reduction of fluidosomes was carried out by two different methods: probe sonication and extrusion, to manufacture homogeneous lipid dispersions with unilamellar vesicles. Following the probe sonication, the lipid suspension was vortexed (Cyclone-Vortex mixer CM-1, Nickel-Electro Ltd) for 60 sec at 2800 rpm, sonicated (Soniprep 150 Plus ultrasonic disintegrator 120V 60Hz, London, UK) for 5 min with a microprobe at an amplitude of 10 microns and left at room temperature for one hour prior to further use.

The second method was extrusion, which was carried out by placing 1 mL of suspension in a tight gas syringe on a mini-extruder (Avanti Polar Lipids) thermostated at 55 °C and manually extruded through a 0.1 µm polycarbonate membrane 11 times. The extruded liposomes were kept at 4°C and were extruded again under the same experimental set up after 12 hours. The double extruded liposomes were stored for further use.

The SUVs vesicles formed with the two different methods were compared in terms of hydrodynamic diameter using photon correlation spectroscopy.

### 3.3.3 Preparation of drug-cyclodextrin inclusion complexes

A 1:1 complex of drug and RAMEB was used for its encapsulation into liposomes. Drug and cyclodextrin were mixed in a 1:1 molar ratio in HEPES buffered saline at pH 7.2. The mixture was left under stirring (190 rpm) for 24 hours.

### 3.3.4 Incorporation of drug/cyclodextrin complexes into liposomes

For the entrapment of drug/CD complexes into fluidosomes, 20 mg of DPPC/DMPG mixture (molar ratio of 18:1), 0.7 mM PPA148 and 0.7 mM RAMEB were used. The 1:1 PPA148/RAMEB complex was prepared as described above in 20 mM HEPES buffered saline, pH 7.2, and was used to hydrate the lipid film as described in section 3.3.1. Extrusion or sonication was applied for size reduction of liposomes (section 3.3.2) and the separation of the liposomes from the untrapped drug/CD was carried through size exclusion chromatography (section 3.3.5).

### 3.3.5 Size Exclusion Chromatography

A Sephadex™ G-25 PD-10 column (GE Healthcare, UK) (packed bed dimensions of 1.45 x 5 cm and particle size range 85-260 µm) was equilibrated with 15 mL (3 washes of 5mL) of 20 mM HEPES buffered saline, pH 7.2. The flow through the column was driven by gravity. Each liposome mixture (1 mL) was allowed to penetrate the gel entirely and the eluted volume was

discarded. Then, aliquots of HEPES buffered saline (1 mL) were added to the column sequentially (8 times) to elute various fractions which were collected separately. Each fraction was characterized for its hydrodynamic diameter, derived count rate, lipid and drug concentration so as to investigate which aliquot contained the majority of the loaded liposomes. Zeta ( $\zeta$ )-potential was used to measure the electrokinetic potential properties of liposomes.

### 3.3.6 Photon Correlation Spectroscopy (PCS)

PCS, also known as Dynamic Light Scattering (DLS), was used to investigate the presence of particles dispersed in a liquid medium and to determine their average hydrodynamic diameter, zeta-potential and derived count rate. This method measures the scattering of light coming from the Brownian motion of the suspended particles. The particles' movement is related to the particle size, which can be measured using the Stokes–Einstein relationship as follows:

$$d_H = \frac{kT}{3\pi\eta D} \quad \text{Equation 3.1}$$

where  $d_H$  is the hydrodynamic diameter,  $k$  is the Boltzman's constant,  $T$  is the absolute temperature,  $\eta$  is the solvent viscosity and  $D$  is Brownian motion diffusion coefficient.

The sample was placed into a disposable semi-micro dynamic light scattering cuvettes (VWR International, UK) and the size and derived count rate was measured by a Malvern Zetasizer (Nano-ZS, Malvern Instruments, UK) at 25 °C with a laser wavelength of 623.8 nm, backscatter detection angle of 173°, viscosity of dispersant of 0.889 cP (water) and refractive index 1.590. Placing detectors at 173° enables scattered light signals of low intensity originating from smaller particles to be revealed and excludes excess scattered light (187).

The Malvern Zetasizer (Nano-ZS, Malvern Instruments, UK) was also used for measuring the  $\zeta$ -potential by electrophoretic light scattering spectroscopy. It provides information on the electrokinetic charge of Fluidosomes and the effect of PBS, pH 7.4 (40 mM NaH<sub>2</sub>PO<sub>4</sub> and 30 mM NaCl) on their stability. A folded disposable capillary cell (Malvern Panalytical, UK) was used to measure the voltage signal at 25 °C with the dielectric constant set at 78.5. The dispersant refractive index and viscosity were set as per the light scattering experiments. The equilibration time for both size and zeta-potential measurements was 120 sec and the appropriate attenuator position was automatically determined by the Nano software. All measurements were carried out in triplicate.

### 3.3.7 Stewart assay

The determination of lipid concentration in the final formulation was achieved using the colorimetric Stewart assay (188). This assay is based on the fact that DPPC forms a complex with a reagent comprising of ferric chloride hexahydrate (0.17 M) and ammonium thiocyanate

(0.4 M) in DI water. The ferrothiocyanate reagent is insoluble in chloroform unless it forms a complex with DPPC.

A calibration curve was established from standard DPPC solutions in chloroform. All standard samples were prepared by vigorously mixing the aqueous solution (2mL) containing the reagent and the chloroform (2mL) containing increasing concentration of lipids (0-0.05 mg/mL). In order to ensure the full partition of the complex into the organic phase, the mixture was vigorously mixed and then centrifuged (Allegra™ X-12 centrifuge, Beckman Coulter, UK) for 10 min at 1000 rpm to separate the two phases. The lower layer (organic phase) was collected and its absorbance measured at 467 nm. A linear relationship was observed between the absorbance and the DPPC concentration in the complex and used as a calibration curve.

For the test samples, the suspension before separation and the 8 eluted aliquots from the PD10 column were used to determine the lipid content in the starting and purified liposomes to detect any material loss during the process. The samples were lyophilized in an Alpha 1-2 LDplus freeze dryer (Martin Christ Gefriertrocknungsanlagen GmbH, Germany), connected with a Chemistry hybrid RC 6 pump (Vaccubrand GMBH, Germany) and then re-suspended in chloroform. A volume of 2 mL was transferred in chloroform (2 mL) which was added into the reagent solution to form the biphasic system. All tubes were vortexed as the standard samples and the DPPC concentration of the test tubes was interpolated from the calibration curve. All measurements were carried out in triplicate.

### 3.3.8 Drug quantification

Drug quantification was carried out using UV/Vis spectroscopy to determine the encapsulation efficiency (EE) and the drug loading (DL) of liposomes. Measurements of the LOD and LOQ were reported in Chapter 2, section 2.3.7. The UV spectrum of PPA148 was recorded on a Lamda 2 spectrophotometer (Perkin Elmer, UK), at 25°C using a 1 cm pathlength quartz cuvette (Hellma 114-QS). The spectra were recorded within the wavelength range 200-550 nm, with spectral slit width of 2 nm and scan speed of 60 nm/min. PPA148 was extracted from all 8 aliquots collected from the size exclusion chromatography used to purify the formulation. Each aliquot was washed with DCM 5 times and the organic phase was collected, dried with magnesium sulfate ( $MgSO_4$ ) and evaporated using a rotary evaporator (Rotavapor® R11, Büchi®, Switzerland) attached to a vacuum pump (KNF Lab, UK). The resulting dry sample was re-suspended in ethanol:water (80:20) and the unknown drug concentration was calculated by interpolating from a linear calibration curve, which was determined under the same experimental conditions. The area under the curve (AUC) of all samples was used for drug quantification and calculated using GraphPad Prism 7.03 software (GraphPad software Inc., USA). The number of test and calibration curve sample measurements was 4 and 3, respectively. The Encapsulation Efficiency (EE) and Drug Loading (DL) were calculated using the following the equations,



$$EE (\%) = \frac{C_T - C_u}{C_T} \times 100\% \quad \text{Equation 3.2}$$

$$DL (\%) = \frac{C_T - C_u}{C_L + C_T - C_u} \times 100\% \quad \text{Equation 3.3}$$

, where  $C_u$  is the un-entrapped drug concentration,  $C_L$  and  $C_T$  are the concentration of lipids and drug added into the liposome system, respectively.

### 3.3.9 Kirby Bauer assay

The Kirby Bauer method, also known as the disk diffusion assay, is used for testing the resistance or susceptibility of bacteria to drugs and chemicals (184,185). It is a well-established assay by the World Health Organization (WHO) and widely accepted by many clinical laboratories. *Escherichia coli* (*E. coli*) was cultured in a Mueller-Hinton (MH) agar (21 g/L MH broth and 17 g/L agar) plate from a gel-bead for 24 h at 37 °C. A few bacterial colonies were taken with a loop from the cultured disk, placed in MH broth and shaken while incubating for 24 h at 37°C. The growth of the bacterial culture was monitored by measuring the optical density (OD) of the bacterial suspension at 600 nm using a single beam JENWAY 6300 Visible Spectrophotometer (Staffordshire, UK) with resolution of 1 nm and spectral bandwidth of 8 nm. An OD<sub>600</sub> of 1, which was achieved for this experiment, means that there are  $\sim 8 \times 10^8$  cells/mL in the suspension. To stop bacterial growth, 1 mL of the suspension was centrifuged at 10,000G for 5 min and the bacterial pellets were re-dispersed in sterile physiological saline (0.9% NaCl). An aliquot of this suspension (100  $\mu$ L) was swabbed on an MH agar plate, and filter disks impregnated with antibiotic were placed on top. The plates were incubated for 24 h at 37°C and the diameter of the inhibition zones was measured after incubation.

Commercially available disks for rifampicin (30  $\mu$ g) and vancomycin (30  $\mu$ g) were used as positive and negative controls based on their ability to inhibit bacterial growth. However, the filter disk for the novel antibiotic (PPA148 1  $\mu$ g) as well as for the complex and final formulation, were prepared in-house. All stock solutions (PPA148 5 mM in DCM, 1:1 complex (0.5 mg/mL) and encapsulated Fluidosomes (0.5 mg/ml) were sterilized using a UV lamp (Spectroline®, ENF-24C/FE, Spectronics corporation, Westbury, New York, USA) at 254 nm (ultraviolet germicidal irradiation). A volume equivalent to PPA148 1  $\mu$ g was placed on the plate, absorbed and evaporated under reduced pressure. Each disk can absorb a maximum of 10  $\mu$ L per deposition. Thus, for the complex- and liposome-impregnated disks the process had to be repeated 5 times because the stock solution/suspension was not concentrated enough. To validate the preparation method of the in-house disks, disks containing 30  $\mu$ g of rifampicin were prepared and the result was compared to that of the commercially available disk.

### 3.3.10 Dispersion stability of empty fluidosomes

Fluidosomes prepared with the probe sonicator were tested for their stability in terms of hydrodynamic size. Dynamic light scattering was measured using the experimental parameters described in section 3.3.6. The stability of the dispersion was investigated by measuring their size over a period of 60 days as a concentrated suspension (1 mg/mL) and diluted in PBS buffer, pH 7.4 (dilution factor of 2, 4, 8 and 16). The effect of adding HP $\beta$ CD (0.1, 1, 2.5 and 5%) on the size of the liposomes (1 mg/mL) was also examined. All samples were kept at 4°C between the measurement intervals and were measured in triplicates.

### 3.3.11 Statistical analysis

All error values were expressed as their mean  $\pm$  standard deviation (SD). Statistical analysis of the data was performed using GraphPad Prism 7. The non-parametric Mann-Whitney U-test was used to detect differences between the empty and loaded liposomes. Statistically significant differences were assumed when  $P \leq 0.05$ . For the disk diffusion assay, simulations of each data set were computed to tabulate 100 runs based on a Gaussian absolute scatter and the standard deviation of each experimental data set. The Brown-Forsythe variability test was conducted to ensure all sample group data was of acceptable distribution ( $P > 0.05$ ) before statistical significance between the groups was assessed by one-way analysis of variance (ANOVA) tests with post-hoc Tukey analysis for multiple comparison. Statistically significant differences were assumed when  $P \leq 0.05$  for the experimental analysis and the simulated observations. P-value style is based on GraphPad Prism 7 and the asterisks symbolize the significance as follows: 0.1244 (ns), 0.0332 (\*), 0.0021 (\*\*), 0.0002 (\*\*\*), <0.0001 (\*\*\*\*).

For the Kirby Bauer microbiological assay, Monte Carlo simulation was performed for the data sets because the number of observations was small, and any outlier could affect the final result. A number of 100 simulated observations were generated based on the mean and standard deviation of the experimental data set. These simulated data were used to perform one-way ANOVA analysis in addition to Tukey's test as described above, which give an estimation of the result if we had 100 experimental observations.

## 3.4 Results

### 3.4.1 Characterization of empty/control Fluidosomes

Liposomes consisting of DPPC/DMPG in a molar ratio of 18:1 were manufactured using the thin film hydration method. Size reduction was performed by either probe sonication of the lipid suspension or extrusion of iced/thawed lipid suspension through a polycarbonate membrane of 100 nm pore size. The lipid suspension was applied to a gravity column, washed 8 times and the eluted aliquots were collected. The column fractions were tested for the presence of liposomes

by measuring the derived count rate and the lipid content by the Stewart assay. The aliquot containing liposomes was further characterized for liposome size and zeta potential.

Dynamic light scattering was initially used to verify the presence of liposomes after the manufacturing and purification process. The derived count rate (DCR) represents the average intensity scattered and is directly related with the number of photons detected and, thus, the concentration and number of particles present in the eluted samples from the PD10 column suspension. The development of the Fluidosome preparation began in parallel with the synthesis and characterization of the drug, described in Chapter 2. During this period, small unilamellar vesicles (SUVs) were prepared by probe sonication and to test their stability over time and dilution. This method produced liposomes (1 mg/mL) with size of  $56.30 \pm 0.50$  nm and Pdl of  $0.21 \pm 0.01$  (Figure 3.2A). The size of the 1 mg/mL liposomes was also tested over time (Figure 3.2A). The shift of the intensity distribution towards higher hydrodynamic size reflects an increase in liposomal size of  $27.3 \pm 2.5\%$  during a period of 2 months (Figure 3.2A), which suggests some aggregation of the liposomes (189).

The effect of PBS on the stability of Fluidosomes was examined by diluting the initial lipid suspension up to 16 times from its original concentration (1 mg/mL). The size of all 4 diluted liposomal suspensions was measured and compared over time (Figure 3.2B). Between measurements, the samples were stored at 4 °C and the measurements were performed at 25 °C. The least concentrated suspension (0.0625 mg/ml) displayed a  $16.0 \pm 3.1\%$  and  $55.3 \pm 2.6\%$  increase 4 days and 2 months after fabrication, respectively (Figure 3.2B). The liposome size in the rest of the samples exceeded the original size by 10%, 11 days after preparation. Their overall size increase ranged between 19 and 29% 1 month after preparation (Figure 3.2B). The results on the stability of liposomes are in agreement with studies on DPPC liposomes at the same concentration (1 mg/mL) (191).

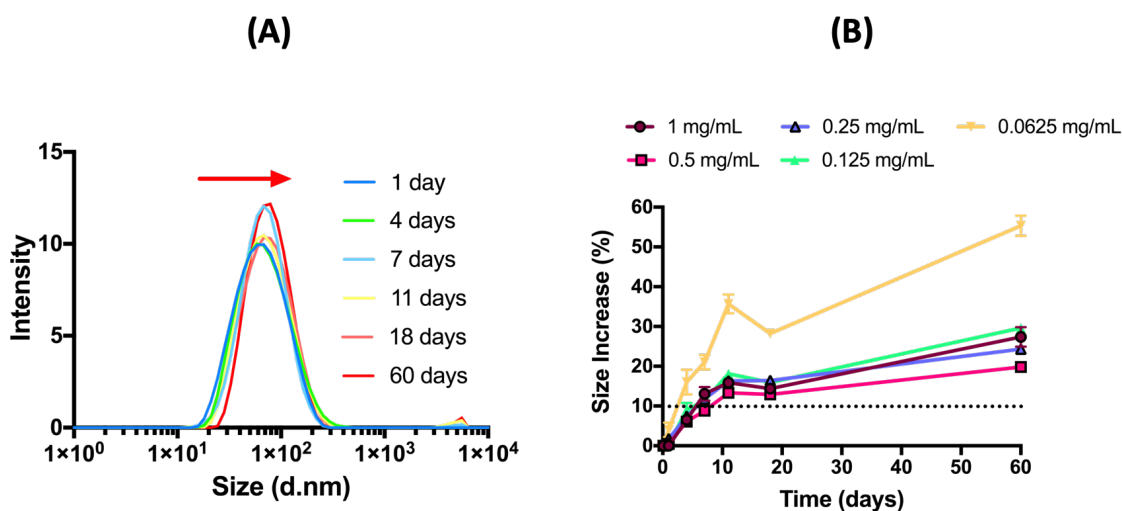


Figure 3.2: Empty Fluidosomes (SUVs, 1mg/mL) were manufactured with the thin film hydration method and probe sonication for size reduction. (A) Effect of liposome integrity in terms of size and intensity distribution profile of liposomes at a concentration of 1 mg/mL and temperature of 25 °C, measured by dynamic light scattering, over a period of 2 months. The samples were stored at 4 °C and tested between measurement intervals. All samples presented a polydispersity index of approximately  $0.2 \pm 0.01$ . (B) Effect of PBS buffer pH 7.4 on the size of a series diluted SUVs (1, 0.5, 0.25, 0.125 and 0.0625 mg/mL) over time.

Since the objective was to produce drug/CD inclusion complexes-in-liposomes, the stability of the fluidosomes in the presence and absence of cyclodextrin (HP $\beta$ CD) over time was also investigated. Liposomes, made in the presence of 0.1, 1, 2.5 and 5% w/w HP $\beta$ CD, produced particles with a size of  $67.70 \pm 0.40$ ,  $54.10 \pm 0.50$ ,  $56.50 \pm 0.50$  and  $53.00 \pm 0.10$  nm, respectively (Figure 3.3A). It is important to mention that liposomes were not purified, therefore, cyclodextrin was present both in the bulk and encapsulated in the liposomes. The addition of cyclodextrin did not affect the size of the original fluidosomes ( $56.30 \pm 0.50$  nm). It can be seen from Figure 3.3 that fluidosomes exhibited a higher stability when HP $\beta$ CD was present. The size increase did not exceed 5% of the initial size over the period of 2 weeks studied. However, the polydispersity index was high (approximately 0.30 for all samples), compared to empty fluidosomes ( $0.21 \pm 0.01$ ), and did not change by increasing the amount of cyclodextrin. Despite the narrowing of the size distribution by adding 5% HP $\beta$ CD, the polydispersity index remains high ( $0.26 \pm 0.01$ ). It is observed that the 0% HP $\beta$ CD in Figure 3.3A presented a broader and not a unimodal distribution compared to the equivalent 1mg/mL empty fluidosome sample in Figure 3.2A. The probe sonication as a size reduction method did not present reproducible liposomal size distribution.

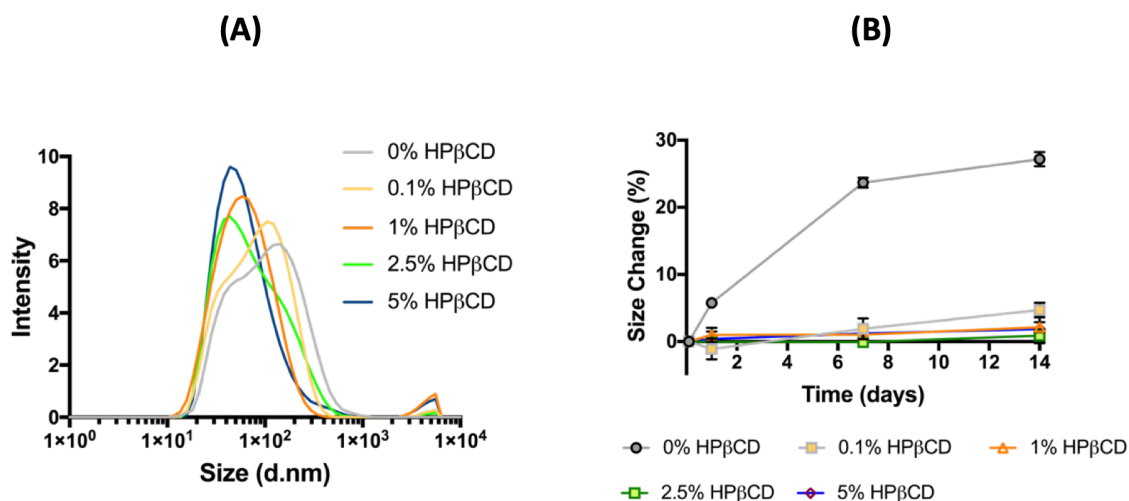


Figure 3.3: Fluidosome (1 mg/mL SUVs) encapsulated with a series of HP $\beta$ CD solutions in PBS buffer pH 7.4 (0.1, 1, 2.5 and 5% w/w) manufactured with thin film hydration method and probe sonication for size reduction. (A) Effect of HP $\beta$ CD on the size and polydispersity of Fluidosomes in terms of the intensity distribution profile of liposomes at 25 °C, measured by dynamic light scattering. All samples presented a polydispersity index of approximately  $0.3 \pm 0.01$ . (B) Comparison of size changes in the absence and presence of HP $\beta$ CD.

Despite the fact that SUV DPPC liposomes are inherently unstable compared to LUVs (190,191), the liposomal size distribution was not reproducible, the polydispersity index was often high and the frequent release of titanium particles into the lipid suspension from the probe-sonicator led us to a new approach for size reduction of liposomes with improved size distribution: the extrusion method, which uses polycarbonate membranes of 100 nm pore size, and produces liposomes with sizes of 100-130 nm (large uni-lamellar vesicles, LUVs). It is also expected that liposomes around 100 nm in diameter are optimum for drug delivery into bacterial cell membranes, since they can trap higher volumes, while preserving high surface tension required to fuse with bacterial membrane (192–195), a size double the one we obtained with probe sonication. The extrusion of liposomes was performed twice with an incubation time of 12 hours in between. After the first extrusion, the light scattering data showed a multimodal size distribution. This profile was transformed into a monomodal distribution as presented in Figure 3.4B and Table C 1 when the already extruded lipid suspension was extruded again after 12 hours. Liposomes of desired size (100 nm) were successfully formed and passed through the size exclusion column. The majority of the particles were eluted in the third fraction with a hydrodynamic size diameter of  $148 \pm 19$  nm and a polydispersity index of  $0.33 \pm 0.07$  (Figure 3.4B). Even though the polydispersity index remains high, the size distribution is narrower and uniform (Figure 3.4B) when compared to that resulting from probe sonication (Figure 3.2A).

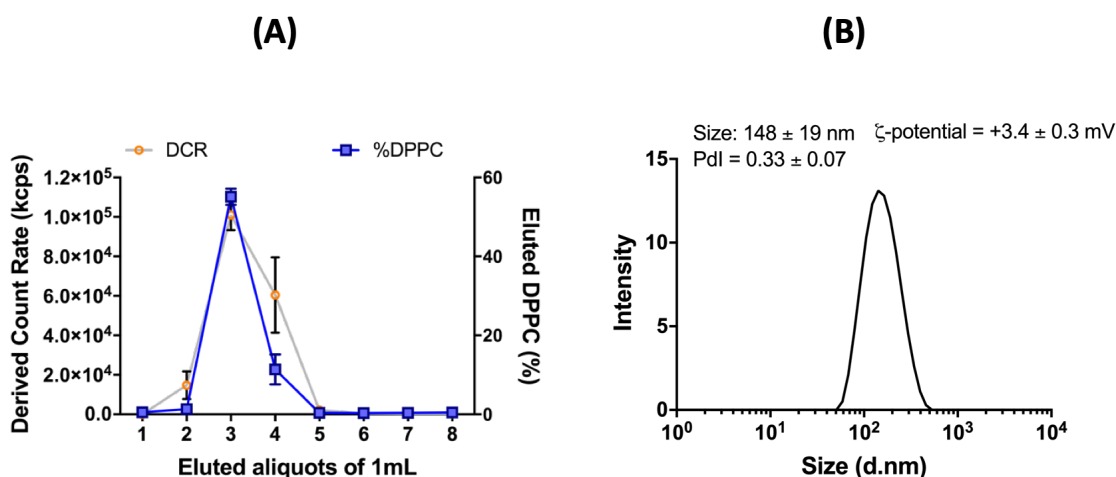


Figure 3.4: Method development for the separation of untrapped material from fluidosomes. Empty liposomes (2.5 mg/mL), prepared with thin film hydration method and extrusion through a 100 nm polycarbonate membrane for size reduction, were passed through a Sephadex PD10G25 size exclusion chromatography column, washed 8 times and the eluted volumes (8 fractions) were collected and analyzed. (A) Elution pattern of empty fluidosomes (2.5 mg/mL). The derived count rate profile and lipid content in each aliquot were measured to investigate the elution of liposomes. (B) Representative intensity distribution of empty fluidosomes in HEPES buffered saline at pH 7.2 (aliquot #3).

The Stewart assay was performed to determine the lipid concentration in each aliquot, which confirmed that liposomes were eluting in the third aliquot, as also shown from the DCR data (Figure 3.4A). In the third fraction,  $1.39 \pm 0.02$  mg/mL lipids were measured, which represents  $55 \pm 2\%$  of the initial lipid suspension concentration (2.5 mg/mL). Overall, there was a  $29.4 \pm 3.7\%$  loss of lipids due to the separation column because the initial lipid concentration agrees with the amount of lipids used to make liposomes.

### 3.4.2 Characterization of drug-CD inclusion complexes in the Fluidosomes

For the fabrication of fluidosomes encapsulated with the drug/CD complex, RAMEB was used because PPA148 showed a higher affinity towards this type of cyclodextrin (Chapter 2). From this point on, RAMEB was used for complex formation in the experiments. A 1:1 complex of PPA148/RAMEB was incorporated into the fluidosomes, and the elution profile of the loaded liposomes (Figure 3.5A) was the same to the one with the empty liposomes (Figure 3.4A, Table C 1). The majority of fluidosomes eluted in the third fraction were of a size of  $129 \pm 10$  nm, which was not significantly different from that of the empty liposomes ( $P = 0.14$ ). A low polydispersity index ( $0.14 \pm 0.03$ , compared to  $0.33 \pm 0.07$  for the empty liposomes) was observed, indicating that the encapsulated drug/cyclodextrin complex improved the monodispersity after the second extrusion. The guidelines for manufacturing liposomes given by AVANTI Polar Lipids additionally recommend to keeping the lipid suspension overnight (aging process) prior to downsizing because it improves the homogeneity of the size distribution (190).

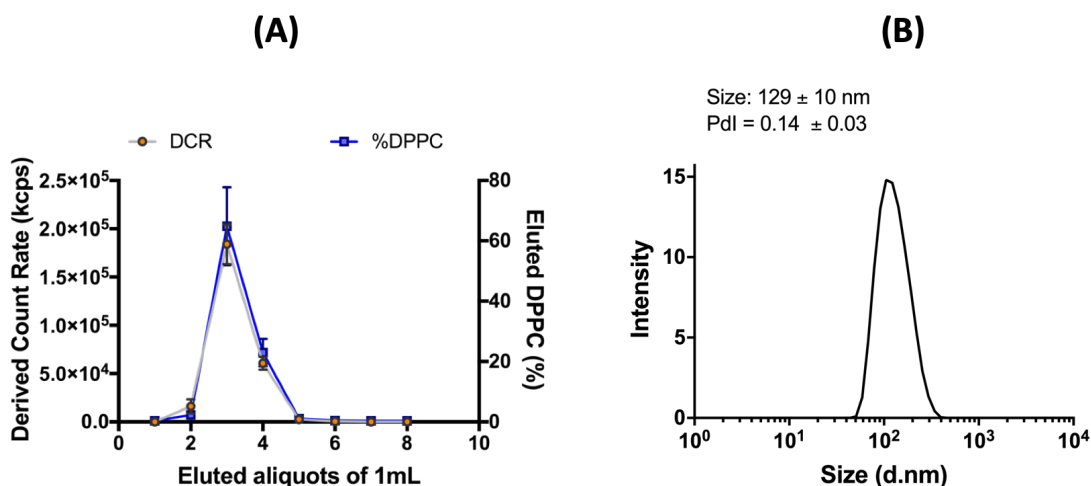


Figure 3.5: (A) Elution pattern of PPA148/RAMEB encapsulated fluidosomes (2.5 mg/mL). The derived count rate profile and lipid content in each aliquot were measured to investigate the elution profile of loaded liposomes. (B). Representative intensity distribution of drug/RAMEB encapsulated fluidosomes in HEPES buffered saline at pH 7.2 (aliquot #3).

The third fraction contained liposomes with  $\zeta$ -potential close to neutrality ( $+3.4 \pm 0.3$  mV), and held  $77 \pm 22\%$  of the initial lipid concentration (10 mg/mL), with an overall lipid loss of  $13 \pm 9\%$ , as assessed by the Stewart assay. Lipid loss due to the extrusion process was not observed (the amount of lipids in the liposomes before separation matches the starting lipid concentration for all batches tested).

### 3.4.3 Encapsulation Efficiency and Drug Loading

The eluted aliquots of the loaded fluidosomes were tested for their drug content. Each aliquot was lyophilized and re-suspended in EtOH/H<sub>2</sub>O (80/20), which was shown in Chapter 2 to be the best solubilizing solvent mixture for PPA148 (Figure 2.13). Their UV/Vis spectrum was recorded. The separation of free drug from the formulation was carried out using size exclusion chromatography as mentioned in section 3.3.5. The drug quantification profile of the eluting fraction is shown in Figure 3.6A. It was performed using the area under the curve (AUC) of the spectra ranging from 250-400 nm. This approach was chosen because the spectra of the extracted PPA148 did not present reproducible spectra in terms of peak shape and position. In Figure 3.6B, the UV spectrum of pure PPA148 in ethanol/water is compared to that of extracted PPA148 from aliquot 3, lyophilized and resuspended in ethanol/water. Pure PPA148 presents two peaks at 295 and 275 nm (Figure 3.6B). PPA148 from aliquot 3 produced either sharper peaks and a shift in  $\lambda_{\max}$ , or one obscure broad peak instead of two and a high baseline even after subtracting the solvent spectrum (Figure 3.6B). The hyperchromic shifted baseline at the red end of the spectrum probably reflects the presence of scattered light which may be a result of incomplete drug extraction leading to the presence of aggregated cyclodextrin and/or lipid particles. Any remaining lipid and CD in the test samples introduced a variety of artefacts and it

was difficult to quantify the drug based on  $\lambda_{\max}$ . In total, four batches were prepared and tested and three had the version 2 profile shown in Figure 3.6B.

The alternative method of the area under the absorbance-wavelength curve (AUC) was considered, as described by Zhang et al. (81). This approach was investigated by building a calibration curve and it was verified that the AUC is proportional to drug concentration (inset of Figure 3.6A) which provided a robust method for the drug quantification.

Based on the separation of the fluidosomes from the untrapped drug/CD, liposomes (empty and containing the drug/CD complex) eluted in the third fraction of the column. The highest drug content ( $280 \pm 120 \mu\text{g/mL}$ ) was found in the same fraction with encapsulation efficiency (EE) of  $67 \pm 11\%$  and drug loading (DL) of  $5 \pm 1\%$ , which were calculated based on Equating 3.2 and 3.3. The EE and DL values of the DPPC/DMPG liposomes employed in this work were consistent with those previously reported using different drugs but similar preparation methods (196,197). The total drug concentration ( $590 \pm 113 \mu\text{g/mL}$ ) obtained from the total eluted volume from the Sephadex column is in agreement – within experimental error - with the initial drug concentration ( $500 \mu\text{g/mL}$ ) which was used to hydrate the lipid film.

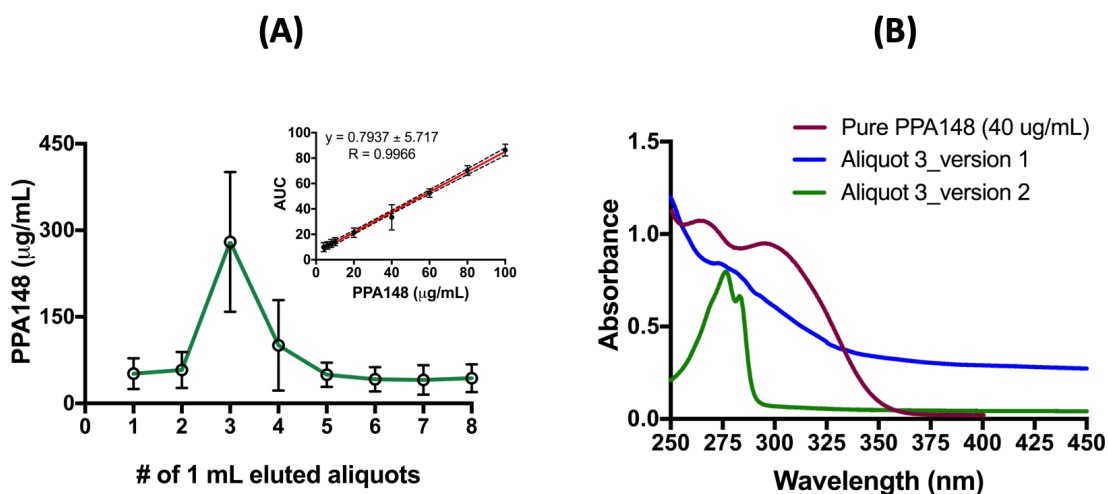


Figure 3.6: (A) Drug quantification profile of the eluted fraction from the PD10G25 size exclusion chromatography column with the inset being the calibration curve ( $y=0.7937x+5.717, R^2=0.9966$ ) is presented as a function of the area under the curve (AUC). (B) The UV spectra of pure and extracted drug in ethanol/water (80:20). Version 1 and 2 and the two UV spectra of extracted PPA148 from aliquot 3, which present changes in drug peak shape.

#### 3.4.4 Kirby Bauer assay

The efficacy of the encapsulated drug/RAMEB complex in liposomes was tested by using the disk diffusion assay. Commercially available disks of rifampicin and vancomycin were used as positive and negative controls against *E. coli* DH5a. Rifampicin causes inhibition of bacterial growth, while vancomycin does not affect the growth, resulting in the absence of an inhibition zone. Disks impregnated with PPA148 ( $1 \mu\text{g/mL}$ ), rifampicin ( $1$  and  $30 \mu\text{g/mL}$ ), RAMEB,



PPA148/RAMEB complex, empty fluidosomes, and encapsulated fluidosomes with PPA148/RAMEB were prepared in-house. In-house rifampicin disks (30 µg/mL) were compared with the commercially available disks of the same concentration to validate the preparation method (data not shown). Figure 3.7 presents the inhibition zone caused by the different systems studied. Rifampicin (30 µg) caused inhibition of bacterial growth, as expected, and was used as a positive control, while vancomycin (negative control) did not affect it.

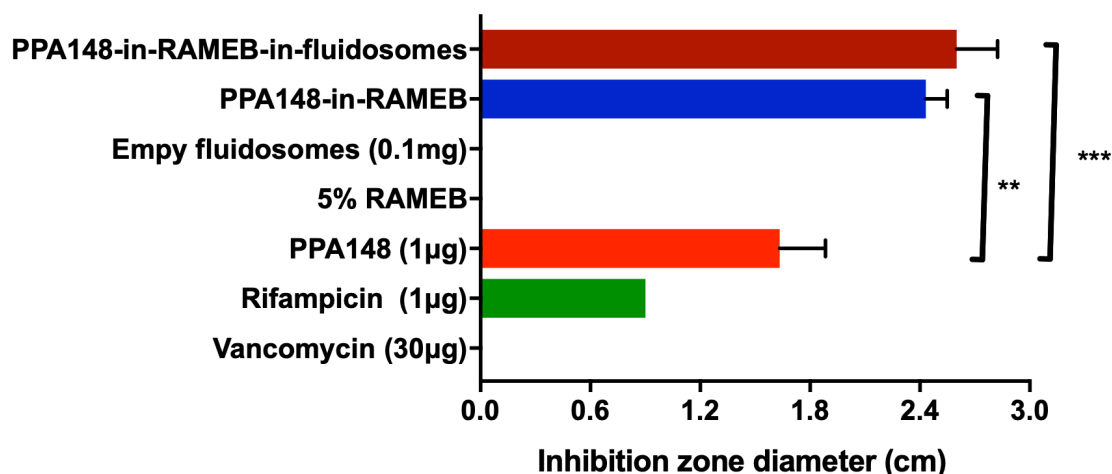


Figure 3.7: Kirby-Bauer assay for measuring the growth inhibition of *Escherichia coli* DH5 $\alpha$ . The inhibition zone diameter was measured for PPA148 as a pure substance and as a formulated drug (in a 5% RAMEB complex and incorporated into 0.1 mg fluidosomes as a complex with 5% RAMEB) after 24 hour incubation at 37 °C. Rifampicin and vancomycin were used as positive and negative control samples. The asterisks denote the level of significance going from lower to higher (as follows) and four asterisks indicate the highest level: 0.1244 (ns), 0.0332 (\*), 0.0021 (\*\*), 0.0002 (\*\*\*), <0.0001 (\*\*\*\*). All samples were tested in triplicate apart from the final formulation (PPA148-in-RAMEB-in-fluidosomes) which was tested 5 times.

One-way ANOVA test showed that, overall, the groups were statistically different ( $P=0.0007$ ) at 90% confidence interval. The multiple comparison showed a clear picture within each group. There was a statistically significant difference between the free drug, RAMEB/PPA148 complex ( $P=0.0041$ ) and PPA148-in-RAMEB-in-liposomes ( $P=0.0006$ ). However, the difference between the means of the drug/CD complex alone and those encapsulated within liposomes was not statistically significant ( $P=0.5483$ ,) (Figure 3.8A). Tukey's test compares the means of all groups to the mean of every other group and is considered the best available method when confidence intervals are desired or if sample sizes are unequal (Figure 3.8B). The interval of PPA148-in-CD and PPA148-in-CD-in-liposome contains the number zero which indicates that the means of those groups is likely to be the same (Figure 3.8A). The residuals denote the difference of each observation of the mean (Figure 3.8B). They are evenly distributed, indicating a good and reliable set of data.

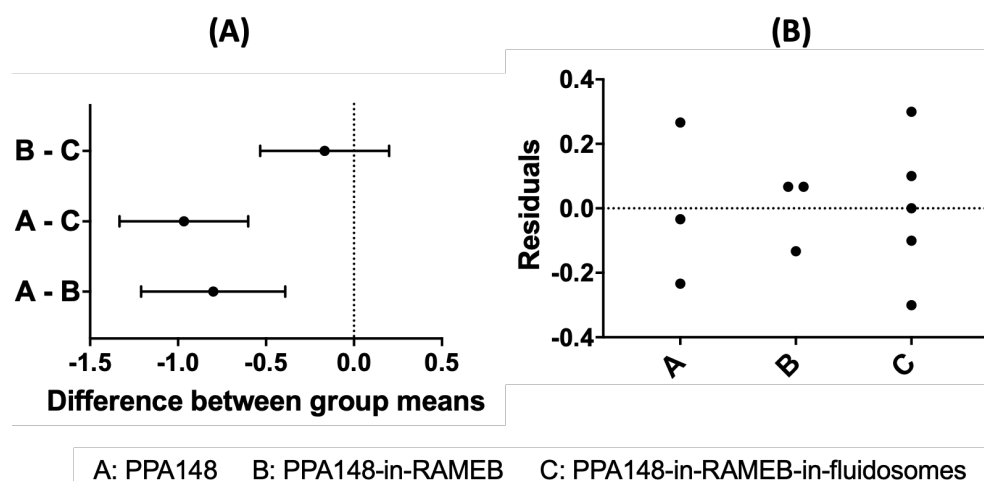


Figure 3.8: Tukey's test of experimental data ( $n=3,5$ ) with confidence interval of 95%. (A) Zero is included in the interval of PPA148-in-CD and PPA148-in-CD-in-liposome which indicates that their mean is not statistically significant. Residuals distribution of experimental observations for each group (B).

However, the number of observations is too small ( $n = 3$  or  $5$ ) and any outliers may affect the result. Therefore, Monte Carlo simulations were conducted. A large number of observations (100) was generated for each group based on the experimental mean and standard deviation. The data sets generated were then used to perform one-way ANOVA analysis and Tukey's test. The simulation resulted in a statistical difference among all sets with a confidence interval of 95% (Figure 3.9A). The P-values for drug vs PPA148-in-RAMEB, PPA148 vs PPA148-in-RAMEB-in-fluidosomes and PPA148-in-RAMEB vs PPA148-in-RAMEB-in-fluidosomes were  $<0.0001$ ,  $<0.0001$  and  $0.0002$  respectively. This model predicts that more replicates should give a statistical difference between the intermediate (complex) and final (drug-in-CD-in-liposome) formulation, too.

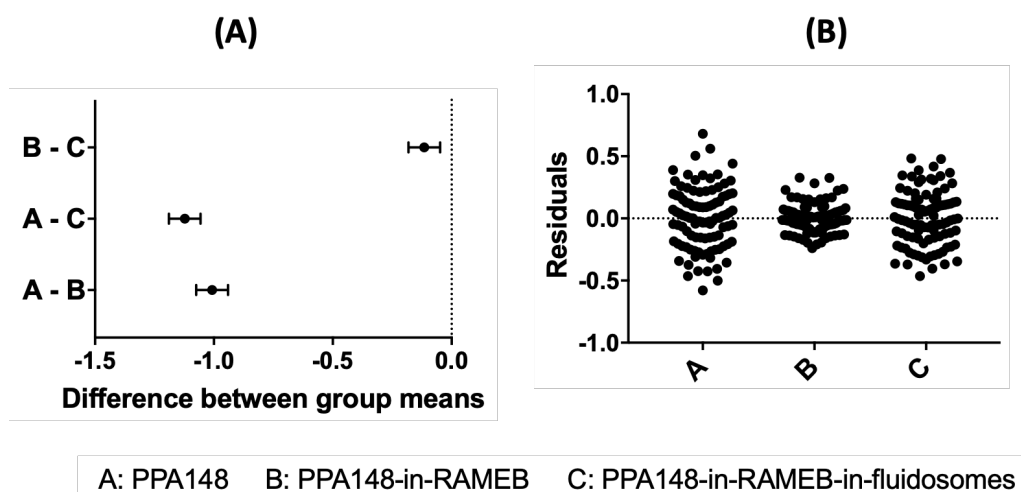


Figure 3.9: Monte-Carlo simulation was carried out based on the standard deviation of the experimental data. 100 observations were generated by the simulation and one-way ANOVA and Tukey's test was carried out with 95% confidence interval (A). All sets of groups have statistical difference. Residual distributions of simulated data (B).

In summary, PPA148 inhibited bacterial growth, as expected from the MIC results (107). Both formulations developed, either simply as an inclusion complex with RAMEB or the same complex in liposomes (DPPC/DMPG, 18:1), which increased the efficacy of this novel agent.

### 3.5 Discussion

In this chapter, PPA148 was formulated with cyclodextrins and a liposome mixture (DPPC/DMPG) to enhance its efficacy against Gram negative bacteria. The rationale behind this formulation is that cyclodextrins (RAMEB and HP $\beta$ CD) enhance drug aqueous solubility, as shown in Chapter 2, and potentially enhance transport through the IM, while the liposome is the drug carrier which will provide an improvement in drug transport through the OM, thus increasing drug efficacy. Fluidosomes were successfully manufactured using the thin film hydration method, followed by either probe sonication or extrusion for size distribution. The probe sonication produced small unilamellar vesicles, because their size is less than 100 nm ( $56.30 \pm 0.50$  nm) and presented low polydispersity index ( $0.21 \pm 0.01$ ) in PBS. A stability study of the SUVs, in terms of size, showed that the hydrodynamic diameter of the liposomes underwent an increase in size over a two-month time period, with the highest increase being 50% for the most diluted sample (0.0625 mg/mL) (Figure 3.2). Due to their small size, i.e. high degree of lipid curvature, DPPC small unilamellar vesicles are inherently unstable and are expected to spontaneously fuse to form larger vesicles when stored below their phase transition temperature because they are in their gel-like state (190), which would be the case for the fluidosomes because they were stored at 4°C in between the measurement intervals.

Apart from the curvature, liposomal stability is dependent on the presence of ions seeing that they affect the hydration state of lipids and, therefore, their packing. There are two hydration centers in phospholipids, namely, the phosphate and the carbonyl groups, which determine the intermolecular lipid interactions (129). Ions and water organization near the different groups esterified in the phosphate group (choline, ethanolamine or glycerol) affect the hydrophobic and repulsive forces between the lipid head-groups at the interface (198,199). Sodium (Na<sup>+</sup>) and potassium (K<sup>+</sup>) bind to the carbonyl groups of POPC, which become slightly more accessible to hydration (200) with the first having a stronger binding compared to the latter, due to their smaller size (201). Although Na<sup>+</sup> and K<sup>+</sup> (0.15 M) bind to the carbonyl group, they cause almost no effect on the POPC packing (202). In this study, small unilamellar DPPC/DMPG (18:1) liposomes were formed in PBS containing Na<sup>+</sup> at concentration of 0.2 M, which possibly did not provide size stability over time (Figure 3.2B).

When a series of HP $\beta$ CD solutions (1-5% w/w) were used to hydrate the lipid film, the hydrodynamic size diameter did not change and the stability of the liposomes was higher, as no significant change in size occurred over a period of two weeks (Figure 3.3). Native and synthetic cyclodextrins have been reported to interact with lipids and have indeed been used in pharmaceutical and food products to either stabilize or solubilize bioactive lipids (203). Generally,

cyclodextrins interact with phospholipids mainly through the inclusion of fatty acid chains into their cavity since the polar headgroup interaction with the CD cavity is limited and weak (203). Native CDs have been reported to form complexes of low solubility with phospholipids while their derivatives present a higher degree of interaction (203). RAMEB (45 mM) has been shown to solubilize phospholipids (181), while non-methylated CD derivatives and in particular HP $\beta$ CD do not increase the permeability of DPPC liposomes for concentrations up to 125 mM (17% w/w) (181,203–205). In this study, we found, from the evolution on size (Figure 3.3), that HP $\beta$ CD (up to 5%) stabilized the fluidosomes rather than solubilizing the lipids as also found by other groups (181). The interaction of both RAMEB and HP $\beta$ CD with lipid monolayers (DPPC/DPPG and POPC/POPG in molar ratio of 3:1) have been studied by surface pressure measurements in a Langmuir trough and are described in Chapter 4. Our results (Chapter 4) show a weak interaction between HP $\beta$ CD and the DPPC/DPPG monolayer, while RAMEB displays a stronger interaction (Figure 4.9).

The instability of SUVs, due to their small size, high curvature and choice of buffer, led us to explore an alternative approach to manufacturing large unilamellar vesicles (LUVs) using extrusion, to achieve sizes above 100 nm. LUVs display higher stability and retain the large encapsulation efficiency of SUV (115,190). LUVs of a hydrodynamic diameter of  $148 \pm 19$  nm and a polydispersity index of  $0.33 \pm 0.07$  (Figure 3.4A) were prepared in HEPES buffered saline containing 20 mM CaCl<sub>2</sub>. Ca<sup>2+</sup> were added into the saline (145 mM) because they tend to stabilize unilamellar lipid PC vesicles at a concentration range of 1-60 mM by forming Ca<sup>2+</sup> bridges between lipids (206). Ca<sup>2+</sup> ions at low concentration (1-5 mM) adsorb deeply into POPC and POPS bilayer (202) and they bind more strongly to the carbonyl, phosphate and carboxylate groups of both PC and PG, compared with Na<sup>+</sup> ions, causing partial dehydration, conformational change and immobilization of the phosphodiester groups (200,207). The influence of 1 mM CaCl<sub>2</sub> is comparable to the one obtained with 150 mM NaCl, which shows the different affinity of each ion to the lipid headgroup (202). The increased size of LUVs, along with the presence of Ca<sup>2+</sup>, creates a more stable environment for fluidosomes. The total ionic strength of HEPES buffered saline containing CaCl<sub>2</sub> was 211 mM which is of the same magnitude as PBS used in the SUV preparation. According to Lapinski et al. (208), if the ionic strength of the two buffers is the same, experimental data on bilayer lipid membranes formed by sonication (SUVs) can, in fact, be compared directly to data on bilayer systems formed by extrusion (LUVs). Based on that finding, the presence of HP $\beta$ CD could possibly stabilize LUVs as found in the case of SUVs (Figure 3.3B).

The LUVs were encapsulated with the PPA148/RAMEB complex and it was observed that the size of the encapsulated liposomes ( $129 \pm 10$  nm) was not statistically different from that of the empty liposomes ( $148 \pm 19$  nm). The stability of the loaded liposomes depends on the competitive binding of either the lipids or the drug (PPA148) to the CD cavity. This may happen because inclusion complexes in solution are in equilibrium with the free molecules (209) and have been

found to extract phospholipids and cholesterol from membranes by forming complexes (181). In Chapter 2 (Figure 2.17A), the affinity of PPA148 to RAMEB was calculated by measuring the binding constant using fluorescence spectroscopy. The binding constant of DPPC/RAMEB complexes has not been measured and no reference was found in the literature. Instead, the binding constant for a 1:1 cholesterol/DIMEB complex is characterized by a binding constant of  $102 \text{ M}^{-1}$  (210), which is similar to the binding constant of drug/RAMEB ( $102 \pm 26 \text{ M}^{-1}$ ) found in Chapter 2. As cholesterol has higher affinity towards cyclodextrin methyl-derivatives than DPPC, it can be speculated that DPPC undergoes weaker binding with RAMEB than PPA148. The presence of drug/CD complex improved the polydispersity index of the lipid suspension, indicating the formation of a more monodisperse system. RAMEB was used at low concentration (0.7 mM) as it is known to solubilize phospholipids above 10-15 mM membrane (181,182). Below this cut-off concentration, RAMEB retains the ability to facilitate lipid exchange without disturbing the membrane (181,182).

The next step was to separate the loaded liposomes from the untrapped material using size exclusion chromatography and characterize the system in terms of encapsulation efficiency and loading capacity. The separation method was first validated using unloaded empty fluidosomes to develop a robust eluting pattern of the fluidosomes. The lipids were eluted from the Sephadex column by 8 successive additions of HEPES buffered saline pH 7.2 after equilibrating the column with 15 mL of buffer. After the separation, an overall loss of lipids of  $29.4 \pm 3.7\%$  and  $13 \pm 9\%$  was observed for the empty and encapsulated liposomes, respectively. The third aliquot of the eluted empty fluidosomes contained  $55 \pm 2\%$  lipids of the initial amount used, as assessed by the Stewart assay (Figure 3.5). The rest (29% lipid loss) was probably retained in the column because lipid loss was not observed during the extrusion stage. When using the liposomes prepared in the presence of the drug/RAMEB complex, the loss of lipids after the separation process was lower, at only  $13 \pm 9\%$  (Figure 3.5). The loss of lipids may be a result of poor column condition before elution. It has been reported elsewhere (211) that pre-saturation of the column with empty liposomes helps to avoid material loss during size exclusion chromatography. The binding and release of liposomes on the dextran stationary phase of a Sephadex column is a dynamic equilibrium process between the free and entrapped liposomes. However, pre-saturation of the column can be problematic as it may contaminate the test sample. Further investigation needs to be done in order to clarify the cause of lipid loss during the size exclusion chromatography.

The high encapsulation efficiency of drug in the liposomes, assessed by the area under the absorbance-wavelength curve ( $67 \pm 11\%$ ) showed that the drug/RAMEB complex was successfully incorporated into the liposomes. Drug quantification was performed after extracting PPA148 from the carrier and cyclodextrin, by washing with DCM. The extracted PPA148 displayed a UV spectra with  $\lambda_{\text{max}}$  shifted compared to the pure drug in ethanol/water and change in the shape of the peak (Figure 3.6B). Based on these data and the findings in Chapter 2 of a

PPA148/RAMEB complex, it was assumed that the extracted PPA148 from the formulation was not pure or had undergone structural conformation changes, leading to an altered UV profile (Figure 3.6B). It is possible that the extraction was incomplete because of incomplete dissociation of the PPA148/RAMEB complexes, the presence of cyclodextrin dimers or even RAMEB/lipid complexes that had not been removed from the mixture. Yamamoto and coworkers investigated the dissociation of cholesterol/ $\beta$ CD complexes and cholesterol recovery was found to be 44% (212). They found that dissociated and undissociated cholesterol was present in the mixture, along with  $\beta$ CD dimers. The encapsulated fluidosomes with PPA148/RAMEB complexes is a very complex system and during the drug extraction several types of aggregates may have been formed, affecting the final drug absorbance. RAMEB may associate with lipid headgroups while being complexed with PPA148 as found with mono-(N-n-alkyl,N,N-dimethylamino)- $\beta$ -cyclodextrin, which can associate with the bilayer of DPPC:cholesterol (7:3) liposomes, while having the adamantoyl moiety of the adamantoylglucose molecule included into the cavity (213). Since the size of the encapsulated fluidosomes did not change and the encapsulation efficiency is high, possibly PPA148 may be inserted into the CD cavity from one side and RAMEB can be attached from the other side with the headgroups of the inner leaflet of the liposomes (Figure 3.10). Although there is no evidence concerning such an arrangement, it may explain the poor drug extraction because of the complexity and difficulty in separating the individual molecules.

The efficacy of PPA148-in-RAMEB-in-liposomes was assessed against live bacteria (*E. coli*, DH5 $\alpha$ ) (Figure 3.7). The disk diffusion assay revealed a statistically significant increase in the inhibition zone of the drug-CD complex on its own and when it is incorporated into liposomes. Due to the small number of observations (n=3-5) the difference between the PPA148/RAMEB complex and the encapsulated liposomes was not significant (Figure 3.8). Based on the fact that cyclodextrin enhance the antimicrobial activity of drugs (171) and the lack of significance between the PPA148/RAMEB complex and the encapsulated fluidosomes, Monte Carlo simulations were conducted in order to investigate this result further. A higher number of simulated observations (100) were generated based on the standard deviation of the experimental data sets and tested using one-way ANOVA. The results showed a statistical difference between the drug/RAMEB and the drug/RAMEB incorporated into liposomes (Figure 3.9). The increased efficacy of antibiotics by encapsulation into liposomes was first reported by Beaulac and co-workers in 1998 and later by Sachetelli et al. in 2000 (102,179). They showed that DPPC/DMPG (18:1) liposomes encapsulated with tobramycin showed a decrease in the bacterial counts in a sub-MIC concentration (102,179). Other reports regarding increased efficacy of antibiotics with fluidosomes and other types of liposomes have been published up to the present time (98). Interestingly, there have been publications regarding the increased efficacy of drugs in the form of cyclodextrin complex or encapsulated into liposomes (Table 1.3, Table 1.4) (90,214), but there is only one report about a drug-in-CD-in-liposomes formulation in the food industry (113), with nerolidol, a sesquiterpene with antibacterial activity and under investigation for its potential as a natural preservative in the food industry. In the next Chapter,

we use lipid monolayers representing the inner and outer bacterial membrane and a model Gram negative bacterial outer membrane to elucidate the mechanisms responsible for the increased activity of this novel antimicrobial agent by using interfacial techniques (Langmuir trough monolayer interaction studies and neutron reflectivity).

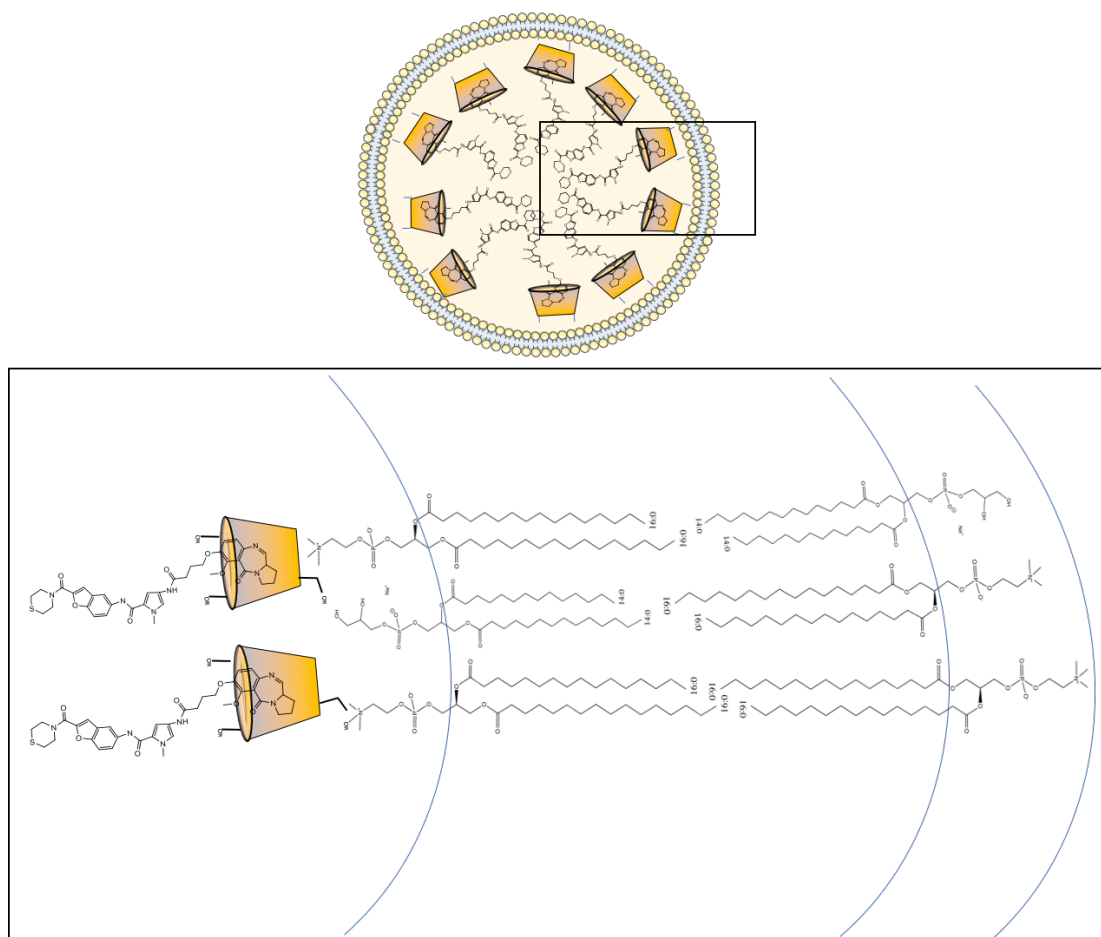


Figure 3.10: Schematic representation of the possible organization of PPA148/RAMEB complex incorporated into Fluidosomes. The electrophilic center of PPA148 is presented inside the CD cavity while the headgroup of DPPC is associated with the exterior hydrogens of the narrow side of RAMEB molecules.

### 3.6 Conclusion

Fluidosomes encapsulated with PPA148/RAMEB complex were successfully manufactured with a size of  $129 \pm 10$  nm, polydispersity index of  $0.14 \pm 0.03$  and high encapsulation efficiency ( $67 \pm 11\%$ ). The separation method of untrapped material from loaded liposomes was developed using empty liposomes. The final formulation was tested against *E. coli* DH5 $\alpha$  and presented a significant increase in drug efficacy. In the next chapter, PPA148 in its pure form and cyclodextrins (HP $\beta$ CD and RAMEB) are assessed over a series of lipid monolayers. The effect of fluidosomes on the outer membrane is tested on a model Gram negative bacterial membrane,

which was developed at the ISIS neutron source (Didcot, Oxfordshire) and neutron reflectivity is used to assess the interaction.



# Chapter 4 A biophysical investigation into the uptake mechanism of PPA148 and its delivery system

## 4.1 Introduction

The uptake of drugs and their delivery systems across the bacterial cell envelope is a complex process, which is difficult to elucidate because of its dynamic nature. The envelope of Gram negative bacteria possesses two membranes, acting as discrete permeability barriers which drugs and nutrients need to cross so as to enter the cytoplasm. The outer membrane (OM) of Gram negatives consists of an asymmetric lipopolysaccharide (LPS) and phospholipid bilayer spanned by porin proteins which play an important role in nutrient and drug uptake (Figure 1.2). The  $\beta$ -barrel porins are transmembrane proteins, which regulate the uptake of nutrients and hydrophilic compounds. The OM also provides protection against environmental stressors and inhibits the uptake of some antibiotics. The second permeability barrier, the inner membrane (IM), consists mostly of intrinsic proteins and phospholipids. The uptake of compounds by the bacterial cell is divided into passive and active processes. The former is characterized by either drug penetration through the lipids or transport through general or specific transporter proteins. The latter requires energy input for the transport of compounds through the proteins. The transmembrane proteins (porins), located in the OM, can act as both passive and active transporters for the influx of beneficial compounds and efflux of unwanted molecules, such as antibiotics. The nature of LPS and the presence of porins challenge the antibiotic uptake by Gram negative bacteria and there is a real need to find means of overcoming these drug permeability obstacles.

In Chapter 3, a drug-in cyclodextrin-in liposome formulation was evaluated, which showed an enhancement of PPA148's solubility and antimicrobial efficiency. The rationale behind this formulation is based on two factors: the results from the microbiological assay (Table B 1; Table B 2) of pure PPA148; and PPA148's physicochemical properties, in particular water solubility and lipophilicity, as calculated by ChemDraw software (Table 1.5). The results from the microbiological assays (minimum inhibitory concentration or MIC) in the presence and absence of the efflux pump inhibitor phenylalanine-arginine- $\beta$ -naphthylamide (PA $\beta$ N) (107,108) revealed difficulties in the transport through the cell envelope and a possible synergistic effect between PPA148 and PA $\beta$ N either by inhibiting the efflux pumps or by PA $\beta$ N's permeabilizing effect on both OM and IM (69). The MIC, in the absence of the pump inhibitor, was relatively high (2  $\mu$ g/mL against *A. baumannii*, 0.25-32  $\mu$ g/mL in *K. pneumoniae* and 16-128  $\mu$ g/mL in *P. aeruginosa*) but decreased dramatically in all bacterial strains tested in its presence (107). In this work, a liposomal carrier was used to overcome PPA148's uptake challenges. The microbiological assay described in Chapter 3 showed an enhanced inhibition of *E. coli* DH5 $\alpha$  bacteria when the drug/RAMEB complex was incorporated into liposomes (Figure 3.7; Figure 3.8; Figure 3.9). Fluidosomes were selected to enhance the transport of PPA148 through the OM because they have been found to fuse through bacterial membranes (179). It was, therefore, hypothesized that the fluidosomes would fuse into the OM while releasing their core content into the periplasmic space. Based on the lipophilicity of PPA148, it was also hypothesized that the novel drug might

partition into the IM in order to reach its site of action inside the cell. The low water solubility of PPA148 may lead to drug precipitation when entering the periplasm, leading to ineffective antimicrobial action. For this reason, RAMEB was successfully used as a solubilizing agent for PPA148 (Chapter 2), which is barely soluble in aqueous solvents as a pure substance. It has also been reported that  $\beta$ -cyclodextrins and their derivatives, such as RAMEB and HP $\beta$ CD, not only enhance water solubility of poorly soluble drugs but also increase their internalization into cells and improve their biological activity against Gram negative bacteria (90,91,94). RAMEB has been found to cause cell lysis and inhibit the growth of the Gram positive *Bacillus* strains (185). While the mechanism of bacterial growth inhibition by RAMEB has not been investigated, native  $\beta$ CD has been found to adhere to the peptidoglycan surface of Gram positive bacteria via hydrogen bonds (215) and to be transported with facilitated diffusion via specific channels (CymA) in the outer membrane of the Gram negative bacterium, *Klebsiella oxytoca* (31). In Gram negative bacteria, increased electrostatic interactions have been observed between the inclusion complex of chlorhexidine/native- $\beta$ CD and the LPS of *Aggregatibacter actinomycetemcomitans*, whose structure is similar to that of *E. coli* (216,217). Therefore, we hypothesized that cyclodextrin may also help the passive transport of PPA148 through the IM via the formation of phospholipid-cyclodextrin complex by releasing pure PPA148 inside the cytoplasm where the site of action (DNA minor groove) is located.

Based on the results from Chapters 2 and 3, this chapter investigates the mechanism of uptake of this novel antimicrobial agent and assesses the effectiveness of a drug-in-cyclodextrin-in-liposome formulation to increase OM and IM permeability. The investigation of the drug-membrane interactions and possible drug penetration was carried out by using interfacial techniques (Langmuir trough and neutron reflectivity) with both monolayer and bilayer model membranes. Passive diffusion can occur either via diffusion across the lipid bilayers for antibiotics with a high degree of lipophilicity and some degree of polarity or via the OM proteins, which can either be specific transporters or general water channels, for small hydrophilic compounds (218). Based on the possible fusion mechanism of fluidosomes, the cyclodextrin-phospholipid complex formation and the high lipophilicity of PPA148, simplified artificial membrane systems were used to mimic the lipidic component of the relevant biological membranes in order to examine the passive diffusion across lipid layers.

In the monolayer studies, lipids representing the outer leaflet of OM and IM of the Gram negative bacterial envelope were used to model the membranes. There are two types of LPS: rough and smooth, which differ by the presence or absence of O-antigen. Mutations into the bacterial genome produces LPS without or with truncated O-antigen which are called rough or semi-rough LPS chemotypes. Within the rough chemotypes, further modifications and mutations lead to the expression of LPS with shorter oligosaccharide, divided into Ra, Rb, Rc, Rd and Re subgroups, depending on the length of their core region (Figure 1.10). Ra LPS has the longest and Re LPS has the shortest core. In this study, the focus is on a Ra-EH100 and Rc-J5 LPS extracted from *E. coli* and Lipid A extracted from the Re-R595 *S. minnesota*. In addition, Rc LPS was used to

form stable planar monolayers because of its short headgroup. This type of LPS and Lipid A extracted from Re LPS were also used to test the influence of the OM steric barrier. The bilayer studies were conducted on a model asymmetric Gram negative bacterial membrane consisting of Ra LPS as the outer leaflet. Ra LPS is a substitute for LPS molecules containing O-antigen because smooth LPS is less hydrophobic than truncated LPS and, thus, Ra LPS does not form water soluble aggregates. It has been found that truncated rough LPS can be deposited as insoluble monolayers (219,220) while smooth LPS act as surfactants by forming micelles in solution (221). The more truncated rough mutant LPS was used to form more stable monolayers and compare the drug-membrane interaction in the presence (Rc LPS) and absence (Re Lipid A) of steric hindrance.

The phospholipids in the OM are zwitterionic and negatively charged and their distribution within the individual OM and IM is inhomogeneous (222). The predominant phospholipids are phosphatidylethanolamine (PE), phosphatidylglycerol (PG) and cardiolipin (CL), while some species, such as *P. aeruginosa*, can also produce phosphatidylcholine (PC) (223). It has been shown that PE and PG are mostly located in the inner and outer leaflet of the plasma membrane (IM) respectively, while CL is evenly distributed in both leaflets of IM (224). *E. coli* polar lipid extract has been extensively studied and its phospholipid composition has been found to be 67% PE, 23.2% PG and 8.9% CL (127). The anionic phospholipids (PG and CL) of the IM represent 18% of the total IM lipids, while they constitute only 9% of the OM lipids. The remaining phospholipid lipid fraction (>98%) in both the inner leaflet of the OM and the whole IM is PE (222).

The structural complexity of LPS and the small size of bacteria make it difficult to obtain detailed molecular information on the interactions between drug molecules and the OM and IM (225). However, biophysical studies of isolated phospholipid and LPS monolayers and bilayers provide an insight into these interactions.

In this work, monolayers composed of the phospholipids or rough mutant LPS were deposited at the air/liquid interface and examined in the presence of PPA148 and cyclodextrin using a Langmuir trough. These experiments provided useful insights into the molecular interactions of the drug on the membranes, either at the level of the polar region when they are in contact with the outer leaflet of the OM or IM of the cell envelope, or at the level of the hydrophobic domain of the lipid bilayer in which they can be partitioned and inserted.

To complement these monolayer studies, a model Gram negative bacterial asymmetric membrane consisting of Ra LPS and DPPC as the outer and inner leaflet of the OM was used to examine the interaction between the liposomal carrier and the OM. This model membrane has been extensively studied and validated by a group of scientists working in collaboration with the Science and Technology Facilities Council (STFS), Rutherford Appleton laboratory in Chilton, UK (225–227). Neutron reflectivity (NR) was used to characterize the structural changes in this

model membrane when put in contact with the formulation. In particular, NR can give information on the relative location of fluidosomes within and at the interface of a supported asymmetric model OM, thus giving clues on the mode of interaction, namely either fusion into the OM or a possible partitioning into the membrane's hydrophobic core and diffusion across the membrane.

## 4.2 Materials

**Lipids:** The phospholipids 1,2-dipalmitoyl-sn-glycero-3-phosphocholine (DPPC, 16:0 PC), 1,2-dimyristoyl-sn-glycero-3-phosphoglycerol, sodium salt (DMPG, 14:0 PG), *E. coli* polar lipid extract (*E. coli* B), 1-palmitoyl-2-oleoyl-sn-glycero-3-phosphocholine (POPC, 16:0-18:1 PC) and 1-palmitoyl-2-oleoyl-sn-glycero-3-phospho-(1'-rac-glycerol) (sodium salt) (POPG, 16:0-18:1 PC) powders were manufactured by Avanti Polar Lipids (Alabama, USA) and supplied by Stratech Scientific (Newmarket, UK). Rc LPS from *E. coli* J5 (purity: protein 1.4%, nucleic acid 0.340%, phosphate 7.3%, Kdo 5.9%), Ra LPS from *E. coli* EH100 and Re Lipid A from *S. minnesota* R595 containing containing  $\leq 0.3\%$  proteins was obtained from Sigma-Aldrich, UK. and were used without further purification.

**Cyclodextrins:** Hydroxy-propyl-beta-cyclodextrin (HP $\beta$ CD) and randomly methylated cyclodextrin (RAMEB) were purchased from Sigma-Aldrich, UK.

**Chemicals and material used in the microbiological assay:** Blank, rifampicin (30 ug) and vancomycin (30 ug) susceptibility disks, agar powder and Muller Hinton broth for microbiology were purchased from Oxoid (UK).

**Solvents:** Dichloromethane (DCM) and chloroform (CHCl<sub>3</sub>) were purchased from Sigma-Aldrich, UK. LC/MS grade water was supplied by Merck, UK. The ultrapure water at 18.2 M $\Omega$  cm was produced by a Purelab Ultra machine from ELGA Process Water (Marlow, UK).

**Salts used for buffer preparation:** Sodium chloride (NaCl), magnesium chloride (MgCl<sub>2</sub>), monosodium phosphate (NaH<sub>2</sub>PO<sub>4</sub>), sodium hydroxide (NaOH) and HEPES ( $\geq 99.5\%$ ) were purchased from Sigma-Aldrich, UK.

**Devices and tubes:** Disposable semi-micro dynamic light scattering cuvettes (volume capacity of 1.5 mL) purchased from VWR International, UK. Silicon crystal (50 \* 80 \* 20 mm) polished with silicon oxide and a customized cell made of PTFE was kindly provided by the ISIS facility (Chilton, UK).

## 4.3 Methods

### 4.3.1 Surface Pressure-Area isotherms at the air-liquid interface

Pressure-area measurements were carried out at a constant temperature of 23°C on a Nima 602A Langmuir trough (Nima Technologies Ltd., Coventry, UK) equipped with a Nima PS4

surface pressure microbalance (0-240 mN/m range, 0.1 mN/m resolution) controlled by a PC via a Nima IU4 computer interface unit. The microbalance was calibrated with a 10 mg standard weight and the area enclosed by the barriers was also calibrated. Prior to use, the PTFE surface of the trough was thoroughly cleaned with ethanol and chloroform in order to remove any impurities. A clean Wilhelmy plate (chromatographic paper roll, Whatman Grade 1, 10 mm width, GE Healthcare life sciences UK, Little Chalfont, UK) was attached to the microbalance, suspended and partially submerged in the subphase (0.9% w/v NaCl or 1 mM MgCl<sub>2</sub>). The subphase surface was examined for dust and contaminants prior to commencing the experiment by repeated compression of the barriers and suction of the surface using a vacuum pump. The subphase was considered clean when, upon compression, the change in surface pressure did not exceed 0.2 mN/m.

Solutions of DPPC/DPPG and POPC/POPG mixtures (in a molar ratio of 3/1), Lipid A from *S. minnesota* (R595 Lipid A) and LPS J5 from *E. coli* (Rc J5 LPS) were prepared in pure chloroform at a total lipid or LPS concentration of 2 mg/mL. To form air/liquid interface monolayers, 30-70  $\mu$ L of lipid solution were deposited dropwise on the subphase surface using a Hamilton syringe (Hamilton Co. Europe, Bonaduz, Switzerland), with the barriers open at their maximum. Before compressing the barriers at a constant rate of 35 cm<sup>2</sup>/min, 10 min were allowed for the solvent to evaporate. During the compression, changes in the surface pressure were recorded until the monolayer reached its collapse point. Each sample was run in triplicate. The molecular area for each monolayer was determined at the pressure of 30 mN/m and compared for their changes in molecular size. In addition, the compressibility modulus ( $E^s$  or  $C_s^{-1}$ ), which is the reciprocal of the area compression modulus of the monolayer ( $C_s$ ) (228), was calculated using the following formula:

$$E_s = \frac{1}{C_s} = -A \times \frac{\Delta\pi}{\Delta A} \quad \text{Equation 4.1}$$

, where  $A$  is the area per molecule and  $\Delta\pi/\Delta A$  is the slope of the isotherm at a defined surface pressure (229). The compressibility modulus ( $C_s^{-1}$ ) of phospholipid and glycolipid monolayers was calculated at 30 mN/m, which is considered as the approximate lateral pressure of a lipid bilayer (130). The compressibility modulus is an indication of the packing elasticity of the lipid monolayer and the equilibrium among the lipids. In the liquid expanded film, the compressibility modulus ranges between 12.5 and 50 mN/m and in for the liquid intermediate takes values below 100 mN/m (228). The liquid condensed phase is characterised by a compressibility modulus of 100-250 mN/m while the condensed state, which is described as closely packed lipids in the equilibrium state, is denoted by values above 250 mN/m (230).

#### 4.3.2 Drug - monolayer interaction

A variation of the adsorption isotherm method (Chapter 2, section 2.3.6) was adopted to investigate the interaction of drugs and the lipid monolayer. The set-up of the reduced area

custom-made Teflon® petri dish was as described in the adsorption studies in Chapter 2 (section 2.3.6). On the clean subphase surface (0.9% NaCl or 1 mM MgCl<sub>2</sub>) a lipid solution (total lipid mixture) was spread dropwise until the surface pressure reached 30-35 mN/m, while stirring the subphase with a 4.5×15 mm magnetic stirrer bar. A period of time (40-60 min) was allowed for the solvent to evaporate and for the monolayer to reach equilibrium (stabilization of the surface pressure). Thereafter, the drug solution in DMSO was injected below the surface using a small disposable plastic syringe with a hypodermic needle (BD biosciences UK, Oxford, UK). The following drug concentrations were used in the trough: 2, 20, 40 and 60 µg/mL when it was tested with DPPC:DPPG (3:1) monolayer; and 20 µg/mL when it was tested with Rc J5 LPS and Re 595 Lipid A. HPβCD and RAMEB were tested against DPPC/DPPG (3/1), DOPC/POPG (3/1) and Re 595 Lipid A monolayers while fluidosomes were tested at 0.1 mg/mL against J5 LPS only. The changes in surface pressure were recorded at constant slow stirring of the subphase, with the magnet speed set at its minimum to avoid a variation of pressure greater than 0.2 mN/m.

The difference in surface pressure change was plotted against time and the binding isotherms produced were fitted with a sigmoidal model, specifically a Hill plot with 3 parameters as it is displayed in GraphPad, Prism to obtain the kinetic parameters as follows:

$$y = \frac{\Delta\pi_{max}x^h}{t_{50\%}^h + x^h} \quad \text{Equation 4.2}$$

,where  $\Delta\pi_{max}$  is the maximum difference in surface pressure,  $h$  is the hill slope, and  $t_{50\%}$  is the time needed to achieve half  $\Delta\pi_{max}$ .

### 4.3.3 Drug - lipid bilayer interaction using fluorescence spectroscopy

#### 4.3.3.1 Preparation of *E. coli* B liposomes encapsulating 5(6)-carboxyfluorescein

Liposomes were prepared by the thin film hydration method. A sample of *E. coli* B lipid extract (10 mg) was dissolved in chloroform. The solution was placed in a vacuum desiccator overnight to let the organic solvent evaporate, resulting in the formation of a dry lipid film. The dried film was then hydrated with 2.5 mL of 40 mM 5(6)-carboxyfluorescein (CF) solution (pH = 7.4) at 30 °C. The mixture was vortexed (Cyclone-Vortex mixer CM-1, Nickel-Electro Ltd) for 60 sec at 2800 rpm, sonicated (Soniprep 150 Plus ultrasonic disintegrator 120V 60Hz, London, UK) for 5 min with an exponential microprobe and amplitude 10 microns and left at room temperature for one hour prior to further use.

The separation of the liposomes from the untrapped dye was carried out using size exclusion chromatography. A Sephadex™ G-25 PD-10 column (GE Healthcare, UK) (packed bed dimensions of 1.45 × 5 cm and particle size range 85-260 µm) was equilibrated with 15 mL (3 washes of 5 mL) of 70 mM sodium chloride. The liposome mixture (1 mL) was then eluted through the column and washed with 1 mL of sodium chloride 5 times. The eluted fractions were collected separately. The fourth fraction contained the liposomes and was used for the CF-release study.

A sodium chloride solution of 70 mM (135 mOsm) was used to match the osmolality of the entrapped CF solution (129 mOsm measured with the advanced MICRO-OSMOMETER, Vitech Scientific Ltd, West Sussex, UK) which should not differ significantly from that of the sodium chloride solution outside of the liposomes (234).

#### 4.3.3.2 5(6)-carboxyfluorescein (CF) release profile

Fluorescence spectroscopy was used to evaluate the ability of chlorhexidine digluconate (CHD) and PP-A148 to disrupt the bilayers of vesicles composed of E. coli lipids. In each experiment 50  $\mu$ L of CF-loaded liposomes were added to 2350  $\mu$ L of NaCl (70 mM) in a cuvette (10  $\times$  10 mm) and the fluorescence intensity was measured using a Varian Cary Eclipse fluorimeter (Agilent, USA) at 25 °C. Antimicrobial solutions (3.15 mM) were added (0.1 ml) after 60 s and the fluorescence intensity of the mixture was again measured at an excitation/emission wavelength of 490/510 nm and a slit width of 2.5 nm for both processes. The fluorescence was monitored at hourly intervals, and at the end of the experiment the total concentration of CF was determined after lysing the liposomes with 100  $\mu$ L of Triton X-100 (10 w/v%). CF-liposomes in sodium chloride (70 mM) were also monitored hourly, to determine their integrity. The data was normalized against controls designed to compensate for the effects of dye photobleaching over the duration of the experiment. The percentage dye release was calculated using the following formula:

$$CF\% = \frac{F_t - F_0}{F_T - F_0} \times 100, \text{ for } t \in [0, T] \quad \text{Equation 4.3}$$

, where  $F_t$  is the fluorescence intensity of each sample at time  $t$ ,  $F_0$  is the fluorescence intensity prior to the addition of the drug (liposomes in NaCl) of each time point, and  $F_T$  is the intensity of each sample after the addition of Triton X-100, which corresponds to 100% dye release.

#### 4.3.4 Neutron reflectivity of asymmetric bilayer of DPPC and LPS and interaction with fluidosomes

##### 4.3.4.1 Asymmetric bilayer deposition

The lipid components of model Gram negative bacterial membranes were deposited on a piranha-cleaned ( $\text{SiO}_2$ ) surface of single silicon crystals (50 $\times$ 80 $\times$ 20 mm), using a Langmuir-Blodgett (LB) trough (KSV-NIMA, Biolin Scientific, Finland) (Figure 4.1). The LB technique was used to deposit the inner leaflet of the membrane ( $d_{62}$ DPPC) on the 50 $\times$ 80 mm polished surface of the crystal, and the Langmuir-Schaefer (LS) deposition used for the outer leaflet of the membrane (Ra LPS) (Figure 4.1). Three isotherm cycles were conducted prior to deposition to examine the stability of the monolayers. For the LB deposition, the silicon block was submerged into the ultrapure non-buffered water subphase (containing 5 mM  $\text{CaCl}_2$ ), cooled to 10°C. A solution of  $d_{62}$ DPPC in chloroform was deposited dropwise (50  $\mu$ L of 2.5 mg/mL) on the subphase surface and compressed slowly to a constant surface pressure of 38 mN/m. The block was lifted



through the air-water interface at a speed of 4 mm/min at a constant surface pressure at 38 mN/m. The LB trough was then cleaned and the air-liquid interfacial monolayer of Ra LPS (2.5 mg/mL) was deposited (from 60% chloroform, 39% methanol and 1% water v/v) on to the same clean non-buffered interface, cooled at 10°C, with a surface pressure of 38 mN/m. The LS deposition was achieved by placing the silicon block covered with a homogeneous d-DPPC monolayer (with the headgroup to the silicon block and the hydrophobic tails facing the environment) to a holder above the water surface with the alcy chains pointed downward, toward the interface. The surface of the crystal was made parallel with the interface by adjusting the angle of the crystal using a built-in automatic levelling device. The silicon block was lowered at a speed of 3 mm/min through the interface in order to allow the lipid monolayer on the block to match the LPS monolayer on the subphase via the hydrophobic chains, producing a bilayer. The block was then allowed to continue moving downwards until the bottom of the trough was reached where a customised PTFE sample cell was placed. The sample cell and silicon block were placed in a custom-made metal holder to ensure the bilayer was fully contained and sealed inside the small water chamber of the sample cell, whose total volume was 3 mL.

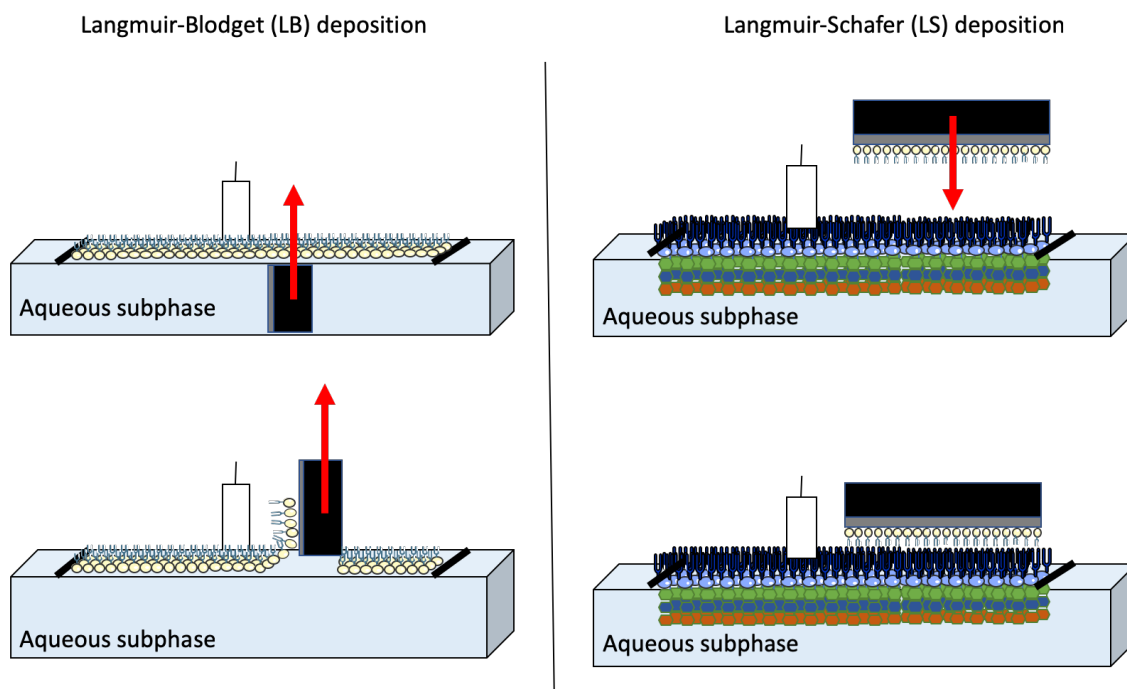


Figure 4.1: Langmuir-Blodgett and Langmuir-Schafer deposition on a silicon crystal to manufacture the assymmetric model outer membrane of Gram negative bacteria.

#### 4.3.4.2 Neutron reflectometry measurements and data analysis

Specular neutron reflectometry (NR) measurements were carried out using the INTER reflectometer at the ISIS neutron source, Rutherford Appleton Laboratory (Oxfordshire, UK), using neutron wavelengths from 1 to 16 Å. The reflected intensity was measured at two incident angles of 0.7° and 2.3° as a function of the momentum transfer  $Q$  ( $Q = \frac{4\pi \sin \theta}{\lambda}$ , where  $\lambda$  is the

wavelength and  $\theta$  is the incident angle). The purpose-built flow cells of the silicon-liquid interface were placed on an anti-vibration sample stage and the inlet of the cell was connected to a L7100 HPLC pump (Merck, Hitachi, Germany). The pump allowed the easy exchange of the isotopic contrast solutions within the cell (3 mL) at a flow rate of 1.5 mL/min. The membrane was measured at a temperature of 25°C and then at 38°C but the challenge with liposomes was measured only at 38°C. Temperature was kept constant throughout the experiment by using a circulating water bath. Empty fluidosomes were manufactured following the thin film hydration method as described in Chapter 3 (section 3.3.1). Lipid film was re-dispersed using ultrapure water and fluidosomes (0.1 mg/mL) were injected into the sample cell and allowed to equilibrate for 1 h. The excess fluidosomes were flushed out of the cell chamber before data acquisition so as to measure the possible changes caused by their interaction with the model OM.

Each sample was examined under three different isotopic contrast conditions, i.e. 100% H<sub>2</sub>O, 100% D<sub>2</sub>O and silicon matched water or SMW (38% D<sub>2</sub>O, 62% H<sub>2</sub>O), all containing CaCl<sub>2</sub>, to highlight the different components of the bilayer structure.

#### 4.3.4.3 NR data and Statistical analysis

The three contrasts produced three reflectivity profiles which were simultaneously fitted using models describing the interfacial structure based on Adele's, and Born and Wolf's matrix formalism using the RaScal software (231,232). In this approach, the interface is described as a series of slabs and the software fits a layered model to the structure by calculating common parameters, i.e. scattering length density (SLD), thickness, roughness and hydration state of each layer.

Table 4.1: Summary of scattering length densities of the lipid components studied, and the solution subphases.

Lipid/Solvent	Neutron Scattering Length Density (SLD)/( $\times 10^{-6} \text{ \AA}^{-2}$ )
Silicon	2.07
Silicon Oxide	3.41
DPPC headgroup	1.98
d-DPPC tails	7.45
Ra-LPS headgroup (core oligosaccharide)/D <sub>2</sub> O	4.28
Ra-LPS headgroup (core oligosaccharide)/H <sub>2</sub> O	2.01

For the model membrane consisting of chain-deuterated d62DPPC and hydrogenous rough Ra-LPS (*E. coli*, EH100), the calculated scattering length density (Table 4.1) and the fitted parameters were used to examine the asymmetry of the bilayer. The lipid coverage in each leaflet was calculated from the volume fraction of bilayer defects across the surface by calculating the water volume fraction and the deuterated PC tail fraction (225). The water volume fraction can

be determined by the difference in SLD of the DPPC and LPS tails in the three solvent contrasts. In the tail region, both lipid tails do not possess labile hydrogens and, therefore, do not undergo changes in SLD ( $\rho$ ). The mathematical model uses the following formulas to calculate the water volume fraction from the raw data, and the parameter is called "Tail-hydration".

$$\rho_{fitted} = \rho_{DPPC}\varphi_{DPPC} + \rho_{LPS}\varphi_{LPS} + \rho_{H2O}\varphi_{H2O} \quad \text{Equation 4.4}$$

$$\varphi_{H2O} = \frac{\rho_{inner\ tail\ contrast\ 1} - \rho_{inner\ tail\ contrast\ 2}}{\rho_{contrast\ 1} - \rho_{contrast\ 2}} \quad \text{Equation 4.5}$$

where  $\rho_{fitted}$  is the fitted SLD value of the bilayer,  $\rho_{DPPC}$ ,  $\rho_{LPS}$ ,  $\rho_{H2O}$  are the calculated SLD of the deuterated DPPC tails, hydrogenous LPS tails and water, respectively,  $\varphi_{DPPC}$ ,  $\varphi_{LPS}$  and  $\varphi_{H2O}$  are the volume fractions,  $\rho_{inner\ tail\ contrast\ 1}$ ,  $\rho_{inner\ tail\ contrast\ 2}$ ,  $\rho_{contrast}$  and are the experimental SLD values of the inner tails in two contrast solutions (for example H<sub>2</sub>O and D<sub>2</sub>O) and the experimental SLD of the two chosen contrast solvents. Based on Equation 4.4 and Equation 4.5, the volume fraction of deuterated DPPC tails was calculated using the following formula:

$$\varphi_{DPPC\ tails} = \frac{\rho - \rho_{H2O}\varphi_{H2O} - \rho_{LPS\ tails}(1 - \varphi_{H2O})}{\rho_{dDPPC} - \rho_{LPS\ tails}} \quad \text{Equation 4.6}$$

, where  $\rho$  is the fitted SLD,  $\rho_{H2O}$ ,  $\rho_{dDPPC}$  and  $\rho_{LPS\ tails}$  is the SLD of the water, DPPC and LPS are the experimental values. The PC-tail volume fraction  $\varphi_{DPPC\ tails}$  was calculated before taking into account the hydration of the bilayer tail region, which is a separate fitted parameter of the mathematical model. Therefore, the volume fraction of the LPS tails  $\varphi_{LPS\ tails}$  was reduced by the following formula:

$$\varphi_{LPS\ tails} = 1 - (\varphi_{DPPC\ tails} + \varphi_{H2O}) \quad \text{Equation 4.7}$$

All three samples (RT, 38°C before and after liposome introduction) shared the same silicon substrate because the same model membrane was measured in different conditions. The models were fitted to the data using a Bayesian Markov Chain Monte Carlo (MCMC) algorithm (227,233). In addition to the model parameters, the backgrounds, scale factors and instrument resolutions were also fitted. A Bayesian approach was followed for the fitting, with prior probability distribution (priors) chosen according to already known information prior to the analysis, posteriors obtained using a Delayed Rejection (DR) algorithm and the best fit parameters taken as the distribution maxima. DR is a way of modifying the standard Metropolis-Hastings (MH) algorithm to improve the efficiency of the resulting MCMC estimators and decrease the asymptotic variance (234). The idea is that upon rejection in an MH algorithm, instead of advancing the run time and retaining the same position, a second stage is proposed with improved distribution. This process can be iterated for a fixed or a random number of stages, and higher stage proposals depend on the proposed and rejected fits. The error analysis was run at 95% confidence intervals for each distribution.

## 4.4 Results

### 4.4.1 Surface Pressure-Area isotherms of Langmuir monolayers at the air-liquid interface

Pressure-area isotherms were used to determine the physical state and mechanical properties of the *E. coli* polar lipid extract, DPPC/DPPG [3/1], POPC/POPG [3/1], Rc LPS J5, Ra LPS EH100 and Lipid A monolayers. *E. coli* B lipid extract and both PC/PG monolayers were used to mimic the Gram negative IM. Rc J5 LPS J5 and R595 Lipid A, both of which were used to model the outer leaflet of the OM. The average molecular weight of each mixture was used to plot the surface pressure-area isotherms (Figure 4.2) which showed the phase transitions of each monolayer during compression. Changes in the slope and shape of the curves during compression resulted from changes in the orientation, packing and arrangement of phospholipids at the interface.

#### 4.4.1.1 Inner membrane model monolayers

All pressure-area isotherms in (Figure 4.2A, C, E) are representative curves chosen from triplicate measurements for each lipid monolayer. The isotherm obtained from pure DPPC monolayers (Figure 4.2C) nearly reached the solid state because the slope was almost perpendicular to the y-axis (235,236), whereas from *E. coli* B, POPC, POPG and POPC:POPG (3:1) (Figure 4.2A, E) displayed typical expanded monolayers.

DPPC (hydrogenous and deuterated) and DPPC/DPPG undergo an L1/L2 transition, marked by a plateau (or pseudo plateau) in the isotherm and a corresponding minimum in the compression modulus plot (Figure 4.2C and D). The transition began at approximately 4 mN/m for h-DPPC and the mixture (237,238), while for d-DPPC it started at 9mN/m (239). The DPPC/DPPG monolayer reached its liquid condensed phase just below 20 mN/m with a maximum  $E_s$  of 197 mN/m. For POPC/POPG, the transition to liquid condensed state was initiated around 25 mN/m, making it less compressible than the DPPC/DPPG monolayer (Figure 4.2E, F). The *E. coli* B display areas of liquid-expanded phases before turning into the coexistence of L1/L2 phase at surface areas of ~ 15 mN/m, and remained until the collapse of the monolayer (Figure 4.2A, B).

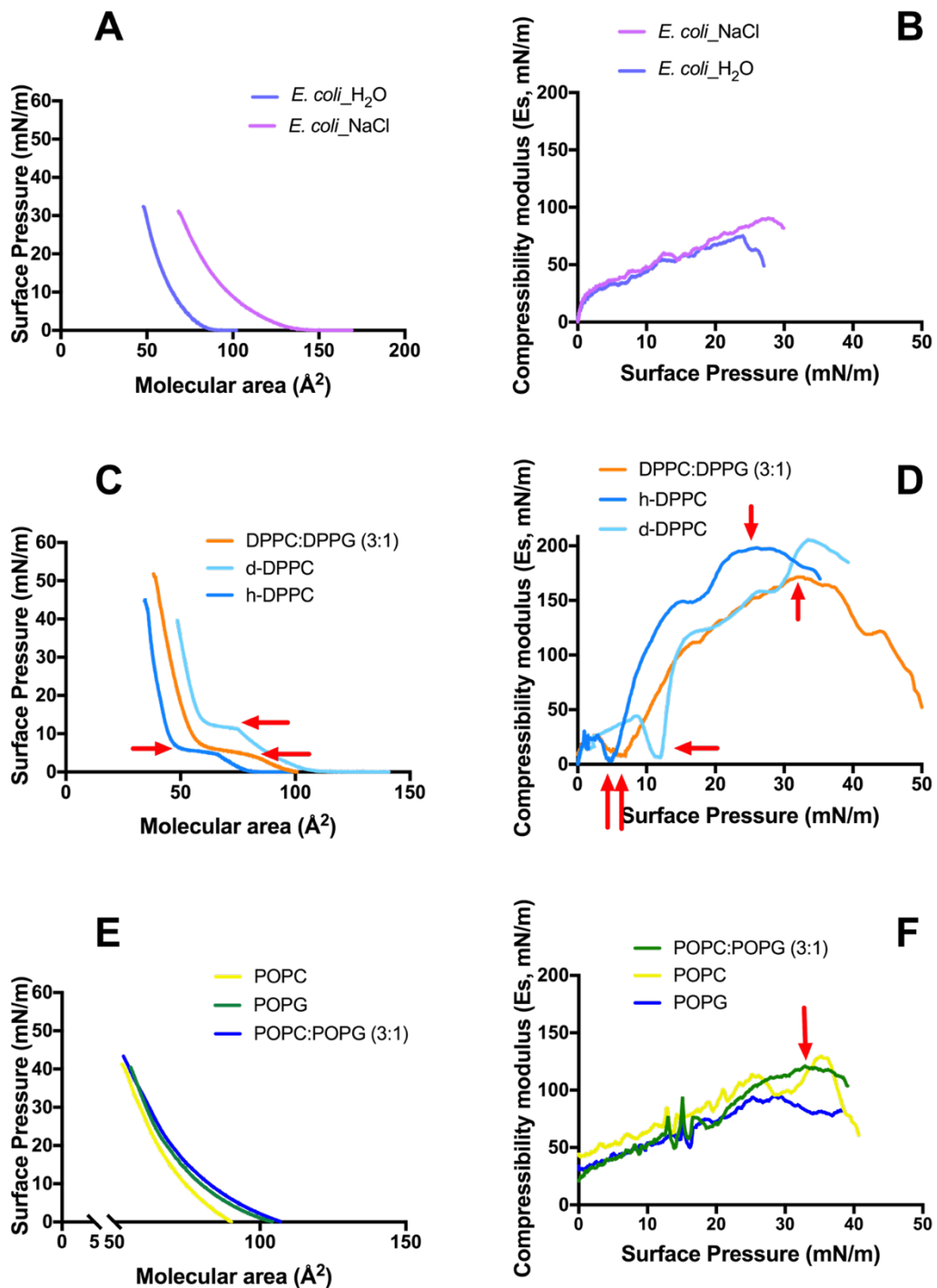


Figure 4.2: A, C and E present the Surface Pressure-Area (P-A) isotherms generated at 23 °C for a series of pure or mixtures of phospholipids (*E. coli* extract, DPPC, DPPG, POPC, POPG). All phospholipids were suspended in chloroform apart from d62DPPC which was prepared in chloroform:methanol:water (6:4:1) before deposition. The subphase used was 1mM MgCl<sub>2</sub> for all monolayers apart from d<sub>62</sub>DPPC which was 5 mM CaCl<sub>2</sub>. The *E. coli* B monolayer was deposited either on ultra pure water or 0.9% NaCl. The subphase for hydrogenous DPPC/DPPG and POPC/POP mixtures monolayers was MgCl<sub>2</sub>. *E. coli* isotherm was measured on ultra pure water and isotonic saline. The red arrows show the L1/L2 and the L2/S transition of the lipids where applicable. B, D and F show the calculated compressibility modulus derived from P-A isotherms at 23 °C. The red arrows show transition phases of the lipids which are more pronounced than in the P-A isotherm.

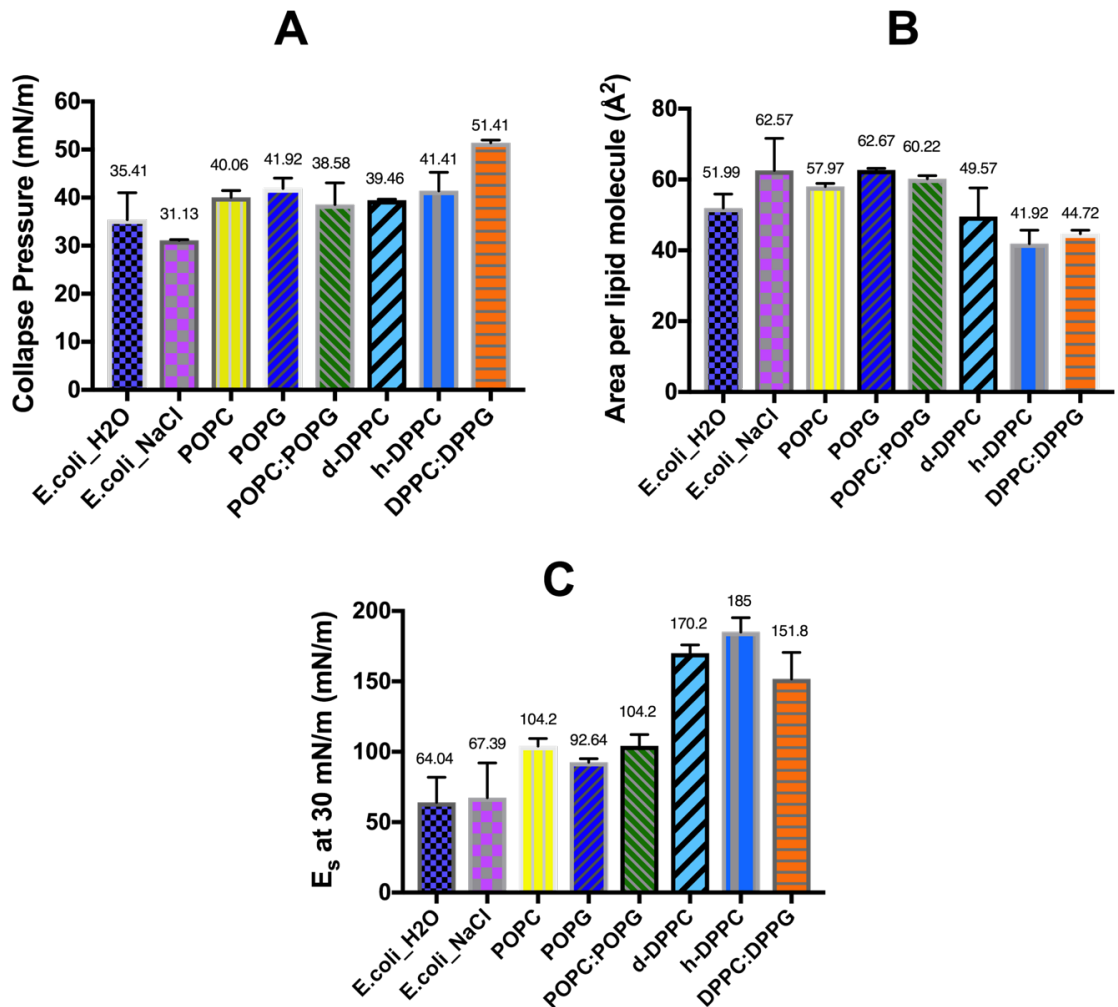


Figure 4.3: Collapse surface pressure (A), area per molecule (B) and compressibility modulus (C) at 30 mN/m of all the phospholipid lipid monolayers

Figure 4.3B presents the area per molecule at 30 mN/m, which is the equivalent lateral pressure of the bacterial inner membrane (130), and the collapse pressure of each lipid monolayer (3 Figure 4.3C). E. coli B present an average area per molecule of  $52.0 \pm 4.0 \text{ \AA}^2$  in water and  $62.6 \pm 9.1 \text{ \AA}^2$  in the presence of 0.9% NaCl, which was not statistically different from that in water at a confidence interval of 95% ( $P=0.6$ ). The collapse pressure of the monolayer is very low considering that 30 mN/m is the equivalent pressure of a bacterial membrane ( $35.4 \pm 5.6$  and  $31.1 \pm 0.1 \text{ mN/m}$  in water and saline respectively) (130). This monolayer caused overflow at the edges of the trough, probably due to the PE shape and orientation.

The structural difference between POPC (C16:0-18:1) and DPPC (16:0) affects their packing and orientation. The average molecular area of POPC, POPG was  $58.0 \pm 0.9 \text{ \AA}^2$  and  $62.7 \pm 0.5 \text{ \AA}^2$ , respectively, with slightly higher collapse pressure (Figure 4.3A). The average area per molecule (A) of an ideal mixture was calculated by the additivity relationship considering the molar fraction X of each component (244):

$$A = X_1A_1 + X_2A_2 \quad \text{Equation 4.8}$$

Based on this rule within a mixed monolayer and the experimental values of the single components (POPC and POPG), the resultant area per molecule would be  $59 \text{ \AA}^2$ , which is in agreement with the experimental value ( $60.2 \pm 0.9 \text{ \AA}^2$ ), assuming an ideal mixing of lipids. DPPC based monolayers (h- and d-) exhibited similar area per molecule (approximately  $40 \text{ \AA}^2$ ) at  $30 \text{ mN/m}$ . Based on the experimental molecular area of h-DPPC from this experiment and that of DPPG published in the literature ( $40 \text{ \AA}^2$ ) (240), the mixed monolayer should have an average molecular area of  $42 \text{ \AA}^2$ , which is in favorable agreement with the experimental value ( $44.72 \text{ \AA}^2$ ). The mixture DPPC:DPPG display high collapse pressure at  $51.4 \pm 0.5 \text{ mN/m}$ , while h-DPPC collapses at  $41.4 \pm 3.9 \text{ mN/m}$ , both of which lie within the normal collapse pressure range (235,241).

#### 4.4.1.2 Outer membrane model monolayers

The initial suspension of Rc J5 LPS, Ra EH100 LPS and R595 Lipid A were used to model the outer membrane under the same experimental procedure. Rc-LPS J5 and Ra EH100 LPS presented a typical expanded isotherm because their compressibility modulus did not exceed  $50 \text{ mN/m}$  with increasing surface pressure (Figure 4.4). Two plateaus (or pseudo-plateaus) were observed for Rc J5 LPS at a surface pressure of approximately  $4$  and  $25 \text{ mN/m}$ , which reflect changes in the lipid packing, while remaining in the L1 phase (Figure 4.4). Re Lipid A from R595 showed a coexistence of L1 and L2 at around  $15 \text{ mN/m}$ , which changed into a more ordered and tightly bound state upon further compression (242–244). A sudden drop in the surface compressibility modulus profile indicates the collapse of the monolayers, which is pronounced for Lipid A (Figure 4.4B).

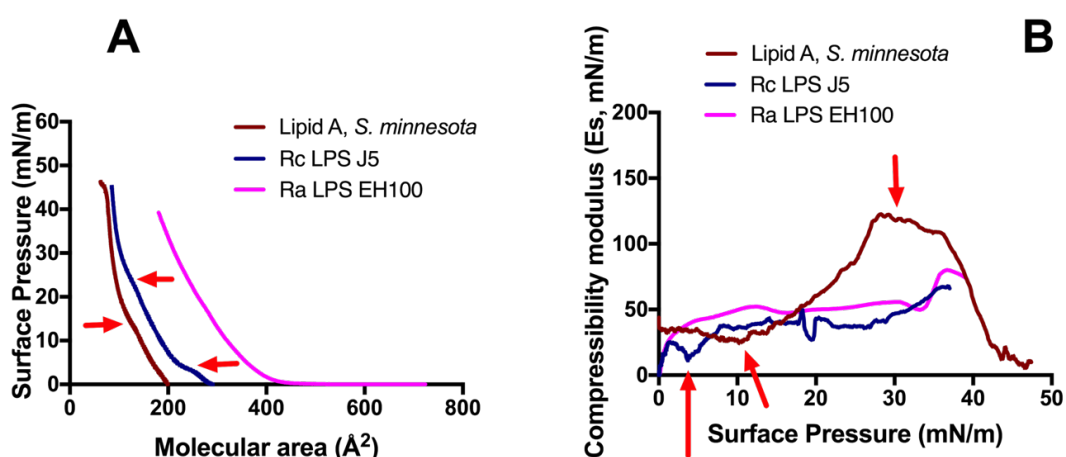


Figure 4.4: (A) Surface Pressure-Area (P-A) isotherms generated at  $23 \text{ }^\circ\text{C}$  for a series of glycolipids: Ra EH100 LPS, Rc J5 LPS and Lipid A. The subphase for Rc-LPS and Lipid A monolayers was  $\text{MgCl}_2$  while  $\text{CaCl}_2$  was used for Ra-LPS. The red arrows show the L1/L2 and the L2/S transition of the lipids where applicable. (B) Compressibility modulus derived from P-A isotherms at  $23 \text{ }^\circ\text{C}$ . The red arrows show transition phases of the lipids which are more pronounced than in the P-A isotherm.

The onset of pressure increase upon compression (Figure 4.4A), also known as the lift-off area, appear over a much larger area per molecule for the Ra-LPS (400 Å<sup>2</sup>) than the corresponding value for the Re-Lipid A (200 Å<sup>2</sup>) and Rc-LPS (269 Å<sup>2</sup>) monolayers, which can be explained by the bulkier head group of LPS Ra, followed by Rc-LPS, and lastly Re-Lipid A.

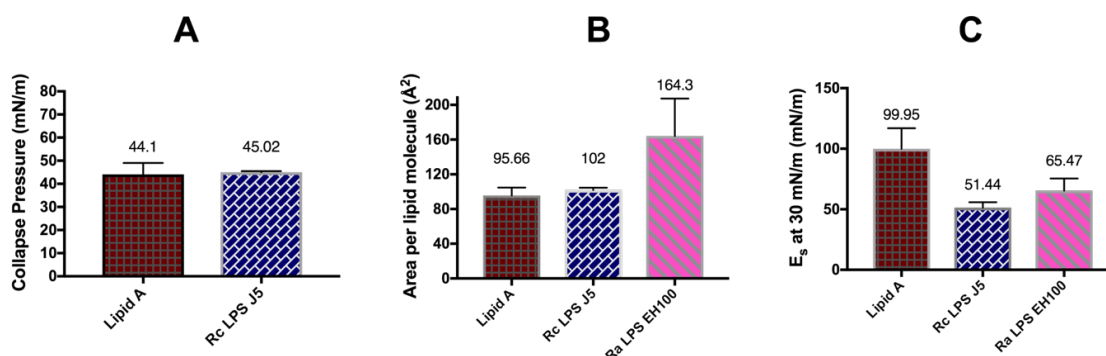


Figure 4.5: Collapse surface pressure (A), area per molecule (B) and compressibility modulus (C) at 30 mN/m of three types of glycolipid monolayers. The Ra-LPS did not reach its collapse pressure and it is excluded from the figure.

Rc-J5 LPS exhibited a molecular area of  $102.0 \pm 2.6$  Å<sup>2</sup> at 30 mN/m at a surface pressure of 30 mN/m with a high collapse pressure ( $45.0 \pm 0.5$  Å<sup>2</sup>) while the Ra-EH100 LPS presented larger area ( $164.0 \pm 43.0$  Å<sup>2</sup>) but did not reach the collapse point (Figure 4.4A, Figure 4.5A, B). Re Lipid A had a molecular area of  $95.66$  Å<sup>2</sup> at 30 mN/m and collapse pressure of 44.1 which conform with the results of Garcia-Verdugo et al. and Jeworrek et al. (219,242). They used a different subphase solution (150 mM NaCl, 5 mM Tris-HCl pH 7.4, 150 μM CaCl<sub>2</sub>) which resulted in a more expanded headgroup with a size of approximately 300 Å<sup>2</sup>.

#### 4.4.2 Drug interactions with model inner membranes

The interaction studies of the monolayers and bilayer with antimicrobial agents and liposomes were carried out at 30-35 mN/m. A comparison of the compressibility modulus at lateral bacterial membrane pressure (Figure 4.3C and Figure 4.5C) revealed differences between the monolayers in terms of orientation and packing, which may have affected the drug-membrane interaction. DPPC/DPPG ( $E_s = 151.8 \pm 18.7$  mN/m) exhibited a more ordered and closely packed monolayer than POPC:POPG ( $E_s = 104.2 \pm 7.9$  mN/m). *E. coli* B monolayer displayed a liquid expanded state. As for the OM model monolayers, Lipid A ( $E_s = 99.9 \pm 16.9$  mN/m) presented a liquid condensed state at 30 mN/m compared to Rc-LPS ( $51.4 \pm 4.3$  mN/m) which remained fluid and less ordered.

The Langmuir monolayer interfacial technique was applied to examine the interaction of drug and cyclodextrin with the lipid monolayers representing the IM and the outer leaflet of the OM. The lipid monolayers were formed on an aqueous subphase at 23°C and a PFA petri dish (50 mm diameter, 20 mL volume capacity) was used to spread the lipids up to the desired surface pressure (30-35 mN/m) before the antibiotic and cyclodextrin solutions were injected below the



surface. The surface pressure was plotted against time and the curve was fitted to a non-linear mathematical model (Hill equation), where applicable, to examine the kinetics of the interaction. The parameters gave an insight into the affinity of the studied molecules towards the monolayers (Hill-slope), the rate of change in surface pressure ( $t_{50\%}$ ), and the efficiency of the interaction in terms of the maximum change in surface pressure ( $\Delta\Pi_{\max}$ ).

Chlorhexidine, rifampicin and gentamicin were used as reference drugs to judge the efficiency of the interaction and investigate the uptake mechanism for the novel antimicrobial agent, PPA148. Chlorhexidine is known as a membrane active drug which breaches the cell envelope and causes leakage of cellular content leading to bacterial death (250). Rifampicin is transported into the cell membrane (OM and IM) by passive diffusion, while gentamicin follows a self-promoted pathway through the OM and needs energy input for its transfer inside the IM by specific porins (32,33,122). The controls will be compared with PPA148's interaction profile to investigate its passive transport and whether the novel drug disrupts the model membranes or diffuses through them.

#### 4.4.2.1 Interaction with *E. coli* polar lipid monolayer

*E. coli* B is a natural lipid extract which was used to model the Gram negative inner membrane. The monolayer presented an liquid expanded phase at 30 mN/m, as found from its isotherm and compressibility profile (Figure 4.3C). The surface pressure-time isotherm clearly shows the disruption effect of CHD on the monolayer (Figure 4.6A). CHD penetrated the monolayer and adsorbed at the air-water interface causing a large increase in surface pressure ( $\Delta\Pi_{\max} = 11.9 \pm 1.7$  mN/m) within seconds (Figure 4.6A).

The interaction between the novel antibiotic PPA148 and the *E. coli* B monolayer was examined by increasing drug concentrations (Figure 4.6C, Table 4.2). The isotherms of 20 and 60  $\mu\text{g/mL}$  (Figure 4.6C) were fitted with the Hill equation to investigate the kinetics of the interaction. PPA148 at 2  $\mu\text{g/mL}$  presented a negative change in surface pressure, possibly indicative of a propensity to cause membrane damage within 8 hours. By increasing PPA148's concentration, the interaction profile showed a positive change in surface pressure with  $\Delta\Pi_{\max}$  of  $14.0 \pm 3.8$  mN/m and  $9.2 \pm 2.9$  mN/m for 20 and 60  $\mu\text{g/mL}$  (Figure 4.6C, Table 4.2).  $\Delta\Pi_{\max}$  was reached within 4 hours and the drug's affinity towards the lipid monolayer was higher at 20  $\mu\text{g/mL}$  PPA148. The magnitude of  $\Delta\Pi_{\max}$  might indicate that PPA148 penetrated the monolayer. Due to poor water solubility of PPA148 ( $30 \pm 1$   $\mu\text{g/mL}$  as ascertained in Chapter 2), drug precipitation was observed after injecting 60  $\mu\text{g/mL}$  into the subphase, possibly explaining the weaker affinity ( $\Delta\Pi_{\max}$ ) of the drug towards the *E. coli* model membrane.

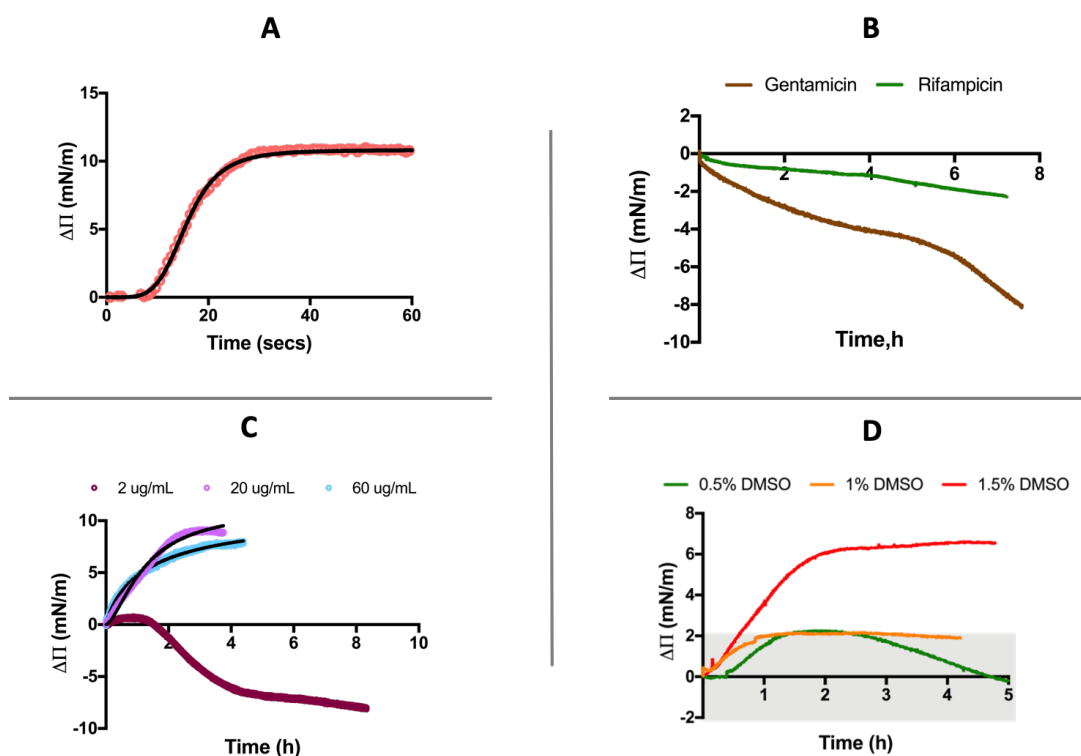


Figure 4.6: Representative surface pressure – time isotherms at 23°C of chlorhexidine digluconate (A), rifampicin (B), gentamicin (B), PPA148 (C) and DMSO (0.5, 1 and 1.5 % v/v) (D) against *E. coli* B monolayer using 0.9% NaCl as a subphase. The black lines are the fitted curves based on the mathematical model, Hill curve, when it was applicable.

Table 4.2: Kinetic parameters obtained from the fitting of the binding isotherms of rifampicin, gentamicin and PPA148 and the *E. coli* B monolayers at 23°C on water sub-phase containing isotonic saline.

Drug	Concentration (µg/mL)	$\Delta\Pi_{max}$ (mN/m)	Hill slope	$t_{50\%}$ (sec or h)
CHD	2	$11.9 \pm 1.7$	$4.6 \pm 2.4$	$19.8 \pm 5.8$ sec
Rifampicin	2	$-3.7 \pm 1.6$	N/A	$3.6 \pm 1.1$ h
Gentamicin	2	$-6.6 \pm 1.5$	N/A	$2.4 \pm 1.1$ h
PPA148	2	$-5.1 \pm 2.7$	N/A	$3.7 \pm 1.3$ h
PPA148	20	$14.0 \pm 3.8$	$1.2 \pm 0.5$	$2.8 \pm 2.2$ h
PPA148	60	$9.2 \pm 2.9$	$0.8 \pm 0.1$	$1.3 \pm 0.3$ h

The injecting solution for PPA148 was 100% DMSO, which is known to affect lipid membranes. Therefore, aliquots of DMSO in 0.5%, 1% and 1.5% v/v (0.001, 0.003 and 0.005 mole fraction of DMSO in the trough) were injected into the subphase below the monolayer (Figure 4.6D). The fractions tested correspond to the injected drug sample volumes (0.1, 0.2 and 0.3 mL). Figure 4.6D shows that DMSO at 0.5 or 1% v/v elicit a maximum change in surface pressure of 2 mN/m or less indicating a very weak or zero interaction of DMSO molecules with the lipid headgroup.

However, at the highest concentration tested (1.5 % v/v), the interaction with lipid molecules was more pronounced, reaching  $\Delta\Pi_{\text{max}}$  of  $7.0 \pm 1.3$  mN/m.

The profile of the two other control drugs (gentamicin and rifampicin) (Figure 4.6B) are incompatible with their established mechanisms of uptake. Gentamicin sulfate, which was used as a negative control, interacted with *E. coli* monolayer by inducing a negative change in surface pressure, thus appearing to solubilize the monolayer (Figure 4.6B). However, rifampicin, the positive control, did not show any sign of interaction. These results suggest this planar monolayer is an unsuitable model for the *E. coli* B lipids. The interaction of non-membrane active compounds might be artefactual due to the monolayer's packing inconsistencies and loosely packed lipids on a planar surface. Therefore, in the next section, fluorescence spectroscopy was used to examine whether PPA148 can really damage a membrane, by measuring the release of a dye from *E. coli* B liposomes.

#### 4.4.2.2 Interaction of PPA148 with *E. coli* B liposomes using fluorescence spectroscopy

The interaction experiments with *E. coli* B monolayer was used as an indication as to whether PPA148 might passively diffuse into the model membrane. The monolayer experiment showed possible damage of the *E. coli* B membrane caused by PPA148. However, the results were inconsistent for rifampicin and gentamicin, and thus further experiments were carried out to gain a better understanding of the interaction. Challenging liposomes with drugs and monitoring the release of carboxyfluorescein illustrates whether a drug can disrupt a membrane. Lipids from the *E. coli* B extract tend to form non lamellar structures and unstable planar monolayers, due to the presence of PE and its negative curvature (Figure 1.3). These lipids are likely to form a more stable configuration when are organized in liposomes. The dye self-quenches inside the liposomes; but when it is released into the bulk solvent it is no longer quenched, resulting in a significant increase in fluorescence intensity (245). Therefore, increase in fluorescence intensity indicates a release of the dye by disruption of the lipid bilayer caused by the antimicrobial agents tested.

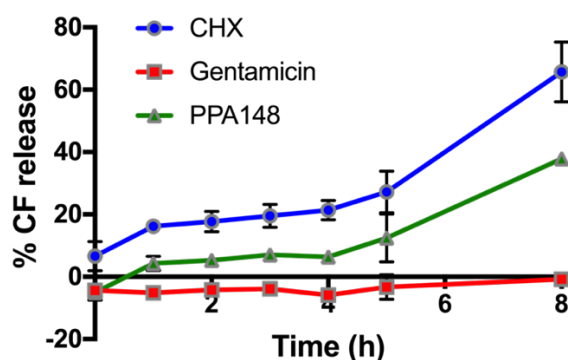


Figure 4.7: CF release from liposomes, manufactured from natural *E. coli* lipid extract, after administration of PPA148, chlorhexidine digluconate and gentamicin at 25°C.

In this experiment chlorhexidine digluconate (CHD) and gentamicin were used as positive and negative control respectively, since the former is known to be a membrane active compound and to damage membranes, while the latter enters the bacterial cells via active transport. The partitioning of CHD proved to be disruptive to the *E. coli* bilayer since the drug caused  $65.7 \pm 9.5\%$  dye release, whereas the detergent effect of PPA148 apparent in the Langmuir isotherm (Figure 4.6C) was not confirmed by the dye release study (Figure 4.7). The novel antimicrobial only elicited a limited degree of dye release ( $4.2 \pm 2.2\%$ ) one hour after the addition of the drug, without any further increase over the next 3 hours. This profile does not describe the solubilizing effect observed using *E. coli* B monolayer. This fact is evidence that the *E. coli* B monolayer is not a good model to study interactions, despite being extracted from bacteria. Therefore, the other interaction experiments using model monolayers at the air/liquid interface were carried out using only DPPC/DPPG lipids, which form a more stable planar monolayer.

#### 4.4.2.3 Interaction with DPPC:DPPG monolayer

A mixture of DPPC/DPPG lipids was used as an alternative IM model to the *E. coli* B monolayer. Rifampicin at  $2 \mu\text{g/mL}$  interacted slowly ( $t_{50\%} = 4.8 \pm 0.9 \text{ h}$ ) with the DPPC:DPPG monolayer by reaching a maximum pressure of  $6.7 \pm 2.0 \text{ mN/m}$  after 10 hours (Figure 4.8A). By increasing the drug concentration from 2 to  $20 \mu\text{g/mL}$ , the Hill slope decreased from  $2.5 \pm 1.0$  to  $0.8 \pm 0.2$  and  $\Delta\Pi_{\text{max}}$  increased to  $15.8 \pm 5.3 \text{ mN/m}$ , indicating a faster and more efficient interaction (Figure 4.8A, Table 4.3). Rifampicin at  $30 \mu\text{g/mL}$  induced  $\Delta\Pi_{\text{max}}$  of  $3.4 \pm 0.6$  and  $t_{50\%}$  of  $1.1 \pm 0.5 \text{ h}$ , reflecting a weaker and slower binding capacity.

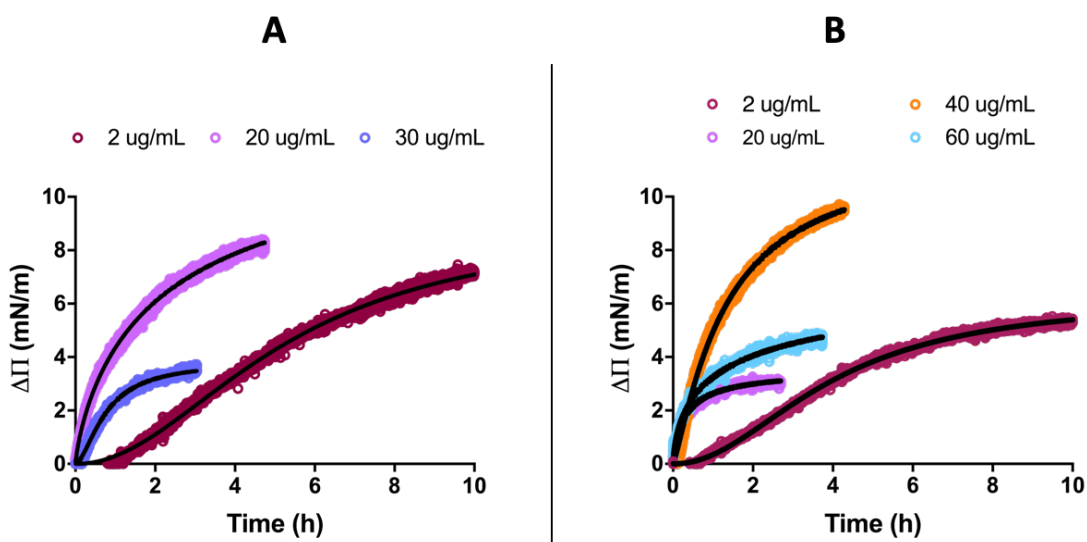


Figure 4.8: Representative surface pressure – time isotherms at  $23^\circ\text{C}$  of rifampicin (A), PPA148 (B), against DPPC/DPPG monolayer using  $1 \text{ mM MgCl}_2$  as a subphase. The black lines are the fitted curves based on the mathematical model when it was applicable.

PPA148 at  $2 \mu\text{g/mL}$  gave rise to a  $\Delta\Pi_{\text{max}}$  of  $8.8 \pm 3.4 \text{ mN/m}$  within 10 hours with a Hill slope of  $1.7 \pm 0.3$  and  $t_{50\%}$  of  $5.5 \pm 1.54 \text{ h}$ , reflecting an efficient but slow interaction with the DPPC/DPPG

monolayer (Figure 4.8B). At higher drug concentrations, the slope of the isotherm was steeper, which indicates an increased affinity towards the lipid monolayer. At 20  $\mu\text{g/mL}$ , the extent of the surface pressure modification was lower and  $\Delta\Pi_{\text{max}}$  reaches only  $3.3 \pm 0.7$  mN/m, compared to the  $\Delta\Pi_{\text{max}}$  obtained with 2, 40 and 60  $\mu\text{g/mL}$  which were, respectively,  $8.8 \pm 3.4$ ,  $9.4 \pm 1.3$  and  $6.4 \pm 1.4$  mN/m (Table 4.3). This might have been a result of drug aggregation, which started at  $\sim 20$   $\mu\text{g/mL}$  and visible aggregates were seen above 30  $\mu\text{g/mL}$ , as found in the turbidimetric assay (Figure 2.15) in Chapter 2 detected by dynamic light scattering.

Overall, the rate of interaction at concentrations above 2  $\mu\text{g/mL}$  indicated a faster process, as observed from the  $t_{50\%}$ . At concentrations above 20  $\mu\text{g/mL}$ , drug precipitation was observed after injecting PPA148 in the trough which agrees with the water solubility ( $30 \pm 1$   $\mu\text{g/mL}$ ) found in Chapter 2, Table 2.3. Overall, the affinity and kinetics of the interaction between PPA148 and DPPC/DPPG is concentration-dependent, with the kinetics having a threshold of 20  $\mu\text{g/mL}$ .

Table 4.3: Kinetic parameters obtained from the fitting of the binding isotherms of rifampicin and PPA148 and the DPPC/DPPG monolayers at 23°C on water sub-phase containing 1 mM  $\text{MgCl}_2$ .

Drug	Concentration ( $\mu\text{g/mL}$ )	$\Delta\Pi_{\text{max}}$ (mN/m)	Hill slope	$t_{50\%}$ (h)
PPA148	2	$8.8 \pm 3.4$	$1.7 \pm 0.3$	$5.5 \pm 1.54$
	20	$3.3 \pm 0.7$	$1.2 \pm 0.7$	$0.7 \pm 0.4$
	40	$9.4 \pm 1.3$	$1.1 \pm 0.4$	$0.9 \pm 0.2$
	60	$6.4 \pm 1.4$	$0.6 \pm 0.0$	$1.3 \pm 0.2$
Rifampicin	2	$6.7 \pm 2.0$	$2.5 \pm 1.0$	$4.8 \pm 0.9$
	20	$15.8 \pm 5.3$	$0.8 \pm 0.2$	$3.2 \pm 2.4$
	30	$3.4 \pm 0.6$	$1.2 \pm 0.6$	$1.1 \pm 0.5$

#### 4.4.2.4 Interaction between cyclodextrins and IM model membranes

One of the hypotheses of this project is that cyclodextrin will enhance not only PPA148's water solubility but also its transport through the inner bacterial membrane. Therefore, the effect of HP $\beta$ CD and RAMEB on the IM was tested using phospholipid model monolayers. Both types of cyclodextrins showed a solubilization effect on all lipid monolayers by eliciting a negative change in surface pressure. DPPC/DPPG (3:1) monolayers underwent a significant loss of molecules from the surface when challenged with HP $\beta$ CD and RAMEB (Figure 4.9A, B). However, RAMEB had a stronger effect against POPC/POPG than HP $\beta$ CD by producing a greater drop in surface pressure. The curves therefore indicate damage to the phospholipid monolayer rather than partitioning of the cyclodextrins.

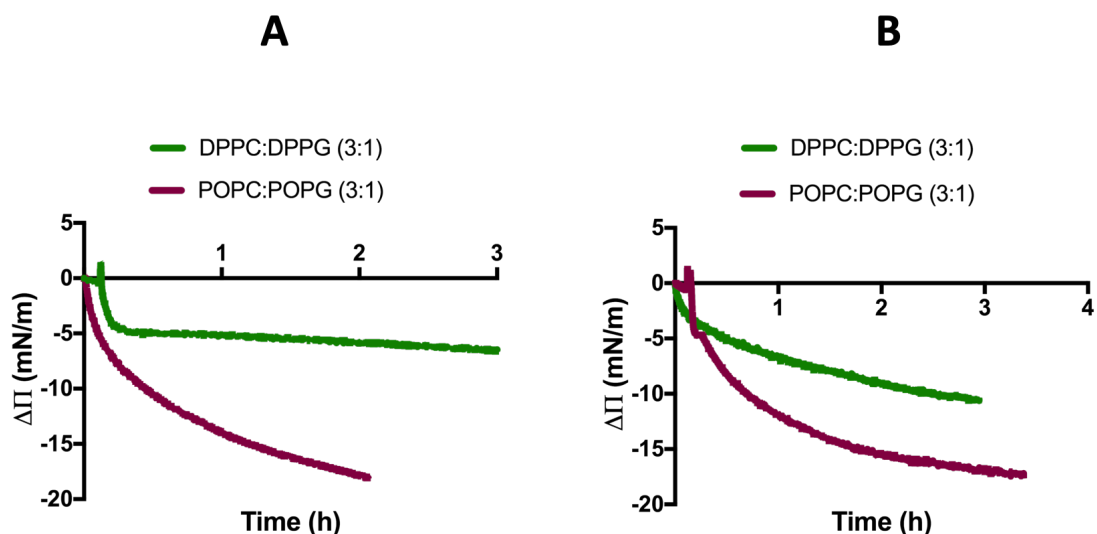


Figure 4.9: Representative surface pressure – time isotherms at 23°C of HP $\beta$ CD (A) and RAMEB (B), against DPPC/DPPG (3:1) and POPC/POPG (3:1) monolayers using MgCl<sub>2</sub> as a subphase.

#### 4.4.3 Drug interaction with model outer membranes

##### 4.4.3.1 Interaction between PPA148, fluidosomes, and model OM monolayers

Lipid A and Rc-LPS J5 monolayers were used to investigate the effect of steric barrier from the OM on PPA148, rifampicin and fluidosomes. Lipid A constitutes the innermost compartment of LPS and lacks the polysaccharide chain region. In this experiment rifampicin was used as a positive control because it shows a very good correlation with PPA148 when tested against model IM lipid monolayers (Figure 4.8). Rifampicin (20  $\mu$ g/mL) did not affect the packing of the Lipid A monolayer and the surface pressure remained constant for 2 h (Figure 4.10B). Instead, PPA148 produced an increase in surface pressure of  $6.9 \pm 0.7$  mN/m, reaching a plateau in less than an hour with a high binding affinity (Hill slope =  $1.3 \pm 0.2$ ) (Figure 4.10A).

When PPA148 was used to challenge Rc-LPS J5 monolayers, it revealed low efficiency ( $\Delta\Pi_{\max} = 3.7 \pm 2.1$  mN/m), weak binding capacity (Hill slope =  $3.7 \pm 2.6$ ) but a fast rate of  $t_{50\%} = 0.2 \pm 0.1$  h (Figure 4.10A). The presence of the polysaccharide chain hindered the interaction of PPA148 with the J5 LPS monolayer, probably due to a steric effect. The affinity (Hill slope) and efficiency ( $\Delta\Pi_{\max}$ ) of PPA148 towards J5 LPS was non-reproducible (Table 4.4).

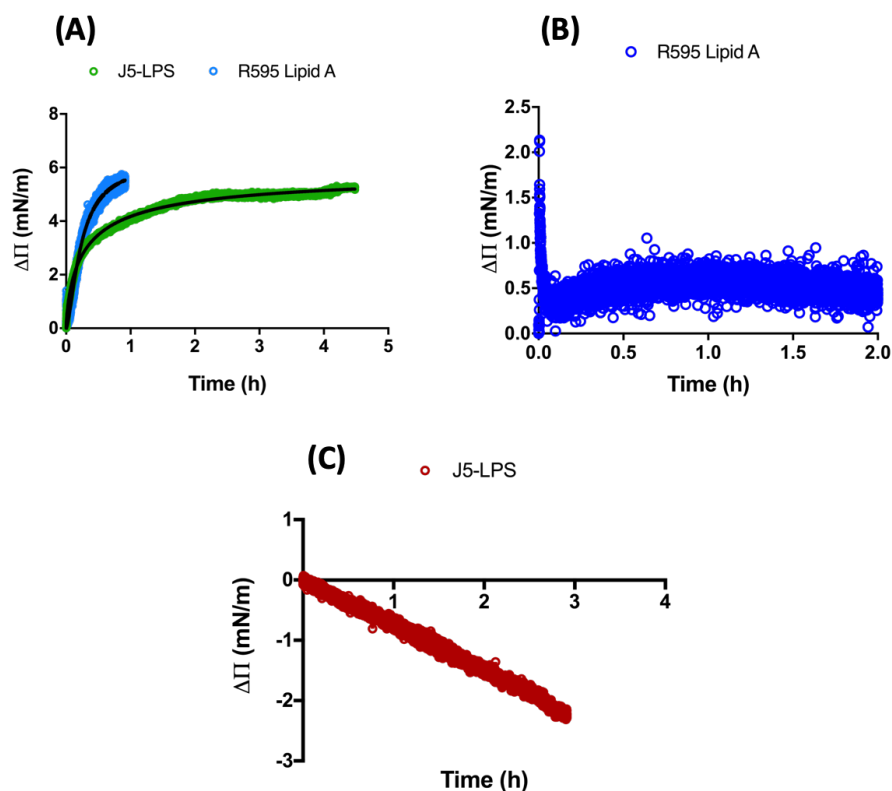


Figure 4.10: Interaction isotherm of 20  $\mu\text{g/mL}$  PPA148 (A), 20  $\mu\text{g/mL}$  rifampicin (B) and 0.1 mg/mL fluidosomes (C) against different types of OM lipid monolayers (Lipid A and Rc-LPS J5) at constant surface area at 23 °C. The profile was fitted, when applicable, to specific binding Hill slope model to investigate the kinetics and affinity of the interaction. The black lines are the fitted curves based on the mathematical model.

Fluidosomes were tested against J5 LPS monolayer and showed a linear decrease in surface pressure (Figure 4.10C). A  $\Delta\Pi_{\text{max}}$  of  $2 \pm 0.4$  mN/m was reached 3 h after injection of the final formulation below the monolayer, without any sign of reaching a plateau, suggesting removal of the lipids from the surface.

Table 4.4: Kinetic parameters obtained from fitting the binding isotherms of rifampicin and PPA148 and the Rc J5 LPS and R595 Lipid A monolayers at 23°C on a water sub-phase containing 1 mM  $\text{MgCl}_2$ .

Drug	Parameters	Rc J5 LPS	Re R595 Lipid A
PPA148	$\Delta\Pi_{\text{max}}$ (mN/m)	$3.7 \pm 2.1$	$7.9 \pm 0.7$
	Hill slope	$3.7 \pm 2.6$	$1.3 \pm 0.2$
	$t_{50\%}$ (h)	$0.2 \pm 0.1$	$0.3 \pm 0.1$
Rifampicin	$\Delta\Pi_{\text{max}}$ (mN/m)	-	$0.0 \pm 0.0$
	Hill slope	-	N/A
	$t_{50\%}$ (h)	-	N/A

## 4.4.3.2 Interaction between cyclodextrins and model OM monolayers

Although cyclodextrins were primarily used in this study to enhance PPA148's water solubility (Figure 2.17, Table 2.3) and help its transport through the IM, they were also examined for their interaction with OM LPS. Lipid A and Rc-LPS J5 remained largely undisturbed by HP $\beta$ CD, as reflected by the minimal surface pressure change (within  $\pm 2$  mN/m), whereas RAMEB induced a weak interaction with a more important change in surface pressure (approximately -5% mN/m) (Figure 4.11). These findings show that there was no significant interaction between the two cyclodextrins and the OM model membranes.

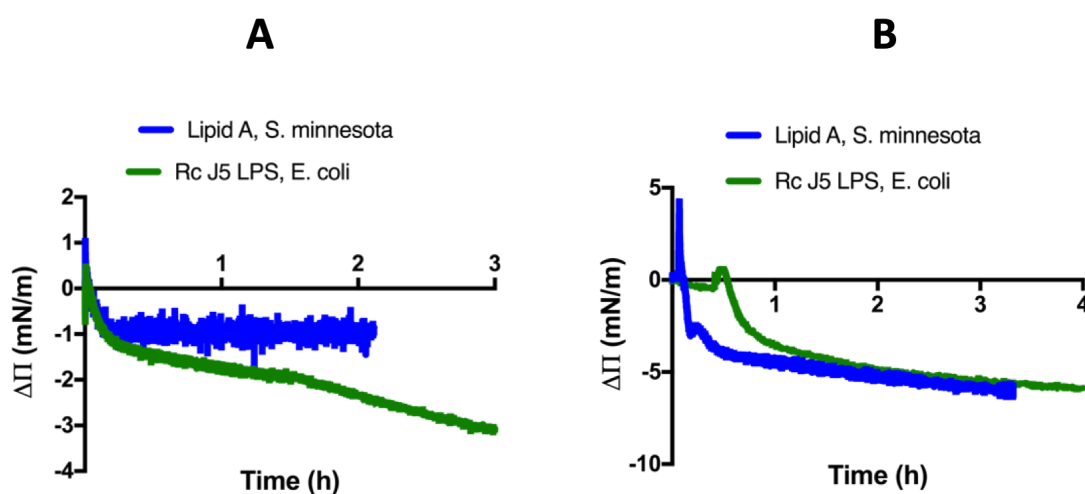


Figure 4.11: Pressure-time interaction isotherm of HP $\beta$ CD (A) and RAMEB (B) with 2 monolayers under constant surface area at 23°C.

## 4.4.3.3 Interaction between fluidosomes and model OM using neutron reflectivity (NR)

NR was used to further explore the effect of fluidosomes on a model bilayer representing the Gram negative OM. The structure of the model membrane was characterized at room temperature and at 38 °C prior to being challenged with the liposomal carrier (hydrogenated DPPC/DMPG at a molar ratio of 18:1) at 38 °C. Each contrast variation ( $H_2O$ ,  $D_2O$  and SMW) was fitted by mathematical models, describing the various layers of the membrane. The interface has been described as a series of slabs, each characterized by its SLD, thickness, hydration and roughness. This model membrane has been extensively studied by other research groups and the preparation process gives robust results with minor differences among samples (135,225,226).

Figure 4.12 shows the reflectivity and SLD profile of the model outer membrane at room temperature. The NR data were fitted to a five-layer model, thereby seeing the minimal number of layers with which the reflectivity data could be fitted. The interference fringe observed in the  $D_2O$  contrast (Figure 4.12A) reflects the presence of the bilayer. The layers, presented as a



background to the fitted SLD curves, are the silicon, silicon oxide, inner d-DPPC headgroups, inner d-DPPC tails, outer Ra-LPS tails, Ra-LPS core region (headgroup) and bulk solution.

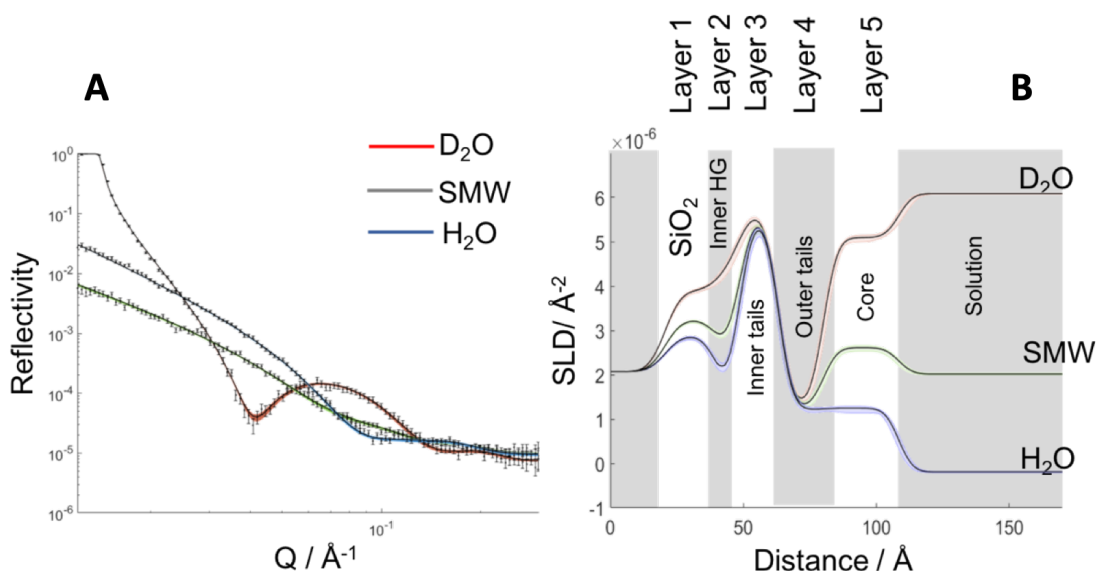


Figure 4.12: Neutron reflectivity profile (A) and model data fits with their scattering length density profiles (B) for an asymmetrically deposited DPPC (inner leaflet) and Ra-LPS (outer leaflet) model membrane at room temperature. The sample was measured at three isotopic contrasts (100% D<sub>2</sub>O, 100% H<sub>2</sub>O and SMW). The model membrane was fitted into five-layered mathematical model: Silicon oxide (SiO<sub>2</sub>), DPPC headgroup (Inner HG), DPPC tails (Inner tails), Ra LPS tails (Outer tails) and Ra LPS headgroups (Core).

The results reveal that a highly asymmetric lipid bilayer was formed on the silicon oxide-coated surface of the substrate with an average lipid coverage of 99%, derived from the combined volume fractions of d-DPPC and LPS (Table 4.5). The results have shown a mixing of DPPC and LPS within the bilayer because the DPPC composition in the inner and outer leaflet was found to be 77% and 20% respectively (Table 4.5). This is in good agreement with published values (226). A total of 1.3% water was found within the tail layers with a bilayer roughness of 4.15 Å. (Table 4.6)

Table 4.5: Volume fractions of deuterated DPPC tails, hydrogenous LPS tails and water within the bilayers of Ra-LPS/d-DPPC at room temperature (25 °C).

Layer	$\varphi_{DPPC}$	$\varphi_{RaLPS}$	$\varphi_{water}$
SiO <sub>2</sub>	n/a	n/a	0.16 (0.15, 0.17)
Inner Headgroup	0.77	0.22	
Inner Tails	(0.75, 0.78)	(0.21, 0.24)	0.013 (0.012, 0.013)
Outer Tails	0.20	0.79	
Outer Headgroup/Core	(0.19, 0.21)	(0.77, 0.80)	

At 38 °C the membrane displayed a similar reflectivity profile and the data were fitted using the same five-layer model (Figure 4.13). However, the structural parameters changed slightly (Table 4.6; Table 4.7). The d-DPPC volume fraction did not change in the inner leaflet (0.78) whilst increasing (0.14) in the outer leaflet. The thickness of the inner and outer headgroups decreased from 7.66 Å and 28.35 Å at 25 °C to 7.41 Å and 23.06 Å at 38 °C respectively. Moreover, the hydration of the inner headgroup decreased from ~50 % to  $\sim 28 \pm 1$  % and the bilayer roughness increased by  $\sim 2$  Å, which was expected due to the increase in fluidity of the bilayer.

Table 4.6: Structural parameters, thickness, hydration and roughness, of the Ra-LPS/DPPC membrane at room temperature and 38 °C as obtained from the fitting of the neutron reflectivity data. The numbers in parentheses are the 95% confidence interval error.

Layer	Asymmetric bilayer at:					
	RT			38 °C		
	Thickness (Å)	% water	Roughness (Å)	Thickness (Å)	% water	Roughness (Å)
SiO <sub>2</sub>	20.13 (19.58, 20.72)	16.27 (15.56, 16.90)	4.61 (4.39, 4.86)	20.13 (19.58, 20.72)	16.27 (15.56, 16.90)	4.61 (4.39, 4.86)
Inner HG	7.66 (7.346, 7.98)	50.10 (47.86, 52.38)	4.15 (4.02, 4.30)	7.41 (7.03, 7.80)	28.27 (27.13, 29.48)	6.35 (5.99, 6.70)
Inner Tails	14.94 (14.35, 15.6)	1.26 (1.22, 1.30)		14.7 (14.32, 15.10)	1.26 (1.22, 1.30)	
Outer Tails	16.87 (16.70, 16.99)			14.84 (14.44, 15.29)		
Outer HG/Core	28.35 (27.66, 28.98)	53.59 (51.42, 55.97)		23.06 (22.36, 23.68)	51.77 (49.61, 54.06)	

HG: Headgroup

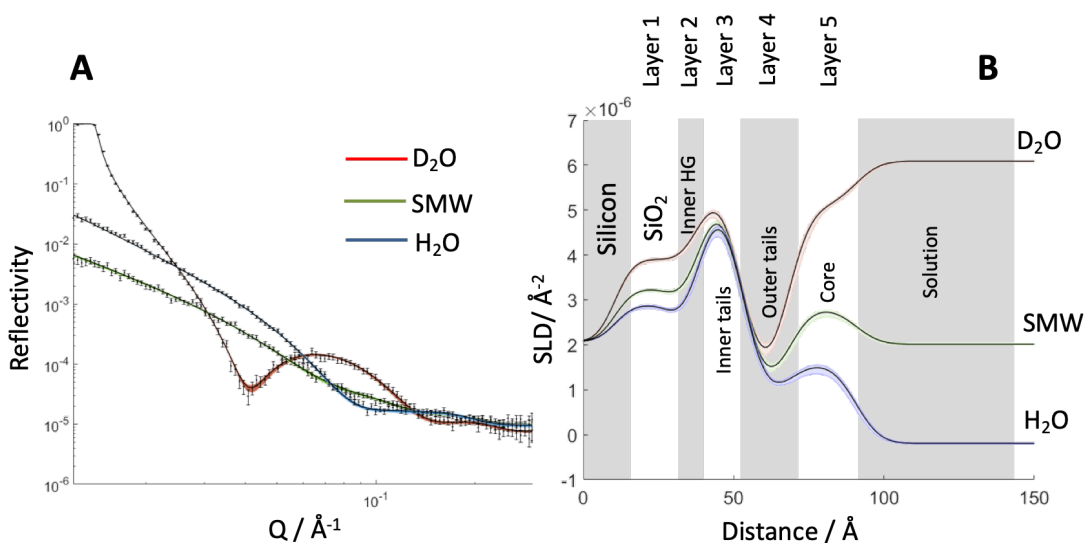


Figure 4.13: Neutron reflectivity profile (A) and model data fits with their scattering length density profiles (B) for an asymmetrically deposited DPPC (inner leaflet) and Ra-LPS (outer leaflet) model membrane at 38 °C. The sample was measured in three isotopic contrasts (100% D<sub>2</sub>O, 100% H<sub>2</sub>O and 38% D<sub>2</sub>O/SMW). The model membrane was fitted into a five-layered mathematical model: Silicon oxide (SiO<sub>2</sub>), DPPC headgroup (Inner HG), DPPC tails (Inner tails), Ra LPS tails (Outer tails) and Ra LPS headgroups (Core).

Table 4.7: Volume fraction of deuterated DPPC tails, hydrogenous LPS tails and water within the bilayers of Ra-LPS/d-DPPC 38 °C before and after the challenge by the fluidosomes.

Layer	Asymmetric bilayer at 38 °C					
	Before challenge			After challenge		
	$\varphi_{DPPC}$	$\varphi_{RaLPS}$	$\varphi_{water}$	$\varphi_{DPPC}$	$\varphi_{RaLPS}$	$\varphi_{water}$
SiO <sub>2</sub>	n/a	n/a	0.16 (0.15, 0.17)	n/a	n/a	0.16 (0.16, 0.17)
Inner Headgroup	0.78 (0.77, 0.79)	0.21 (0.21, 0.20)	0.013 (0.012, 0.013)	0.65 (0.64, 0.67)	0.35 (0.34, 0.31)	0.0003 (0.0003, 0.0003)
Inner Tails						
Outer Tails	0.14 (0.13, 0.16)	0.85 (0.85, 0.83)		0.21 (0.20, 0.22)	0.79 (0.77, 0.78)	
Outer Headgroup (Core)						

Next, the reflectivity profile of the model membrane after interaction with fluidosomes was studied. The damaging effect of fluidosomes on the Rc J5 LPS, which had been seen in the air/liquid interface experiments (Figure 4.10C) was further investigated by measuring changes in the structure of the fully characterised d-DPPC:h-Ra-LPS bilayer after being challenged with 0.1 mg/mL empty fluidosomes for 1 h. The reflectivity profile of the system was measured after flushing out excess fluidosomes, composed of hydrogenated lipids (DPPC:DMPG). Most of the structural changes occurring following the addition of fluidosomes involved the tail and outer headgroup regions. The exposure of the bilayer to fluidosomes resulted in the addition of a fringe

in the reflectivity profile, reflecting the presence of two lipid bilayer, one being the model OM and the second being described as floating bilayer (7th layer) in the SLD profile (Figure 4.14B).

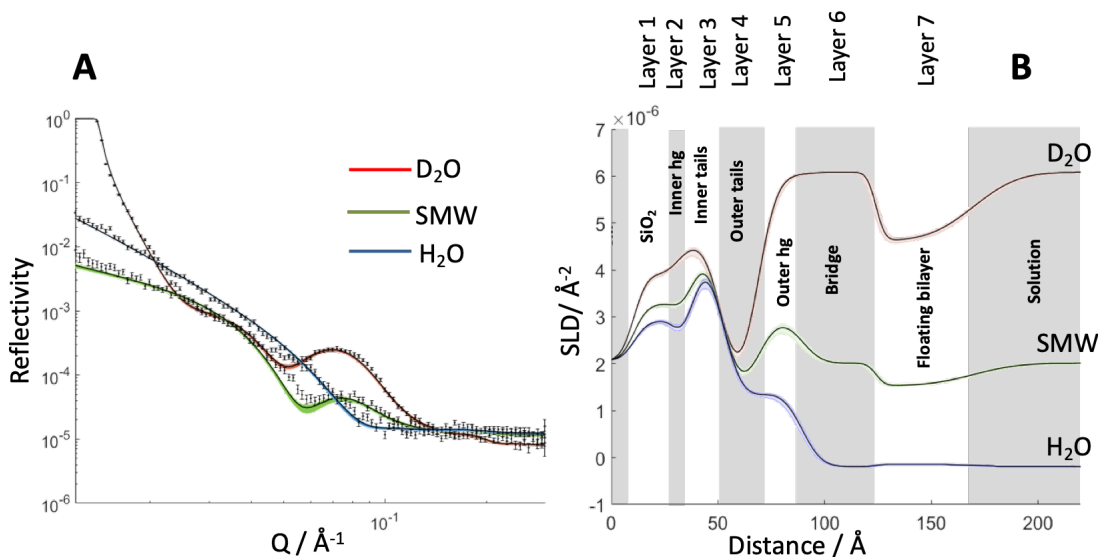


Figure 4.14: Neutron reflectivity profile (A) and model data fits with their scattering length density profiles (B) for an assymmetrically deposited DPPC (inner leaflet) and Ra-LPS (outer leaflet) model membrane after being challenged with 0.1 mg/mL fluidosomes (DPPC/DMPG, 18:1) at 38 °C. The sample was measured in three isotopic contrasts (100%  $D_2O$ , 100%  $H_2O$  and 38%  $D_2O$ /SMW). The model membrane was fitted into a seven-layered mathematical model: Silicon oxide ( $SiO_2$ ), DPPC headgroup (Inner HG), DPPC tails (Inner tails), Ra LPS tails (Outer tails) and Ra LPS headgroups (Core), Bridge and Floating bilayer.

Mixing of lipids within the bilayer region occurred, as derived from the lipid composition in the model membrane, with the inner leaflet consisting of 65% d-DPPC and 34% h-Ra LPS, while the outer leaflet of 21% d-DPPC and 78% LPS (Table 4.7). It can be observed that the contribution of hydrogenous phospholipids in the inner leaflet layers, which might be either h-Ra LPS or h-phospholipids from fluidosomes, had increased from 21% to 34% after adding the fluidosomes. In addition, the fitting parameters in Table 4.8 showed an increase of the model OM roughness from 6.3  $\text{\AA}$  to 7.1  $\text{\AA}$ , before and after the challenge, respectively, which illustrates structural changes of the membrane. A thinner inner headgroup region (5.7  $\text{\AA}$ ) with higher hydration levels (48.44 %) and a thicker outer headgroup region (21.0  $\text{\AA}$ ) with lower hydration (35.95 %) were also observed, compared to the unchallenged membrane (Table 4.6) under the same conditions.

Of the two additional layers formed, the one adjacent to the membrane is a solvent layer (99.94% water content) with an SLD of  $1.78 \times 10^{-7}$  ( $1.7224 \times 10^{-7}$ ,  $1.8266 \times 10^{-7}$ )  $\text{\AA}^{-2}$ , thickness of 34.6 and roughness of 3.4  $\text{\AA}$ . The outermost layer has high water content (75.80%) with an SLD of  $2.6 \times 10^{-8}$  ( $2.4608 \times 10^{-8}$ ,  $2.7494 \times 10^{-8}$ )  $\text{\AA}^{-2}$ . If liposomes were intact on the membrane surface, their tail SLD would have been similar to the reported SLD of h- or d-DPPC tails ( $-0.4$  or  $7.4 \times 10^{-6}$   $\text{\AA}^{-2}$  respectively) as published by Clifton and coworkers (226). The thickness of the additional layers was found to be 35 and 46  $\text{\AA}$  for the 6th and 7th layer, respectively.

This profile may reflect fusion of liposomes in the membrane because of the close to zero SLD of the bridge layer and the increase of hydrogenous lipid tails within the bilayer (Figure 4.15, Table 4.7).

Table 4.8: Structural parameters, namely, thickness, hydration and roughness, of the challenged Ra-LPS/DPPC membrane at 38 °C as obtained from fits to the neutron reflectivity data shown in Figure 4.14.

Layer	Asymmetric bilayer at 38 °C					
	Before challenge			After challenge		
	Thickness (Å)	% water	Roughness (Å)	Thickness (Å)	% water	Roughness (Å)
SiO <sub>2</sub>	20.13 (19.58, 20.72)	16.27 (15.56, 16.90)	4.61 (4.39, 4.86)	20.13 (19.58, 20.72)	16.27 (15.57, 16.89)	4.61 (4.39, 4.86)
Inner HG	7.41 (7.03, 7.80)	28.27 (27.13, 29.48)	6.35 (5.99, 6.70)	5.75 (5.51, 5.95)	48.44 (47.04, 49.65)	7.15 (6.84, 7.54)
Inner Tails	14.7 (14.32, 15.10)	1.26 (1.22, 1.30)		15.28 (14.81, 15.71)	0.03 (0.03, 0.03)	
Outer Tails	14.84 (14.44, 15.29)			16.76 (16.50, 16.97)		
Outer HG/Core	23.06 (22.36, 23.68)	51.77 (49.61, 54.06)		21.05 (20.16, 22.07)	35.97 (34.49, 37.55)	
Bridge	-	-	-	34.59 (33.43, 35.74)	99.94 (99.85, 99.99)	3.36 (3.26, 3.47)
Vesicles/Bilayer	-	-	-	45.82 (44.89, 46.882)	75.80 (75.02, 76.73)	16.62 (15.91, 17.34)

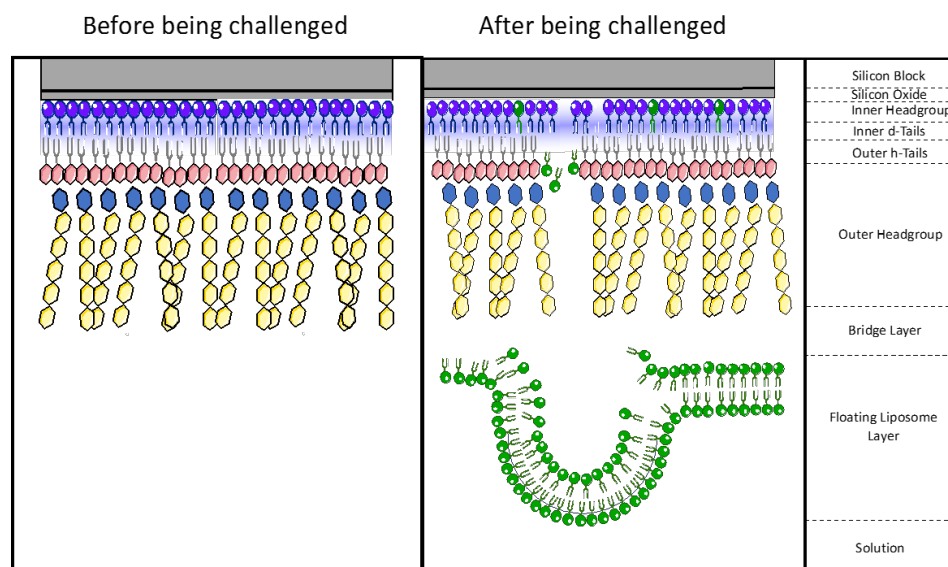


Figure 4.15: Representation of the possible structural changes in the model OM system after being challenged by fluidosomes.

## 4.5 Discussion

In this chapter, the uptake mechanism of PPA148 and its carrier were investigated in terms of their biophysical interaction with model systems mimicking the lipidic components of the two membranes of the Gram negative cell envelope. The main hypothesis of this project was that a drug-in-cyclodextrin-in-liposome formulation would enhance PPA148's efficiency against Gram negative bacteria by fusion with the OM, releasing the drug/CD complex. Cyclodextrin increased PPA148's water solubility by inclusion complex formation (Chapter 2), but it was hypothesized that it could also enhance the drug's transport through the IM. Fluidosomes were selected as the carrier of the drug-CD complex because it is known that they can fuse into the bacterial OM and, thereby release their payload into the periplasmic space.

The ability of PPA148 to passively diffuse through a model OM was investigated using Rc J5 LPS and Re R595 Lipid A monolayers in a Langmuir trough at the air/liquid interface (Figure 4.10A). PPA148 has been found to interact weakly with Rc J5 LPS and showed a high affinity towards the R595 Lipid A monolayer. Although the J5-LPS monolayer was in a mixed liquid expanded/liquid condensed state at 30 mN/m (Figure 4.5C), it produced the cross-link of the anionic molecules in the presence of  $Mg^{2+}$ . The steric barrier produced hindered the interaction which presented significant deviation in terms of the affinity towards the lipids ( $\Delta\Pi_{max}$ ) and the speed of the interaction (Hill slope). Hydrated oligosaccharide chains in Rc J5 LPS prevent the entrance of hydrophobic or surface-active molecules and make the hydrophobic bilayer inaccessible as was found by Clifton and co-workers using X-ray and neutron reflectivity techniques (225). R595 Lipid A underwent a more condensed state at 30 mN/m owing to the absence of oligosaccharide chain, leading to a higher drug affinity observed in the pressure/time isotherm. The smaller headgroup allows the R595 Lipid A monolayer to have more closely

packed molecules (Figure 4.5C), presenting a weaker steric hindrance to PPA148. Although PPA148 interacted with R595 Lipid A, rifampicin did not show any interaction (Figure 4.10B), which was unexpected based on its proposed mechanism of uptake. This can be explained by the topological polar surface area (tPSA), a parameter predicting the passive drug permeation through the Gram-negative (tPSA of 165 Å<sup>2</sup>) and Gram-positive (tPSA 243 Å<sup>2</sup>) bacterial envelope (12). It was estimated by ChemDraw that PPA148 has a tPSA of 141 Å<sup>2</sup> (Table 2.1), which indicates a less polar compound than rifampicin (tPSA of 217 Å<sup>2</sup>). Thus the novel drug is more likely to interact with the R595 Lipid A, as found in the air/liquid monolayer experiments.

We also obtained evidence that PPA148 interacts with the IM lipid monolayers (Figure 4.6C, Figure 4.8B). Despite some stability difficulties with the *E. coli* B monolayer (Figure 4.6C, Figure 4.7), it was found that PPA148 interacted with phospholipids, but it did not cause membrane damage as happened with chlorhexidine (Figure 4.7). *E. coli* B lipid monolayer is a poor model of the membrane because it contains a diverse mixture of lipids (Table 1.6), which, in live bacteria, would form an asymmetric bilayer, with the lipids which impart negative curvature localized on the inside (124,125). Instead, in a monolayer, these lipids are forced to adopt a planar configuration and, thus, the monolayer presents packing discontinuities without a reproducible interaction profile (Figure 4.6C).

Using a monolayer model, composed of DPPC/DPPG (3:1), it was observed that PPA148 and rifampicin presented a similar interaction profile (Figure 4.8). The findings for rifampicin are in agreement with its mechanism of transport: that it partitions in DPPC monolayers by establishing ionic bonds with the head groups of DPPC in an acidic environment of pH=5 (255). Since the kinetic profile of PPA148 was similar to that of rifampicin, it is suggested that PPA148 is likely to enter the cell via diffusion through the membrane. However, PPA148 cannot be ionized (Figure 2.2) and, thus, the possibility of this type of interaction occurring with phospholipids was discounted. It is more likely that PPA148 is partitioning into the membrane because of its hydrophobicity.

As PPA148's solubilizers, HPβCD and RAMEB were examined separately for their interaction with both model OM and IM monolayers (Figure 4.9; Figure 4.11). It was found that HPβCD did not affect the OM monolayer, while RAMEB presented a weak interaction with it, possibly resulting from the different substituted groups (Figure 4.11). RAMEB is a methyl substituted βCD derivative with high hydrophobicity which makes it more likely to partition into LPS. It has been reported that complexes of drug-β-cyclodextrin and its derivatives, such as RAMEB, improve antibiotic potency but the mechanism has not been clarified yet. It is hypothesized that β-CD may drive internalization of the β-CD-antibiotic complex via (i) the OM protein CymA (cyclodextrin metabolism A), (ii) enhanced adhesion to the bacterial surface with potential local release of the antibiotic, and (iii) destabilization of the bacterial envelope (215,216,246). The transport through the CymA channels is a controversial issue seeing that some scientists have found that α-CD and β-CD bind and can be transported into the cell via those porins but others have found that only

the permeation of  $\alpha$ -CD can be mediated by CymA (247) due to the channels' cut-off size of 950Da. In the current work, porin channels have not been investigated as a mechanism of uptake, so, based on our results, RAMEB might just enhance the adhesion to the OM.

The interaction of HP $\beta$ CD and RAMEB with model IM resulted in a drop of surface pressure to negative values (Figure 4.9), suggesting a lipid solubilizing effect of both DPPC/DPPG and POPC/POPG monolayers. It was found that upon cyclodextrin-membrane interaction, the packing of phospholipids at the air/liquid interface and the type of  $\beta$ CD derivative (hydroxy-propyl- and methyl- substituted groups) affect the efficiency of the interaction (Figure 4.9). POPC/POPG formed a liquid condensed monolayer at 30 mN/m (Figure 4.3C) which favours the drug membrane interaction because the lipids have lateral and rotational mobility, promoting the molecular process of binding (Figure 4.16). Both types of cyclodextrin resulted in  $\Delta\Pi_{\max}$  of -20 mN/m, which suggests strong interaction with POPC/POPG by removing lipids from the surface. DPPC/DPPG monolayer produced a condensed film at the air/liquid interface, with which HP $\beta$ CD interacted weakly. The tight packing of lipids and the saturated hydrocarbon chains hindered the interaction. RAMEB shows a high affinity towards the DPPC/DPPG monolayer, which was expected because RAMEB has been reported to induce phospholipid exchange more efficiently than HP $\beta$ CD (181). In addition, it has also been reported that RAMEB forms soluble complexes with DPPC (210), which might explain the negative surface pressure of the isotherm, but it was not examined further in the current work.

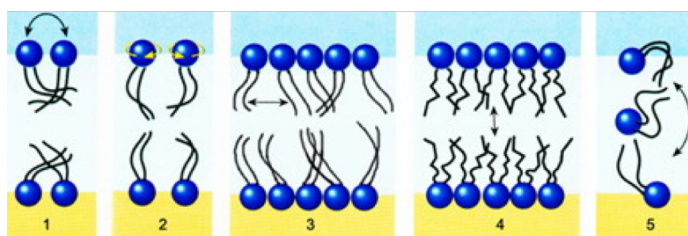


Figure 4.16: Schematic representation of the movement of phospholipids within a membrane: transpose diffusion (1), rotation (2), swing (3), flexion (4) and transverse diffusion or “flip-flop” movement (248).

Fluidosomes (DPPC/DPMG, 18:1) were used as a carrier to overcome the barrier of the OM because monolayer interaction studies showed that PPA148 cannot diffuse through the OM model membranes (Figure 4.10A). It was hypothesized that fluidosomes could release their content (drug-in cyclodextrin) by fusion into the OM membrane as found by Wang et al. for a DPPC/DMPG (9:1) system by lipid mixing assay (249). The air/liquid monolayer interaction experiment revealed a strong interaction between fluidosomes and Rc J5 LPS (Figure 4.10C). The interaction isotherm revealed a lipid solubilizing effect upon fluidosome injection in the subphase, containing 1 mM MgCl<sub>2</sub>. Wang et al. reported that the aggregation and fusion of fluidosomes with Gram negative bacterial membrane is promoted by the presence of Ca<sup>2+</sup> or other divalent cations by inducing the neutralization of the negatively charged Lipid A part and dehydration of phospholipids of the membrane (249).



To further investigate the interaction between fluidosomes and OM, neutron reflectivity was used on an asymmetric model Gram negative bacterial membrane consisting of Ra-EH100 LPS and DPPC in the outer and inner leaflet, respectively. Before introducing fluidosomes into the system, the model membrane was characterized in terms of structural properties at room temperature (25 °C) and 38 °C (Figure 4.12; Figure 4.13). At 38 °C lipids become more flexible (250,251) as found in this work. The thickness of all the individual compartments of the model membrane decreased as the temperature increased (Table 4.6). Membrane rigidity was modulated thermodynamically by changes in temperature and decreased with increasing temperature. Changes in orientation and hydration of lipids upon increasing temperature caused thinning of lipid bilayers (250) because the hydrocarbon lipid chains became more flexible (Figure 4.17). The roughness of the membrane increased with increasing temperature which indicated a liquid crystalline phase of the lipids, allowing a less rigid structure of the membrane (Table 4.6). In a liquid crystalline membrane, lipids can simply transpose with neighboring molecules (transpose diffusion), rotate quickly around their axis, swing from side to side, following contraction movement or, less frequent, undergo flip-flop movement (transverse diffusion) (Figure 4.16; Figure 4.17) (248). The lipid movement creates a more favorable environment for interaction with the membrane.

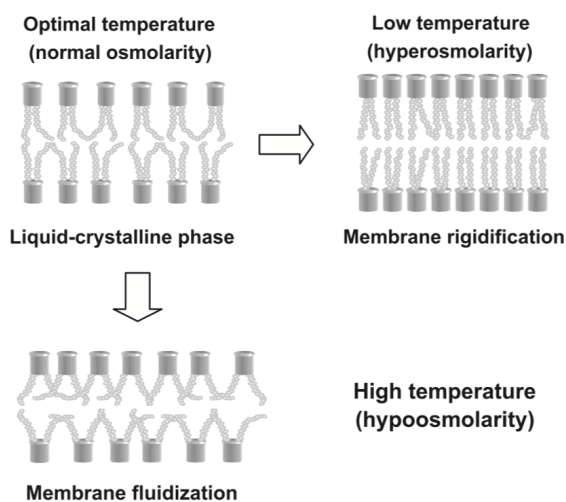


Figure 4.17: Schematic representation of the effect of temperature change on membrane structure and behavior of lipid bilayers adapted from Los and Murata (250). Low temperatures cause “rigidification” of membranes, whereas high temperatures cause “fluidization” of membranes.

The effect of fluidosomes on the asymmetric model OM was observed at 38 °C (Figure 4.14; Figure 4.15). The NR profile of the membrane after addition of fluidosomes revealed a lipid mixing profile with an additional bilayer associated with the deposited membrane. The roughness of the model OM increased compared to the membrane before being challenged by the fluidosomes, and the volume fractions of deuterated and hydrogenous tails of the inner and outer leaflets changed, revealing a mixing of the lipids (Table 4.6; Table 4.7; Table 4.8). More specifically, the volume fraction of  $d_{62}$ DPPC increased in the outer leaflet, while hydrogenous lipids increased in

the inner leaflet of the membrane. Based on the fitted parameters, the SLD of the additional layer adjacent to the membrane was close to zero, indicating that it is composed of both deuterated and hydrogenous material to adjust the SLD at  $0.18 \times 10^{-7} \text{ \AA}^{-2}$ . The outermost additional layer presented a similar thickness (46 Å) to a DPPC bilayer (50 Å) in the presence of  $\text{CaCl}_2$  (206). This strongly suggests that fluidosomes fused into the OM membrane by creating a  $\text{Ca}^{2+}$  bridge layer between the outer leaflets of the membrane and liposome at the contact site (Figure 4.15).  $\text{Ca}^{2+}$  is able to keep fluidosomes attached to the model membrane by interacting with both liposomes and LPS accompanied by local dehydration, lowering the free energy and creating local packing defects on the outer leaflet of both systems (Figure 4.15). Moreover, fluidosomes tend to destabilize thermodynamically at 38 °C which also aids their fusion with the bacterial OM (252). Vesicle fusion with bacterial membranes, promoted by divalent cations, requires fluidity which is achieved at a temperature higher than the phase transition temperature of fluidosomes (approximately 35°C ) (249). The thinning of the model OM and increased flexibility of lipids at 38 °C (Table 4.6) facilitate the fusion of fluidosomes with the model Gram negative bacterial membrane.

After considering both the air/liquid interface interaction and the NR experiment, it is suggested that both fluidosomes and model OM underwent conformational changes, leading to their collapse and fusion at the point of contact (Figure 4.15).

## 4.6 Conclusion

In the current study, the uptake mechanism of PPA148 and its formulation was studied using biophysical interfacial techniques. The monolayer studies suggest that PPA148 slowly diffuses through the lipidic components of the PC/PG model IM while it presents weak interaction with the model OM consisting of DPPC and Ra-EH100 LPS as the inner and outer leaflet, respectively. When compared to the pressure-time isotherm profile of chlorhexidine, rifampicin and gentamicin, whose mechanism of uptake is known, PPA148 showed a similar profile with that of rifampicin, indicating that PPA148 passively diffuses through the IM. The interaction of PPA148 with the LPS monolayer, characterized by slow kinetics, suggests that the main mechanism of PPA148's transport through the OM is dependent on non-specific or self-promoted diffusion or even active transport. In this chapter, it was found that cyclodextrins might act as permeation enhancers through the IM, in addition to increasing the drug's water solubility. The structural changes occurring in the model membrane upon being exposed to fluidosomes were examined by neutron reflectivity and suggest that fluidosomes enter into the LPS leaflet of the OM through a fusion mechanism.

## Chapter 5

## General Conclusion

Experience has demonstrated that bacteria are quick to develop resistance to new antibiotics. This predictable resistance is essentially related to the mechanism of action of traditional antibiotics with five main specific targets in the cell: cell wall synthesis, DNA-gyrase, DNA-directed-RNA-polymerase, protein synthesis and enzymes (253), and the speed at which mutation may facilitate target alteration. The development of new classes of antibiotics with specificity towards bacteria, but which act non-specifically against novel targets, needs to be pursued as a possible method to delay the onset of resistance.

At King's College London, an antimicrobial compound, PPA148, was synthesized, which is active against Gram-negative bacteria with a novel antimicrobial mechanism of action. PPA148's bactericidal activity is attributed to its binding onto the minor-groove of bacterial DNA. It showed promising activity against the Gram negative members of the ESKAPE organisms, and little toxicity to human cells (107,108). Nevertheless, in some clinical strains, difficulties in drug uptake, due to the bacterial semi-permeable OM and/or the efflux mechanisms, was observed. It is known that intracellular drug accumulation is a complex process including drug uptake into the cell, retention and distribution in the cell, and efflux from the cell. At any given time, the accumulation of a drug in cells is dependent upon the different rates of drug uptake and efflux (254). Overexpression of efflux mechanisms leads to a decrease in drug accumulation resulting in drug-resistant cells.

Based on our knowledge of the physicochemical properties of PPA148, reducing particle aggregation and enhancing water solubility was the first step towards developing a formulation to enhance its antibacterial efficacy against Gram negative bacteria. The solubility increased 6-fold by incorporating PPA148 into cyclodextrin's cavity (Table 2.3; Table 2.4). Fluorescence spectroscopy was used to determine the binding constant of a 1:1 complex with HP $\beta$ CD and RAMEB, which was found to be  $63 \pm 20 \text{ M}^{-1}$  and  $102 \pm 26 \text{ M}^{-1}$ , respectively (Table 2.4). Evidence of the formation of inclusion complex include NMR spectroscopy, which presented a shift of the DIMEB proton at position 5 protruding towards the CD cavity (Figure 2.19). The results revealed the formation of a 1:2 PPA148/DIMEB complex.

The next step was to incorporate the 1:1 PPA148/RAMEB complex into fluidosomes (DPPC/DMPG, 18:1) and test the efficacy of the drug in its pure and formulated form. The entrapment of the water-soluble inclusion complex into fluidosomes led to accommodation of the insoluble PPA148 in the aqueous phase of neutral vesicles with a size of  $129 \pm 10 \text{ nm}$  and high encapsulation efficiency ( $67 \pm 11\%$ ). Loaded fluidosomes presented a more monodisperse system than the empty fluidosomes (Figure 3.4; Figure 3.5), indicating that the presence of the complex created structures with increased integrity. Generally, in liposomes, cyclodextrin complexation competes with liposomal membrane binding, which in our case led to a more intact system because the affinity of the drug towards CD is higher than that of lipids. The LT experiment showed weak interaction of RAMEB with a DPPC/DPPG monolayer (Figure 4.9), which describes interrelation with the lipid headgroups without causing any damage to the

membrane. PPA148 might be inserted into the CD cavity from one side while the other side of RAMEB can be attached with the headgroups of the inner leaflet of the liposomes, thus forming more stable vesicles (Figure 3.10).

The efficacy of PPA148 against the *E. coli* DH5 $\alpha$  (PPA148-in-RAMEB-in-fluidosomes) increased when it was complexed with RAMEB. Pure PPA148 created an inhibition zone of  $1.6 \pm 0.2$  cm, while the complex generated a  $2.4 \pm 0.1$  cm inhibition zone (Figure 3.7). The difference was statically significant (Figure 3.8), thus showing that the efficacy of PPA148 was enhanced. Therefore, RAMEB has a dual role in (1) increasing the solubility of the PPA148 and (2) transporting drug molecules across membranes (intrinsic antimicrobial activity). The efficacy was also enhanced when the complex was incorporated into fluidosomes with an inhibition zone of  $2.7 \pm 0.2$  cm which was statistically significantly different from the pure drug; but the difference between the inhibition zone of the complex and the final formulation (Figure 3.8) was not statistically significant, which might be a result of the small number of experimental observations. To further elucidate the efficiency of the final formulation, Monte Carlo simulation was performed by building a probability distribution and creating a substituted set of data (100 observations) based on the experimental observations. Predicted data were analyzed, and it was estimated that the difference between the efficacy of the final formulation and the complex would be statistically significant (Figure 3.9). This preliminary microbiological test presented in this thesis has some statistical limitations due to the small number of observations, nevertheless it shows that the final formulation increased the antimicrobial activity of the novel compound.

Following the microbiological assay, a biophysical approach was pursued to investigate the mechanism of uptake of PPA148 and its carriers. Knowing the physicochemical properties of PPA148, passive diffusion through lipid monolayers was hypothesized as a possible mechanism of uptake. The LT experiments at the air/liquid interface revealed that PPA148 slowly diffuses through both the IM (DPPC/DPPG) (Figure 4.8B) and OM (Rc J5 LPS and R595 Lipid A) (Figure 4.10A) model monolayers. The use of Lipid A and LPS revealed the steric barrier created by the oligosaccharide chains which hinders the permeation of PPA148 through the OM. These results, in combination with the inhibition caused in live bacteria, reveal that the main mechanism of PPA148's transport is dependent on non-specific or self-promoted diffusion or even active transport.

HP $\beta$ CD and RAMEB presented a strong interaction with POPC/POPG monolayers but a weak interaction with those formed from DPPC/DPPG (Figure 4.9). Neither was cyclodextrin able to interact strongly with the OM model membrane (Figure 4.11), yet it enhanced the antimicrobial efficacy of the drug when tested against *E. coli* DH5 $\alpha$  live bacteria. These results reveal that RAMEB is able to potentiate the transport of PPA148 by improving the adhesion to the bacterial surface with potential local release of the antibiotic through the IM, without causing any damage to the membrane.

It is suggested that fluidosomes act as drug carriers, releasing their content via fusion with the bacterial OM. Langmuir trough experiments at the air/liquid interface presented a strong interaction between fluidosomes and Rc J5 LPS (Figure 4.10C), revealing the removal of lipids from the surface. This behaviour was investigated in depth using neutron reflectivity, which provides a better insight into the mechanism of action of fluidosomes focusing at the molecular level on the localization of vesicles interacting with membrane models. Fluidosomes challenged an asymmetric Gram negative bacterial OM, consisting of Ra EH100 LPS and d62-DPPC as the outer and inner leaflet, respectively (Figure 4.14). The results suggested the mixing of lipids induced by fluidosomes because the volume fraction of d62-DPPC increased in the outer leaflet, while hydrogenous lipids increased in the inner leaflet of the membrane (Table 4.7). The NR profile presented two additional layers attached to the model membrane, the one describing a water layer connecting the membrane with fluidosomes and the other being the bilayer of the fluidosomes (Figure 4.14; Figure 4.15).

Overall, the data gathered in this thesis has shown that drug-in-RAMEB-in-fluidosomes is a promising formulation for antimicrobial applications and should be tested in a range of Gram negative bacterial membrane. This work has demonstrated that fluidosomes fuse into the model bacterial OM, facilitating the release of its core content (Figure 4.15) and derivatives of  $\beta$ CD (HP $\beta$ CD and RAMEB) enable possibly the transport through the IM. This work is also the first characterization of the novel antimicrobial compound, PPA148, in terms of solubility, environmental stability (temperature and pH) and spectroscopic profile.

### 5.1.1 Future Work

This thesis was an attempt to characterize a novel antimicrobial compound, and enhance its water solubility and efficacy against Gram negative bacteria. The hypotheses of this project were driven by PPA148's predicted physicochemical properties and its MIC against a range of bacterial strains. The MIC of pure PPA148 presented a drop in the presence of PA $\beta$ N, which may have been either due to its efflux pump inhibitory action or its bacterial membrane permeabilizing behavior. Therefore, future work should include the assessment of the integrity of bacterial cell membranes using the fluorescent probe, 8-anilino-1-naphthylsulfonic acid (ANS). ANS is a neutrally charged, hydrophobic probe that fluoresces weakly in aqueous environments, but exhibits enhanced fluorescence in non-polar/hydrophobic environment (255). This will give an insight on the effect of PA $\beta$ N on PPA148's antibacterial activity which in turn will provide invaluable information about the drug's mechanism of action. The interaction studies would provide structural insights on the complexes and the spherical morphology of the loaded liposomes (110). Future work should also include a drug release profile of PPA148, or any other antimicrobial compound encapsulated in cyclodextrin/liposome formulation to determine the degree of drug leakage over time. The dialysis method is applied widely and drug analysis with UV/Vis spectroscopy will identify the released drug concentration. Stability of the drug in the

formulation over time is another important aspect that needs to be defined using mass spectroscopy to detect any possible decomposed products.

In this study, the fusion of fluidosomes with the lipidic component of a model asymmetric Gram negative bacterial membrane was observed using neutron reflectivity. Development of advanced models of Gram negative membranes containing proteins are in progress (256). Using these advanced model membranes to investigate the fusion will give an insight on whether proteins affect this mechanism of action. For a more realistic approach, in vitro experiments on live bacteria should be applied using spectroscopic techniques to localize the formulation within the bacterial cell. Even though the lipid composition in eukaryotic and prokaryotic cells is different (223,224), the toxicity profile of fluidosomes should also be investigated with human epithelial cells to ascertain whether there are any possible side effects for host cells.

Disk diffusion assay was used to assess the susceptibility of bacteria to PPA148-in-RAMEB-in-liposomes. The microbiological assay was focused only on one bacterial strain (*E coli* DH5 $\alpha$ ) yet, to obtain more conclusive data regarding the efficacy of the final formulation on Gram negative bacteria, it must be tested across a wide range of antibiotic-resistant bacteria, such as *P. aeruginosa*. In this test, which is qualitative, the diameter of the inhibition zone is related to the susceptibility of the isolate and to the diffusion rate of the drug through the agar medium. The drawback of this method is that the category of susceptibility is derived from the test rather than from the minimum inhibitory concentration (MIC). That being the case, the MIC of the final formulation needs to be determined in the different types of bacteria used. Formulation with other antibiotics, whose target is in the cytoplasm, i.e. rifampicin, and have become ineffective due to the rise of antimicrobial resistance, should also be tested to elucidate the effectiveness of the drug-in-cyclodextrin-in-liposomes formulation. Collecting all the aforementioned data will help to elucidate the antibacterial activity of a drug-in-cyclodextrin-in-fluidosomes.

# References

1. Livermore DM, Blaser M, Carrs O, Cassell G, Fishman N, Guidos R, et al. Discovery research: the scientific challenge of finding new antibiotics. *J Antimicrob Chemother.* 2011 Sep;66(9):1941–1944.
2. Ventola CL. The antibiotic resistance crisis: part 1: causes and threats. *P T Peer-Rev J Formul Manag.* 2015 Apr;40(4):277–83.
3. Gould IM, Bal AM. New antibiotic agents in the pipeline and how they can help overcome microbial resistance. *Virulence.* 2013 Feb;4(2):185–91.
4. Wright GD. Something old, something new: revisiting natural products in antibiotic drug discovery. *Can J Microbiol.* 2014 Mar;60(3):147–154.
5. Rossolini GM, Arena F, Pecile P, Pollini S. Update on the antibiotic resistance crisis. *Curr Opin Pharmacol.* 2014 Oct;18:56–60.
6. Piddock LJ. The crisis of no new antibiotics—what is the way forward? *Lancet Infect Dis.* 2012 Mar;12(3):249–253.
7. Yocum RR, Rasmussen JR, Strominger JL. The mechanism of action of penicillin. Penicillin acylates the active site of *Bacillus stearothermophilus* D-alanine carboxypeptidase. *J Biol Chem.* 1980 May;255(9):3977–86.
8. Wehrli W. Rifampin: mechanisms of action and resistance. *Rev Infect Dis.* 1983;5 Suppl 3:S407–11.
9. Levy SB, Marshall B. Antibacterial resistance worldwide: causes, challenges and responses. *Nat Med.* 2004 Dec;10(12s):S122–S129.
10. Clatworthy AE, Pierson E, Hung DT. Targeting virulence: a new paradigm for antimicrobial therapy. *Nat Chem Biol.* 2007 Sep;3(9):541–548.
11. van Saene R, Fairclough S, Petros A. Broad- and narrow-spectrum antibiotics: a different approach. *Clin Microbiol Infect Off Publ Eur Soc Clin Microbiol Infect Dis.* 1998 Jan;4(1):56–57.
12. O'Shea R, Moser HE. Physicochemical Properties of Antibacterial Compounds: Implications for Drug Discovery. *J Med Chem.* 2008 May;51(10):2871–2878.
13. Macielag MJ. Chemical Properties of Antimicrobials and Their Uniqueness. In: Dougherty T, Pucci M, editors. *Antibiotic Discovery and Development.* Boston, MA: Springer US; 2012. p. 793–820.
14. Leeson PD, Davis AM. Time-Related Differences in the Physical Property Profiles of Oral Drugs. 2004;47(25):6338–6348.
15. ChemBioDraw Ultra 14.0 Suite - Adept Scientific [Internet]. [cited 2018 Oct 6]. Available from: <http://www.adeptscience.co.uk/products/lab/chembiodraw/chembiodraw-ultra-suite.html>
16. Fernandes J, Gattass CR. Topological Polar Surface Area Defines Substrate Transport by Multidrug Resistance Associated Protein 1 (MRP1/ABCC1). *J Med Chem.* 2009 Feb;52(4):1214–1218.



17. Hou TJ, Zhang W, Xia K, Qiao XB, Xu XJ. ADME Evaluation in Drug Discovery. 5. Correlation of Caco-2 Permeation with Simple Molecular Properties. *J Chem Inf Comput Sci*. 2004 Sep;44(5):1585–1600.
18. Silhavy TJ, Kahne D, Walker S. The bacterial cell envelope. *Cold Spring Harb Perspect Biol*. 2010 May;2(5):a000414.
19. Galanos C, Freudenberg MA. Bacterial endotoxins: biological properties and mechanisms of action. *Mediators Inflamm*. 1993;2(7):S11–16.
20. Homma JY, Matsuura M, Kanegasaki S, Kawakubo Y, Kojima Y, Shibukawa N, et al. Structural requirements of lipid A responsible for the functions: a study with chemically synthesized lipid A and its analogues. *J Biochem (Tokyo)*. 1985 Aug;98(2):395–406.
21. Kotani S, Takada H, Tsujimoto M, Ogawa T, Takahashi I, Ikeda T, et al. Synthetic lipid A with endotoxic and related biological activities comparable to those of a natural lipid A from an *Escherichia coli* re-mutant. *Infect Immun*. 1985 Jul;49(1):225–237.
22. Merck KGaA. Lipopolysaccharides - Structure, Function and Application | Sigma-Aldrich [Internet]. 2018 [cited 2018 Oct 20]. Available from: <https://www.sigmaaldrich.com/technical-documents/articles/biology/glycobiology/lipopolysaccharides.html>
23. Rivera M, McGroarty EJ. Analysis of a common-antigen lipopolysaccharide from *Pseudomonas aeruginosa*. *J Bacteriol*. 1989 Apr;171(4):2244–2248.
24. Steimle A, Autenrieth IB, Frick J-S. Structure and function: Lipid A modifications in commensals and pathogens. *Int J Med Microbiol*. 2016 Aug;306(5):290–301.
25. Wydro P, Flasiński M, Broniatowski M. Molecular organization of bacterial membrane lipids in mixed systems—A comprehensive monolayer study combined with Grazing Incidence X-ray Diffraction and Brewster Angle Microscopy experiments. *Biochim Biophys Acta BBA - Biomembr*. 2012 Jul;1818(7):1745–1754.
26. Piddock LJV. Clinically Relevant Chromosomally Encoded Multidrug Resistance Efflux Pumps in Bacteria. *Clin Microbiol Rev*. 2006 Apr;19(2):382–402.
27. Livermore DM. Antibiotic uptake and transport by bacteria. *Scand J Infect Dis Suppl*. 1990;74:15–22.
28. Tipper DJ. Mode of action of beta-lactam antibiotics. *Pharmacol Ther*. 1985;27(1):1–35.
29. Fernandez L, Hancock REW. Adaptive and Mutational Resistance: Role of Porins and Efflux Pumps in Drug Resistance. *Clin Microbiol Rev*. 2012 Oct;25(4):661–681.
30. Vila J, Martí S, Sánchez-Céspedes J. Porins, efflux pumps and multidrug resistance in *Acinetobacter baumannii*. *J Antimicrob Chemother*. 2007 Jun;59(6):1210–1215.
31. Pajatsch M, Andersen C, Mathes A, Böck A, Benz R, Engelhardt H. Properties of a cyclodextrin-specific, unusual porin from *Klebsiella oxytoca*. *J Biol Chem*. 1999 Aug;274(35):25159–66.
32. Taber HW, Mueller JP, Miller PF, Arrow AS. Bacterial uptake of aminoglycoside antibiotics. *Microbiol Rev*. 1987 Dec;51(4):439–457.
33. Nikaido H. Molecular basis of bacterial outer membrane permeability revisited. *Microbiol Mol Biol Rev MMBR*. 2003 Dec;67(4):593–656.

34. Bolla J-M, Alibert-Franco S, Handzlik J, Chevalier J, Mahamoud A, Boyer G, et al. Strategies for bypassing the membrane barrier in multidrug resistant Gram-negative bacteria. *FEBS Lett.* 2011 Jun;585(11):1682–1690.
35. Amaral L, Martins A, Spengler G, Molnar J. Efflux pumps of Gram-negative bacteria: what they do, how they do it, with what and how to deal with them. *Front Pharmacol.* 2014;4:168.
36. Lewis K. New approaches to antimicrobial discovery. *Biochem Pharmacol.* 2017 Jun;134:87–98.
37. Kennedy DA, Read AF. Why does drug resistance readily evolve but vaccine resistance does not? *Proc Biol Sci.* 2017 Mar;284(1851):20162562.
38. Barber M, Whitehead JEM. Bacteriophage types in penicillin-resistant staphylococcal infection. *Br Med J.* 1949 Sep;2(4627):565–9.
39. Zaman SB, Hussain MA, Nye R, Mehta V, Mamun KT, Hossain N. A Review on Antibiotic Resistance: Alarm Bells are Ringing. *Cureus.* 2017 Jun;9(6):e1403.
40. Högberg LD, Heddini A, Cars O. The global need for effective antibiotics: challenges and recent advances. *Trends Pharmacol Sci.* 2010 Nov;31(11):509–515.
41. Dahal RH, Chaudhary DK. Microbial Infections and Antimicrobial Resistance in Nepal: Current Trends and Recommendations. *Open Microbiol J.* 2018;12:230–242.
42. Antibiotic / Antimicrobial Resistance | CDC [Internet]. [cited 2018 Oct 6]. Available from: <https://www.cdc.gov/drugresistance/index.html>
43. European Antimicrobial Resistance Surveillance Network (EARS-Net) [Internet]. [cited 2018 Oct 6]. Available from: <https://ecdc.europa.eu/en/about-us/partnerships-and-networks/disease-and-laboratory-networks/ears-net>
44. WHO | Antimicrobial resistance. WHO [Internet]. 2018; Available from: <http://www.who.int/antimicrobial-resistance/en/>
45. Delcour AH. Outer membrane permeability and antibiotic resistance. *Biochim Biophys Acta.* 2009;1794(5):808–16.
46. Pagès J-M, Masi M, Barbe J. Inhibitors of efflux pumps in Gram-negative bacteria. *Trends Mol Med.* 2005 Aug;11(8):382–9.
47. Webber MA, Piddock LJV. The importance of efflux pumps in bacterial antibiotic resistance. *J Antimicrob Chemother.* 2003 Jan;51(1):9–11.
48. Rice LB. Challenges in Identifying New Antimicrobial Agents Effective for Treating Infections with *Acinetobacter baumannii* and *Pseudomonas aeruginosa*. *Clin Infect Dis.* 2006;43:100–105.
49. Meletis G. Carbapenem resistance: overview of the problem and future perspectives. *Ther Adv Infect Dis.* 2016 Feb;3(1):15–21.
50. Okdah L, Le Page S, Olaitan AO, Dubourg G, Hadjadj L, Rolain J-M. New therapy from old drugs: synergistic bactericidal activity of sulfadiazine with colistin against colistin-resistant bacteria, including plasmid-mediated colistin-resistant *mcr-1* isolates. *Int J Antimicrob Agents.* 2018 May;51(5):775–783.
51. Watkins RR, Bonomo RA.  $\beta$ -Lactam Antibiotics. *Infect Dis.* 2017 Jan;1203–1216.e2.

52. O'neil J. Securing New Drugs For Future Generations: The Pipeline Of Antibiotics [Internet]. 2015. Available from: [https://amr-review.org/sites/default/files/SECURING NEW DRUGS FOR FUTURE GENERATIONS FINAL WEB\\_0.pdf](https://amr-review.org/sites/default/files/SECURING_NEW_DRUGS_FOR_FUTURE_GENERATIONS_FINAL_WEB_0.pdf)
53. Tacconelli E, Carrara E, Savoldi A, Kattula D, Burkert F. Global Priority List Of Antibiotic-Resistant Bacteria To Guide Research, Discovery, And Development Of New Antibiotics [Internet]. 2017. Available from: <http://www.cdc.gov/drugresistance/threat-report-2013/>
54. Bassetti M, Righi E. New antibiotics and antimicrobial combination therapy for the treatment of gram-negative bacterial infections. *Curr Opin Crit Care*. 2015 Oct;21(5):402–411.
55. Tängdén T. Combination antibiotic therapy for multidrug-resistant Gram-negative bacteria. *Ups J Med Sci*. 2014 May;119(2):149–53.
56. Worthington RJ, Melander C. Combination approaches to combat multidrug-resistant bacteria. *Trends Biotechnol*. 2013 Mar;31(3):177–84.
57. WHO publishes list of bacteria for which new antibiotics are urgently needed [Internet]. [cited 2018 Oct 6]. Available from: <http://www.who.int/news-room/detail/27-02-2017-who-publishes-list-of-bacteria-for-which-new-antibiotics-are-urgently-needed>
58. Tamma PD, Cosgrove SE, Maragakis LL. Combination Therapy for Treatment of Infections with Gram-Negative Bacteria. *Clin Microbiol Rev*. 2012 Jul;25(3):450–470.
59. Tascini C, Tagliaferri E, Giani T, Leonildi A, Flammioni S, Casini B, et al. Synergistic activity of colistin plus rifampin against colistin-resistant KPC-producing *Klebsiella pneumoniae*. *Antimicrob Agents Chemother*. 2013 Aug;57(8):3990–3.
60. Melander RJ, Melander C. The Challenge of Overcoming Antibiotic Resistance: An Adjuvant Approach? *ACS Infect Dis*. 2017;3(8):559–563.
61. Rolinson GN. The history and background of Augmentin. *South Afr Med J Suid-Afr Tydskr Vir Geneesk*. 1982 Jul;62(5 Spec No):3A–4A.
62. Coates ARM, Hu Y. Novel approaches to developing new antibiotics for bacterial infections. *Br J Pharmacol*. 2007 Dec;152(8):1147–54.
63. Pagès J-M, Amaral L. Mechanisms of drug efflux and strategies to combat them: Challenging the efflux pump of Gram-negative bacteria. *Biochim Biophys Acta BBA - Proteins Proteomics*. 2009 May;1794(5):826–833.
64. Torres A, Zhong N, Pacht J, Timsit J-F, Kollef M, Chen Z, et al. Ceftazidime-avibactam versus meropenem in nosocomial pneumonia, including ventilator-associated pneumonia (REPROVE): a randomised, double-blind, phase 3 non-inferiority trial. *Lancet Infect Dis*. 2018 Mar;18(3):285–295.
65. Castanheira M, Rhomberg PR, Flamm RK, Jones RN. Effect of the  $\beta$ -Lactamase Inhibitor Vaborbactam Combined with Meropenem against Serine Carbapenemase-Producing Enterobacteriaceae. *Antimicrob Agents Chemother*. 2016 Sep;60(9):5454–5458.
66. Zhanel GG, Chung P, Adam H, Zelenitsky S, Denisuik A, Schweizer F, et al. Ceftolozane/Tazobactam: A Novel Cephalosporin/ $\beta$ -Lactamase Inhibitor Combination with Activity Against Multidrug-Resistant Gram-Negative Bacilli. *Drugs*. 2014 Jan;74(1):31–51.
67. Lomovskaya O, Warren MS, Lee A, Galazzo J, Fronko R, Lee M, et al. Identification and Characterization of Inhibitors of Multidrug Resistance Efflux Pumps in *Pseudomonas*

- aeruginosa: Novel Agents for Combination Therapy. *Antimicrob Agents Chemother*. 2001 Jan;45(1):105–116.
68. Lomovskaya O, Bostian KA. Practical applications and feasibility of efflux pump inhibitors in the clinic—A vision for applied use. *Biochem Pharmacol*. 2006 Mar;71(7):910–918.
69. Lamers RP, Cavallari JF, Burrows LL. The Efflux Inhibitor Phenylalanine-Arginine Beta-Naphthylamide (PA $\beta$ N) Permeabilizes the Outer Membrane of Gram-Negative Bacteria. *PLOS ONE*. 2013 Mar 27;8(3):e60666.
70. Lewis K. Platforms for antibiotic discovery. *Nat Rev Drug Discov*. 2013 May;12(5):371–387.
71. Edwards DI. Nitroimidazole drugs—action and resistance mechanisms. I. Mechanisms of action. *J Antimicrob Chemother*. 1993 Jan;31(1):9–20.
72. Fleck LE, North EJ, Lee RE, Mulcahy LR, Casadei G, Lewis K. A Screen for and Validation of Prodrug Antimicrobials. *Antimicrob Agents Chemother*. 2014 Mar;58(3):1410–1419.
73. Brewster ME, Loftsson T. Cyclodextrins as pharmaceutical solubilizers. *Adv Drug Deliv Rev*. 2007 Jul;59(7):645–666.
74. French D. The Schardinger Dextrins. *Adv Carbohydr Chem*. 1957 Jan;12:189–260.
75. Loftsson T, Másson M, Brewster ME. Self-Association of Cyclodextrins and Cyclodextrin Complexes. *J Pharm Sci*. 2004 May;93(5):1091–1099.
76. Biwer A, Antranikian G, Heinzle E. Enzymatic production of cyclodextrins. *Appl Microbiol Biotechnol*. 2002 Sep;59(6):609–617.
77. Ryzhakov A, Do Thi T, Stappaerts J, Bertoletti L, Kimpe K, Sá Couto AR, et al. Self-Assembly of Cyclodextrins and Their Complexes in Aqueous Solutions. *J Pharm Sci*. 2016 Sep;105(9):2556–2569.
78. González-Gaitano G, Rodríguez P, Isasi JR, Fuentes M, Tardajos G, Sánchez M. The Aggregation of Cyclodextrins as Studied by Photon Correlation Spectroscopy. *J Incl Phenom Macrocycl Chem*. 2002;44(1/4):101–105.
79. Santosh S. Terdale, Dagade and DH, Patil\* KJ. Thermodynamic Studies of Molecular Interactions in Aqueous  $\alpha$ -Cyclodextrin Solutions: Application of McMillan–Mayer and Kirkwood–Buff Theories. 2006;110(37):18583–18593.
80. Coleman AW, Nicolis I, Keller N, Dalbiez JP. Aggregation of cyclodextrins: An explanation of the abnormal solubility of  $\beta$ -cyclodextrin. *J Incl Phenom Mol Recognit Chem*. 1992 Jun;13(2):139–143.
81. Zhang J, Ma PX. Cyclodextrin-based supramolecular systems for drug delivery: Recent progress and future perspective. *Adv Drug Deliv Rev*. 2013 Aug;65(9):1215–1233.
82. Sharma N, Baldi A. Exploring versatile applications of cyclodextrins: an overview. *Drug Deliv*. 2016 Jul;23(3):1–19.
83. Gidwani B, Vyas A. Inclusion complexes of bendamustine with  $\beta$ -CD, HP- $\beta$ -CD and Epi- $\beta$ -CD: in-vitro and in-vivo evaluation. *Drug Dev Ind Pharm*. 2015 Dec;41(12):1978–1988.
84. GRAS Notices [Internet]. 2016 [cited 2018 Oct 6]. Available from: [https://www.accessdata.fda.gov/scripts/fdcc/index.cfm?set=GRASNotices&sort=Date\\_of\\_closure&order=DESC&showAll=true&type=basic&search=](https://www.accessdata.fda.gov/scripts/fdcc/index.cfm?set=GRASNotices&sort=Date_of_closure&order=DESC&showAll=true&type=basic&search=)

85. Medicines Agency E. Background review for cyclodextrins used as excipients [Internet]. 2014. Available from: [www.ema.europa.eu/contact](http://www.ema.europa.eu/contact)
86. Annex to the European Commission guideline on “Excipients in the labelling and package leaflet of medicinal products for human use” (SANTE-2017-11668) Excipients and information for the package leaflet [Internet]. 2017. Available from: [https://www.ema.europa.eu/documents/scientific-guideline/annex-european-commission-guideline-excipients-labelling-package-leaflet-medicinal-products-human\\_en.pdf](https://www.ema.europa.eu/documents/scientific-guideline/annex-european-commission-guideline-excipients-labelling-package-leaflet-medicinal-products-human_en.pdf)
87. Szente, Szejtli. Highly soluble cyclodextrin derivatives: chemistry, properties, and trends in development. *Adv Drug Deliv Rev.* 1999 Mar;36(1):17–28.
88. Uekama K, Otagiri M. Cyclodextrins in drug carrier systems. *Crit Rev Ther Drug Carrier Syst.* 1987;3(1):1–40.
89. Tiwari G, Tiwari R, Rai AK. Cyclodextrins in delivery systems: Applications. *J Pharm Bioallied Sci.* 2010 Apr;2(2):72–79.
90. Shastri VR, Yue I, Hildgen P, Sinistera RD, Langer R. Method of increasing the efficacy Of Antibiotics By Complexing With Cyclodextrins. US2003/0078215A1., 2003.
91. Agnes M, Thanassoulas A, Stavropoulos P, Nounesis G, Miliotis G, Miriagou V, et al. Designed positively charged cyclodextrin hosts with enhanced binding of penicillins as carriers for the delivery of antibiotics: The case of oxacillin. *Int J Pharm.* 2017 Oct;531(2):480–491.
92. Thatiparti TR, von Recum HA. Cyclodextrin Complexation for Affinity-Based Antibiotic Delivery. *Macromol Biosci.* 2010 Jan;10(1):82–90.
93. Taha M, Chai F, Blanchemain N, Neut C, Goube M, Maton M, et al. Evaluation of sorption capacity of antibiotics and antibacterial properties of a cyclodextrin-polymer functionalized hydroxyapatite-coated titanium hip prosthesis. *Int J Pharm.* 2014 Dec;477(1–2):380–389.
94. Paczkowska M, Mizera M, Szymanowska-Powalowska D, Lewandowska K, Błaszczyk W, Gościńska J, et al.  $\beta$ -Cyclodextrin complexation as an effective drug delivery system for meropenem. *Eur J Pharm Biopharm.* 2016 Feb;99:24–34.
95. Ferrari F, Sorrenti M, Rossi S, Catenacci L, Sandri G, Bonferoni MC, et al. Vancomycin–Triacetyl Cyclodextrin Interaction Products for Prolonged Drug Delivery. *Pharm Dev Technol.* 2008 Jan;13(1):65–73.
96. Deygen IM, Egorov AM, Kudryashova EV. Structure and stability of fluoroquinolone-(2-hydroxypropyl)- $\beta$ -cyclodextrin complexes as perspective antituberculosis drugs. *Mosc Univ Chem Bull.* 2016 Jan;71(1):1–6.
97. Jones MN, Song Y-H, Kaszuba M, Reboiras MD. The Interaction of Phospholipid Liposomes with Bacteria and Their Use in the Delivery of Bactericides. *J Drug Target.* 1997 Jan;5(1):25–34.
98. Rukavina Z, Vanić Ž. Current Trends in Development of Liposomes for Targeting Bacterial Biofilms. *Pharmaceutics.* 2016 May;8(2):18.
99. Schifflers R, Storm G, Bakker-Woudenberg I. Liposome-encapsulated aminoglycosides in pre-clinical and clinical studies. *J Antimicrob Chemother.* 2001 Sep;48(3):333–344.
100. Meers P, Neville M, Malinin V, Scotto AW, Sardaryan G, Kurumunda R, et al. Biofilm penetration, triggered release and in vivo activity of inhaled liposomal amikacin in chronic

- Pseudomonas aeruginosa* lung infections. *J Antimicrob Chemother.* 2008 Feb;61(4):859–868.
101. Beaulac C, Sachetelli S, Lagacé J. Aerosolization of Low Phase Transition Temperature Liposomal Tobramycin as a Dry Powder in an Animal Model of Chronic Pulmonary Infection Caused by *Pseudomonas aeruginosa*. *J Drug Target.* 1999 Jan;7(1):33–41.
  102. Beaulac C, Sachetelli S, Lagace J. In-vitro bactericidal efficacy of sub-MIC concentrations of liposome- encapsulated antibiotic against gram-negative and gram-positive bacteria. *J Antimicrob Chemother.* 1998 Jan;41(1):35–41.
  103. Beaulac C, Clément-Major S, Hawari J, Lagacé J. Eradication of mucoid *Pseudomonas aeruginosa* with fluid liposome-encapsulated tobramycin in an animal model of chronic pulmonary infection. *Antimicrob Agents Chemother.* 1996 Mar;40(3):665–669.
  104. Halwani M, Yebio B, Suntres ZE, Alipour M, Azghani AO, Omri A. Co-encapsulation of gallium with gentamicin in liposomes enhances antimicrobial activity of gentamicin against *Pseudomonas aeruginosa*. *J Antimicrob Chemother.* 2008 Sep;62(6):1291–1297.
  105. Manca ML, Sinico C, Maccioni AM, Diez O, Fadda AM, Manconi M. Composition influence on pulmonary delivery of rifampicin liposomes. *Pharmaceutics.* 2012 Nov;4(4):590–606.
  106. WHO. ANTIBACTERIAL AGENTS IN CLINICAL DEVELOPMENT [Internet]. 2017. Available from: <http://www.who.int/about/licensing>.
  107. Rahman KM, Sutton JM, Picconi P. Pbd antibacterial agents. WO 2017/098257 A1, 2017.
  108. Picconi P, Miraz Rahman Anthony Coates Mark Sutton K. Design, Synthesis and Biological Evaluation of Minor Groove Binders as Antibacterial Agents Against Multi-Drug Resistant Pathogens. 2017;
  109. Park DR. The microbiology of ventilator-associated pneumonia. *Respir Care.* 2005 Jun;50(6):742–63; discussion 763–5.
  110. Zhang L, Zhang Q, Wang X, Zhang W, Lin C, Chen F, et al. Drug-in-cyclodextrin-in-liposomes: A novel drug delivery system for flurbiprofen. *Int J Pharm.* 2015 Aug;492(1–2):40–45.
  111. McCormack B, Gregoriadis G. Entrapment of Cyclodextrin-Drug Complexes into Liposomes: Potential Advantages in Drug Delivery. *J Drug Target.* 1994 Jan;2(5):449–454.
  112. Sebaaly C, Charcosset C, Fourmentin S, Greige-Gerges H. Potential Applications of Cyclodextrin Inclusion Complexes, Liposomes, and Drug-in-Cyclodextrin-in-Liposome in Food Industry and Packaging. *Role Mater Sci Food Bioeng.* 2018 Jan;187–234.
  113. Azzi J, Auezova L, Danjou P-E, Fourmentin S, Greige-Gerges H. First evaluation of drug-in-cyclodextrin-in-liposomes as an encapsulating system for nerolidol. *Food Chem.* 2018 Jul;255:399–404.
  114. Gharib R, Greige-Gerges H, Fourmentin S, Charcosset C, Auezova L. Liposomes incorporating cyclodextrin–drug inclusion complexes: Current state of knowledge. *Carbohydr Polym.* 2015 Sep;129:175–186.
  115. Maestrelli F, González-Rodríguez ML, Rabasco AM, Mura P. Effect of preparation technique on the properties of liposomes encapsulating ketoprofen–cyclodextrin complexes aimed for transdermal delivery. *Int J Pharm.* 2006 Apr;312(1–2):53–60.

116. Fatouros DG, Hatzidimitriou K, Antimisiaris SG. Liposomes encapsulating prednisolone and prednisolone-cyclodextrin complexes: comparison of membrane integrity and drug release. *Eur J Pharm Sci Off J Eur Fed Pharm Sci.* 2001 Jun;13(3):287–96.
117. Bragagni M, Maestrelli F, Mennini N, Ghelardini C, Mura P. Liposomal formulations of prilocaine: effect of complexation with hydroxypropyl- $\beta$ -cyclodextrin on drug anesthetic efficacy. *J Liposome Res.* 2010 Dec;20(4):315–322.
118. Hagiwara Y, Arima H, Hirayama F, Uekama K. Prolonged Retention of Doxorubicin in Tumor Cells by Encapsulation of  $\gamma$ -Cyclodextrin Complex in Pegylated Liposomes. *J Incl Phenom Macrocycl Chem.* 2006 Oct;56(1–2):65–68.
119. Dhule SS, Penfornis P, Frazier T, Walker R, Feldman J, Tan G, et al. Curcumin-loaded  $\gamma$ -cyclodextrin liposomal nanoparticles as delivery vehicles for osteosarcoma. *Nanomedicine Nanotechnol Biol Med.* 2012 May;8(4):440–451.
120. Škalko N, Brandl M, Bećirević-Laćan M, Filipović-Grčić J, Jalšenjak I. Liposomes with nifedipine and nifedipine-cyclodextrin complex: calorimetric and plasma stability comparison. *Eur J Pharm Sci.* 1996 Nov;4(6):359–366.
121. Zhu Q, Guo T, Xia D, Li X, Zhu C, Li H, et al. Pluronic F127-modified liposome-containing tacrolimus-cyclodextrin inclusion complexes: improved solubility, cellular uptake and intestinal penetration. *J Pharm Pharmacol.* 2013 Aug;65(8):1107–1117.
122. Muheim C, Götzke H, Eriksson AU, Lindberg S, Lauritsen I, Nørholm MHH, et al. Increasing the permeability of *Escherichia coli* using MAC13243. *Sci Rep.* 2017 Dec;7(1):17629.
123. Komljenović I, Marquardt D, Harroun TA, Sternin E. Location of chlorhexidine in DMPC model membranes: a neutron diffraction study. *Chem Phys Lipids.* 2010 Jun;163(6):480–487.
124. Dickey A, Faller R. Examining the contributions of lipid shape and headgroup charge on bilayer behavior. *Biophys J.* 2008 Sep;95(6):2636–2646.
125. Jouhet J. Importance of the hexagonal lipid phase in biological membrane organization. *Front Plant Sci.* 2013;4:494.
126. Khalifat N, Fournier J-B, Angelova MI, Puff N. Lipid packing variations induced by pH in cardiolipin-containing bilayers: The driving force for the cristae-like shape instability. *Biochim Biophys Acta BBA - Biomembr.* 2011 Nov;1808(11):2724–2733.
127. White GF, Racher KI, Lipski A, Hallett FR, Wood JM. Physical properties of liposomes and proteoliposomes prepared from *Escherichia coli* polar lipids. *Biochim Biophys Acta BBA - Biomembr.* 2000 Sep;1468(1–2):175–186.
128. Brown RE, Brockman HL. Using Monomolecular Films to Characterize Lipid Lateral Interactions. *Methods Mol Biol Clifton NJ.* 2007;398:41–58.
129. Brockman H. Dipole potential of lipid membranes. *Chem Phys Lipids.* 1994 Sep;73(1–2):57–79.
130. Marsh D. Lateral pressure in membranes. *Biochim Biophys Acta.* 1996 Oct;1286(3):183–223.
131. Penfold J, Thomas RK. The application of the specular reflection of neutrons to the study of surfaces and interfaces. *J Phys Condens Matter.* 1990 Feb;2(6):1369–1412.

132. Doshi DA, Dattelbaum AM, Watkins EB, Brinker CJ, Swanson BI, Shreve AP, et al. Neutron Reflectivity Study of Lipid Membranes Assembled on Ordered Nanocomposite and Nanoporous Silica Thin Films. *Langmuir*. 2005;21(7):2865–2870.
133. Sivia, D. S. (St John's College O. Elementary Scattering Theory: For X-ray and Neutron Users. 1st ed. Oxford University Press; 2011.
134. Lakey JH. Neutrons for biologists: a beginner's guide, or why you should consider using neutrons. *J R Soc Interface*. 2009 Oct;6 Suppl 5(Suppl 5):S567–573.
135. Clifton LA, Neylon C, Lakey JH. Examining Protein–Lipid Complexes Using Neutron Scattering. In: *Methods in molecular biology*. 2013. p. 119–150.
136. Lu JR, Su TJ, Thomas RK. Structural Conformation of Bovine Serum Albumin Layers at the Air–Water Interface Studied by Neutron Reflection. *J Colloid Interface Sci*. 1999 May;213(2):426–437.
137. Leimgruber W, Stefanović V, Schenker F, Karr A, Berger J. Isolation and characterization of anthramycin, a new antitumor antibiotic. *J Am Chem Soc*. 1965 Dec;87(24):5791–5793.
138. Mantaj J, Jackson PJM, Karu K, Rahman KM, Thurston DE. Covalent Bonding of Pyrrolobenzodiazepines (PBDs) to Terminal Guanine Residues within Duplex and Hairpin DNA Fragments. *PloS One*. 2016;11(4):e0152303.
139. Tse H, Gu Q, Sze K-H, Chu IK, Kao RY-T, Lee K-C, et al. A tricyclic pyrrolobenzodiazepine produced by *Klebsiella oxytoca* is associated with cytotoxicity in antibiotic-associated hemorrhagic colitis. *J Biol Chem*. 2017 Sep;292(47):19503–19520.
140. Gerratana B. Biosynthesis, synthesis, and biological activities of pyrrolobenzodiazepines. *Med Res Rev*. 2012 Mar;32(2):254–93.
141. Basher MA, Rahman KM, Jackson PJM, Thurston DE, Fox KR. Sequence-selective binding of C8-conjugated pyrrolobenzodiazepines (PBDs) to DNA. *Biophys Chem*. 2017 Nov;230:53–61.
142. Mantaj J, Jackson PJM, Rahman KM, Thurston DE. From Anthramycin to Pyrrolobenzodiazepine (PBD)-Containing Antibody–Drug Conjugates (ADCs). *Angew Chem - Int Ed*. 2017;56(2):462–488.
143. Brucoli F, Guzman JD, Basher MA, Evangelopoulos D, McMahon E, Munshi T, et al. DNA sequence-selective C8-linked pyrrolobenzodiazepine–heterocyclic polyamide conjugates show anti-tubercular-specific activities. *J Antibiot (Tokyo)*. 2016 Dec;69(12):843–9.
144. Brown DG, May-Dracka TL, Gagnon MM, Tommasi R. Trends and Exceptions of Physical Properties on Antibacterial Activity for Gram-Positive and Gram-Negative Pathogens. *J Med Chem*. 2014 Dec;57(23):10144–10161.
145. Upadhyay S, Kumar G. NMR and molecular modelling studies on the interaction of fluconazole with  $\beta$ -cyclodextrin. *Chem Cent J*. 2009 Aug;3(1):9.
146. Loftsson T, Jarho P, Másson M, Järvinen T. Cyclodextrins in drug delivery. *Expert Opin Drug Deliv*. 2005 Mar;2(2):335–351.
147. Loftsson T, Másson M. Evaluation of cyclodextrin solubilization of drugs. *Int J Pharm*. 2005;302:18–28.
148. Gabelica V, Galic N, Pauw E. On the specificity of cyclodextrin complexes detected by electrospray mass spectrometry. *J Am Soc Mass Spectrom*. 2002 Aug;13(8):946–953.



149. Correia I, Bezenine N, Ronzani N, Platzer N, Beloeil J-C, Doan B-T. Study of inclusion complexes of acridine with  $\beta$ - and (2,6-di-O-methyl)- $\beta$ -cyclodextrin by use of solubility diagrams and NMR spectroscopy. *J Phys Org Chem*. 2002 Sep;15(9):647–659.
150. Tolman JA, Williams RO. Advances in the pulmonary delivery of poorly water-soluble drugs: influence of solubilization on pharmacokinetic properties. *Drug Dev Ind Pharm*. 2010 Jan;36(1):1–30.
151. Valero M, Castiglione F, Mele A, da Silva MA, Grillo I, González-Gaitano G, et al. Competitive and Synergistic Interactions between Polymer Micelles, Drugs, and Cyclodextrins: The Importance of Drug Solubilization Locus. *Langmuir ACS J Surf Colloids*. 2016 13;32(49):13174–86.
152. Nigam S, Durocher G. Spectral and Photophysical Studies of Inclusion Complexes of Some Neutral 3H-Indoles and Their Cations and Anions with  $\beta$ -Cyclodextrin. *J Phys Chem*. 1996 Jan;100(17):7135–7142.
153. Peeters J, Neeskens P, Tollenaere JP, Van Remoortere P, Brewster ME. Characterization of the interaction of 2-hydroxypropyl- $\beta$ -cyclodextrin with itraconazole at pH 2, 4, and 7. *J Pharm Sci*. 2002 Jun;91(6):1414–1422.
154. Chen A, Liu M, Dong L, Sun D. Study on the effect of solvent on the inclusion interaction of hydroxypropyl- $\beta$ -cyclodextrin with three kinds of coumarins by phase solubility method. *Fluid Phase Equilibria*. 2013 Mar;341:42–47.
155. Loftsson T, Brewster ME. Cyclodextrins as Functional Excipients: Methods to Enhance Complexation Efficiency. *J Pharm Sci*. 2012 Sep;101(9):3019–3032.
156. Huang CY. Determination of binding stoichiometry by the continuous variation method: The job plot. *Methods Enzymol*. 1982 Jan;87:509–525.
157. Bertholet P, Gueders M, Dive G, Albert A, Barillaro V, Perly B, et al. The effect of cyclodextrins on the aqueous solubility of a new MMP inhibitor: phase solubility, <sup>1</sup>H-NMR spectroscopy and molecular modeling studies, preparation and stability study of nebulizable solutions. *J Pharm Pharm Sci Publ Can Soc Pharm Sci Soc Can Sci Pharm*. 2005 Jul;8(2):163–174.
158. Angiolini L, Agnes M, Cohen B, Yannakopoulou K, Douhal A. Formation, characterization and pH dependence of rifampicin: heptakis(2,6-di-O-methyl)- $\beta$ -cyclodextrin complexes. *Int J Pharm*. 2017 Oct;531(2):668–675.
159. Hirayama F, Kurihara M, Horiuchi Y, Utsuki T, Uekama K, Yamasaki M. Preparation of heptakis(2,6-di-O-ethyl)-beta-cyclodextrin and its nuclear magnetic resonance spectroscopic characterization. *Pharm Res*. 1993 Feb;10(2):208–13.
160. Iza N, Guerrero-Martínez A, Tardajos G, Ortiz MJ, Palao E, Montoro T, et al. Using Inclusion Complexes with Cyclodextrins To Explore the Aggregation Behavior of a Ruthenium Metallosurfactant. *Langmuir*. 2015 Mar;31(9):2677–2688.
161. Poór M, Zand A, Szente L, Lemli B, Kunsági-Máté S, Poór M, et al. Interaction of  $\alpha$ - and  $\beta$ -zeaxalenols with  $\beta$ -cyclodextrins. *Molecules*. 2017 Nov;22(11):1910.
162. Tewes F, Brillault J, Couet W, Olivier J-C. Formulation of rifampicin–cyclodextrin complexes for lung nebulization. *J Controlled Release*. 2008 Jul;129(2):93–99.
163. Chadha R, Saini A, Gupta S, Arora P, Thakur D, Jain DVS. Encapsulation of rifampicin by natural and modified  $\beta$ -cyclodextrins: characterization and thermodynamic parameters. *J Incl Phenom Macrocycl Chem*. 2010 Jun;67(1–2):109–116.

164. He D, Deng P, Yang L, Tan Q, Liu J, Yang M, et al. Molecular encapsulation of rifampicin as an inclusion complex of hydroxypropyl- $\beta$ -cyclodextrin: Design; characterization and in vitro dissolution. *Colloids Surf B Biointerfaces*. 2013 Mar;103:580–585.
165. International Conference on Harmonization. Impurities in New Drug Products - Q3B (R2) [Internet]. 2006 p. 12. Report No.: June. Available from: [http://scholar.google.com/scholar?hl=en&btnG=Search&q=intitle:Q3B\(R2\)+-+Impurities+in+New+Drug+Products#2](http://scholar.google.com/scholar?hl=en&btnG=Search&q=intitle:Q3B(R2)+-+Impurities+in+New+Drug+Products#2)
166. Dabkowski J, Zagórska I, Dabkowska M, Koczorowski Z, Trasatti S. Adsorption of DMSO at the free surface of water: surface excesses and surface potential shifts in the low concentration range. *J Chem Soc Faraday Trans*. 1996 Jan;92(20):3873–3878.
167. David S. Karpovich, Ray D. Adsorption of Dimethyl Sulfoxide to the Liquid/Vapor Interface of Water and the Thermochemistry of Transport across the Interface. *J Phys Chem B*. 1998;102(4):649–652.
168. Christian F. Wertz, Santore MM. Effect of Surface Hydrophobicity on Adsorption and Relaxation Kinetics of Albumin and Fibrinogen: Single-Species and Competitive Behavior. *Langmuir*. 2001;17(10):3006–3016.
169. Wang J, Matayoshi E. Solubility at the molecular level: development of a critical aggregation concentration (CAC) assay for estimating compound monomer solubility. *Pharm Res*. 2012 Jul;29(7):1745–54.
170. Bonev B, Hooper J, Parisot J. Principles of assessing bacterial susceptibility to antibiotics using the agar diffusion method. *J Antimicrob Chemother*. 2008 Mar;61(6):1295–1301.
171. Loftsson T. Non-inclusion cyclodextrin complexes [Internet]. US7,115,586B2, 2004. Available from: <https://patentimages.storage.googleapis.com/6d/3b/97/875e2cd02c0c26/US7115586.pdf>
172. Upadhye SB, Kulkarni SJ, Majumdar S, Avery MA, Gul W, ElSohly MA, et al. Preparation and characterization of inclusion complexes of a hemisuccinate ester prodrug of delta9-tetrahydrocannabinol with modified beta-cyclodextrins. *AAPS PharmSciTech*. 2010 Jun;11(2):509–17.
173. Ferreira DA, Ferreira AG, Vizzotto L, Federman Neto A, de Oliveira AG. Analysis of the molecular association of rifampicin with hydroxypropyl- $\beta$ -cyclodextrin. *Rev Bras Ciênc Farm*. 2004 Mar;40(1):43–51.
174. Drulis-Kawa Z, Gubernator J, Dorotkiewicz-Jach A, Doroszkiewicz W, Kozubek A. In vitro antimicrobial activity of liposomal meropenem against *Pseudomonas aeruginosa* strains. *Int J Pharm*. 2006 Jun;315(1–2):59–66.
175. Loftsson T, Hreinsdóttir D, Másson M. The complexation efficiency. *J Incl Phenom Macrocycl Chem*. 2007 Mar;57(1–4):545–552.
176. Liu L, Guo Q-X. The Driving Forces in the Inclusion Complexation of Cyclodextrins. *J Incl Phenom Macrocycl Chem*. 2002;42(1–2):1–14.
177. Antimicrobial resistance (EARS-Net) - Annual Epidemiological Report for 2014 [Internet]. [cited 2018 Oct 6]. Available from: <https://ecdc.europa.eu/en/publications-data/antimicrobial-resistance-ears-net-annual-epidemiological-report-2014>
178. Peleg AY, Hooper DC. Hospital-Acquired Infections Due to Gram-Negative Bacteria. *N Engl J Med*. 2010 May;362(19):1804–1813.

179. Sachetelli S, Khalil H, Chen T, Beaulac C, Sénéchal S, Lagacé J. Demonstration of a fusion mechanism between a fluid bactericidal liposomal formulation and bacterial cells. *Biochim Biophys Acta*. 2000 Feb;1463(2):254–66.
180. Akbarzadeh A, Rezaei-Sadabady R, Davaran S, Joo SW, Zarghami N, Hanifehpour Y, et al. Liposome: classification, preparation, and applications. *Nanoscale Res Lett*. 2013 Feb;8(1):102.
181. Huang Z, London E. Effect of Cyclodextrin and Membrane Lipid Structure upon Cyclodextrin–Lipid Interaction. *Langmuir*. 2013 Nov;29(47):14631–14638.
182. Anderson TG, Tan A, Ganz P, Seelig J. Calorimetric measurement of phospholipid interaction with methyl-beta-cyclodextrin. *Biochemistry*. 2004 Mar;43(8):2251–2261.
183. Lioffi AS, Ntountaniotis D, Kellici TF, Chatziathanasiadou MV, Megariotis G, Mania M, et al. Exploring the interactions of irbesartan and irbesartan–2-hydroxypropyl- $\beta$ -cyclodextrin complex with model membranes. *Biochim Biophys Acta BBA - Biomembr*. 2017 Jun;1859(6):1089–1098.
184. Hudzicki J. Kirby-Bauer Disk Diffusion Susceptibility Test Protocol. *Am Soc Microbiol*. 2009 Dec;1–23.
185. Zhang H-M, Li Z, Uematsu K, Kobayashi T, Horikoshi K. Antibacterial activity of cyclodextrins against *Bacillus* strains. *Arch Microbiol*. 2008 Nov;190(5):605–609.
186. Szoka F, Papahadjopoulos D. Comparative Properties and Methods of Preparation of Lipid Vesicles (Liposomes). *Annu Rev Biophys Bioeng*. 1980 Jun;9(1):467–508.
187. Bhattacharjee S. DLS and zeta potential – What they are and what they are not? *J Controlled Release*. 2016 Aug;235:337–351.
188. Stewart JCM. Colorimetric determination of phospholipids with ammonium ferrothiocyanate. *Anal Biochem*. 1980 May;104(1):10–14.
189. Bozzuto G, Molinari A. Liposomes as nanomedical devices. *Int J Nanomedicine*. 2015 Feb;10:975–999.
190. Burgess S. Liposome Preparation - Avanti® Polar Lipids | Sigma-Aldrich [Internet]. 1998 [cited 2018 Oct 7]. Available from: <https://www.sigmaaldrich.com/technical-documents/articles/biology/liposome-preparation.html>
191. Wetterau JR, Jonas A. Effect of dipalmitoylphosphatidylcholine vesicle curvature on the reaction with human apolipoprotein A-I. *J Biol Chem*. 1982 Sep;257(18):10961–10966.
192. Huang C-M, Chen C-H, Pornpattananangkul D, Zhang L, Chan M, Hsieh M-F, et al. Eradication of drug resistant *Staphylococcus aureus* by liposomal oleic acids. *Biomaterials*. 2011 Jan;32(1):214–221.
193. Hope MJ, Bally MB, Mayer LD, Janoff AS, Cullis PR. Generation of multilamellar and unilamellar phospholipid vesicles. *Chem Phys Lipids*. 1986 Jun;40(2–4):89–107.
194. Connor J, Sullivan S, Huang H L. Monoclonal Antibody And Liposomes. *Pharmacol Ther*. 1985;28(3):341–365.
195. Drulis-Kawa Z, Dorotkiewicz-Jach A. Liposomes as delivery systems for antibiotics. *Int J Pharm*. 2010 Mar;387(1–2):187–198.

196. Drulis-Kawa Z, Gubernator J, Dorotkiewicz-Jach A, Doroszkiewicz W, Kozubek A. A comparison of the *in vitro* antimicrobial activity of liposomes containing meropenem and gentamicin. *Cell Mol Biol Lett*. 2006;11(3):360–375.
197. Tandrup Schmidt S, Foged C, Smith Korsholm K, Rades T, Christensen D. Liposome-Based Adjuvants for Subunit Vaccines: Formulation Strategies for Subunit Antigens and Immunostimulators. *Pharmaceutics*. 2016 Mar;8(1):7.
198. Disalvo EA, Hollmann A, Martini MF. Hydration in Lipid Monolayers: Correlation of Water Activity and Surface Pressure. *Subcell Biochem*. 2015;71:213–231.
199. Disalvo EA, Lairion F, Martini F, Tymczynsyn E, Frías M, Almaleck H, et al. Structural and functional properties of hydration and confined water in membrane interfaces. *Biochim Biophys Acta BBA - Biomembr*. 2008 Dec;1778(12):2655–2670.
200. Binder H, Zschörnig O. The effect of metal cations on the phase behavior and hydration characteristics of phospholipid membranes. *Chem Phys Lipids*. 2002 May;115(1–2):39–61.
201. Gurtovenko AA, Vattulainen I. Effect of NaCl and KCl on Phosphatidylcholine and Phosphatidylethanolamine Lipid Membranes: Insight from Atomic-Scale Simulations for Understanding Salt-Induced Effects in the Plasma Membrane. *J Phys Chem B*. 2008 Feb;112(7):1953–1962.
202. Melcrová A, Pokorna S, Pullanchery S, Kohagen M, Jurkiewicz P, Hof M, et al. The complex nature of calcium cation interactions with phospholipid bilayers. *Sci Rep*. 2016 Dec;6(1):38035.
203. Szente L, Fenyvesi É. Cyclodextrin-Lipid Complexes: Cavity Size Matters. *Struct Chem*. 2017 Apr;28(2):479–492.
204. Szejtli J, Cserhádi T, Szögyi M. Interactions between cyclodextrins and cell-membrane phospholipids. *Carbohydr Polym*. 1986 Jan;6(1):35–49.
205. Nishijo J, Shiota S, Mazima K, Inoue Y, Mizuno H, Yoshida J. Interactions of cyclodextrins with dipalmitoyl, distearoyl, and dimyristoyl phosphatidyl choline liposomes. A study by leakage of carboxyfluorescein in inner aqueous phase of unilamellar liposomes. *Chem Pharm Bull (Tokyo)*. 2000 Jan;48(1):48–52.
206. Uhríková D, Kučerka N, Teixeira J, Gordeliy V, Balgavý P. Structural changes in dipalmitoylphosphatidylcholine bilayer promoted by Ca<sup>2+</sup> ions: a small-angle neutron scattering study. *Chem Phys Lipids*. 2008 Oct;155(2):80–89.
207. Pedersen UR, Leidy C, Westh P, Peters GH. The effect of calcium on the properties of charged phospholipid bilayers. *Biochim Biophys Acta BBA - Biomembr*. 2006 May;1758(5):573–582.
208. Lapinski MM, Castro-Forero A, Greiner AJ, Ofoli RY, Blanchard GJ. Comparison of Liposomes Formed by Sonication and Extrusion: Rotational and Translational Diffusion of an Embedded Chromophore. *Langmuir*. 2007 Nov;23(23):11677–11683.
209. Connors KA, Pendergast DD. Microscopic binding constants in cyclodextrin systems: complexation of .alpha.-cyclodextrin with sym-1,4-disubstituted benzenes. *J Am Chem Soc*. 1984 Nov;106(24):7607–7614.
210. Nishijo J, Moriyama S, Shiota S. Interactions of cholesterol with cyclodextrins in aqueous solution. *Chem Pharm Bull (Tokyo)*. 2003 Nov;51(11):1253–1257.

211. Ruyschaert T, Marque A, Duteyrat J-L, Lesieur S, Winterhalter M, Fournier D. Liposome retention in size exclusion chromatography. *BMC Biotechnol.* 2005 May;5(1):11.
212. Yamamoto S, Kurihara H, Mutoh T, Xing X, Unno H. Cholesterol recovery from inclusion complex of  $\beta$ -cyclodextrin and cholesterol by aeration at elevated temperatures. *Biochem Eng J.* 2005 Feb;22(3):197–205.
213. Machut-Binkowski C, Hapiot F, Cecchelli R, Martin P, Monflier E. A versatile liposome/cyclodextrin supramolecular carrier for drug delivery through the blood-brain barrier. *J Incl Phenom Macrocycl Chem.* 2007 Mar;57(1–4):567–572.
214. Donova MV, Nikolayeva VM, Dovbnya DV, Gulevskaya SA, Suzina NE. Methyl-beta-cyclodextrin alters growth, activity and cell envelope features of sterol-transforming mycobacteria. *Microbiology.* 2007 Jun;153(6):1981–1992.
215. Suárez DF, Consuegra J, Trajano VC, Gontijo SML, Guimarães PPG, Cortés ME, et al. Structural and thermodynamic characterization of doxycycline/ $\beta$ -cyclodextrin supramolecular complex and its bacterial membrane interactions. *Colloids Surf B Biointerfaces.* 2014 Jun;118:194–201.
216. Rosa Teixeira KI, Araújo PV, Almeida Neves BR, Bohorquez Mahecha GA, Sinisterra RD, Cortés ME. Ultrastructural changes in bacterial membranes induced by nano-assemblies  $\beta$ -cyclodextrin chlorhexidine: SEM, AFM, and TEM evaluation. *Pharm Dev Technol.* 2013 Jun;18(3):600–608.
217. Li X, Zhou L, Takai H, Sasaki Y, Mezawa M, Li Z, et al. *Aggregatibacter actinomycetemcomitans* lipopolysaccharide regulates bone sialoprotein gene transcription. *J Cell Biochem.* 2012 Sep;113(9):2822–2834.
218. Santos RS, Figueiredo C, Azevedo NF, Braeckmans K, De Smedt SC. Nanomaterials and molecular transporters to overcome the bacterial envelope barrier: Towards advanced delivery of antibiotics. *Adv Drug Deliv Rev.* 2017 Dec;136–137:28–48.
219. Jeworrek C, Evers F, Howe J, Brandenburg K, Tolan M, Winter R. Effects of Specific versus Nonspecific Ionic Interactions on the Structure and Lateral Organization of Lipopolysaccharides. *Biophys J.* 2011 May;100(9):2169–2177.
220. Le Brun AP, Clifton LA, Halbert CE, Lin B, Meron M, Holden PJ, et al. Structural characterization of a model gram-negative bacterial surface using lipopolysaccharides from rough strains of *Escherichia coli*. *Biomacromolecules.* 2013 Jun;14(6):2014–2022.
221. Santos NC, Silva AC, Castanho MARB, Martins-Silva J, Saldanha C. Evaluation of Lipopolysaccharide Aggregation by Light Scattering Spectroscopy. *ChemBioChem.* 2003 Jan;4(1):96–100.
222. Furse S, Scott DJ. Three-Dimensional Distribution of Phospholipids in Gram Negative Bacteria. *Biochemistry.* 2016 Aug;55(34):4742–4747.
223. Sohlenkamp C, Geiger O. Bacterial membrane lipids: diversity in structures and pathways. Narberhaus F, editor. *FEMS Microbiol Rev.* 2016 Jan;40(1):133–159.
224. Marquardt D, Geier B, Pabst G. Asymmetric Lipid Membranes: Towards More Realistic Model Systems. *Membranes.* 2015 May;5(2):180–196.
225. Clifton LA, Skoda MWA, Le Brun AP, Ciesielski F, Kuzmenko I, Holt SA, et al. Effect of Divalent Cation Removal on the Structure of Gram-Negative Bacterial Outer Membrane Models. *Langmuir.* 2015 Jan;31(1):404–412.

226. Clifton Luke A, Ciesielski F, Skoda MWA, Paracini N, Holt SA, Lakey JH. The Effect of Lipopolysaccharide Core Oligosaccharide Size on the Electrostatic Binding of Antimicrobial Proteins to Models of the Gram Negative Bacterial Outer Membrane. *Langmuir*. 2016 Apr;32(14):3485–3494.
227. Clifton LA, Holt SA, Hughes AV, Daulton EL, Arunmanee W, Heinrich F, et al. An Accurate In Vitro Model of the E. coli Envelope. *Angew Chem Int Ed*. 2015 Oct;54(41):11952–11955.
228. Clausell A, Garcia-Subirats M, Pujol M, Busquets MA, Rabanal F, Cajal Y. Gram-negative outer and inner membrane models: insertion of cyclic cationic lipopeptides. *J Phys Chem B*. 2007 Jan;111(3):551–563.
229. Vollhardt D, Fainerman VB. Progress in characterization of Langmuir monolayers by consideration of compressibility. *Adv Colloid Interface Sci*. 2006 Nov;127(2):83–97.
230. Dynarowicz-Łatka P, Hac-Wydro K. Interactions between phosphatidylcholines and cholesterol in monolayers at the air/water interface. *Colloids Surf B Biointerfaces*. 2004 Aug;37(1–2):21–5.
231. Hughes AV. RasCAL download | SourceForge.net [Internet]. 2013 [cited 2018 Oct 7]. Available from: <https://sourceforge.net/projects/rscl/>
232. Born M, Wolf Emil. Principles of optics: electromagnetic theory of propagation, interference and diffraction of light. Cambridge University Press; 1999. 952 p.
233. Haario H, Laine M, Mira A, Saksman E. DRAM: Efficient adaptive MCMC. *Stat Comput*. 2006 Dec;16(4):339–354.
234. Haario H, Saksman E, Tamminen J. An Adaptive Metropolis Algorithm. *Bernoulli*. 2001 Apr;7(2):223.
235. Duncan SL, Larson RG. Comparing Experimental and Simulated Pressure-Area Isotherms for DPPC. *Biophys J*. 2008 Apr;94(8):2965–2986.
236. Zuo YY, Chen R, Wang X, Yang J, Policova Z, Neumann AW. Phase Transitions in Dipalmitoylphosphatidylcholine Monolayers. *Langmuir*. 2016 Aug;32(33):8501–8506.
237. Shapovalov VL. Interaction of DPPC monolayer at air–water interface with hydrophobic ions. *Thin Solid Films*. 1998 Aug;327–329:599–602.
238. Dahmen-Levison U, Brezesinski G, Möhwald H. Specific adsorption of PLA2 at monolayers. *Thin Solid Films*. 1998 Aug;327–329:616–620.
239. Campbell RA, Saaka Y, Shao Y, Gerelli Y, Cubitt R, Nazaruk E, et al. Structure of surfactant and phospholipid monolayers at the air/water interface modeled from neutron reflectivity data. *J Colloid Interface Sci*. 2018 Dec;531:98–108.
240. Harvey RD, Ara N, Heenan RK, Barlow DJ, Quinn PJ, Lawrence MJ. Stabilization of Distearoylphosphatidylcholine Lamellar Phases in Propylene Glycol Using Cholesterol. *Mol Pharm*. 2013 Dec;10(12):4408–4417.
241. Galdston M, Shah DO. Surface properties and hysteresis of dipalmitoyllecithin in relation to the alveolar lining layer. *Biochim Biophys Acta BBA - Lipids Lipid Metab*. 1967 Apr;137(2):255–263.
242. García-Verdugo I, Cañadas O, Taneva SG, Keough KMW, Casals C. Surfactant Protein A Forms Extensive Lattice-Like Structures on 1,2-Dipalmitoylphosphatidylcholine/Rough-Lipopolysaccharide- Mixed Monolayers. *Biophys J*. 2007 Nov;93(10):3529–3540.

243. Herrmann M, Schneck E, Gutschmann T, Brandenburg K, Tanaka M. Bacterial lipopolysaccharides form physically cross-linked, two-dimensional gels in the presence of divalent cations. *Soft Matter*. 2015 Jul;11(30):6037–6044.
244. Michel JP, Wang YX, Dé E, Fontaine P, Goldmann M, Rosilio V. Charge and aggregation pattern govern the interaction of plasticins with LPS monolayers mimicking the external leaflet of the outer membrane of Gram-negative bacteria. *Biochim Biophys Acta BBA - Biomembr*. 2015 Nov;1848(11):2967–2979.
245. Lee H, Wu W, Oh JK, Mueller L, Sherwood G, Peteanu L, et al. Light-Induced Reversible Formation of Polymeric Micelles. *Angew Chem Int Ed*. 2007 Mar;46(14):2453–2457.
246. Athanassiou G, Michaleas S, Lada-Chitiroglou E, Tsitsa T, Antoniadou-Vyza E. Antimicrobial activity of  $\beta$ -lactam antibiotics against clinical pathogens after molecular inclusion in several cyclodextrins. A novel approach to bacterial resistance. *J Pharm Pharmacol*. 2003 Mar;55(3):291–300.
247. Bhamidimarri SP, Prajapati JD, van den Berg B, Winterhalter M, Kleinekathöfer U. Role of Electroosmosis in the Permeation of Neutral Molecules: CymA and Cyclodextrin as an Example. *Biophys J*. 2016 Feb;110(3):600–611.
248. Charitat T, Lecuyer S, Fragneto G. Fluctuations and destabilization of single phospholipid bilayers. *Biointerphases*. 2008 Jun;3(2):FB3–FB15.
249. Wang Z, Ma Y, Khalil H, Wang R, Lu T, Zhao W, et al. Fusion between fluid liposomes and intact bacteria: study of driving parameters and in vitro bactericidal efficacy. *Int J Nanomedicine*. 2016;11:4025–4036.
250. Los DA, Murata N. Membrane fluidity and its roles in the perception of environmental signals. *Biochim Biophys Acta BBA - Biomembr*. 2004 Nov;1666(1–2):142–157.
251. Chow AHL, Hsia CK, Gordon JD, Young JWM, Vargha-Butler EI. Assessment of wettability and its relationship to the intrinsic dissolution rate of doped phenytoin crystals. *Int J Pharm*. 1995 Dec;126(1–2):21–28.
252. Desjardins A, Chen T, Khalil H, Sayasith K, Lagacé J. Differential Behaviour of Fluid Liposomes Toward Mammalian Epithelial Cells and Bacteria: Restriction of Fusion to Bacteria. *J Drug Target*. 2002 Jan;10(1):47–54.
253. Coates A, Hu Y, Bax R, Page C. The future challenges facing the development of new antimicrobial drugs. *Nat Rev Drug Discov*. 2002 Nov;1(11):895–910.
254. Shen F, Chu S, Bence AK, Bailey B, Xue X, Erickson PA, et al. Quantitation of Doxorubicin Uptake, Efflux, and Modulation of Multidrug Resistance (MDR) in MDR Human Cancer Cells. *J Pharmacol Exp Ther*. 2007 Oct;324(1):95–102.
255. Loh B, Grant C, Hancock RE. Use of the fluorescent probe 1-N-phenylnaphthylamine to study the interactions of aminoglycoside antibiotics with the outer membrane of *Pseudomonas aeruginosa*. *Antimicrob Agents Chemother*. 1984 Oct;26(4):546–51.
256. Hatty CR, Le Brun AP, Lake V, Clifton LA, Liu GJ, James M, et al. Investigating the interactions of the 18kDa translocator protein and its ligand PK11195 in planar lipid bilayers. *Biochim Biophys Acta BBA - Biomembr*. 2014 Mar 1;1838(3):1019–30.

# Appendix A

## Quantum-mechanic rule

According to Planck's hypothesis, an oscillating wave of frequency,  $\nu$ , is directly proportional to a defined energy,  $E$  ('quantum'), via Planck's constant,  $h$  (Equation A1. 1). The velocity of the periodic waves is related to the frequency,  $f$ , and the wavelength,  $\lambda$ , according to Equation A1. 2. Therefore, Planck's equation is transformed as in Equation 1.3

$$E = hf \quad \text{Equation A1. 1}$$

$$v = \lambda f \quad \text{Equation A1. 2}$$

$$E = h \frac{v}{\lambda} \quad \text{Equation A1. 3}$$

De Broglie connected the particle properties (mass and velocity) with a length scale by proposing Equation A1. 4.

$$\lambda = \frac{h}{p} \quad \text{Equation A1. 4}$$

, where  $p$  is momentum of the particle is defined by the vectorial factor between the mass  $m_n$  and velocity  $v$  of the neutron.

$$p = m_n v \quad \text{Equation A1. 5}$$

Taking into account Equation A1. 4 and Equation A1. 5, the particle-like behaviour of the neutron is linked to its kinetic energy  $E$  by the following equation:

$$E = \frac{1}{2} m_n v^2 = \frac{1}{2} \frac{h^2}{m_n \lambda^2} \quad \text{Equation A1. 6}$$

The kinetic energy of a beam of neutrons is thus related to the wavelength of the periodic neutron wave. The energy of the neutron is also dependent upon the temperature  $T$  by a simplified relationship:

$$E = k_B T \quad \text{Equation A1. 7}$$

, in which  $k_B$  is the Boltzmann's constant.



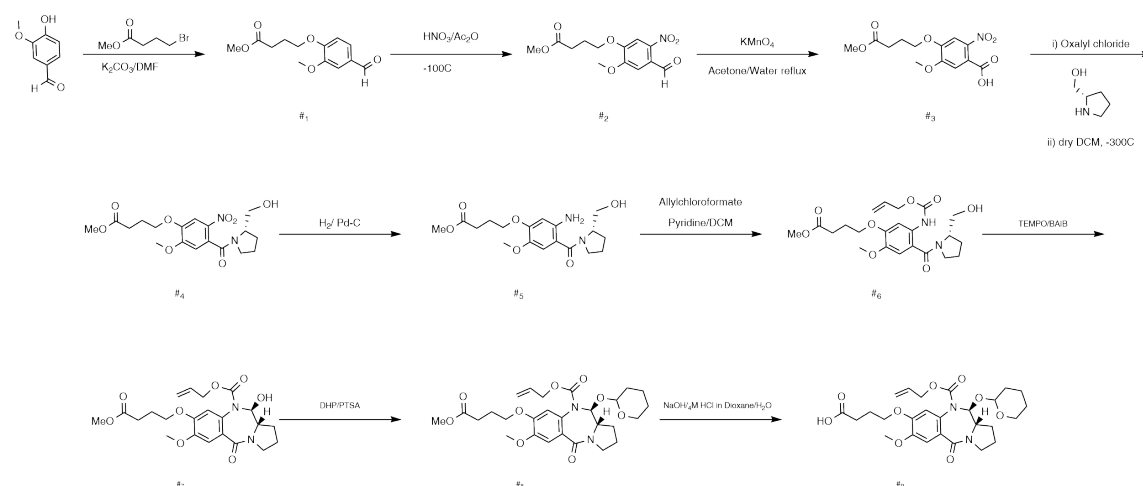
# Appendix B

Table B 1: Minimum Inhibitory concentrations (MIC) of PPA148 against Gram-negative bacteria in the absence and presence of the efflux pump inhibitor Pa $\beta$ N.

Compound	MIC ( $\mu$ g/mL)					
	Acinetobacter baumannii		K. pneumoniae		P. aeruginosa	
	ATCC 17978	AYE	M6	NCTC 13368	PA01	NCTC 13437
PP-A148	2	2	0.25-0.5	16-32	128	16
PP-A148 with Pa $\beta$ N	0.125-0.5	0.125-0.5	0.125-0.25	2-8	4-8	0.25-2

Table B 2: Minimum Inhibitory concentrations (MIC) of PPA148 against Gram-positive bacteria in the absence and presence of the efflux pump inhibitor Pa $\beta$ N.

Compound	MIC ( $\mu$ g/mL)					
	VRE		VSE		MRSA	MSSA
	NCTC 12201	NCTC 12204	NCTC 775	EMRSA 15	EMRSA 16	ARCC 9144
PP-A148	0.25-0.5	0.01	1	2	2	0.5
PP-A148 with Pa $\beta$ N	<0.125	<0.125	<0.125	<0.125	<0.125	<0.125



Scheme B 1: Complete synthetic route of PPA148.

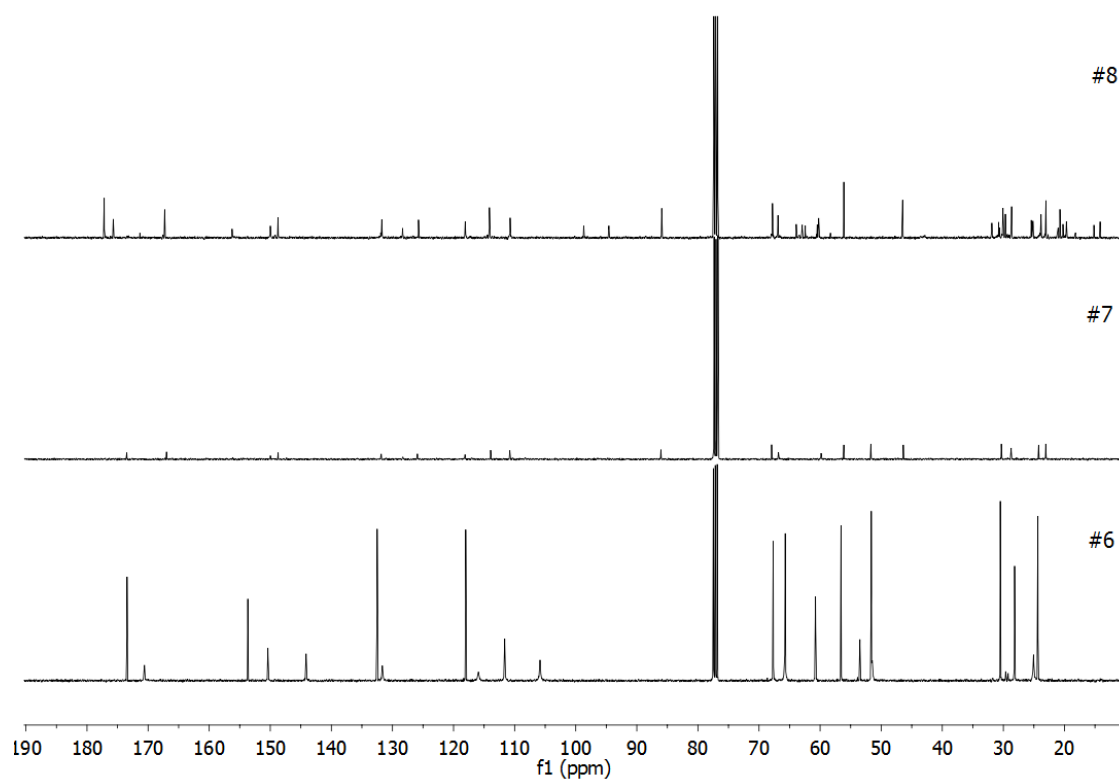


Figure B 1:  $^{13}\text{C}$ NMR of intermediate compounds of the PBD core synthesis. The samples were suspended in deuterated chloroform.

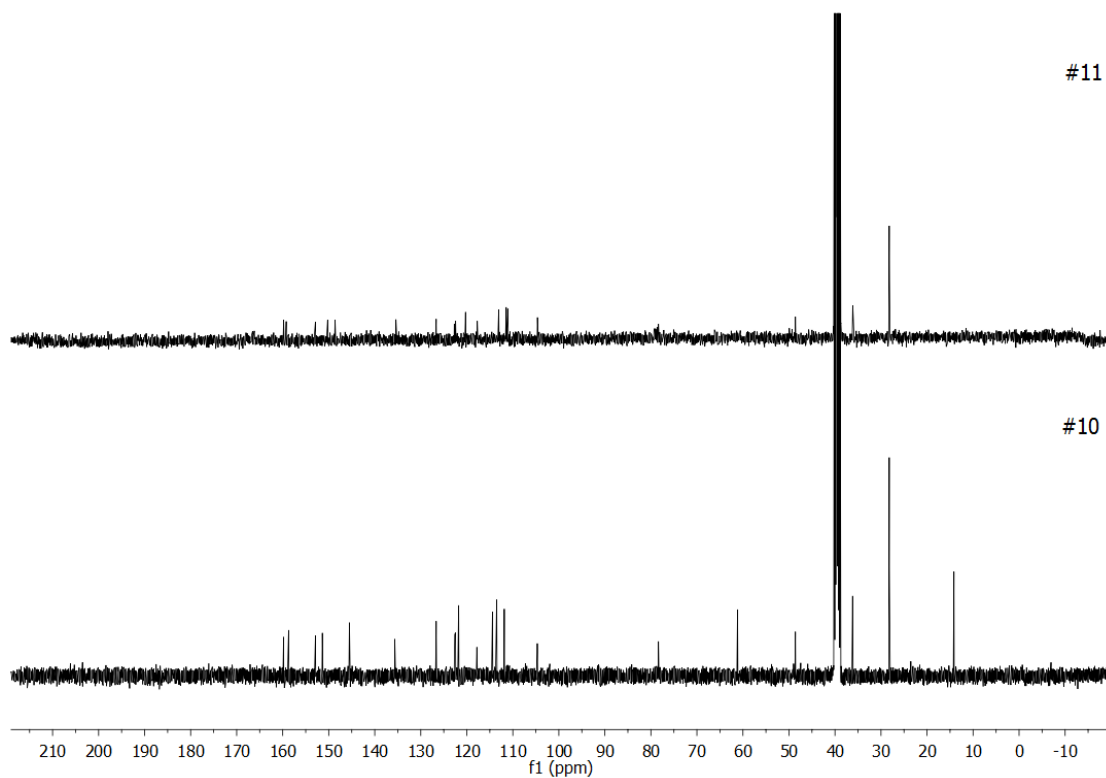


Figure B 2:  $^{13}\text{C}$ NMR of intermediate compounds of the tail synthesis. The samples were suspended in deuterated DMSO.

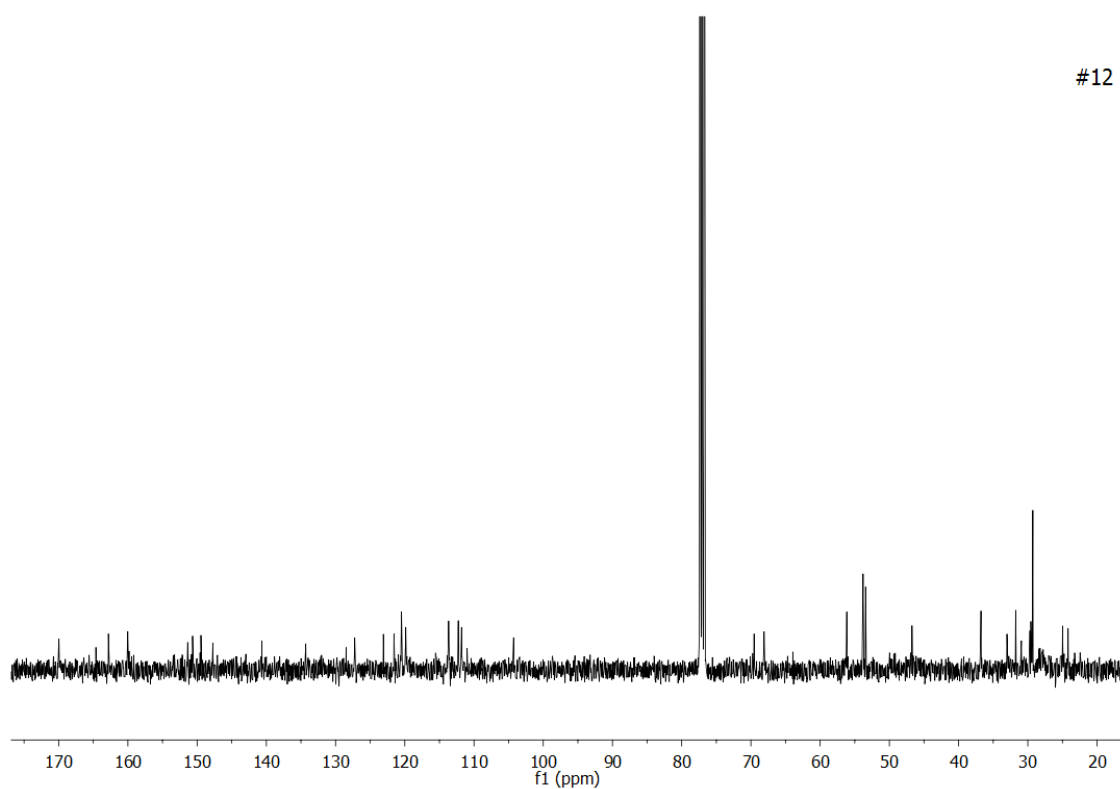


Figure B 3:  $^{13}\text{C}$ NMR of the final compound, PPA148. The sample was suspended in deuterated chloroform.

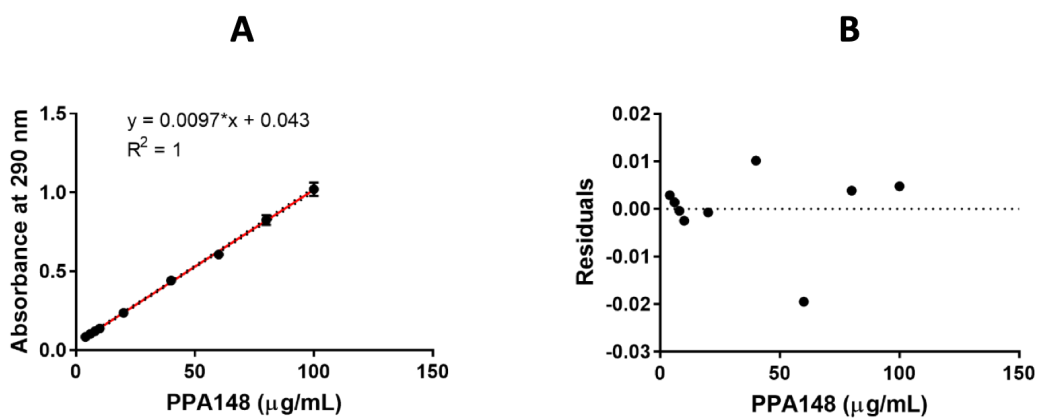


Figure B 4: The linear regression (A) met the assumptions that the residuals follow a normal distribution (B) and their variance is constant (B).

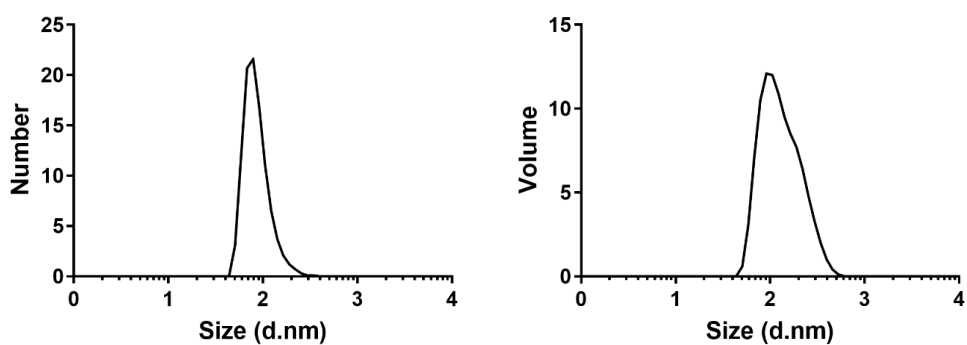
# Appendix C

Table C 1: Number and Volume distribution of empty and loaded fluidosomes.

---

## Empty

---



---

## Loaded with PPA148-RAMEB complex

---

